

# Structure-property relationships and mixed conductivity in layered hybrid perovskites based on phenyl-derived spacers

Présentée le 30 août 2022

Faculté des sciences de base  
Laboratoire de photonique et interfaces  
Programme doctoral en chimie et génie chimique

pour l'obtention du grade de Docteur ès Sciences

par

**Algirdas DUCINSKAS**

Acceptée sur proposition du jury

Prof. M. Chergui, président du jury  
Prof. M. Graetzel, Prof. J. Maier, directeurs de thèse  
Prof. E. Deleporte, rapporteuse  
Prof. A. Mohite, rapporteur  
Prof. K. Sivula, rapporteur

# Acknowledgements

It has been a long journey to arrive at this point. I have met many people and learned a lot, both professionally and personally. This would not have happened if Professor Michael Gratzel had not hired me. Thank you for providing this opportunity, supporting me, and for the freedom, I had during my PhD studies. I was fortunate to work with you, Jovana. Thank you for introducing me to the kingdom of layered perovskites and sharing your passion and optimism when I was experiencing my PhD lows. You are an excellent mentor and manager, and I am confident that a bright future is ahead of you. Hvala! Furthermore, I was highly privileged to conduct part of my PhD work at Max Planck Institute for Solid State Research. Thank you, Professor Joachim Maier, for warmly welcoming me in your group and your support and all the scientific seminars and discussions at Ringberg and Reissensburg Castles. I extend my gratitude to Davide Moia, who readily provided critical feedback, guidance, and supervision; Alessandro Senocrate, who taught me a lot at the beginning of my PhD; and Gee Yeong Kim, for fruitful collaboration and scientific support. Thank you, Heidi, Carmen, Sara, and Madeleine, for handling all the administrative work to ensure that my PhD journey is smooth.

Of course, PhD is not only about science and serious business. Thanks to all my colleagues and PhD fellows with whom I had fun and crazy memories. Thomas, we had a great time sharing the office. Almost every day, we talked about some random things and continuously joked around. I hope our neighboring office-mates were not distracted too much! Natalie, Jun, it was great to start the lunch group with you and enjoy the hikes! Moj čovjek Viktor, I enjoyed your company a lot; you are a crazy guy with lots of positive energy! Sooner or later, I will visit you in Berlin. Thanks, Essa, Olivier, and George, for being my after-work beer buddies. Thank you, Mina and Ya-Ru, for all the dinners and trips we had while staying in Stuttgart. Anand, Jin Hyun, Felix, Sandy, Lukas, Yameng, Ghewa, I enjoyed our chats, lunches, and BBQs. And the list goes on and on. Thank you all!

To my Lithuanian fellows, thanks for continuous support and encouragement. I felt your support every time I was back in Lithuania. Most importantly, I would like to thank my closest ones for believing in me and motivating me to carry on. Without my family and their unconditional love, enormous support, and dedication, I won't be where I am right now. Lastly, I want to share my biggest gratitude to my girlfriend, Emilija. It was a bumpy journey for us, but we persevered and grew stronger and more resilient. Ačiū Tau už viską, maže!

# Abstract

Hybrid halide perovskites are currently one of the most studied semiconductors. However, due to poor intrinsic and extrinsic stability, further developments to commercialize devices based on hybrid halide perovskites are limited. Many different strategies have been used to tackle this issue. Dimensionality reduction of hybrid halide perovskites has proven to be one of the most promising to improve stability or change material functionality. Thus, in my thesis, I focus on the phenyl-derived spacer molecules which form Dion-Jacobson (DJ) type layered hybrid perovskites.

In Chapter 2, I investigated the stability properties of DJ layered hybrid perovskites based on 1,4-phenylenedimethan ammonium (PDMA) spacers. I demonstrated its propensity to hydrate when exposed to a humid environment. Unlike  $\text{MAPbI}_3$ , hydration is reversible as no  $\text{PbI}_2$  was detected after several hydration cycles. Furthermore, we found that the hydration occurs within minutes. It can be significantly slowed down by post-annealing samples in the air. Nonetheless, our results revealed that layered hybrid perovskites are susceptible to humidity.

In Chapter 3, I have extended the study by looking at the spacer size effects on material properties. More specifically, I looked at the role of the alkyl chain length in bifunctional phenyl-derived spacers. We found that in para configuration, at least one methylene group, linking aromatic core and ammonium cation, is needed to form layered hybrid perovskites. Perovskites with the longest spacers show the best stability in humid environments.

In Chapter 4, I have looked at the effects of spacer fluorination. We expected to control the  $\pi$ - $\pi$  interactions between the spacer molecules by incorporating perfluorinated PDMA (F-PDMA) spacers, which have opposite quadrupole moments compared to their nonfluorinated counterpart. However, our study reveals nanosegregation in layered hybrid perovskites based on mixed spacers. Stability tests unveiled higher materials durability in a humid environment when using F-PDMA spacers, which are more hydrophobic than PDMA.

In Chapter 5, I investigated the mechanical properties of DJ and Ruddlesden-Popper (RP) layered hybrid iodide and bromide perovskites. Materials were subject to hydrostatic pressure in the 0–0.35 GPa range to study structure-property relationships. Both RP and DJ perovskites show the most significant compression along the layer stacking direction leading to the reduced quantum confinement evidenced by the redshift in

---

the optical bandgap. Among all the compositions, benzylammonium lead bromide ((BzA)<sub>2</sub>PbBr<sub>4</sub>) exhibited the most significant optical and structural property changes. It is attributed to the non-centrosymmetric crystal structure.

In Chapter 6, I have described the electrical properties of both DJ and RP hybrid iodide perovskites based on PDMA and BzA spacers, respectively. Our results revealed that both perovskites are mixed conductors with very comparable conductivities, which are significantly lower than MAPbI<sub>3</sub>. Surprisingly, the iodine exchange rate in these samples is comparable to three-dimensional hybrid perovskites. The iodine doping experiments suggest that iodide vacancies are the main ionic carriers. Lastly, we obtained 0.6-0.9 eV activation energy for ionic carriers, larger than 3D perovskites. This implies that dimensionality reduction is an effective strategy to reduce ion migration.

**Keywords:** layered hybrid perovskites, hydration, structure-property relationships, mixed conductivity, aromatic spacers



# Résumé

Les pérovskites à halogénure hybrides constituent actuellement l'une des classes de semi-conducteurs les plus étudiées. Cependant, en raison de leur faible stabilité, les développements visant à commercialiser des dispositifs basés sur cette technologie sont limités. De nombreuses stratégies différentes ont été utilisées pour résoudre ce problème. Pourtant, la réduction de la dimensionnalité des pérovskites aux halogénures hybrides s'est avérée être l'une des plus prometteuses pour améliorer la stabilité ou modifier la fonctionnalité des matériaux. Ainsi, dans cette thèse, je me concentre sur les molécules d'espacement dérivées du phényle qui forment des pérovskites hybrides en couches de type Dion-Jacobson (DJ).

Dans le chapitre 2, j'ai étudié la stabilité de pérovskites en couche de type DJ basés sur des molécules d'espacement de type 1,4-phenylenedimethanammmonium (PDMA). J'ai démontré leur propension à s'hydrater lorsqu'exposé à un environnement humide. A la différence de MAPbI<sub>3</sub>, l'hydratation est réversible, comme démontré par l'absence de PbI<sub>2</sub> résiduel après plusieurs cycles d'hydratation. De plus, nous avons observé que l'hydratation prend place dans les premières minutes d'exposition et que ce processus peut être considérablement ralenti en procédant à la cuisson des échantillons à l'air libre. Néanmoins, nos résultats démontrèrent que les pérovskites hybrides en couche sont sensibles à l'humidité.

Dans le chapitre 3, j'ai poussé plus en avant l'étude en me focalisant sur les effets de la taille des espaceurs sur les propriétés des matériaux. Plus spécifiquement, j'ai observé le rôle de la longueur de la chaîne alkyl des molécules d'espacement bifonctionnels dérivés du phényl. Nous avons découvert qu'en configuration para, au moins un des groupes méthylène, liant le noyau aromatique au cation ammonium, est nécessaire pour former une structure en couche. De plus, les pérovskites basés sur les molécules d'espacement avec les linkers les plus étendus montrent la meilleure stabilité dans les environnements humides.

Dans le chapitre 4, j'ai étudié les effets de fluoration de l'espaceur. Nous nous attendions à contrôler les interactions  $\pi$ - $\pi$  entre les molécules d'espacement en incorporant des molécules d'espacement PDMA perfluoré (F-PDMA), qui présentent un moment quadropolaire opposé à leur contrepartie non perfluoré. Cependant, notre étude a révélé l'apparition de nanoségrégation dans les pérovskites en couches basés sur des molécules d'espacement mixtes. Les tests de stabilité démontrèrent une meilleure durabilité en environnement humide pour les structures utilisant des molécules d'espacement perfluorés, étant donné leur caractère plus hydrophobe que le PDMA non fluoré.

---

Dans le chapitre 5, je me suis intéressé aux propriétés mécaniques des pérovskites en couches à base d'iode et de brome en organisation DJ et Ruddlesden-Popper (RP). Les matériaux ont été sujets à une pression hydrostatique comprise entre 0 et 0.35 GPa dans le but d'étudier les relations entre structure et propriétés. Tant les pérovskites DJ que RP subissent la compression la plus importante le long de leur direction d'empilement, menant à un confinement quantique réduit, comme démontré par le redshift dans la bande interdite optique. Parmi toutes les compositions, le bromure de benzylammonium de plomb ((BzA)<sub>2</sub>PbBr<sub>4</sub>) subit les changements de propriétés optiques et structurales les plus importantes. Ceci est attribué à sa structure cristalline non-centrosymétrique.

Dans le chapitre 6, j'ai décrit les propriétés électriques tant des pérovskites hybrides DJ que RP basés sur les molécules d'espacement PDMA et BzA, respectivement. Nos résultats démontrèrent que les deux pérovskites sont des conducteurs mixtes présentant des conductivités très similaires, et qui sont bien moindre que celle de MAPbI<sub>3</sub>. Étonnamment, la vitesse d'échange d'iode dans ces échantillons est comparable aux pérovskites hybrides tridimensionnels. L'expérience de dopage d'iode suggère que les vacances d'iode sont les principaux conducteurs d'ions et nous avons obtenu des énergies d'activation pour les transporteurs d'ions comprises entre 0.6 et 0.9 eV, ce qui est significativement plus grand que pour les pérovskites hybrides en 3D. Ceci implique que la réduction de la dimensionnalité des pérovskites est une stratégie efficace pour prévenir et diminuer la migration d'ion.

Mots-clés: pérovskites hybrides en couches, hydratation, relations structure-propriétés, conductivité mixte, molécules d'espacement aromatiques

# Contents

Acknowledgements .....	i
Abstract .....	ii
Résumé.....	iv
<b>Chapter 1      Introduction .....</b>	<b>9</b>
1.1 The call for sustainable energy technologies .....	9
1.2 Hybrid halide perovskites .....	11
1.3 Layered hybrid perovskites.....	12
1.3.1 Building blocks of spacers molecules .....	15
1.3.2 Prospects of DJ layered hybrid perovskites .....	16
1.4 Thesis goals.....	17
<b>Chapter 2      Stability of Dion-Jacobson hybrid layered perovskites in humid environment .....</b>	<b>18</b>
2.1 Introduction.....	18
2.2 Results and discussion .....	19
2.2.1 Characterization of pristine (PDMA)PbI <sub>4</sub> thin films.....	19
2.2.2 Hydration of (PDMA)PbI <sub>4</sub> thin films .....	21
2.2.3 Reversibility of hydration process.....	24
2.2.4 Kinetics of hydration process .....	25
2.3 Conclusions.....	28
<b>Chapter 3      Effect of increasing alkyl chain length in bifunctional phenyl derived spacers .....</b>	<b>29</b>
3.1 Introduction.....	29
3.2 Results and discussion .....	30
3.2.1 Structural characterization of thin films.....	30
3.2.2 Optical characterization of thin films .....	34
3.2.3 Implications on stability in a humid environment.....	37
3.3 Conclusions.....	40

---

<b>Chapter 4</b>	<b>Effect of spacer perfluorination .....</b>	<b>41</b>
4.1	Introduction.....	41
4.2	Results and discussion .....	42
4.2.1	Structural analysis .....	42
4.2.2	Optical properties .....	45
4.2.3	Stability in a humid environment .....	46
4.3	Conclusions.....	48
<b>Chapter 5</b>	<b>Pressure induced changes in RP and DJ perovskites.....</b>	<b>50</b>
5.1	Introduction.....	50
5.2	Results and discussion .....	53
5.2.1	Structural characterization by means of XRD.....	53
5.2.2	Structural characterization by means of DFT.....	57
5.2.3	Mechanochromic properties .....	59
5.2.4	Correlation between structural and optical properties.....	63
5.3	Conclusions.....	64
<b>Chapter 6</b>	<b>Mixed conductivity of layered hybrid perovskites .....</b>	<b>65</b>
6.1	Introduction.....	65
6.2	Results and discussion .....	67
6.2.1	Thin films for in-plane conductivity .....	67
6.2.2	Galvanostatic measurements of RP and DJ samples.....	68
6.2.3	Iodine incorporation and excorporation kinetics.....	70
6.2.4	Defect chemistry model.....	71
6.2.5	Iodine partial pressure dependent conductivity measurements.....	73
6.2.6	Thermal stability.....	75
6.2.7	Activation energy .....	76
6.3	Conclusions.....	78
<b>Chapter 7</b>	<b>Summary .....</b>	<b>79</b>
7.1	Achieved results.....	79
7.2	Future development .....	81
<b>References</b>	<b>.....</b>	<b>82</b>
<b>Chapter 8</b>	<b>Appendix .....</b>	<b>101</b>
8.1	Supplementary information of Chapter 2 .....	101
8.1.1	Materials and Methods .....	101
8.1.2	X-ray Crystal Structure Analysis .....	102
8.1.3	Thermogravimetric analysis of (PDMA)PbI <sub>4</sub> and (PDMA)I <sub>2</sub> powders .....	103

---

8.1.4	Solid-state NMR Spectroscopy .....	104
8.1.5	Supplementary Spectral Data .....	105
8.2	Supplementary information of Chapter 3 .....	107
8.2.1	Materials and Methods .....	107
8.2.2	PDA Solution Instability and its Effects on Thin Film Properties .....	110
8.2.3	Grazing Incidence Wide Angle X-ray Scattering (GIWAXS) .....	112
8.2.4	Transient Absorption Spectroscopy .....	112
8.3	Supplementary information of Chapter 4 .....	113
8.3.1	Materials and methods.....	113
8.3.2	NMR spectroscopy .....	116
8.3.3	Supplementary data .....	117
8.4	Supplementary information of Chapter 5 .....	119
8.4.1	Materials and Methods .....	119
8.4.2	Supplementary figures and tables.....	122
8.4.3	Synchrotron data analysis and beam damage .....	125
8.5	Supplementary information of Chapter 6 .....	127
8.5.1	Galvanostatic measurements of mixed conductors .....	127
8.5.2	Iodine partial pressure control.....	129
	<b>Curriculum Vitae.....</b>	<b>130</b>

# Chapter 1 Introduction

## 1.1 The call for sustainable energy technologies

Energy is central to the development of humanity. For ages, biomass had been one of the primary energy sources, which was substituted by coal which is more energy-dense. Coal played a crucial role in the first industrial revolution as it had been used to produce coke, the primary fuel in metallurgy to smelt iron. Moreover, coal had been the fuel to power the steam engines in the XVIII-XIX centuries. With the increasing human population and accelerated technological development, more energy resources were needed. Subsequently, the modern era of using oil and gas started in the XIX century, which was adopted in most industry sectors. The demand and investments stimulated an increase in oil production without knowing that the relentless dependence on fossil fuels would pose an existential threat to humanity and the entire ecosystem.<sup>1,2</sup>

Energy from fossil fuels is extracted via combustion reaction with carbon dioxide ( $\text{CO}_2$ ) as a byproduct, which traps heat by absorbing and re-emitting infrared light. Historical data reveals a steadily increasing concentration of  $\text{CO}_2$  (Figure 1:1a).<sup>3</sup> As the concentration of  $\text{CO}_2$  increases, more heat is trapped. The excess heat raises the global temperature, which induces secondary effects, such as methane release from the thawing of permafrost, and increased water vapor content in the atmosphere, effectively trapping more heat and causing global warming. This process features a negative feedback loop that can only be resolved by reducing  $\text{CO}_2$  emissions, which requires controlling the use of fossil fuels as limited and polluting energy resources. However, there is a geopolitical challenge to this issue as vast oil and gas resources are controlled by several countries that are part of the Organization of the Petroleum Exporting Countries (OPEC), which could manipulate oil and gas prices by altering the levels of supply,<sup>4</sup> triggering far-reaching effects on the global economy.<sup>5,6</sup>

In addition, oil and gas can be used as weapons in modern warfare, as exemplified by the currently ongoing Russo-Ukrainian war. For instance, Europe is in a highly vulnerable position due to its heavy reliance on Russian oil and gas. Thus, fossil fuels are inflicting not only global warming but also wars, which could lead to devastating consequences. Therefore, there is substantial pressure on humanity to stop using fossil fuels as soon as possible. This can be facilitated by relying on alternative energy resources to replace fossil fuels. For instance, nuclear, hydro, biomass, wind, and solar energies have already been identified as viable substitutes. Among these energy sources, solar energy has the most significant potential (Figure 1:1b).<sup>7</sup>

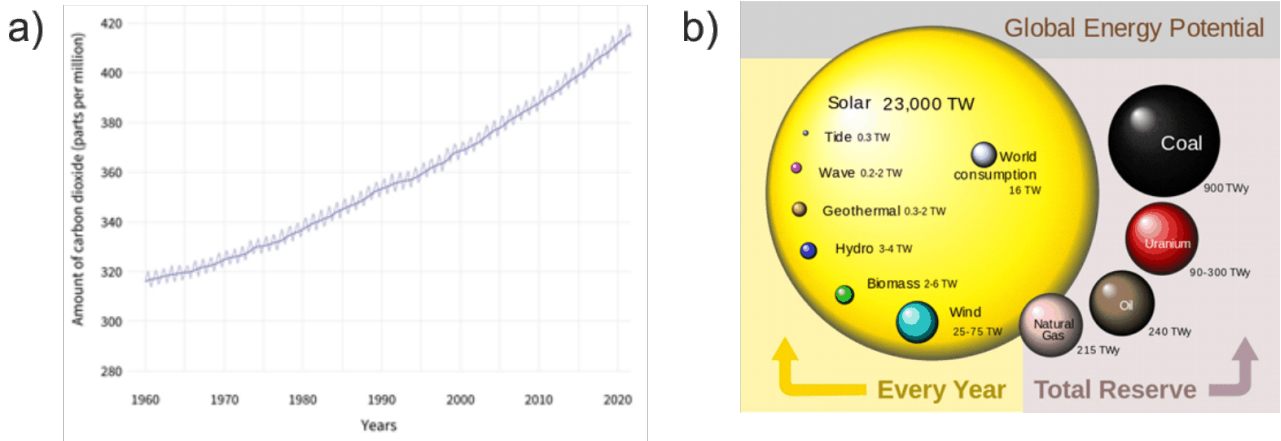


Figure 1:1. (a) Evolution of CO<sub>2</sub> concentration in the atmosphere in 1960-2021,<sup>3</sup> (b) global energy potential by fuel type.<sup>7</sup>

Solar power can be converted into thermal or electrical energy. For solar-to-thermal energy conversion, thermal radiation is collected by the flat solar thermal collectors which transfer the power to the heat exchanger that warms the water in the households. On the utility-scale, solar concentrators, such as parabolic mirrors, are used to improve efficiency. Alternatively, an array of heliostats can be used to focus the sunlight on the receiver, which contains heat transfer fluid such as molten glass. In this case, thermal energy is used to generate steam which powers the electricity generators. However, this technology is not very scalable since it requires large areas to install the arrays of mirrors with two-axis rotors, which help track the motion of the sun. In this regard, technologies converting solar energy directly into electricity are more attractive.

Technologies that utilize photons to generate electricity are called photovoltaic (PV) cells, which are commonly based on stacks of semiconductor materials. The main component in a PV cell is a photoactive semiconductor, which effectively absorbs light and converts it to electron and hole pairs. PV cells can be divided into generations based on the photoactive layer. The 1<sup>st</sup> generation solar cells employ single-crystal or polycrystalline silicon wafers for light harvesting, which is the most mature technology. The 2<sup>nd</sup> generation PV cells are based on thin-film semiconductors such as amorphous silicon, cadmium telluride (CdTe), and gallium arsenide (GaAs). Lastly, the 3<sup>rd</sup> generation is based on the novel photoactive materials, such as organic semiconductors, dye sensitizers, quantum dots, and hybrid halide perovskites. In particular, hybrid halide perovskite solar cells have captured a tremendous amount of attention in the past decade due to its photovoltaic performance (Figure 1:2), which has approached performance levels (25.7 %) of mature technologies such as single crystal silicon cells in just a decade.

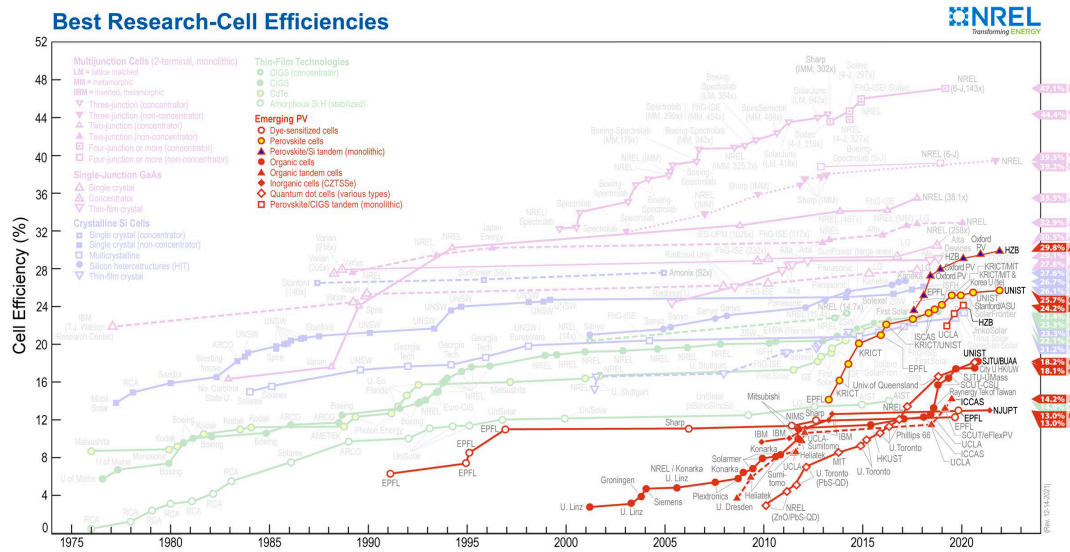


Figure 1:2. Best research-cell solar-to-electric power conversion efficiency chart highlighting the emerging photovoltaic technologies.<sup>8</sup>

## 1.2 Hybrid halide perovskites

Hybrid halide perovskite materials are based on both organic and inorganic building blocks defined by a chemical formula  $ABX_3$ .<sup>9,10</sup> The inorganic sublattice is formed by a three-dimensional network of corner-shared  $BX_6^{4-}$  octahedra, where B are divalent metal cations, such as  $Pb^{2+}$  or  $Sn^{2+}$ , and X are halide anions ( $Cl^-$ ,  $Br^-$  or  $I^-$ ), while A central cations fill the cuboctahedral cavities. Due to geometric limitations reflected in the empirical Goldschmidt's tolerance factor,<sup>11</sup> only certain A cations are compatible with the perovskite structure, such as methylammonium ( $MA^+$ ), formamidinium ( $FA^+$ ), and cesium ( $Cs^+$ ).<sup>12,13</sup> Nonetheless, the chemical space of hybrid halide perovskites offers a vast variety of possible compositions.<sup>14</sup>

Compositional engineering has been extensively used to tune the properties of hybrid perovskite materials.<sup>15</sup> Halide mixing proved to be an effective strategy to modulate the bandgap.<sup>16,17</sup> Alternatively, Pb substitution with Sn can also control the optical bandgap,<sup>18</sup> as the conduction and valence band edges are formed by B and X orbitals.<sup>19</sup> However, Sn-based perovskites suffer from poor stability due to  $Sn^{2+}$  oxidation,<sup>20</sup> making these materials predominantly Pb-based. Lastly, the optical bandgap can be modulated by mixing A cations.<sup>21,22</sup> In this case, local strain affects the lattice parameters and octahedral tilting, changing the B and X orbital overlap and the resulting (opto)electronic structure.<sup>23</sup> It has been demonstrated that A cation can be one of the critical parameters for solar cell performance.<sup>13</sup> Initial studies focused on perovskites based on MA cations,<sup>24</sup> whereas a significant boost was achieved when FA substitutes MA cations.<sup>25</sup> The gains in performance are ascribed to a more optimal bandgap,<sup>26</sup> allowing to reach 25.7 % of power conversion efficiency that is close to the thermodynamic (Shockley-Queisser) limit for the single junction PV cells.<sup>27</sup>



Despite their excellent optoelectronic properties, the perovskite solar cell technology has not yet been fully exploited due to poor material stability. This is related to the effect of external factors, such as humidity, oxygen, heat, and light, which can cause degradation.<sup>28,29</sup> Furthermore, hybrid halide perovskites are mixed ionic-electronic conductors with a significant ionic component. Under operational conditions, the migrating ions might lead to hysteresis effects,<sup>30</sup> suppressed PV performance,<sup>31</sup> or even photodecomposition via iodine excorporation.<sup>32,33</sup> All these shortcomings hold perovskite technology back from full commercialization.<sup>34,35</sup> Many studies report the improved stability after perovskite surface passivation or bulk incorporation with organic ligands, which could lead to the formation of low-dimensional perovskites.<sup>36–40</sup> These materials are thermodynamically more stable than their 3D counterparts due to higher formation energies, as well as higher resilience to external degradation factors.<sup>41–43</sup> This particularly refers to layered (two-dimensional) hybrid perovskites, which belong to the class of low dimensionality perovskites.

### 1.3 Layered hybrid perovskites

The dimensionality of hybrid halide perovskites is defined by the connectivity of the  $\{BX_6\}$  octahedral network (Figure 1:3a). In archetypical perovskite compositions, such as  $MAPbI_3$  and  $FAPbI_3$ ,  $\{BX_6\}$  octahedra extends in three dimensions. On the other hand, layered (two-dimensional, 2D) perovskites consist of perovskite slabs that form a 2D-like network. Further reduction in the octahedron connectivity results in one-dimensional (1D) perovskites followed by zero-dimensional (0D).<sup>44</sup> While three-dimensional perovskites consist of corner-sharing octahedra network, different binding modes (edge, phase-sharing) (Figure 1:3b) are available in lower-dimensional perovskites.

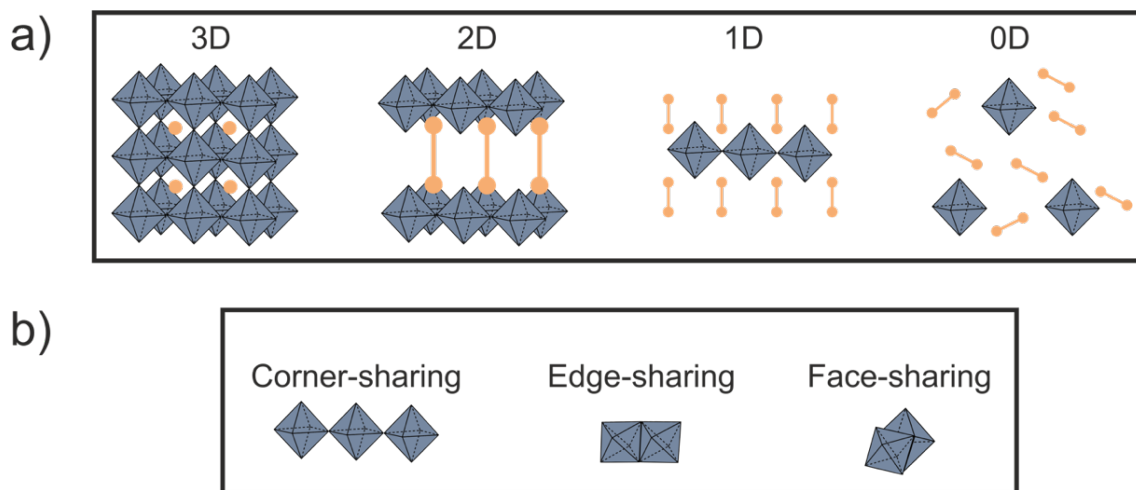


Figure 2:3. (a) Schematic of octahedron network dimensionality. In the 3D case, the network expands in all directions; the 2D connectivity extends along two axes. In the 1D example, the octahedron connects along a single axis, and no network is formed in the 0D case. (b) Possible modes of octahedron connectivity.

Depending on the crystallographic plane that bisects the three-dimensional (3D) perovskite framework (Figure 1:4a-b), layered perovskites can be further classified into (100), (110), or (111) phases.<sup>45</sup> The latter is the least common structure, as it requires trivalent B ions or incorporation of the vacancies on the A site.<sup>46</sup> <100> oriented perovskites (Figure 1:4c) are the most commonly reported. They can be classified into Ruddlesden-Popper (RP),<sup>47</sup> Dion-Jacobson (DJ),<sup>48</sup> and alternating cations (AC),<sup>49</sup> which can be viewed as a combination of RP and DJ archetypes (Figure 1:5). The chemical formula of RP perovskites is  $(A')_2A_{n-1}Pb_nX_{3n+1}$ , with  $A'$  denoting monofunctional spacer and  $n$  the number of perovskite layers, which are displaced with respect to each other by half a unit cell parameter along the in-plane directions (1/2, 1/2).<sup>50</sup> On the other hand, DJ perovskite layers are not displaced and they commonly involve bifunctional spacer molecules binding neighboring perovskite layers, with the chemical formula  $(A'')A_{n-1}Pb_nX_{3n+1}$ , where  $A''$  is a bifunctional spacer. Both DJ and RP phases can be further categorized into compositions based on the number of octahedral perovskite layers ( $n$ ).

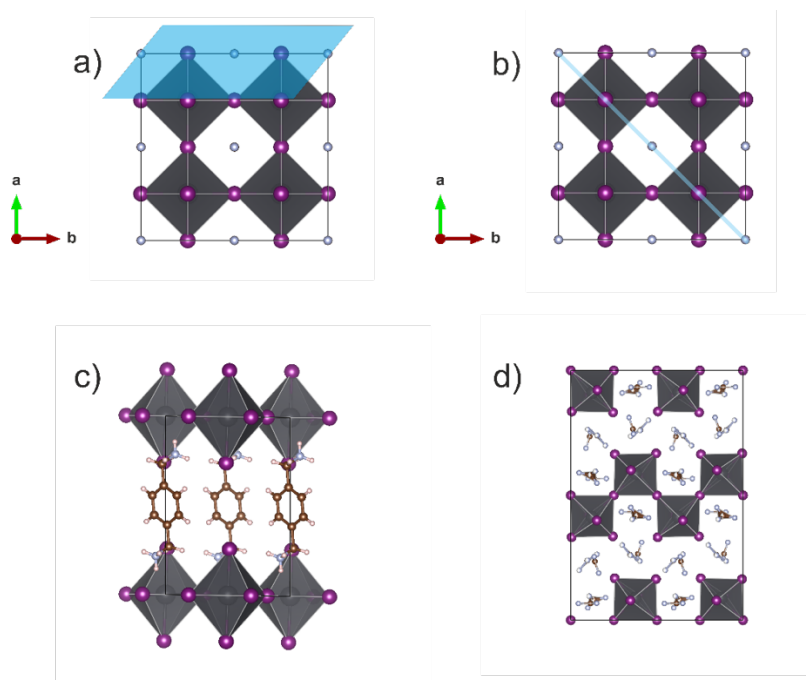


Figure 1:4. Representation of cubic three-dimensional perovskite lattice and its cuts along (a) (100) and (b) (110) direction. Corresponding examples of (c) <100> and (d) <110> oriented layered hybrid perovskites.

Layered hybrid perovskites can be treated as natural quantum well structures as their charge carriers are confined to perovskite slabs, with increasing exciton binding energy as compared to 3D phases.<sup>51</sup> Moreover, the bandgap of common 2D perovskites, such as Pb and I-based  $n = 1$  composition, is above 2 eV,<sup>50</sup> undermining their potential use as efficient photoactive layers. The introduction of quasi-layered perovskites ( $n > 1$ ) allows tuning optical properties as the confinement effects are reduced with an increasing layer thickness

( $n$ ).<sup>50,51</sup> However, maintaining a phase-pure quasi-layered structure is a challenge, as the formation energy of compositions with different  $n$  is closely comparable, leading typically to the formation of mixed phases of various  $n$  compositions that are not determined by the stoichiometry of the precursors.<sup>43</sup>

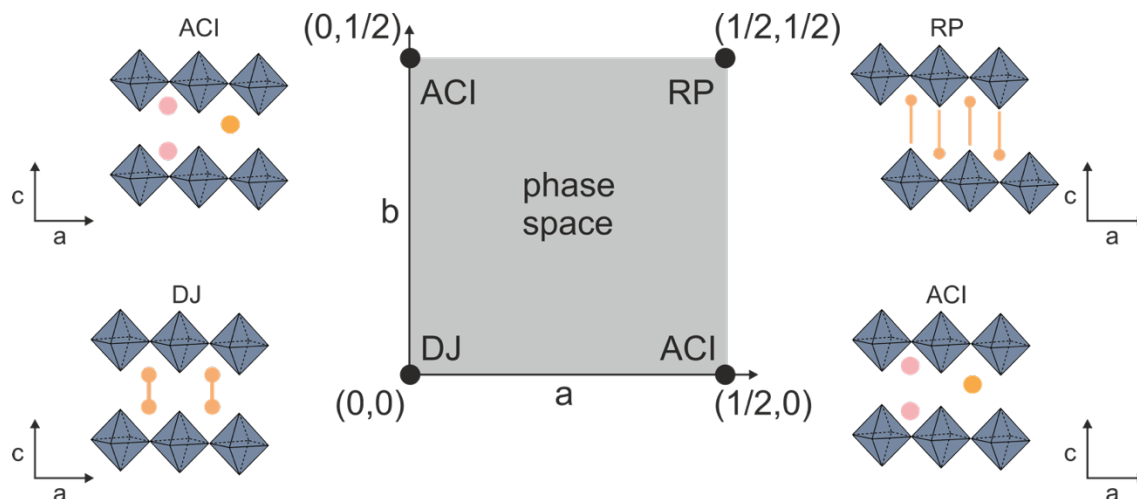


Figure 1:5. Schematic representation of layered hybrid perovskites and their phase which indicate the relative displacements with the adjacent perovskite layers. Layers in DJ perovskites stack directly on top of each other with no displacement (0,0), while RP and ACI form staggered packing arrangements with the (1/2,1/2) and (1/2,0) or (0,1/2), respectively.

The structural and optoelectronic properties of layered hybrid perovskites are dependent on the organic spacer. There are no strict selection rules concerning spacer molecules as long as they are geometrically compatible with the perovskite lattice since the layered structure is more flexible to accommodate various cation sizes, extending the chemical space of layered hybrid perovskites. Based on their functionality, the spacer molecules can be electronically insulating, electroactive, or photoactive.<sup>52</sup> The majority of organic spacers designed to date are electronically insulating, which template the structure of the layered hybrid perovskites and do not directly contribute to the modulation of (opto)electronic properties. (Figure 1:6a) On the contrary, electroactive spacers not only template the growth of layered hybrid perovskites but also contribute to the electronic bandgap formation through the alignment of their highest occupied molecular orbital (HOMO) and/or lowest occupied molecular orbital LUMO levels with the conduction band (CB) and valence band (VB) edges (Figure 1:6b-d).<sup>53,54</sup>

However, the electroactive spacers consist of sterically demanding polycyclic aromatic cores, such as pyrene, perylene, and naphthalene, making their incorporation into perovskite structure challenging. Alternatively, photoactive spacer contributes to the resulting functionality in response to light, such as by undergoing cross-linking via photopolymerization reaction under irradiation.<sup>55</sup> To date, the most attention is attracted to insulating spacers due to their relatively simple structure and accessibility, as well as good compatibility with three-dimensional perovskites and enormous diversity.<sup>56</sup>

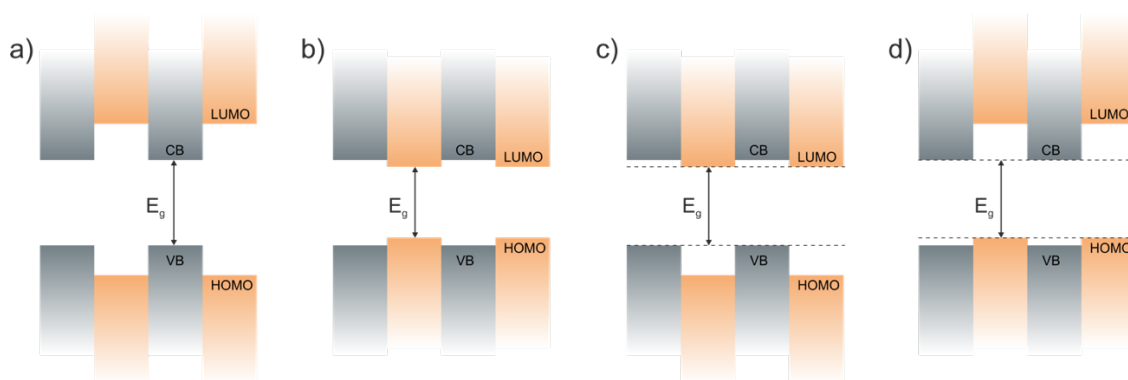


Figure 1:6. Example of the band diagram of layered hybrid perovskites with (a) insulating spacer layers and (b-d) electroactive spacers.

### 1.3.1 Building blocks of spacers molecules

When designing spacer molecules, one should consider three components, namely the core (backbone), anchoring group, and the substituent (functional) groups. The core of the spacer can be aliphatic or aromatic moieties. The former provides flexibility to the spacer, while the latter contributes to its rigidity. This profoundly affects the charge transport properties as the exciton diffusivity increases with the spacer rigidity.<sup>57</sup> Moreover, the length of the aliphatic spacer might affect the light absorption properties<sup>58</sup> and stability<sup>59,60</sup> or even crystal growth and orientation.<sup>61,62</sup> Moreover, the size of the aromatic spacers can influence the phase distribution in quasi-layered perovskites.<sup>63</sup> Additionally, the length and position of the linkers, which connect the core of the spacer with the anchoring group, play a crucial role in controlling the steric hindrance effect. Extended linkers release hindrance, allowing stronger interactions.<sup>53</sup> Alternatively, bifunctional aromatic spacers with para-substitution have the least steric hindrance.<sup>64</sup>

Typically, organic spacers are primary ammonium ions that bind to the inorganic framework. The introduction of secondary, tertiary, or quaternary ammonium salts might be unfavorable due to decreased number of hydrogen bonds and increased steric demand. On the other hand, this opens new avenues for molecular engineering to tune material properties. For instance, it has been demonstrated the propensity of tertiary dipropylammonium iodide salt to form layered perovskites, which shows higher thermal stability than its 3D counterpart.<sup>65</sup> This has been attributed to the higher number of van der Waals interactions which compensate for the negative effect of the lower number of hydrogen bonds. Even spacers with quaternary ammonium anchoring groups (e.g. phenyltrimethylammonium) forms layered perovskites with improved stability.<sup>66</sup> Nonetheless, bulky anchoring groups might induce significant distortions in the perovskite slabs, which would result in larger bandgaps, which is detrimental for PV applications.<sup>67</sup>

---

Other functional substituent groups (-H, -F, -Cl, -OH, -CH<sub>3</sub>) can be incorporated into the spacer, thereby affecting its assembly.<sup>68-70</sup> The position of the substituent can significantly affect the structural disorder in the thin film samples. For example, para-fluorinated phenylethylammonium (PEA) spacers were found to be co-aligned and packed in an ordered way, while ortho- and meta-isomers assemble in a less ordered manner.<sup>70</sup> Although not beneficial to photovoltaics so far, such rearrangements might break the crystal centrosymmetry, providing additional functionality for the potential applications in piezoelectricity or second harmonics generation.<sup>71</sup> Lastly, perfluorinated spacers have enhanced environmental stability due to increased hydrophobicity.<sup>72,73</sup> Other functional groups can contribute to tailoring the assemblies of the spacer layer through various noncovalent interactions, indirectly affecting the properties in perovskite materials and devices.<sup>52</sup>

### 1.3.2 Prospects of DJ layered hybrid perovskites

The nature of spacer cations further defines the layered perovskite phase. Specifically, DJ type layered perovskites typically contain monolayers of bifunctional spacers, whereas RP structure is supported by the bilayers of monofunctional spacers which interact via van der Waals forces. With an additional degree of freedom, monofunctional spacers are more flexible to penetrate deeper into perovskite slabs and establish stronger hydrogen bonding interactions. Due to enhanced attractive forces, in-plane octahedral distortion can be induced.<sup>74</sup> Consequently, B and X orbital overlap reduces as the layers get more distorted, leading to an increase of the bandgap.<sup>75,76</sup> In addition, owing to the van der Waals gap, the interlayer distances in RP perovskites are larger, leading to strengthened charge confinement effects,<sup>77</sup> leading to high exciton binding energies.<sup>51</sup> This impedes charge carrier extraction, which is essential for PV applications. In this regard, DJ type perovskites have more prospects, benefiting from weaker confinement<sup>78,79</sup> due to short interlayer spacing, which might be further reduced under the light.<sup>80</sup>

Environmental stability is one of the most attractive advantages of layered hybrid perovskites. Due to the hydrophobicity of the organic spacer, layered perovskites are reported to have better stability in humid atmospheres than their 3D counterparts.<sup>40,81</sup> The stability depends on the strength of the interaction between organic cations and the inorganic framework.<sup>13</sup> Thus, the stability of layered hybrid perovskites relates to the strength of the assemblies, such as due to hydrogen bonding and van der Waals interactions. This is particularly relevant when comparing DJ and RP phases.<sup>82-84</sup>

The structural difference between DJ and RP perovskite phases might also reflect the mechanical properties, which are very important for strain engineering that has become a topic in the perovskite community.<sup>85,86</sup> Currently, it is known that layered hybrid perovskites are softer than their 3D counterparts, which is attributed to the compressible organic spacer layers.<sup>87,88</sup> Studies on pressure-dependent structural properties

---

report similar behavior of both aliphatic and aromatic spacers.<sup>77,89</sup> However, little is known about the role of the van der Waals gap in determining the mechanical properties.

Finally, ionic migration in layered hybrid perovskites is expected to be reduced due to reduced dimensionality and the insulating spacer layer, consequently further benefiting their intrinsic stabilities. Early reports demonstrated that ion migration in materials based on monovalent spacers, such as n-butylammonium (BA)<sup>90</sup> and 2-phenylethylammonium (PEA)<sup>91</sup> is suppressed, confirming the initial hypothesis. However, the literature on this topic is presently very scarce. Yet, the role of the van der Waals gap in controlling ion migration remains elusive as there are no reports investigating the ionic transport properties of DJ systems. This is an important gap in knowledge on the structure-property relationships of these materials of interest to their application in optoelectronics as well as the emerging field of optoionics,<sup>92</sup> stimulating ongoing investigations.

## 1.4 Thesis goals

This thesis focuses on unraveling the critical structure-property relationships of layered hybrid perovskites based on Dion-Jacobson phases. The research is therefore based on  $n=1$  compositions employing phenyl-derived spacer moieties as model systems, with more emphasis on the DJ phases, which are underrepresented in despite their potential advantages over RP analogues. This has been addressed through the following questions in the thesis.

- How stable are DJ-type perovskites in a humid environment? (Chapter 2)
- What is the role of alkyl chain length of the spacers? (Chapter 3)
- Can perfluorination of the spacer affect the material properties? (Chapter 4)
- How does the van der Waals gap affect the mechanical properties? (Chapter 5)
- What are the mixed conductivity properties of layered hybrid perovskites? (Chapter 6)

Chapters 2 to 5 are based on published studies that were completed over the course of my doctoral research, while Chapter 6 contains the results of the work, which is in preparation for publication. Each of the following chapters includes a more focused introduction to the questions enlisted above while providing specific objectives and methodologies employed in the course of this research.

---

# Chapter 2 Stability of Dion-Jacobson hybrid layered perovskites in humid environment

This chapter is based on the publication in *ACS Energy Letters* entitled:

## Unravelling the Behavior of Dion–Jacobson Layered Hybrid Perovskites in Humid Environments

by:

**Algirdas Dučinskas**, Gee Yeong Kim, Davide Moia, Alessandro Senocrate, Ya-Ru Wang, Michael A. Hope, Aditya Mishra, Dominik J. Kubicki, Miłosz Siczek, Wojciech Bury, Thomas Schneeberger, Lyndon Emsley, Jovana V. Milić, Joachim Maier, Michael Grätzel

My contribution:

Led the project, conceptualized the study, established collaborations, performed most of the experiments, made most of the figures, and wrote the manuscript.

DOI:

<https://doi.org/10.1021/acsenenergylett.0c02344>

## 2.1 Introduction

Despite exceptional photo-electrochemical properties,<sup>9,10</sup> hybrid halide perovskites materials show poor intrinsic and extrinsic stability (towards temperature, electrical bias, light, oxygen and moisture).<sup>29</sup> A possible strategy to improve stability is to introduce large organic cations which, according to the Goldschmidt tolerance factor, cannot fit into the A site,<sup>93</sup> but are able to act as spacer molecules connecting neighboring inorganic layers. The resulting materials are referred to as layered (2D) hybrid perovskites.<sup>94–96</sup> They can be further divided into two main categories, namely Ruddlesden-Popper (RP) phases,<sup>97,98</sup> with chemical formula  $A'_2A_{n-1}B_nX_{3n+1}$  based on monovalent organic spacer ( $A'$ ) bilayers, and Dion–Jacobson (DJ) phases defined by the  $A''A_{n-1}B_nX_{3n+1}$  formula featuring divalent spacer ( $A''$ ) monolayers.<sup>99</sup> For both classes of materials,  $n$  is the number of perovskite layers between each layer of spacer molecules.<sup>73,100,101</sup> The spacer molecules render 2D hybrid perovskites more resilient to moisture as compared to their 3D counterparts,<sup>81,40</sup> therefore, increasing the organic spacer content (i.e. reducing the number of perovskite layers,  $n$ ) is expected to enhance the stability against moisture. Accordingly, it was reported that RP-type layered perovskites based on 2-phenylethylammonium ( $PEA^+$ ) spacer moieties in  $n = 5$  compositions disproportionate upon exposure to humid atmosphere into lower ( $n < 5$ ) compositions.<sup>102</sup> Similar observations apply to butylammonium ( $BA^+$ )-based layered hybrid perovskites.<sup>103–105</sup> Moreover, RP perovskites based on a 1-propylamine spacer exhibit inferior stability as compared to DJ perovskites based on 1,3-diaminopropane analogues, which was attributed to the removal of the van der Waals gap present in RP hybrid perovskites.<sup>106</sup> This

---

suggests that the structure of layered perovskites plays an important role in their stability against humidity and that DJ perovskites have the potential to exhibit enhanced moisture tolerance. However, their behavior in humid environments has not been critically assessed.

Bifunctional spacers directly connect the perovskite layers of the DJ phase,<sup>99,107</sup> resulting in the shorter inter-layer spacing, which could improve charge transfer.<sup>108</sup> For this reason, DJ perovskites have been implemented in PV devices and reached a power conversion efficiency of 18%.<sup>109</sup> Even though DJ phases are expected to exhibit improved extrinsic stability, a few hydrated structures have been reported for perovskites based on bifunctional spacers, such as 2-(aminomethylpyridinium)<sup>110</sup> and 1,4-phenylenediammonium.<sup>111</sup> The examples of hydrated phases comprising bifunctional spacers suggest that DJ perovskite phases might be prone to hydration, which has so far not been demonstrated, despite its relevance for their optoelectronic applications. Therefore, in this chapter I present an study on hydration effects in DJ layered hybrid perovskites based on 1,4-phenylenedimethan ammonium (PDMA<sup>2+</sup>) spacer, which has been reported to be a promising candidate for PV applications.<sup>100,112,113</sup> In contrast to the expected resilience to moisture, we reveal that thin films and powders of (PDMA)PbI<sub>4</sub> ( $n = 1$ ) undergo hydration upon exposure to  $\geq 65 \pm 5\%$  relative humidity, as demonstrated by X-ray diffraction (XRD) and UV-vis absorption spectroscopy, as well as thermogravimetric analysis (TGA) and solid-state NMR spectroscopy. However, the corresponding changes in structural and optical properties could be reverted upon annealing at 150 °C and suppressed by post-synthetic annealing in air. The latter phenomenon was attributed to the generation of PbI<sub>2</sub> that acts as a self-protective layer, retarding humidity-induced changes.

## 2.2 Results and discussion

### 2.2.1 Characterization of pristine (PDMA)PbI<sub>4</sub> thin films

Perovskite thin films of (PDMA)PbI<sub>4</sub> were fabricated via spin-coating with a solution obtained by mixing stoichiometric quantities of the corresponding precursors, followed by annealing at 150 °C for 10 min (detailed information about films preparation is presented in Annex, Section 8.1.1). While  $n = 1$  compositional representatives, such as (PDMA)PbI<sub>4</sub>, might not be the best candidates for photovoltaic applications,<sup>99</sup> they feature the highest relative content of the spacer layer that are thus expected to present the greatest resilience to moisture. Furthermore, unlike  $n > 1$  compositions that form mixtures of quasi-2D and 2D/3D phases in thin films,<sup>94-96</sup> rendering their critical assessment more complex,  $n = 1$  compositions are known to form well-defined 2D phases in thin films. Therefore, they represent appropriate model systems to evaluate the behavior of this class of materials in humid environments.



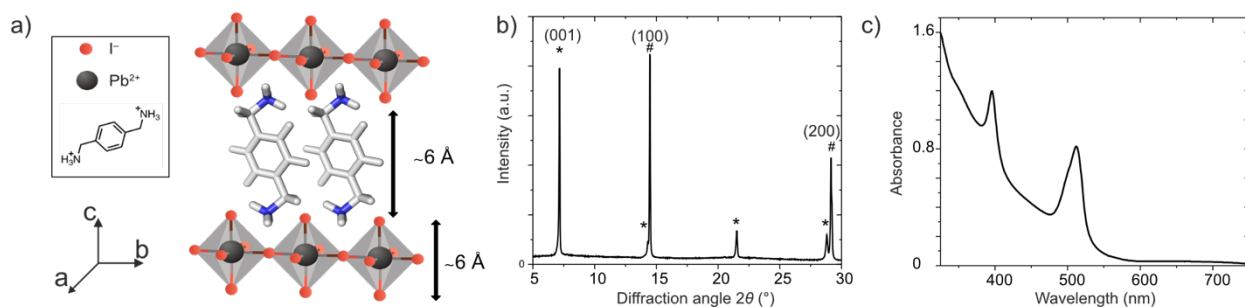


Figure 2:1. (a) Structural representation of the (PDMA)PbI<sub>4</sub> layered structure. Pb<sup>2+</sup> is shown in grey, I<sup>-</sup> is depicted in dark purple, and the PDMA<sup>2+</sup> is depicted with its DFT-calculated structure.<sup>114</sup> (b) XRD of (PDMA)PbI<sub>4</sub> thin films on microscope glass. Peaks denoted with \* belong to (00l) Bragg planes and # to (h00) planes. (c) UV-vis spectrum of (PDMA)PbI<sub>4</sub> thin films on microscope glass.

To confirm the formation of the layered (PDMA)PbI<sub>4</sub> perovskite structure, the films were analyzed by XRD. The diffraction pattern (Figure 2:1b) exhibits a peak at a low diffraction angle ( $2\theta = 7.2^\circ$ ), corresponding to an inter-planar d-spacing of 12.2 Å, which provides a fingerprint of the layered structure.<sup>100, 115</sup> Considering that the PDMA<sup>2+</sup> molecule length and the [PbI<sub>6</sub>]<sup>4-</sup> octahedron size are both approximately 6 Å (Figure 2:1a), this peak is attributed to the (001) reflection. The higher-order (00l) diffraction peaks are found at 14.3, 21.5, and 28.8°. This indicates the presence of crystallites that consist of perovskite layers that are parallel to the substrate.<sup>116, 117</sup> The further peak at 14.5° is assigned to the (100) reflection since the corresponding d-spacing of approximately 6 Å is comparable to the size of the [PbI<sub>6</sub>]<sup>4-</sup> octahedron. The (200) reflection is also observed at 29.1°, and these correspond to crystallites with the perovskite layers perpendicular to the substrate.<sup>81, 118</sup> Thus, crystallites in the analyzed (PDMA)PbI<sub>4</sub> thin films have both perpendicular and parallel orientations, which is in good agreement with previous reports.<sup>100, 115, 119</sup>

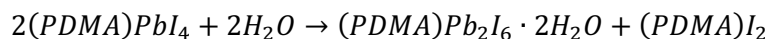
Having demonstrated that (PDMA)PbI<sub>4</sub> forms a layered structure and taking into account that the van der Waals radius of iodide is smaller than the spacing between the inorganic layers,<sup>120</sup> quantum confinement is expected to take place, where the 2D layer of corner-sharing [PbI<sub>6</sub>]<sup>4-</sup> octahedra forms a quantum well structure.<sup>119</sup> Indeed, the UV-vis absorption spectrum of (PDMA)PbI<sub>4</sub> shows a strong excitonic absorption peak located at 510 nm (Figure 2:1c), which indicates significant confinement of the excitons (exciton binding energy  $\gg kT$ ).<sup>51</sup> In addition to the main excitonic peak, an absorption peak is detected at 395 nm, which could correspond to optical transitions to the Rydberg states.<sup>51</sup> This, however, appears unlikely since the energy difference between the two absorption peaks is 0.7 eV, which is higher than the reported exciton binding energies.<sup>51, 121</sup> Alternatively, the absorption peak could be caused by a secondary phase, which is not observed by XRD. Amorphous phases such as reaction intermediates incorporating solvent molecules<sup>122</sup> could be responsible for this second feature. However, a clear solvent dependence of the absorption peak has not been observed (Annex, Figure 8:1:4).

### 2.2.2 Hydration of (PDMA)PbI<sub>4</sub> thin films

Upon exposing the (PDMA)PbI<sub>4</sub> films to  $65 \pm 5\%$  RH, their color changes and the films become pale (Figure 2:2a, inset). These treated films will be further referred to as *hydrated*. Their UV-Vis absorption spectra (Figure 2:2a) clearly indicate that the excitonic peak at 510 nm, which is attributed to the layered structure, is suppressed, whereas the 395 nm absorption peak is enhanced. This observation supports the argument that the 395 nm peak is not caused by the optical transitions to a Rydberg state associated with the low energy absorption peak. Such a strong, localized optical absorption at 395 nm suggests that this peak could come from a phase with reduced dimensionality that forms upon hydration, as reported previously for low-dimensional perovskite materials.<sup>123,39</sup> For instance, hydration studies on MAPbI<sub>3</sub> revealed that, upon exposure to humid air, MAPbI<sub>3</sub> transforms into a 1D hydrated phase,<sup>123,39</sup> which features a localized absorption at c.a. 400 nm, or to a 0D structure.<sup>123</sup> Earlier studies on 1D iodoplumbates also show optical absorption in the 400 nm region.<sup>40</sup> In addition to the reduction in dimensionality, changes in connectivity between [PbI<sub>6</sub>]<sup>4-</sup> octahedra may cause variation in the optical band gap;<sup>41</sup> 1D perovskites with face-sharing octahedra have larger band gaps than their 2D corner-sharing counterparts.<sup>41</sup> Alternatively, the spacing between inorganic perovskite layers may also have an effect on the absorption properties,<sup>124</sup> yet XRD patterns of pristine samples (Figure 2:2b) do not include signals that reveal larger d-spacings. From this we conclude that the absorption at 395 nm corresponds to a low-dimensional phase, the origin of which is not determined in the pristine sample.

To assess variations in the crystal structure and changes in crystallinity, the structural properties of hydrated (PDMA)PbI<sub>4</sub> samples were analyzed by XRD (Figure 2:2b, blue). The most intense peaks of hydrated samples are recorded at 8 and 13° without a set of clear (00 $l$ ) reflections, which implies that the layered structure is disrupted. This observation is in agreement with the decrease in the absorption of the excitonic peak. Moreover, the absence of the peak at 12.8° suggests that the samples do not undergo degradation to form PbI<sub>2</sub>, unlike 3D halide perovskites under comparable experimental conditions.<sup>123</sup> Furthermore, crystallization from a water-based solution enabled a single crystal to be isolated (detailed information about crystal growth is available in Annex, Section 8.1.2). The structure determined by XRD (Figure 2:2b, red) confirms the propensity to form 1D perovskite-like structures with PDMA<sup>2+</sup> in the presence of water. The crystals were found to have a stoichiometry of (PDMA)Pb<sub>2</sub>I<sub>6</sub>·2H<sub>2</sub>O, crystallizing in the monoclinic  $P2_1/n$  space group, with the [Pb<sub>2</sub>I<sub>6</sub>]<sup>2-</sup><sub>n</sub> forming an infinite polymeric chain structure along the crystallographic  $a$ -axis. The PDMA<sup>2+</sup> cations are also aligned, forming stacks along the same axis, whereby the aromatic rings of neighboring spacers interact by parallel-displaced  $\pi \cdots \pi$  stacking interactions with a distance of 3.54 Å. Water molecules and NH<sub>3</sub><sup>+</sup> moieties of the PDMA<sup>2+</sup> ions are involved in the formation of N-H $\cdots$ O hydrogen bonds, forming ladder-like polymeric chains along the  $a$ -axis, which separate [Pb<sub>2</sub>I<sub>6</sub>]<sup>2-</sup><sub>n</sub> polyanions. The simulated XRD pattern of the (PDMA)Pb<sub>2</sub>I<sub>6</sub>·2H<sub>2</sub>O structure (Figure 2:2b, red) closely matches the experimental XRD pattern of the hydrated films (Figure 2:2b, blue), which indicates that this is the 1D phase that forms upon exposure of

(PDMA)PbI<sub>4</sub> to humidity. However, since the PDMA:Pb ratio is different between the initial 2D DJ and hydrated 1D phases, the hydration reaction must also form (PDMA)I<sub>2</sub>, according to the following reaction (Equation 2:1). This is consistent with the (PDMA)I<sub>2</sub> signals observed in the XRD pattern (Figure 2:2b, grey). The scattering power of the lighter (PDMA)I<sub>2</sub> is significantly less than for (PDMA)Pb<sub>2</sub>I<sub>6</sub>·2H<sub>2</sub>O, but the ratios of the observed reflections are approximately consistent with the expected 1:1 atomic ratio.



Equation 2:1 – Hydration reaction formula.

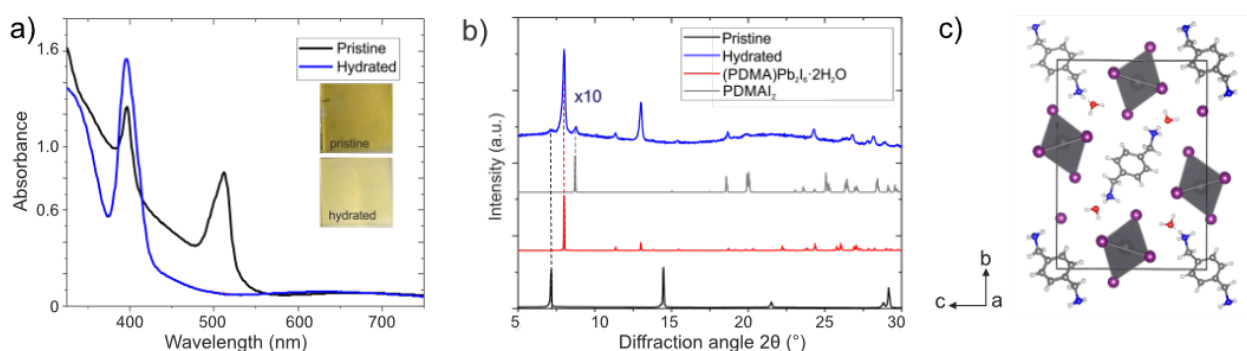


Figure 2:2. (a) UV-Vis absorption spectra of (PDMA)PbI<sub>4</sub> films, before (black) and after (blue) exposure to 65 ± 5% RH. After hydration, the peak at 510 nm is suppressed whereas the one at 395 nm is enhanced. The inset shows photos of pristine (stored in 5 % RH) and hydrated films. (b) XRD patterns of pristine (black), hydrated (blue) films, and the simulated patterns of the hydrated 1D (PDMA)Pb<sub>2</sub>I<sub>6</sub>·2H<sub>2</sub>O structure (red) (shown in c; CCDC number 2041350) and (PDMA)I<sub>2</sub> structure (grey; CCDC number 2041787) based on the single crystal analysis, indicating the disruption of the layered structure upon hydration. The XRD intensity of the hydrated sample is multiplied by 10.

In order to quantitatively determine the water uptake by the thin films and powders, we performed thermogravimetric analysis (TGA) on (PDMA)PbI<sub>4</sub> powders (Annex, Section 8.1.3). This study reveals that at 35 ± 2% RH, there is around 4 at% hydration (Annex, Figure 8:1:1). In comparison, for the (PDMA)I<sub>2</sub> precursor salt, even less hydration was observed (1.8 at% hydration at 35 ± 2% RH) (Annex, Figure 8:1:2). It is assumed that PbI<sub>2</sub> does not hydrate at 35 ± 2% RH since PbI<sub>2</sub> films do not exhibit changes in optical absorption after exposure to a 65 ± 5% RH atmosphere (Annex, Figure 8:1:5). This suggests that it is the structure and packing of such layered perovskites that are required for significant hydration and not the properties of the constituents.<sup>125</sup> The (PDMA)PbI<sub>4</sub> powders show a higher water uptake under 65 ± 5% RH conditions; TGA measurements indicate a hydration stoichiometry of 0.98 ± 0.02 H<sub>2</sub>O per PDMA<sup>2+</sup> (Annex, Figure 8:1:3), in accordance with the 1:1 ratio predicted by hydration reaction (Equation 2:1). Unlike hydrates of MAPbI<sub>3</sub>, which are reported to spontaneously revert to the initial perovskite structure when returned to a 35% RH atmosphere at room temperature,<sup>123</sup> the hydrated (PDMA)PbI<sub>4</sub> phase does not spontaneously convert back to

the layered perovskite structure when the humidity is lowered. Dehydration was not observed even when samples were stored under a ~15% RH argon atmosphere (Annex, Figure 8:1:6). This suggests that the hydrated phase is stable at room temperature.

The structural changes and degree of hydration were further characterized by solid-state NMR of the (PDMA) $I_2$  precursor, mechanosynthesis (PDMA)Pb $I_4$ , and scraped thin films of hydrated (PDMA)Pb $I_4$  (Annex, Section 8.1.4). Following the mechanosynthesis of (PDMA)Pb $I_4$ , significant changes in the  $^1H$  resonances of the PDMA $^{2+}$  moiety are observed compared to the precursor (PDMA) $I_2$  salt (Figure 2:3), corresponding to the substantial change in structure. Upon hydration, the  $^1H$  spectrum changes significantly (Figure 2:3), confirming the considerable structural change shown by XRD. The components arising from (PDMA)Pb $I_6 \cdot 2H_2O$  and (PDMA) $I_2$  cannot be fully resolved. However, an additional intensity corresponding to the  $H_2O$  is observed, and quantification of the  $^1H$  spectrum yields a hydration stoichiometry of 0.86 – 0.99  $H_2O$  per PDMA $^{2+}$  (Annex, Table 8:1:1), which shows that the reactivity of the thin films is the same as for the powders studied by TGA.

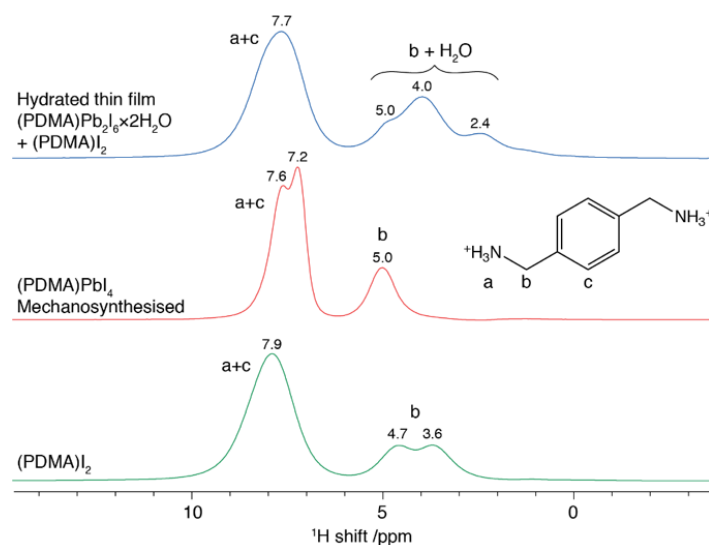


Figure 2:3.  $^1H$  NMR spectra of (PDMA) $I_2$ , mechanosynthesised (PDMA)Pb $I_4$ , and scraped thin films of (PDMA)Pb $I_4$  following hydration. Spectra were recorded at 21.1 T and 50 kHz MAS with a Hahn echo pulse sequence and a 10 s recycle delay. Resonances are labelled with their chemical shift, and assignment according to the inset structure of PDMA $^{2+}$ . Note that in (PDMA) $I_2$  there are two crystallographically distinct  $CH_2$  (b) environments in the structure and for the hydrated sample the PDMA $^{2+}$  resonances in (PDMA)Pb $I_6 \cdot 2H_2O$  and (PDMA) $I_2$  overlap and cannot be fully resolved.

### 2.2.3 Reversibility of hydration process

To probe the reversibility of the hydration process, in-situ temperature-dependent XRD measurements were performed starting from already hydrated powders. Upon heating under a nitrogen atmosphere, the hydrated form reverts to the layered structure at 150 °C, as shown by the disappearance of the diffraction peaks at 8, 9, and 13° (Annex, Figure 8:1:7). Comparable diffraction patterns are observed for pristine and dehydrated samples (Figure 2:4d). However, the crystallinity of the dehydrated (PDMA)PbI<sub>4</sub> is lower compared to the pristine sample. Furthermore, no signals of PbI<sub>2</sub> species can be distinguished, which excludes irreversible degradation during the hydration–dehydration process. In addition, upon dehydration (150 °C for 10 min under an inert atmosphere), the absorption spectra of dehydrated (PDMA)PbI<sub>4</sub> films closely resemble those of the pristine films (Figure 2:4a). The recovery of the optical properties was further assessed by measuring photoluminescence (PL) (Figure 2:4b). While pristine films emit at 517 nm, hydrated samples have broad and weak emission in the range of 400–470 nm. This PL signal is expected to originate from the hydrated phase via trap-assisted emission.<sup>126</sup> Dehydrated samples exhibit strong emission at 518 nm accompanied by a broad emission in the range of 400–470 nm. These results suggest partial reversibility of the hydration-induced structural and optoelectronic changes.

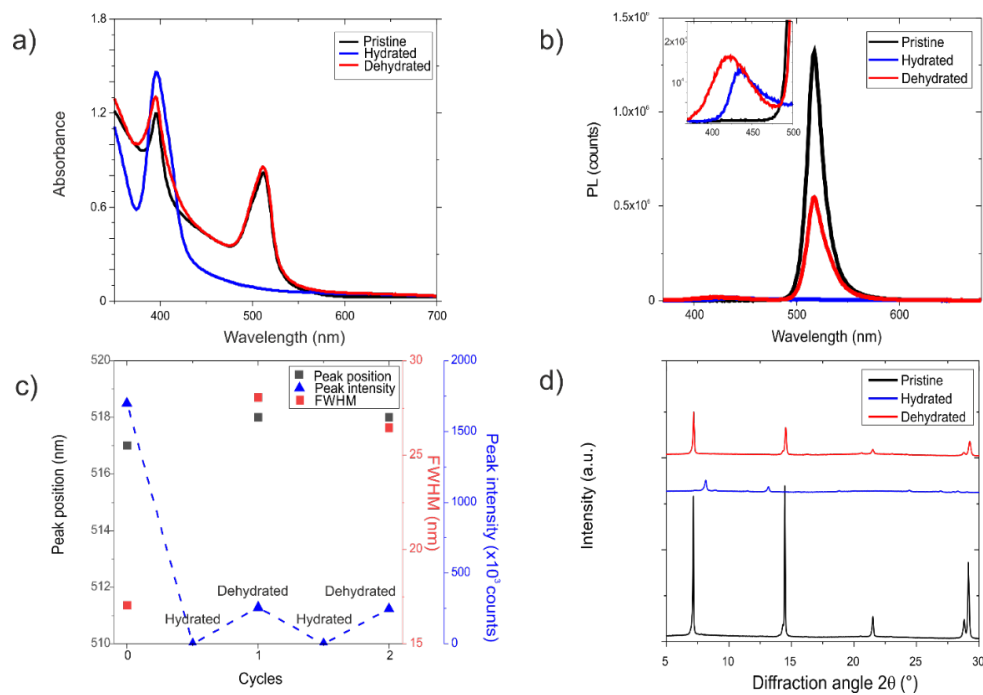


Figure 2:4. (a) UV-Vis absorption spectra of (PDMA)PbI<sub>4</sub> films at different hydration states. (b) PL emission spectra; the inset shows emission in 370 nm to 500 nm, which is attributed to the hydrated (lower-dimensional) phase. Dehydrated samples were heated at 150 °C for 10 min under argon. (c) Evolution of PL parameters: peak position (black rectangles), full width at half maximum (FWHM) (red rectangles), and PL peak intensity (blue triangles) over two hydration and dehydration cycles. (d) XRD diffraction patterns of pristine (black), hydrated (blue), and dehydrated (red) films also indicate the reversible nature of the process.

In order to further address the reversibility of this process, PL emission properties were monitored for two consecutive hydration–dehydration cycles (Figure 2:4c). Pristine films exhibit stronger and narrower PL emission than films after hydration–dehydration, however, the PL emission properties of films after the first and second hydration–dehydration cycles are closely comparable. The drop in PL intensity and peak broadening could be attributed to the structural rearrangements during the 1<sup>st</sup> hydration–dehydration cycle and reduced sample crystallinity. (Figure 2:4d). Such changes in structural and optoelectronic properties upon hydration are observed for the thin films of (PDMA)FAPb<sub>2</sub>I<sub>7</sub>  $n = 2$  compositions as well, indicating that higher compositional representatives are also prone to hydration under comparable mechanism. The XRD pattern of hydrated (PDMA)FAPb<sub>2</sub>I<sub>7</sub> film show diffraction peaks that closely correspond to (PDMA)Pb<sub>2</sub>I<sub>6</sub>·2H<sub>2</sub>O and (PDMA)I<sub>2</sub>, suggesting that the hydration process of  $n = 2$  phases is comparable to the hydration in  $n = 1$  systems (Figure 2:5a). However, unlike  $n = 1$  compositions, they show a lower level of reversibility under comparable experimental conditions as dehydrated films exhibit more prominent  $n = 1$  excitonic peak (Figure 2:5b), which is likely to be associated with higher structural rearrangements that require further analysis which is beyond the scope of this investigation.

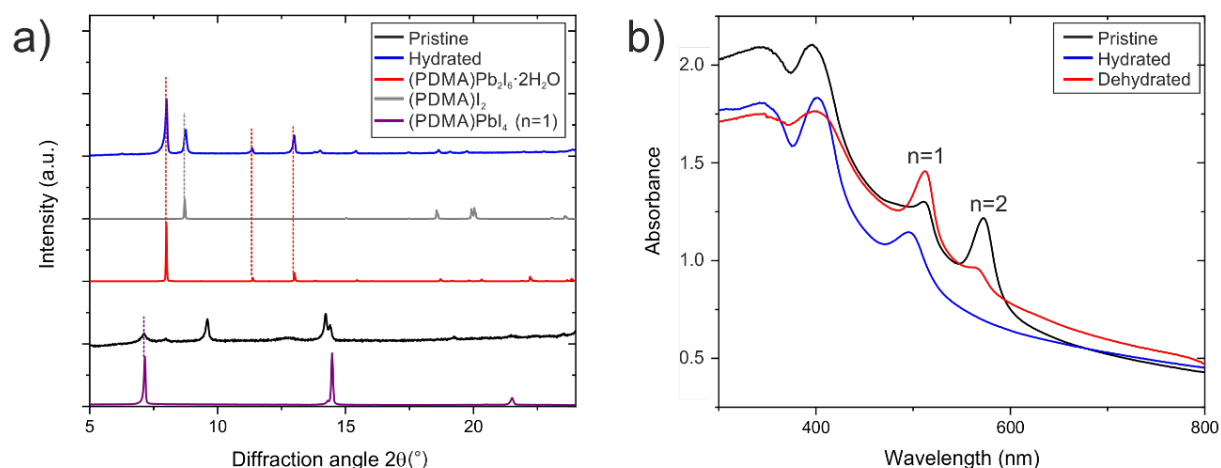


Figure 2:5. (a) XRD patterns of pristine (black) and hydrated (blue) (PDMA)FAPb<sub>2</sub>I<sub>7</sub> ( $n = 2$ ), pristine (purple) (PDMA)PbI<sub>4</sub> ( $n = 1$ ) films, along with the simulated patterns of the hydrated 1D (PDMA)Pb<sub>2</sub>I<sub>6</sub>·2H<sub>2</sub>O (red) and (PDMA)I<sub>2</sub> (grey). (b) UV-Vis spectra of pristine (black), hydrated (blue), and dehydrated (red) (PDMA)FAPb<sub>2</sub>I<sub>7</sub>  $n = 2$  films.

## 2.2.4 Kinetics of hydration process

The reversibility of water-induced changes of structural and optoelectronic properties is highly relevant to the protective role of 2D perovskites in perovskite solar cells. For this purpose, it is important to estimate the rate of such changes. We, therefore, performed in-situ UV–vis absorption measurements of  $n = 1$  samples exposed to a humid ( $65 \pm 5\%$  RH) atmosphere. To determine the kinetic profile of the hydration

process, we monitored the evolution of the optical absorption over time (Figure 2:6a) and analyzed the normalized intensity of optical absorption at 510 nm at different time instances (Figure 2:6c). The evolution of the absorption suggests that pristine (PDMA)PbI<sub>4</sub> films hydrate within minutes at  $65 \pm 5\%$  RH. The hydration kinetics are dependent on the relative humidity level, with higher RH ( $\sim 80\%$ ) atmospheres causing a faster hydration process (Annex, Figure 8:1:8), which is in agreement with previous observations.<sup>127,128</sup>

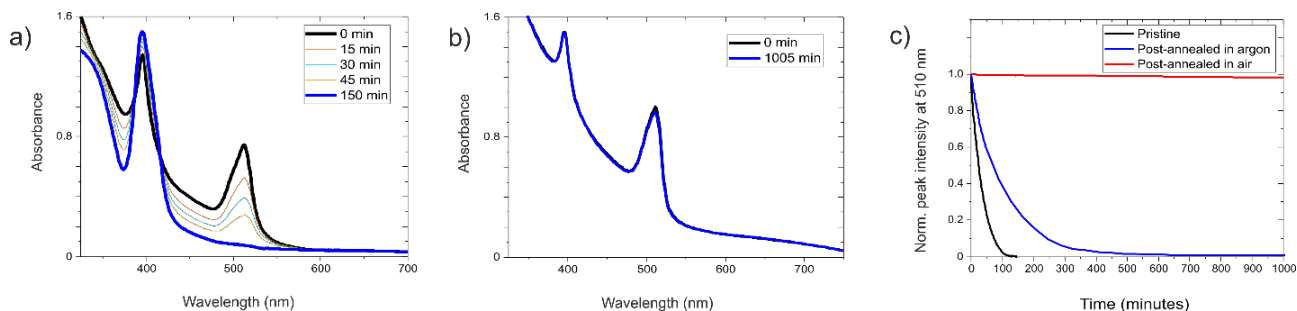


Figure 2:6. (a) In-situ UV-Vis absorption spectra of pristine (PDMA)PbI<sub>4</sub> films that have been exposed to the  $65 \pm 5\%$  RH in argon atmosphere for 150 min; the excitonic peak at 510 nm is gradually suppressed and it completely diminishes after 150 min (blue line). (b) In-situ UV-Vis absorption spectra of samples post-annealed in air for 10 min at 150 °C before (black line) and after being exposed to  $65 \pm 5\%$  RH argon atmosphere for 16 h and 45 min (blue line). (c) The hydration kinetic profiles of pristine (black), post-annealed in argon (blue), and post-annealed in air (red) samples were acquired by monitoring the intensity of the absorption peak at 510 nm.

Thus far, we have analyzed data referring to thin films or powders of (PDMA)PbI<sub>4</sub> which were annealed in argon atmosphere. We now explore the effect of supplementary post-synthetic annealing (hereinafter referred to as *post-annealing*) step performed either in argon or ambient atmosphere. The hydration is suppressed by post-annealing samples in air at 150 °C for 10 min prior to the hydration step, with the samples showing a remarkably improved resilience to moisture (Figure 2:6b). A comparison of the optical absorption as a function of time (Figure 2:6c) unambiguously shows that the hydration rate is slowed significantly when the sample had been post-annealed in air (red curve) as compared to the pristine sample (black curve) or to a sample that had been post-annealed in argon (blue curve).

To identify the origin of hydration resilience, we performed X-ray photoelectron spectroscopy (XPS) and monitored the changes in surface chemistry. During the post-annealing process in air, (PDMA)PbI<sub>4</sub> may react with oxygen and form PbO/PbO<sub>2</sub>,<sup>129</sup> we therefore investigated the possibility of forming such a capping layer that could slow down the hydration. However, Pb 4f core level spectra (Figure 2:7a) show no difference between pristine and post-annealed in air samples, which is corroborated by the I 3d and O 1s spectra (Annex, Figure 8:1:9), implying that PbO/PbO<sub>2</sub> is not generated upon post-annealing in air. Alternatively, instead of lead oxides, a PbI<sub>2</sub> layer could form during the post-annealing step.<sup>129</sup> This could also act as a protective layer since PbI<sub>2</sub> films do not appear to hydrate upon exposure to humidity, as monitored by in-situ UV-Vis measurements. As the chemical environments of Pb<sup>2+</sup> ions in (PDMA)PbI<sub>4</sub> and PbI<sub>2</sub> are comparable, XPS is



unable to discern the difference. Therefore, we analyzed the films using grazing-incidence XRD measurements. The recorded diffraction patterns of pristine samples and those post-annealed in argon and air (Figure 2:7b) do not exhibit significant differences in either peak positions or peak intensities, in accordance with a comparable crystal structure for all samples. However, the inset shows that post-annealed in air samples feature a very small diffraction peak at  $12.8^\circ$ , which corresponds to  $\text{PbI}_2$ . After longer post-annealing in air, the diffraction peak at  $12.8^\circ$  becomes more pronounced (Annex, Figure 8:1:10) strongly indicating that during this process the  $\text{PbI}_2$  is gradually generated.

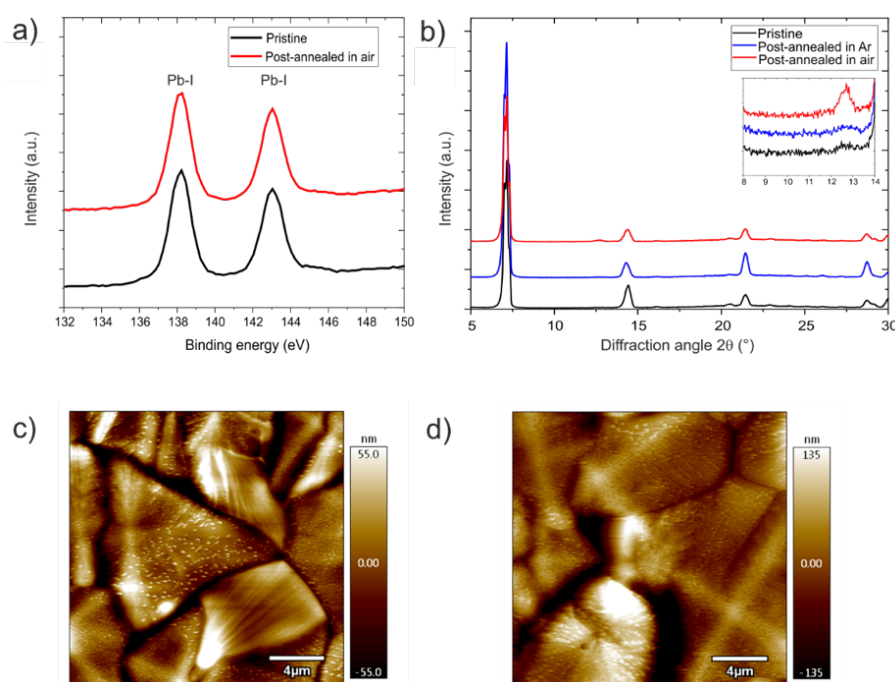


Figure 2:7. (a) X-ray photoelectron spectra (XPS) in the Pb 4f core level range of pristine (black) and post-annealed (red) samples of  $(\text{PDMA})\text{PbI}_4$ . (b) Grazing incidence XRD measurements of pristine (black), post-annealed in argon (blue) and post-annealed in air (red) samples of  $(\text{PDMA})\text{PbI}_4$  before hydration indicate comparable crystal structures. However, the inset shows a very small  $\text{PbI}_2$  peak that is apparent when the sample is post-annealed in air. (c–d) Surface morphology images obtained by atomic force microscopy (AFM) suggest that both pristine (c) and post-annealed (d) films consist of grains that are of comparable size. Post-annealing was performed for 10 min at  $150^\circ\text{C}$  in air.

Based on the observation of a low degree of hydration for  $\text{PbI}_2$  thin films, this result suggests that  $\text{PbI}_2$  formation may be responsible for the increased resilience to hydration of samples post-annealed in air. Another possibility is that the difference in hydration rates is due to differences in the sample microstructure. For example, assuming that water molecules have a faster diffusion through grain boundaries, the hydration of polycrystalline materials with larger grains should be slower. Atomic force microscopy (AFM) images of pristine  $(\text{PDMA})\text{PbI}_4$  films reveal large grains of several  $\mu\text{m}$  (Figure 2:7c). Upon post-annealing in air, the sample roughness increases, yet the grain size remains comparable (Figure 2:7d). We can thus conclude that the morphology does not significantly contribute to the suppression of the hydration, which can instead be



---

mainly attributed to the generation of  $\text{PbI}_2$ . However, future work will be needed to assess if and how the grain boundaries are involved in the hydration process, as well as to determine a detailed mechanistic understanding of this phenomenon. From our findings, we infer that during the post-annealing process in air, a thin self-protective layer of  $\text{PbI}_2$  is generated, and consequently, the structure and optical absorption of post-annealed 2D perovskites stabilize in humid environments. This provides a new route for increasing the moisture stability of layered hybrid perovskites. Furthermore, the analysis of the 2D  $n = 1$  composition provides the basis for extending the understanding to  $n > 1$  quasi-2D and 2D/3D perovskite systems that are expected to be highly relevant for photovoltaic applications in the future.

## 2.3 Conclusions

In this chapter, I have presented the results of investigations of the effects of humidity on Dion–Jacobson-type 2D layered hybrid perovskites of  $(\text{PDMA})\text{PbI}_4$  composition. I have demonstrated that within minutes of exposure to  $65 \pm 5\%$  RH, a structural transformation takes place that disrupts the layered perovskite structure, as observed by XRD, solid-state NMR and UV-vis optical absorption spectroscopy. The formation of 1D perovskite-like chains with water molecules is further evidenced by single-crystal X-ray structure analysis. The observed hydration-induced processes are partially reversible when annealing the powders and thin films at  $150^\circ\text{C}$  in an inert atmosphere, while the rate of hydration could be retarded by post-synthetic annealing in air before exposure to humidity. We assign this effect to the formation of a thin layer of  $\text{PbI}_2$ , which likely protects the 2D perovskite. This study thereby evidences the tendency of a 2D DJ layered perovskite to hydrate in humid atmosphere. Moreover, it provides a new strategy to improve the resilience of layered hybrid perovskites against moisture, which is relevant for the stabilization of hybrid perovskite-based optoelectronic devices.

---

## Chapter 3 Effect of increasing alkyl chain length in bifunctional phenyl derived spacers

This chapter is based on the publication in *The Journal of Physical Chemistry Letters* entitled:

### **The Role of Alkyl Chain Length and Halide Counter Ion in Layered Dion–Jacobson Perovskites with Aromatic Spacers**

by:

**Algirdas Dučinskas**, George C. Fish, Michael A. Hope, Lena Merten, Davide Moia, Alexander Hinderhofer, Loïc C. Carbone, Jacques-Edouard Moser, Frank Schreiber, Joachim Maier, Jovana V. Milić, Michael Grätzel

My contribution:

Led the project, conceptualized the study, performed optical, XRD measurements, made most of the figures, and wrote the manuscript.

DOI:

<https://doi.org/10.1021/acs.jpcclett.1c02937>

### 3.1 Introduction

While the use of layered perovskites significantly widens the compositional space available for optoelectronic devices, there are several intrinsic problems. The identification of compounds that can be processed into phase-pure 2D perovskite films with suitable structural and optical properties is a key challenge.<sup>130–132</sup> Depending on the application, environmental stability can also be an important constraint.<sup>133</sup> Furthermore, due to insulating spacer molecules, the conductivity of these materials is lower as compared to the 3D hybrid perovskites.<sup>134</sup> This can be to some extent circumvented by changing the number ( $n$ ) of perovskite layers, which defines the quantum well thickness and optoelectronic properties.<sup>135</sup> Nonetheless, as  $n$  increases the phase purity becomes an issue.<sup>130–132</sup> Moreover, recent work showed that even the issue of photo-induced phase instability also affects mixed halide 2D systems.<sup>136,137</sup>

To address these and other challenges, significant effort has been spent towards the development and investigation of suitable spacers, including aliphatic,<sup>106,138,139</sup> aromatic,<sup>140,141</sup> heterocyclic,<sup>107,116</sup> and polycyclic aromatic molecules.<sup>142</sup> Due to the plethora of spacers available, a holistic understanding of structure–property relationships in layered perovskites is essential to provide material design rules. Typically, when designing a spacer, one should consider its geometry and functional groups, including the core of the spacer (e.g. aromatic moieties), the length of the anchoring group (e.g. alkylammonium chain), and the counter ions (e.g.  $\Gamma^-$ ,  $\text{Br}^-$ ). Based on the previous reports for RP-type layered perovskites, the penetration depth of the anchoring

group into the perovskite layers, which correlates with the length of the alkylammonium chain, has a strong effect on structural and optoelectronic properties.<sup>54,141</sup> Hitherto, the corresponding effect of the length of the anchoring alkylammonium group on the DJ phases is not well understood, despite the importance of the spacer group on the resulting properties.

In this study, we analyze hybrid halide perovskites based on bifunctional 1,4-phenylene derived analogues of one of the most studied organic spacers, 2-phenethylammonium (PEA),<sup>143,144</sup> namely 1,4-phenylenediammonium (PDA), 1,4-phenylenedimethylammonium (PDMA) and 1,4-phenylenediethylammonium (PDEA) (Figure 3:1a). While I-based systems incorporating PDA or PDMA spacers have been previously reported,<sup>100,111,133,145</sup> PDEA remains unexplored. To minimize the level of complexity and issues associated with phase purity we focus on  $n = 1$  layered perovskite compositions based on iodide and bromide halides (Figure 3:1b). We demonstrate that the control of the spacer length affects material dimensionality, optical properties, and environmental stability, which is particularly enhanced for longer alkyl chains and bromide compositions.

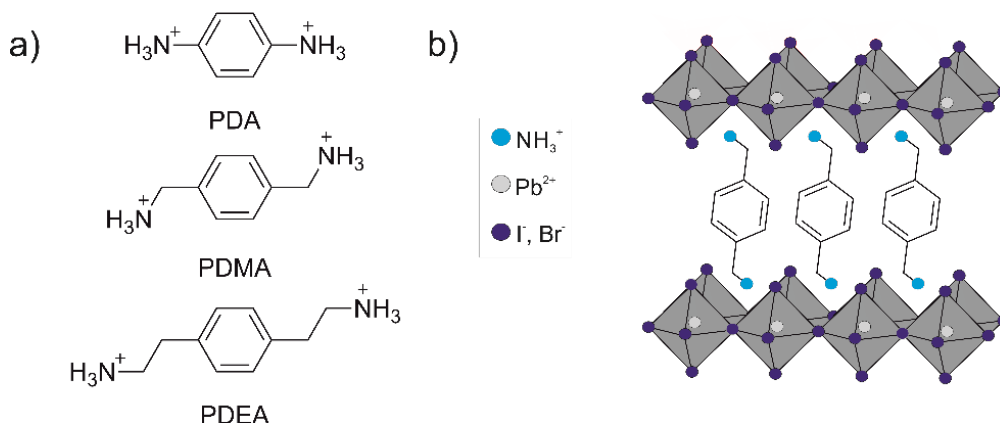


Figure 3:1. (a) Molecular structures of PDA, PDMA and PDEA organic spacers. (b) Illustration of layered DJ perovskite structure based on (PDMA) $\text{PbX}_4$  composition.

## 3.2 Results and discussion

### 3.2.1 Structural characterization of thin films

We studied layered hybrid perovskites based on the (S) $\text{PbX}_4$  ( $n = 1$ ) composition, where S = PDA, PDMA, or PDEA, and X = I or Br. The synthetic procedure is detailed in the Appendix, Section 8.2.1. For simplicity, (S) $\text{PbX}_4$  materials based on PDA, PDMA, or PDEA spacers will be denoted as PDA-X, PDMA-X, and PDEA-X, respectively, depending on the halide counter ion (X = I, Br). The structure of thin films deposited on glass substrates was investigated by means of X-ray diffraction (XRD). The XRD pattern of PDA-I (Figure 3:2a, black) corresponds to the (PDA) $\text{PbI}_4 \cdot 2\text{H}_2\text{O}$  dihydrate (Figure 3:2a, green), which is a

one-dimensional (1D) perovskite, indicating that a layered phase has not formed.<sup>111</sup> This is likely due to the lack of flexibility of the PDA spacer,<sup>146</sup> as well as its lower level of penetration into the neighboring perovskite layers, which prevents the formation of a layered phase.<sup>147,148</sup> In addition, the PDA-I precursor solution changes its properties over time, which is likely due to the oxidation and subsequent polymerization of (PDA)I<sub>2</sub> (Appendix, Section 8.2.2).<sup>149</sup> A significant difference in the behavior of the spacer was observed when the alkyl chain length of the spacers was extended by one methylene ( $-\text{CH}_2-$ ) group; the PDMA-I films show typical layered perovskite diffractograms with a sharp diffraction peak at  $7.19^\circ$ , which corresponds to the (001) reflection with a layer spacing of  $12.3 \text{ \AA}$ , along with higher order diffraction peaks of the (00 $l$ ) Bragg planes family (Figure 3:2a, red).<sup>100,133</sup> Further extension of the spacer to PDEA led to a larger lattice parameter, evidenced by the diffraction peak located at  $6.98^\circ$  (Figure 3:2a, blue), corresponding to a layer spacing of  $12.7 \text{ \AA}$ . However, the crystallinity of the PDEA-I system appears to be lower as compared to PDMA-I, resulting in broader diffraction peaks and the higher order reflections are hardly resolved.<sup>150</sup>

The XRD patterns of Br-based films (Figure 3:2b) show the effect of the halide on structural properties. In contrast to PDA-I, the Br-based analogue forms crystalline films with the most intense peak at  $7.42^\circ$ , corresponding to a  $d$ -spacing of  $11.9 \text{ \AA}$ , accompanied by higher order reflections (Figure 3:2b, black). However, there are two additional peaks below  $10^\circ$  located at  $5.90^\circ$  and  $7.0^\circ$ , which are not attributable to a layered structure. This might be related to the unstable PDA-Br solution (Appendix, Section 8.2.2). In addition, considering previous reports on the corrugated structure of perovskites based on a monofunctional (4-bromophenyl)ammonium spacer,<sup>151</sup> which is comparable to PDA, we suspect that the PDA-Br system might form a corrugated structure. As in the iodide-based systems, the extension of the alkyl chain by one methylene resulted in a well-defined layered PDMA-Br material with the basal peak centered at  $7.26^\circ$  (Figure 3:2b, red), corresponding to a  $d$ -spacing of  $12.2 \text{ \AA}$ . The XRD of PDEA-Br showed only a single broad peak located at  $7.01^\circ$  with a layer spacing of  $12.6 \text{ \AA}$  (Figure 3:2b, blue), hinting at a lower crystallinity and an increased lattice parameter as compared to PDMA-Br.

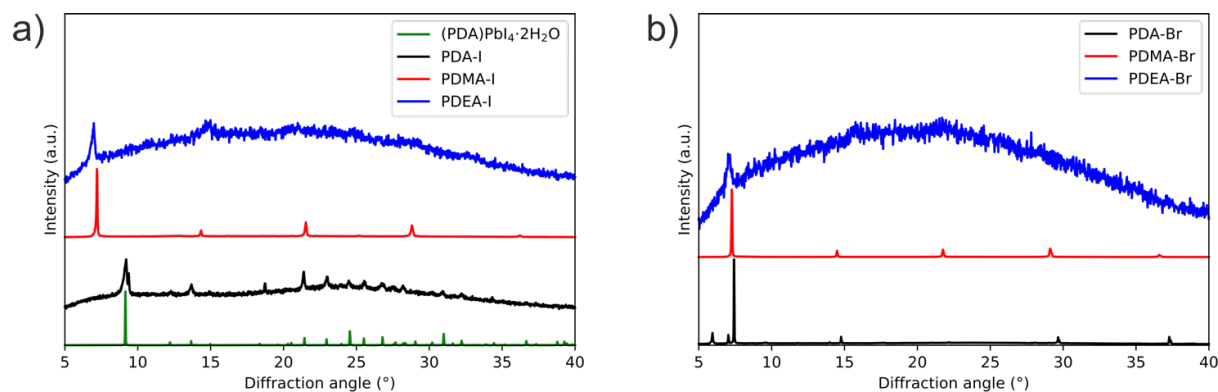


Figure 3:2: X-ray diffraction pattern of (a) I- and (b) Br-based  $n = 1$  layered perovskites. Black: PDA, red: PDMA, blue: PDEA. The green line in a) shows the simulated diffractogram of (PDA)PbI<sub>4</sub>·2H<sub>2</sub>O (CCDC no. 632922 based on ref.<sup>111</sup>).

To acquire more information about the structure and crystallite orientation, we used synchrotron radiation to perform grazing incidence wide-angle X-ray scattering (GIWAXS) measurements (Figure 3:3a-d).<sup>152</sup> While in the samples of PDMA-based perovskites (Figure 3:3a,c) a well-ordered out-of-plane stacking was indicated by pronounced intensity maxima of the scattering signal in the vertical direction, ring-like signals were observed for the PDEA systems (Figure 3:3b,d). These reveal a random orientation of crystallites with no preferred stacking orientation, which is in accordance with the XRD data that probe the vertical direction and, therefore, yield a much larger signal for the well-ordered layered structure as opposed to the randomly oriented crystallites. I- and Br-systems showed the same orientation of crystallites and the layer spacings obtained from GIWAXS are consistent with those from XRD (Table 3:1). Both methods show a trend of increasing layer spacing with longer spacer molecules, in accordance with the expectations. Moreover, I- had a slightly larger unit cell than Br-systems due to the larger ionic radius. For the PDA-based films, the difficulties to form a layered phase are further apparent (Appendix, Figure 8:2:3). In summary, PDMA and PDEA spacers form thin films with 2D structures, while increasing the spacer length from PDMA to PDEA results in a more isotropic distribution in crystallite orientation for both I- and Br-based materials.

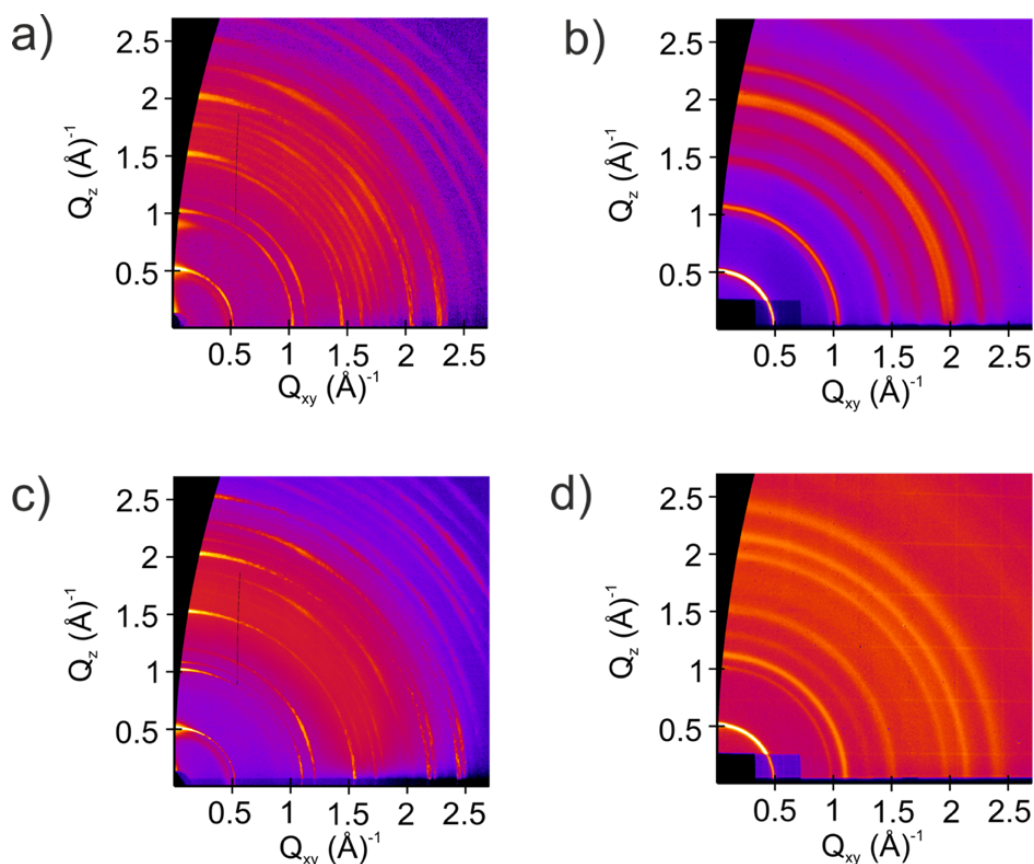


Figure 3:3. GIWAXS images of (a) PDMA-I, (b) PDEA-I, (c) PDMA-Br, and (d) PDEA-Br.

Table 3:1. Layer spacing from GIWAXS measurements.

Composition	Layer spacing [Å]
(PDMA)PbI <sub>4</sub>	12.28 ± 0.011
(PDMA)PbBr <sub>4</sub>	12.22 ± 0.006
(PDEA)PbI <sub>4</sub>	12.73 ± 0.007
(PDEA)PbBr <sub>4</sub>	12.65 ± 0.008

Due to the weak diffraction of PDEA-based perovskites, to confirm the formation of a layered structure, mechanosynthesized powders of PDEA-I were studied by solid-state NMR spectroscopy, which is highly sensitive to the local structure and dimensionality of hybrid perovskite systems despite possible differences in morphology compared to thin films (Figure 3:4a, b).<sup>153,154</sup>

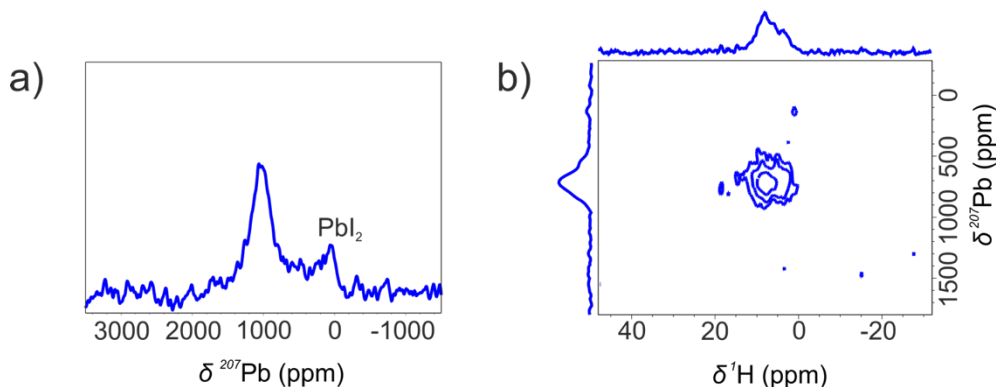


Figure 3:4. Solid-state magic angle spinning (MAS) NMR spectra of mechanochemically prepared PDEA-I powder: (a) Room temperature  $^{207}\text{Pb}$  spectrum and (b)  $^{207}\text{Pb} \rightarrow ^1\text{H}$  HETCOR spectrum at 100 K.

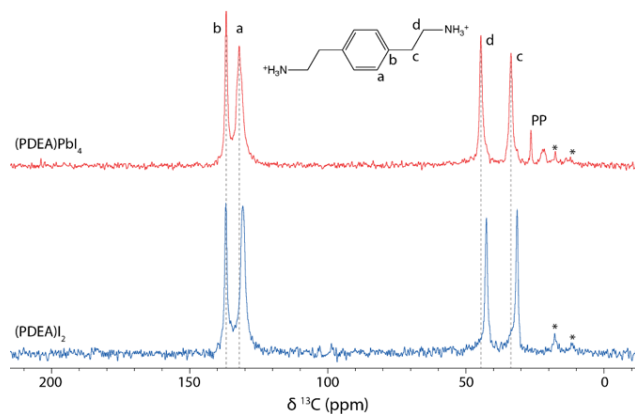


Figure 3:5.  $^1\text{H} \rightarrow ^{13}\text{C}$  cross polarisation spectra of (PDEA)PbI<sub>4</sub> and (PDEA)I<sub>2</sub> recorded at 15 kHz MAS with a 3 s recycle delay and a 1 ms contact time. The assignment is given and spinning sidebands are marked with an asterisk. The signals arising from the polypropylene Eppendorf used for ball-milling of the (PDEA)PbI<sub>4</sub> are marked with PP.

The room temperature  $^{207}\text{Pb}$  NMR spectrum (Figure 3:4a) exhibits a major signal at ~1030 ppm, which is characteristic of a 2D  $n = 1$  structure,<sup>155</sup> as well as a minor signal at ~50 ppm due to unreacted PbI<sub>2</sub>. Furthermore, the  $^{207}\text{Pb} \rightarrow ^1\text{H}$  HETCOR spectrum recorded at 100 K (Figure 3:4b) shows a clear correlation between

the  $^{207}\text{Pb}$  environment in the perovskite layers and the  $^1\text{H}$  signals of the PDEA spacer (both the  $-\text{NH}_3^+$  signal at  $\sim 8$  ppm and the alkyl signals at  $\sim 4.5$  ppm), proving atomic-scale contact between the two; notably, the  $\text{PbI}_2$  impurity is absent due to the lack of  $^1\text{H}$  in this phase. The spectrum was recorded at 100 K to avoid dynamics of the spacer, which reduce the efficiency of cross-polarization;<sup>156</sup> consequently, the temperature-dependent  $^{207}\text{Pb}$  signal is observed at a lower shift of 720 ppm.<sup>156,157</sup> The modification of the PDEA cation environment in formation of the layered perovskite can also be seen by the change in the  $^{13}\text{C}$  NMR signals, particularly those of the alkyl carbons, which are closer to the perovskite layers (Figure 3:5). Taken together, these observations provide strong evidence for the formation of a layered PDEA-I perovskite structure.

### 3.2.2 Optical characterization of thin films

The role of alkyl chain length in the optical properties by UV-vis absorption and of steady state photoluminescence (PL) spectroscopy. The absorption of RP-type  $n = 1$  perovskites can be modulated by controlling the length of the organic spacer; shorter spacers reduce the exciton absorption energy.<sup>141,158,159</sup> The variations in the alkyl chain length change the potential barrier width between lead halide layers<sup>160</sup> and further affect the perovskite structure by inducing octahedral tilting.<sup>161</sup> This is particularly important as the optical properties of layered perovskites are influenced by the Pb–X distances, Pb–X–Pb angles,<sup>162</sup> and quantum and dielectric confinement.<sup>77</sup> Typically,  $n = 1$  layered perovskites based on Pb and I feature exciton peaks at around 500 nm ( $\sim 2.5$  eV), which can be detected at room temperature due to the strong exciton binding energy ( $E_b \gg kT$ ).<sup>51</sup>

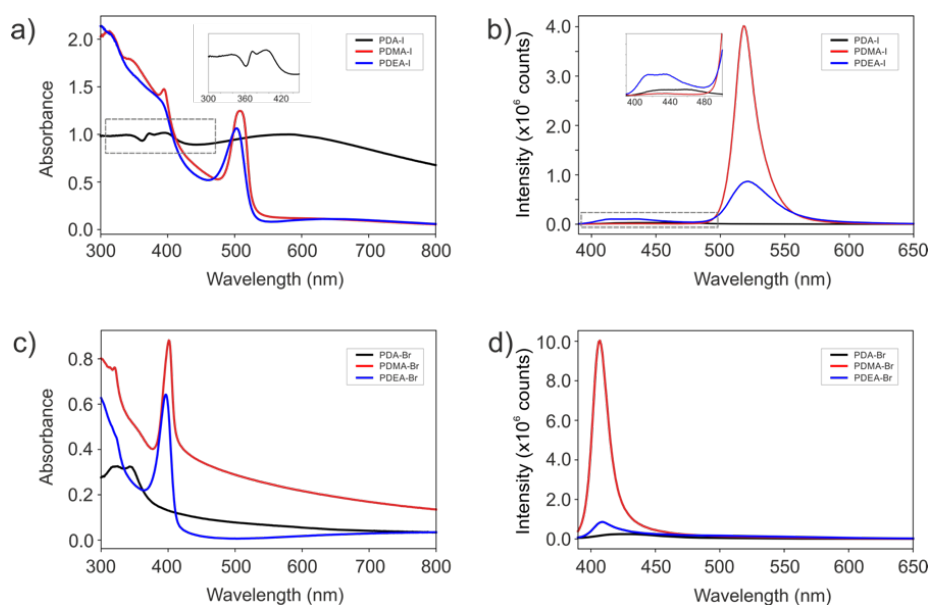


Figure 3:6. (a–b) UV-Vis and steady state PL emission spectra of PDA-I (black), PDMA-I (red) and PDEA-I (blue). The inset in (a) shows zoomed-in absorption in the 300 – 440 nm range, whereas the inset in (b) represents the zoomed-in emission in the 380 – 500 nm interval. (c–d) UV-Vis and steady-state PL emission spectra of PDA-Br (black), PDMA-Br (red) and PDEA-Br (blue).

This is clearly demonstrated in the optical absorption spectra of the films (Figure 3:6a), which show pronounced excitonic peaks for both PDEA-I and PDMA-I samples at 503 nm and 508 nm, respectively, in accordance with the reduced alkyl chain length. One would expect an even further exciton absorption energy reduction in the PDA-based perovskites if they formed well-defined layered perovskites. Instead, we observe a resonant absorption at 380 – 400 nm, which is attributed to the 1D iodoplumbates.<sup>163</sup>

The emission maxima of the PDMA-I and PDEA-I samples are located at 518 nm and 522 nm (Figure 3:6b). The larger Stokes shift in PDEA-I might be associated with energy loss via vibrational relaxation and it could also be influenced by higher structural disorder, consistent with the increase in the PL peak width upon extending the alkyl chain of the spacer (Figure 3:7a-d).<sup>151,164</sup>

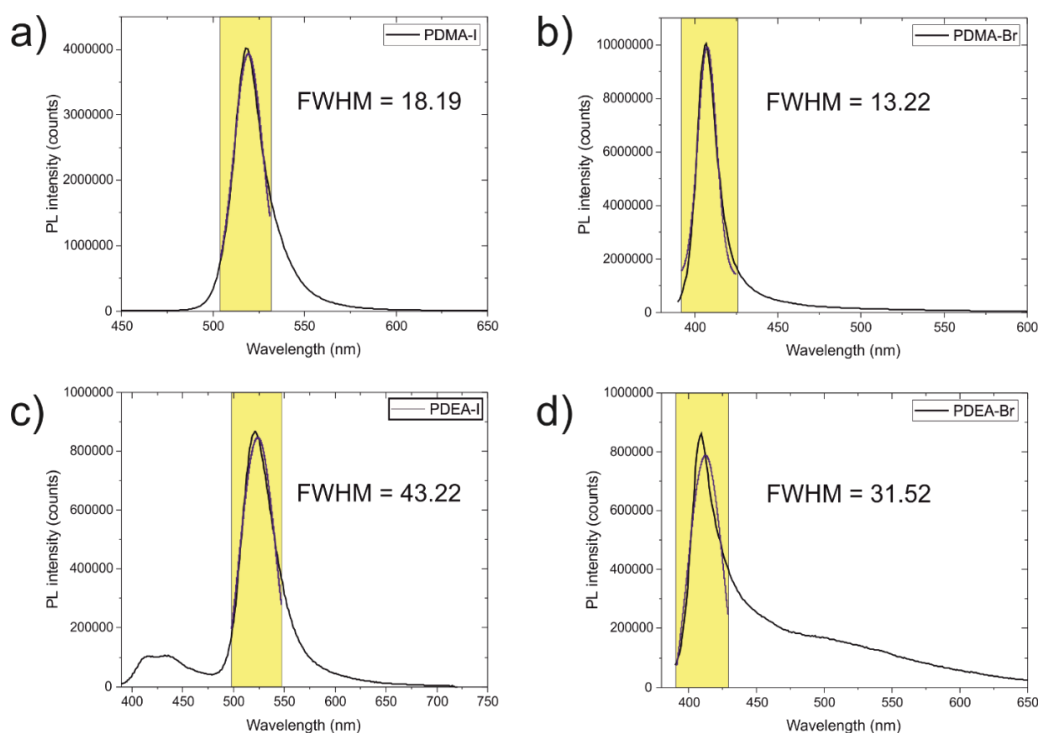


Figure 3:7. (a-d) Gaussian fits for main PL emission peaks with the corresponding values of full width at half maximum (FWHM): (a) PDMA-I, (b) PDMA-Br, (c) PDEA-I and (d) PDEA-Br.

The broad emission detected in PDEA-I in the 400 – 500 nm range might originate from surface species, such as intermediate 1D iodoplumbate phases,<sup>133,163</sup> given the similarity to the PDA-I emission (Figure 3:6b, inset). The substitution of I with Br resulted in wider PDMA-Br, PDEA-Br optical bandgaps with excitonic peaks centered at 401 nm and 397 nm, respectively (Figure 3:6c). The long absorption tail in PDMA-Br sample might be attributed to the high surface roughness. For the PDA-Br, an absorption peak at ~350 nm suggests that carriers are not solely confined in 2D structures. The emission properties of Br-based films reveal that the PL peaks of both PDMA-Br and PDEA-Br are centered at 407–408 nm, whereas PDA-Br has a very broad emission in the 400–500 nm region (Figure 3:6d). As in the I-based systems, PDEA-Br thin films



exhibit a larger Stokes shift and emission bandwidth as compared to PDMA-Br (Figure 3:7b, d). While both PDMA- and PDEA-based 2D perovskite films feature pronounced excitonic optical absorption and emission, a sharper emission for the PDMA systems is likely related to a higher structural homogeneity, resulting from the more oriented grain distribution compared to PDEA.

To gain more insights into the role of alkyl chain length with regard to charge carrier dynamics, we performed transient absorption (TA) spectroscopy measurements (Figure 3:8a–c). We focus our analysis on the I-based samples due to setup limitations in the UV region. The TA spectra of PDMA-I and PDEA-I (Figure 3:8b,c) display similar features, consisting of a negative photobleaching signal at 500 and 510 nm, respectively, as well as two positive features. The presence of a single photobleaching signal indicates an  $n = 1$  phase with no higher order phases being present.<sup>132</sup> On the other hand, the PDA-I TA spectrum shows no appreciable features (Figure 3:8a), further demonstrating the absence of a layered  $n = 1$  structure in this system. The shape of the signal in both the PDMA-I and PDEA-I spectra appears to closely match that of the second derivative of the absorption spectra, shown by the dashed black line, which allows us to conclude that the positive features arise due to a photoinduced Stark effect. Stark effects, first evidenced in hybrid perovskite materials in 2014,<sup>165</sup> and subsequently in 2D-perovskites<sup>166,167</sup> and perovskite nanocrystals,<sup>168</sup> arise due to a change in the absorption of a material in the presence of an electric field; in the case of the photoinduced Stark effect, the electric field is a photoinduced (local) field.

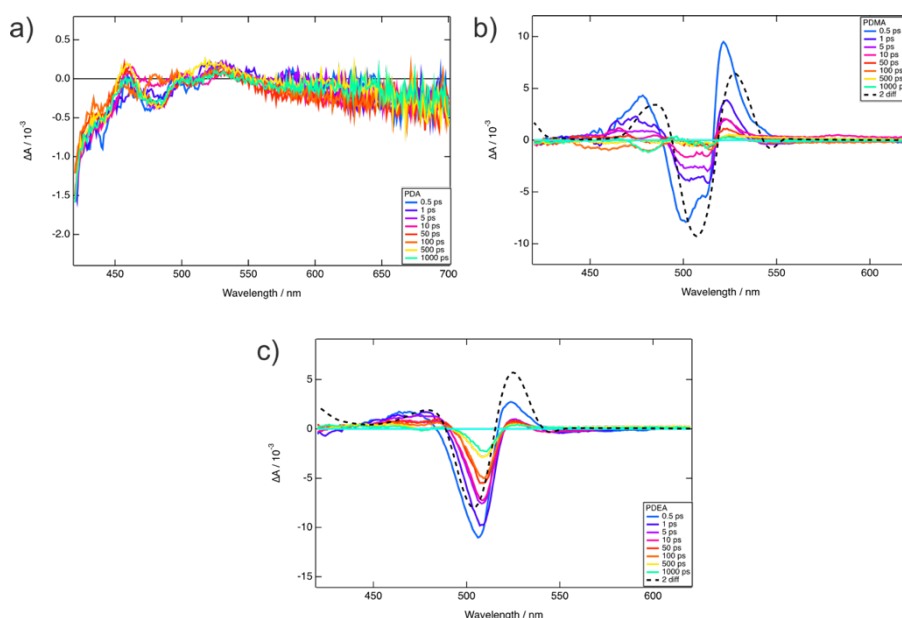


Figure 3:8. Transient absorption spectra of (a) PDA-I, (b) PDMA-I, and (c) PDEA-I. Samples were excited at 389 nm with a fluence of  $23.2 \mu\text{J cm}^{-2}$  (PDA-I) and  $3.26 \mu\text{J cm}^{-2}$  (PDMA-I and PDEA-I). The dashed black line corresponds to the second derivative of the absorption spectrum.

---

The photoinduced signal,  $\Delta A$ , has been shown to comprise of a linear combination of the first and second derivatives of the absorption spectrum.<sup>169</sup> Changes in the dipole moment are associated with the second derivative of the absorption spectrum, whereas changes in the polarizability of the sample are associated with the first derivative.<sup>167</sup> Therefore, in the PDMA-I and PDEA-I samples the photoinduced Stark effect arises due to a change in the dipole moment, caused by the photogeneration of charge transfer (CT) excitons.

Kinetics traces of the Stark effect feature reveal that the lifetime of CT excitons is comparable between the samples; this implies that the time constant for exciton separation into free charges will be similar between the two samples (Appendix, Figure 8:2:4). The Stark effect feature appears to be larger in the PDMA-I sample, when compared to the PDEA-I, which might be rationalized by the shorter spacer length and smaller layer spacing, resulting in a stronger electric field due to the charge transfer exciton across the layers. Furthermore, layered perovskites have been shown to form multiple quantum well structures,<sup>170</sup> and tunnelling between these structures can also increase the contribution of the second derivative to the TA signal,<sup>167</sup> which stimulates a follow-up investigation.

### 3.2.3 Implications on stability in a humid environment

In the previous chapter, it was demonstrated that the PDMA-I system hydrates within minutes when exposed to an atmosphere  $\geq 65 \pm 5$  % relative humidity (RH).<sup>133</sup> We further extended the analysis of the environmental stability to other DJ perovskites by exposing the samples to a  $70 \pm 5$  % relative humidity (RH) atmosphere for 20 min at 28 °C. The results revealed unchanged structural (Figure 3:9a), optical absorption (Figure 3:10a) and emission (Figure 3:11a) properties of PDA-I samples, which is expected since the starting structure is already in a dihydrate phase. The Br analogue changed its structure (Figure 3:9d), and new diffraction peaks emerged below  $10^\circ$ , while the optical properties did not change remarkably (Figures 3:10b and Figure 3:10b). Typically, optical properties are sensitive to changes in the material structure. For example, when PDMA-I samples undergo a transformation from 2D into a 1D structure (Figure 3:9b), optical properties exhibit significant blue shift (Figure 3:10c and 3:11c), which is attributed to the enhanced confinement effects in the lower dimensional perovskite structures.

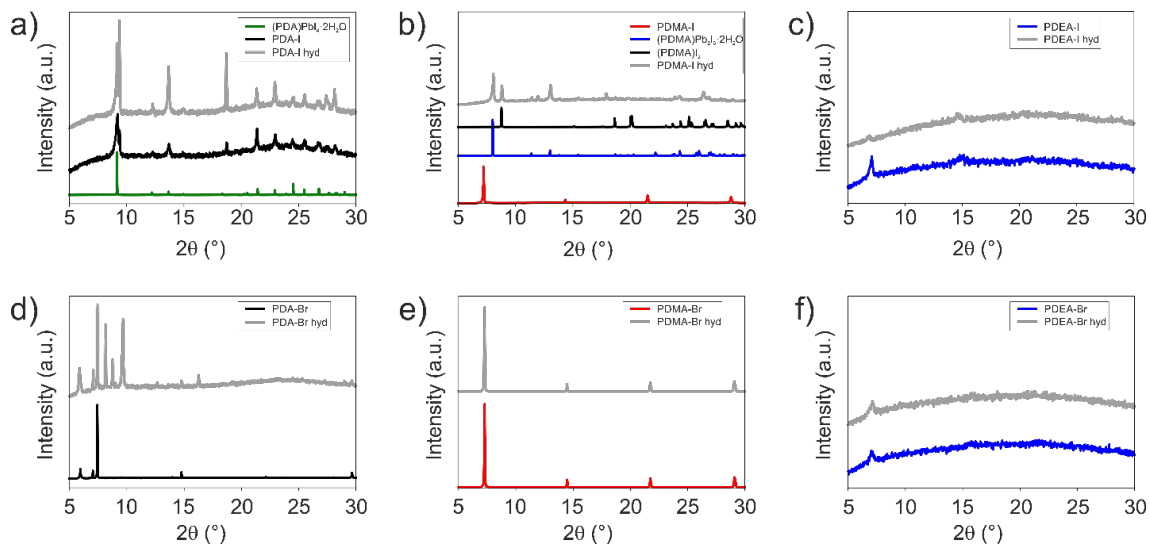


Figure 3:9. X-ray diffractograms of (a) pristine (black) and hydrated (grey) PDA-I films and the calculated pattern for  $(\text{PDA})\text{PbI}_4 \cdot 2\text{H}_2\text{O}$  (green);<sup>111</sup> (b) pristine (red) and hydrated (grey) PDMA-I films, and the calculated patterns for  $(\text{PDMA})\text{PbI}_6 \cdot 2\text{H}_2\text{O}$  (blue) and  $(\text{PDMA})\text{I}_2$  (black);<sup>133</sup> (c) pristine (blue) and post-treated (grey) PDEA-I films. Diffraction patterns of Br-based samples using PDA, PDMA, and PDEA spacers are shown in panels (d), (e), and (f), respectively.

The replacement of  $\text{I}^-$  with  $\text{Br}^-$  counter ion has a significant effect on the propensity of PDMA-based systems to hydrate, as the crystal structure was retained in the PDMA-Br sample upon exposure to humid conditions (Figure 3:7e), showing no blue shift in optical properties (Figure 3:8d and 3:9d). The resilience to humidity might be associated with the contracted lattice, which hampers water intercalation into the crystal structure,<sup>171</sup> or stronger hydrogen bonds between Br and the spacer molecules,<sup>172</sup> increasing the hydration enthalpy.

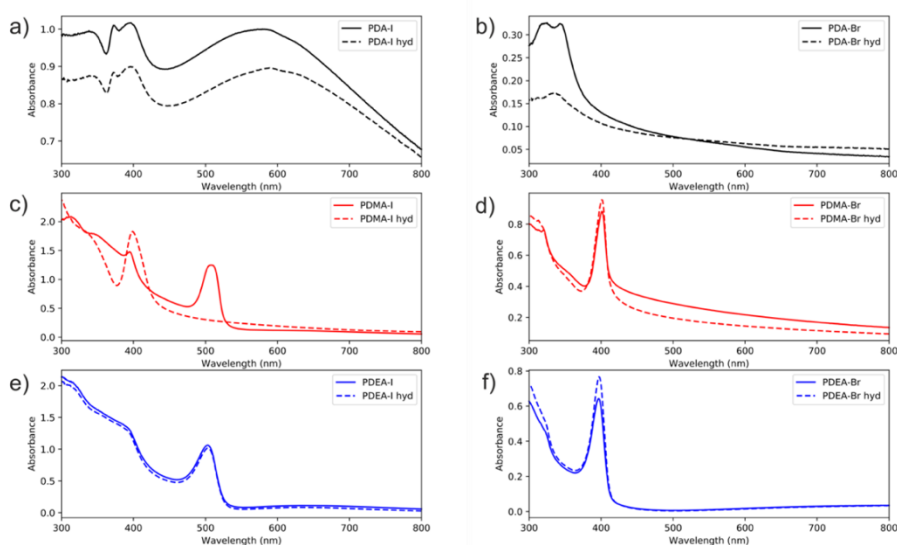


Figure 3:10. UV-Vis absorption spectra of (a) PDA-I, (b) PDA-Br, (c) PDMA-I, (d) PDMA-Br, (e) PDEA-I and (f) PDEA-Br. Solid lines represent absorption of pristine samples, whereas post-treated sample absorption is shown as dashed curves.

The longest spacer molecules might benefit from the reduced steric hindrance effects, allowing ammonium cations to form strong hydrogen bonds, which could improve material robustness in humid environments. In fact, the results of this study revealed improved stability of PDEA-I and PDEA-Br thin films, as structural (Figure 3:9c, f) and optical (Figure 3:10e, f and Figure 3:11e, f) properties were retained after exposure to a humid environment. Moreover, contact angle measurements revealed an improved hydrophobicity of PDEA-I based films (Figure 3:12a-c) also hinting at better stability. However, Br-based films were not necessarily more hydrophobic (Figure 3:12d-f), suggesting that other factors might play a role.

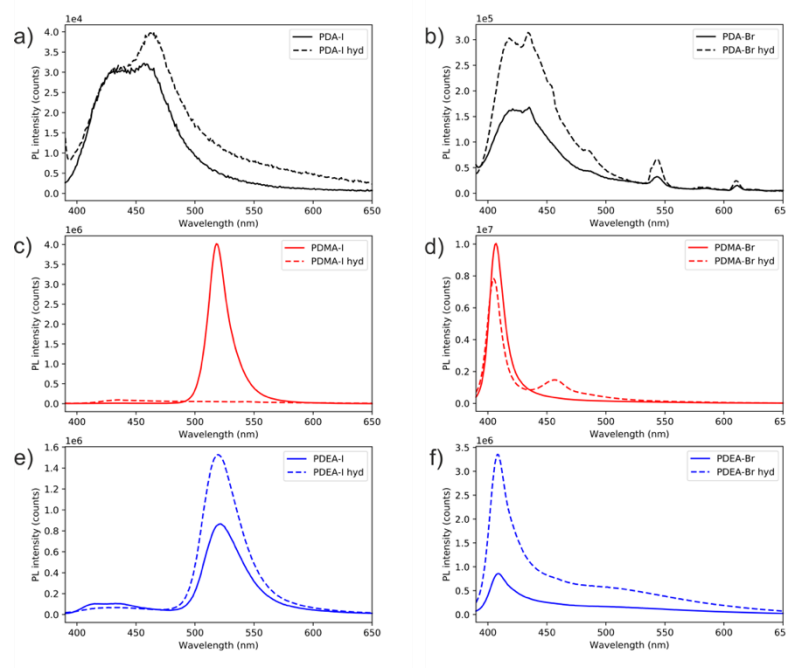


Figure 3:11. PL emission spectra of (a) PDA-I, (b) PDA-Br, (c) PDMA-I, (d) PDMA-Br, (e) PDEA-I and (f) PDEA-Br. Solid lines represent the emission of pristine samples, whereas post-treated sample emission is shown as dashed curves.

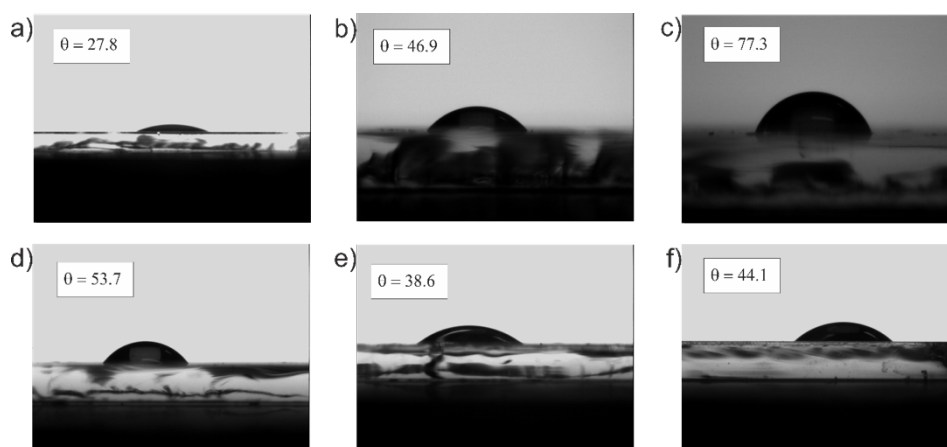
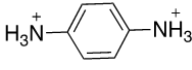
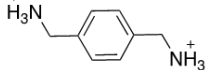
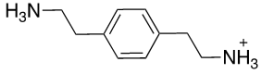


Figure 3:12. Images of water drop on (a) PDA-I, (b) PDMA-I, (c) PDEA-I, (d) PDA-Br, (e) PDMA-Br and (f) PDEA-Br thin films and its corresponding contact angles.

All in all, the length of the organic spacer and the counter ion affect the stability of DJ perovskites as well as structural and optoelectronic properties (Table 3:2). While extended spacer systems and Br-based analogues provide enhanced stabilities, they may however affect the resulting charge carrier mobilities and conductivities of the resulting materials, which remain to be assessed.

Table 3:2. Summary of the main findings of this study: the formation of a layered structure, hydration stability, and absorption (A) and emission (PL) wavelengths.

												
Br	2D <sup>a</sup>	Hyd. <sup>b</sup>	A	PL	2D <sup>a</sup>	Hyd. <sup>b</sup>	A	PL	2D <sup>a</sup>	Hyd. <sup>b</sup>	A	PL
			–	–			401 nm	407 nm			397 nm	408 nm
I	2D <sup>a</sup>	Hyd. <sup>b</sup>	A	PL	2D <sup>a</sup>	Hyd. <sup>b</sup>	A	PL	2D <sup>a</sup>	Hyd. <sup>b</sup>	A	PL
			–	–			508 nm	518 nm			503 nm	522 nm

<sup>a</sup> The feasibility to acquire well-defined layered perovskite thin films. Green = formed layered perovskite; grey = possibly formed a layered perovskite but not well-defined; red = did not form. <sup>b</sup> Environmental stability with regard to hydration during a 20 min exposure to 70±5 % RH. Green = stable; grey = already hydrated; red = unstable.

### 3.3 Conclusions

In summary, we investigated Dion–Jacobson layered perovskite phases based on phenylene-derived aromatic spacers (S) with different length alkyl chains (i.e. PDA, PDMA, and PDEA) and halide counter ions (X = I, Br) of (S)PbX<sub>4</sub> (*n* = 1) composition. The systems based on the PDA spacer did not form a well-defined layered structure. Instead, we demonstrated that PDA-I forms a hydrated 1D structure. The extension of the alkyl chains in the PDMA and PDEA spacers rendered them compatible with the formation of layered perovskite structures, as evidenced by X-ray diffraction and solid-state NMR spectroscopy. Moreover, GIWAXS measurements revealed that in PDMA-based perovskites crystallites are oriented in out-of-plane directions, whereas there is no preferred stacking orientation in PDEA thin films. Optical bandgap and the emission bandwidth also increase with length of alkyl chain. Moreover, the analysis of charge carrier dynamics by transient absorption spectroscopy revealed in PDMA-I and PDEA-I films a photoinduced Stark effect, which arises due to photogeneration of CT excitons and is related to the length of alkyl chain. Finally, the resilience against moisture increases with the length of the alkyl chain and the substitution of iodide with bromide also proved to be an effective strategy to enhance stability against humidity. These results provide critical insights into material design, offering new strategies for tuning the properties of these materials for optoelectronic applications.

# Chapter 4 Effect of spacer perfluorination

This chapter is based on the publication in *Nanoscale* entitled:

**Nanosegregation in Arene-Perfluoroarene  $\pi$ -Systems for Hybrid Layered Dion–Jacobson Perovskites**

by:

Masaud Almalki,\* **Algirdas Dučinskas**,\* Loï C. Carbone,\* Lukas Pfeiffer, Laura Piveteau, Weifan Luo, Etham Lim, Patricia A. Gaina, Pascal A. Schouwink, Shaik M Zakeeruddin, Jovana V. Milić, Michael Grätzel

\*(equally contributed)

My contribution:

Performed experiments for optical and structural characterization, carried out hydration experiments, assisted and guided Loï C. Carbone, made couple of figures and revised manuscript.

DOI:

<https://doi.org/10.1039/D1NR08311B>

## 4.1 Introduction

While RP phases (Figure 4:1b) have been widely used in perovskite optoelectronics, DJ phases (Figure 4:1c) are underrepresented despite their appealing optoelectronic properties and environmental stability. It is thereby of interest to understand and control their structural and optoelectronic properties, which are highly dependent on the supramolecular self-assembly of the organic spacer layer.<sup>82,109,173,174</sup>

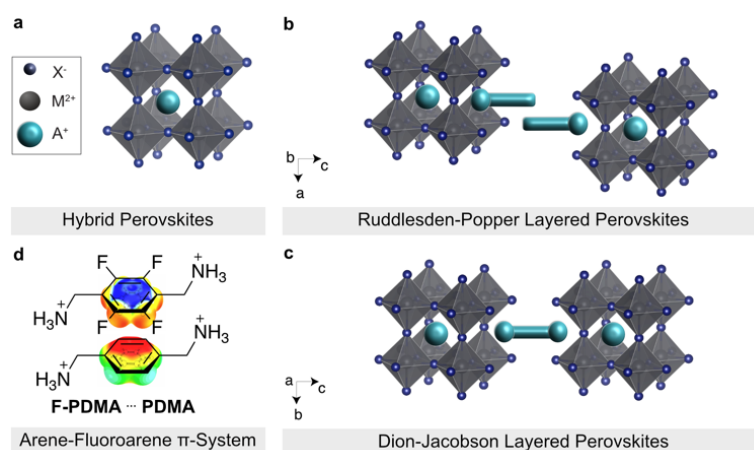


Figure 4:1. Structural representation of (a) 3D and (b–c) 2D layered hybrid perovskite structures, highlighting (b) Ruddlesden-Popper and (c) Dion-Jacobson (b) phases. The grey octahedra represent  $\{PbX_6\}$  frameworks whereas cyan rods illustrate the organic spacers. (d) Schematics of a  $\pi$ -stacking of arene and perfluoroarene moieties, namely 1,4-phenylenedimethylammonium (PDMA) and its analogue containing a perfluorinated phenylene moiety (F-PDMA).

A complementary pair of organic spacers could engage in  $\pi$ - $\pi$  interactions, e.g. between arene and perfluoroarene species, through self-assembly to form an alternating-cation 2D perovskite system.<sup>68</sup> This has been previously analysed based on 2-phenylethylammonium (PEA) and 2-(perfluorophenyl)ethylammonium (FEA), forming an RP phase.<sup>68</sup> Such a favourable interaction is based on the complementarity between the quadrupole moments of the aromatic rings that is expected to yield a more compact parallel ( $\pi$ - $\pi$ ) stacking in arene-perfluoroarene systems (Figure 4:1d).<sup>68,73,175-178</sup> This could alter the optoelectronic properties of the hybrid material.<sup>48,135,145,179,180</sup> In addition, the fluoroarene moieties are expected to increase hydrophobicity and reduce halide ion migration through  $\pi$ -ion interactions, which is relevant to the resulting stability of materials.<sup>73,177,181,182</sup> Such tailored arene-perfluoroarene  $\pi$ -interactions, however, remain unexploited in controlling the properties of DJ perovskite phases.<sup>48,68,72,73</sup>

Here, we investigate a DJ system employing arene and perfluoroarene species, namely 1,4-phenylenedimethylammonium (PDMA) and its analogue comprising a perfluorinated phenyl moiety (F-PDMA), as well as their mixture (1:1 PDMA/F-PDMA, denoted as PF). We evidence the formation of layered perovskite structures by X-ray diffraction (XRD), accompanied by changes in the optoelectronic properties via UV-vis absorption and photoluminescence (PL) spectroscopy. We further demonstrate the formation of nonsegregated structures by solid-state NMR spectroscopy, while revealing enhanced environmental stability of the resulting materials in humid environments, which is relevant to their future application.

## 4.2 Results and discussion

### 4.2.1 Structural analysis

Thin films of layered perovskites were prepared based on  $\text{SPbI}_4$  ( $n = 1$ ) compositions ( $S = \text{PDMA}$ , F-PDMA (NMR spectra confirming structure is available in Appendix, Figure 8:3:1-3), and 1:1 PDMA:F-PDMA, denoted as PF) by solution-processing followed by annealing, in accordance with the procedure reported in the Appendix, Section 8.3.1. Structural properties were investigated by X-ray diffraction (XRD) in the Bragg-Brentano configuration (Figure 4:2). The XRD patterns of the thin films show low angle reflections ( $< 10^\circ$ ) at  $2\theta$  of  $7.22^\circ$ ,  $6.93^\circ$  and  $7.17^\circ$  for  $(\text{PDMA})\text{PbI}_4$ ,  $(\text{F-PDMA})\text{PbI}_4$  and  $(\text{PF})\text{PbI}_4$ , respectively, which is accompanied by periodic patterns typical of layered (2D) perovskite structures.<sup>94,133,135,145</sup> This is particularly the case for  $(\text{PDMA})\text{PbI}_4$  (Figure 4:2a), whereas  $(\text{F-PDMA})\text{PbI}_4$  shows lower intensity peaks with a poor signal-to-noise ratio, suggesting lower crystallinity (Figure 4:2b). We further observed a low angle diffraction for the mixed  $(\text{PF})\text{PbI}_4$  system characteristic for 2D structures, with an increase in relative intensity of the  $14^\circ$  and  $28^\circ$  diffraction peaks (Figure 4:2c). This suggests that the presence of F-PDMA modifies out-of-plane texture of the films. To corroborate this, we analysed the films by grazing incidence wide angle X-ray scattering (GIWAXS) measurements (Figure 4:2d-f and Appendix, Figure 8:3:4). Films with

different (5%, 10%, 25% and 50%) F-PDMA content were investigated (denoted as 5%, 10%, 25%, and 50% (PF), respectively) and compared to the PDMA-based 2D perovskite composition. We observe a very clear dependency of out-of-plane texture on F-PDMA content, which is confirmed by gamma integrations of the diffraction intensity at  $7.3^\circ$  (Appendix, Figure 8:3:5d). Likewise, a visual inspection of GIWAXS images shows that (PDMA)PbI<sub>4</sub> crystallites have a preferred orientation,<sup>133,145</sup> whereas upon the gradual addition of F-PDMA continuous Debye-Scherrer rings appear, indicating a more random distribution of crystallites (Figure 4:2d–f and Appendix, Figure 8:3:4). This suggests that F-PDMA inhibits the formation of texture in the films of PF-based compositions, which is likely a consequence of competing fluorine-based interactions in F-PDMA-based systems, in accordance with previous reports.<sup>72,73</sup>

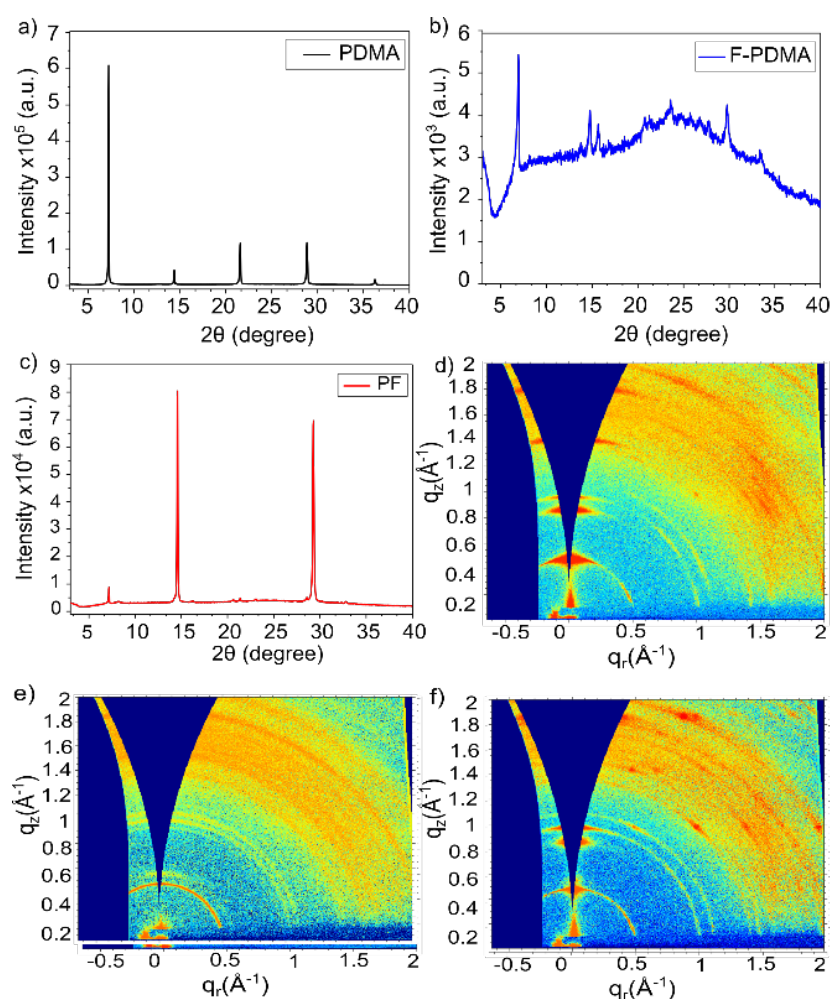


Figure 4:2. Structural properties of layered hybrid perovskites. (a–c) XRD patterns of thin films based on (a) (PDMA)PbI<sub>4</sub> (black), (b) (F-PDMA)PbI<sub>4</sub> (blue), and (c) (PF)PbI<sub>4</sub> (red) compositions on microscope glass. (d–f) GIWAXS patterns of thin films of (d) (PDMA)PbI<sub>4</sub>, (e) (F-PDMA)PbI<sub>4</sub>, and (f) (PF)PbI<sub>4</sub>.

The atomic-level interactions were further analysed by solid-state nuclear magnetic resonance (NMR) spectroscopy (Figure 4:3).<sup>133</sup> Solid-state NMR has emerged as a powerful method to characterize the atomic-level structure of lead-halide perovskite materials.<sup>183–188</sup> To shed light on the coordination and distribution of the



---

spacer ligands within the DJ phases, we relied on our previously developed approach.<sup>68</sup> Specifically,  $^{19}\text{F}$  NMR spectra were recorded for the fluorinated spacer (F-PDMA) and a mechanosynthetic mixture of the two spacers (F-PDMAI<sub>2</sub> and PDMAI<sub>2</sub> stoichiometric 1:1 mixture, denoted as PF), as well as their corresponding 2D perovskites, namely (F-PDMA)PbI<sub>4</sub> and (PF)PbI<sub>4</sub> (Figure 4:3b). The  $^{19}\text{F}$  NMR spectra of the F-PDMA spacer in pure state and within a mixture with PDMA were found to be identical, featuring two fluorine signals at  $-135$  and  $-139$  ppm, indicating that the chemical surrounding of the fluorine atoms is the same in both samples. This suggests that the PDMA and F-PDMA powders do not form a homogeneous phase upon mixing, but remain spatially separated within microcrystalline grains constituted of only one of the two molecules. However, the  $^{19}\text{F}$  NMR spectra of 2D perovskites substantially change as compared to the spectrum of the pristine spacer, with different intensity ratios of the  $^{19}\text{F}$  NMR signals, indicating the formation of new phases. This evidences that the fluorine atoms experience a different chemical surrounding within the perovskite material, in agreement with the incorporation of F-PDMA into the perovskite structure.

Similarly,  $^{19}\text{F}$  NMR of a 2D perovskite phase based on a 1:1 spacer mixtures (PF) reveals the formation of a different phase as it exhibits an additional signal at ca.  $-130$  ppm, whereas the other two signals remain almost unchanged in intensity and chemical shift. This is in accordance with nanosegregation into domains within the 2D perovskite material in which all spacers are fluorinated, forming the same phase as in materials prepared exclusively from F-PDMA. The additional signal at  $-130$  ppm could either originate from the fluorinated spacers at the interface of these domains or from the domains where F-PDMA and PDMA form a homogeneous mixture. We have investigated this further by comparing  $^{13}\text{C}$  cross-polarisation (CP) NMR spectra obtained by transferring polarisation either from  $^1\text{H}$  or from  $^{19}\text{F}$  nuclei (Figure 4:3c). Detailed information is available in Appendix, Section 8.3.1. While the resolution of the  $^{19}\text{F} \rightarrow ^{13}\text{C}$  CP NMR spectra was insufficient to extract any additional structural insight,  $^1\text{H} \rightarrow ^{13}\text{C}$  CP NMR corroborates the co-existence of independent phases, each comprising only one spacer, in the mixed system, further evidencing their nanosegregation. In summary, solid-state NMR further confirms that F-PDMA is integrated into the DJ 2D perovskite structure, while evidencing that the mixture of spacers (F-PDMA and PDMA) leads to phase segregation, which is in accordance with a previous report on the perfluorinated spacers in RP phases.<sup>68</sup> These structural changes are directly reflected in the optoelectronic properties of the films.

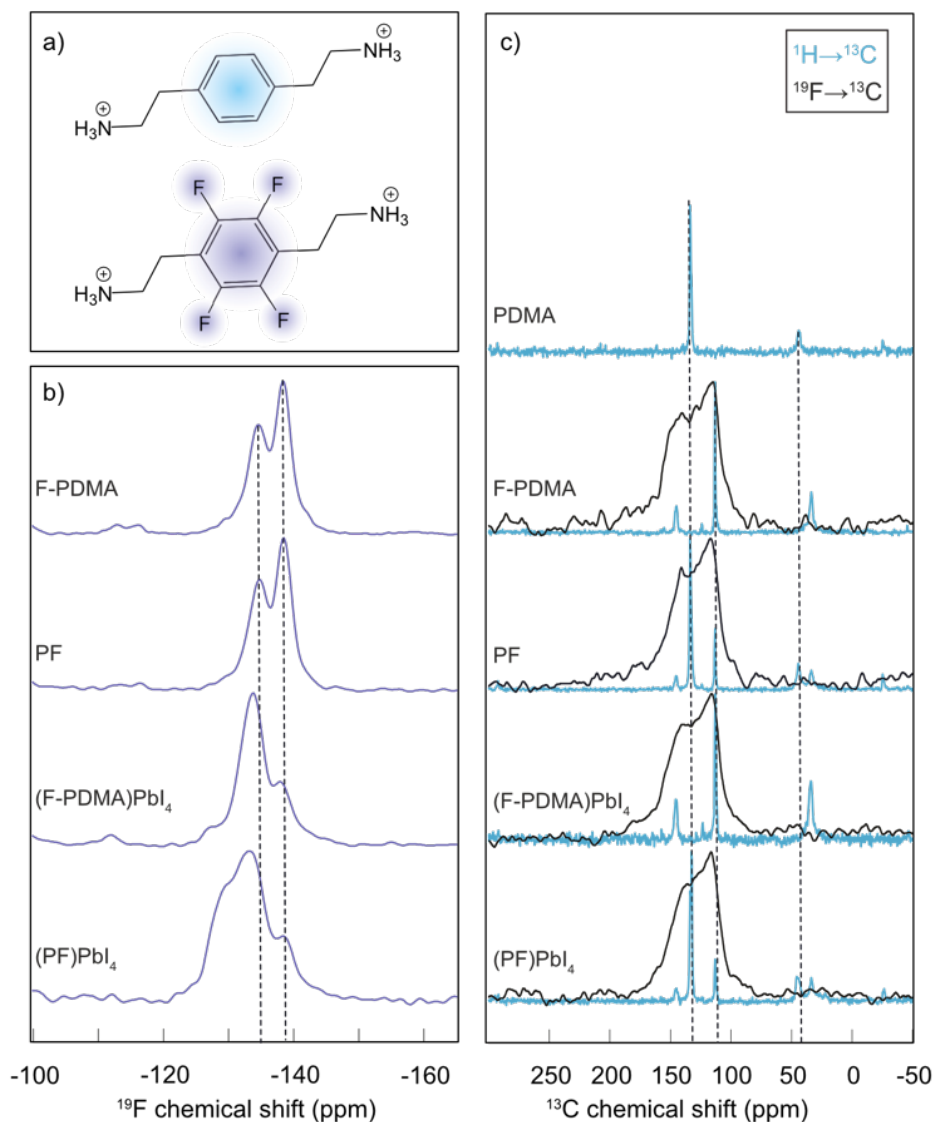


Figure 4.3. Atomic-level structure of layered hybrid perovskites. (a) Structural representation of PDMA (top) and F-PDMA (bottom). (b)  $^{19}\text{F}$  NMR spectra of F-PDMAI<sub>2</sub>, 1:1 spacer mixture (PF), and the corresponding 2D perovskites. (c)  $^{13}\text{C}$  CP NMR spectra of arene spacer (PDMA), the perfluoroarene analogue (F-PDMA), a mixture of the two spacers (PF) as well as their 2D perovskites structures. The  $^{13}\text{C}$  spectra obtained by transferring polarization from  $^1\text{H}$  to  $^{13}\text{C}$  are depicted in dark blue and the spectra obtained when transferring polarization from  $^{19}\text{F}$  to  $^{13}\text{C}$  are depicted in black.

#### 4.2.2 Optical properties

The optical properties of the thin films were analysed by UV-vis absorption and PL spectroscopy. The excitonic features in the absorption spectrum in the range of 490–500 nm are in agreement with the formation of layered 2D structures.<sup>100,133,135</sup> For (PDMA) $\text{PbI}_4$ , (F-PDMA) $\text{PbI}_4$  and (PF) $\text{PbI}_4$ , absorption maxima were observed at 510 nm, 480 nm, and 505 nm, respectively (Figure 4:4a). Thin films containing mixtures of arene and perfluoroarene spacers with increasing amounts of F-PDMA (5%, 10%, and 25%) feature a gradual blue shift of the absorption maximum to 510 nm, 509 nm, and 507 nm, respectively

(Appendix, Figure 8:3:5b). Similarly, PL spectra (Figure 4:4b and Appendix, Figure 8:3:5c) show minor Stokes shifts of ca. 20 nm, 10 nm, and 15 nm for (PDMA)PbI<sub>4</sub>, (F-PDMA)PbI<sub>4</sub> and (PF)PbI<sub>4</sub>, respectively. Furthermore, PDMA-based layered perovskites showed the highest photoluminescence quantum yield (PLQY) of about 0.2%, whereas F-PDMA revealed a very low PLQY of 0.08% (Appendix, Figure 8:3:6c). For PDMA/F-PDMA mixtures, increasing the F-PDMA ratio (5, 10, 25, 50%) resulted in the reduction of the PLQY (to 0.17, 0.14, 0.11, and 0.75%, respectively), and which is in the agreement with the reduction in crystallinity revealed by XRD measurements. The corresponding PL spectra of neat F-PDMA-based thin films also appear to involve multiple signals. None of the features could be ascribed to the spacer as no perceptible PL signal was detected in the 470-520 nm range (Appendix, Figure 8:3:6a, b). Therefore, we suspect that structural disorder in F-PDMA might result in this type of emission profile, however, further investigations are needed to validate this hypothesis.

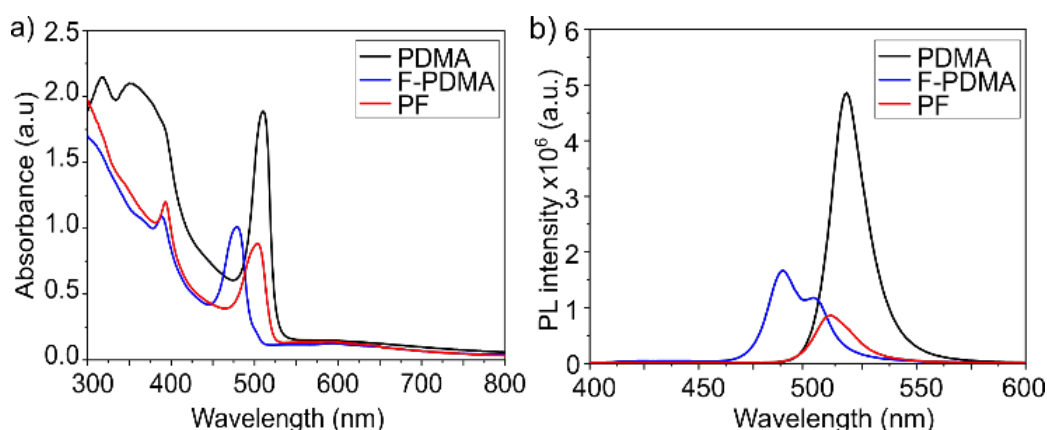


Figure 4:4. Optoelectronic properties of layered hybrid perovskites. (a) UV-vis absorption spectra and (b) PL spectra of thin films based on (PDMA)PbI<sub>4</sub> (black), (F-PDMA)PbI<sub>4</sub> (blue), and (PF)PbI<sub>4</sub> (red) on microscope glass.

#### 4.2.3 Stability in a humid environment

Having evidenced the 2D perovskite formation through optical and structural properties, the stability of the materials was analysed by monitoring the behaviour of the films in humid environments.<sup>133,171</sup> For this purpose, we measured contact angles (Figure 4:5) for the films based on F-PDMA, PDMA and with various amounts of F-PDMA (5%, 10%, 25% and 50%) with respect to PDMA in 2D perovskite compositions. With increasing F-PDMA content from 0%, over 5%, 10%, 25%, up to 50%, contact angles of 49.6°, 59.6°, 62.1°, 63.3°, and 60.1° were obtained, respectively, showing a substantial increase in hydrophobicity in presence of F-PDMA. The system based on 25% F-PDMA demonstrated the greatest hydrophobicity, which was accompanied by the highest intensity of diffraction peaks that are commonly associated with the crystallites of perovskite layers that are perpendicular to the substrate (Appendix, Figure 8:3:5a).<sup>133</sup> This suggests that the changes in hydrophobicity are likely not only associated with the fluoroarene

content but also with the orientation of crystallites and the organic spacers in the films. The environmental stability was further assessed by measuring optical (UV-vis absorption and PL spectra) as well as structural properties (XRD) after exposing the samples to a relative humidity of  $70\pm5\%$  for 15 min. While (PDMA)PbI<sub>4</sub> is known to hydrate in humid conditions (Figure 4:6a),<sup>133</sup> (F-PDMA)PbI<sub>4</sub> did not undergo any change (Figure 4:6b). However, the UV-vis absorption spectra of mixed (PF)PbI<sub>4</sub> films changed when exposed to humid conditions (Figure 4:6c), with a 25 nm blue shift of the absorption peak at 510 nm and an increase of absorbance in the 405 nm region. Furthermore, recorded XRD patterns (Figure 4:6d) reveal a transformation that could be depicted as a superimposition of the patterns of two species, i.e. the hydrated PDMA-based phase and the co-existing (F-PDMA)PbI<sub>4</sub> phase.

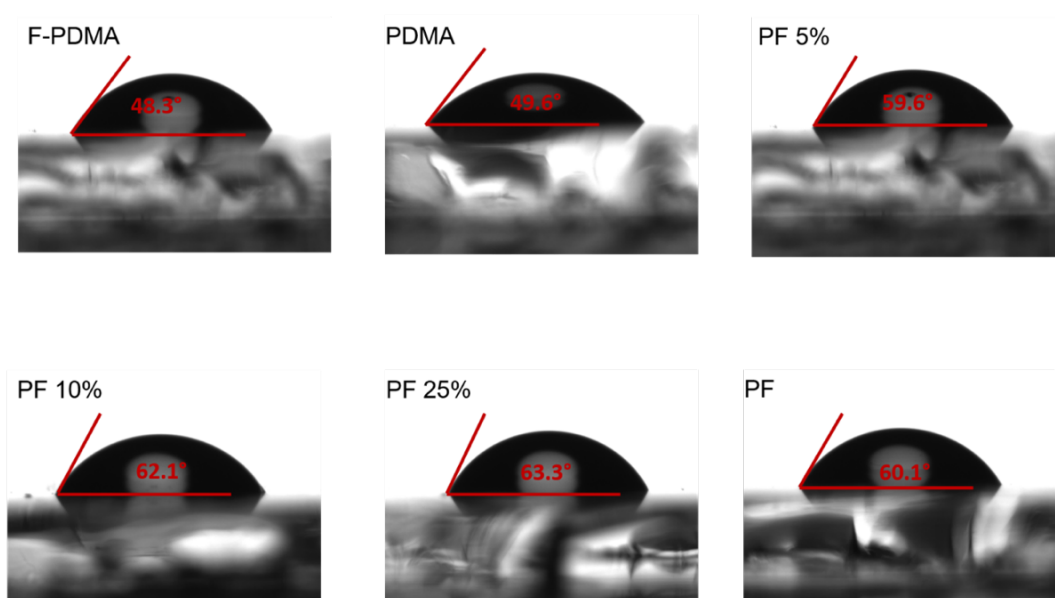


Figure 4:5. Contact angles of water droplets on F-PDMA (48°), PDMA (49.6°), F-PDMA 5% (59.6°), F-PDMA 10% (62.1°), F-PDMA 5% (63.3°), and F-PDMA 50% (60.1°) films.

This observation is in accordance with the formation of a segregated structure of the perovskite phases based on two spacer moieties in mixed thin films (Figure 4:6e), as indicated by solid-state NMR spectroscopy. Since PDMAI-based films are known to hydrate, whereas F-PDMAI-based ones are resistant to hydration, the mixed cation system is expected to be more resilient to moisture. Instead, the formation of a hydrated PDMA phase suggests that, in contrast to the previous reports on arene-fluoroarene-based systems,<sup>189,190</sup> the corresponding DJ systems remain nanosegregated like recently reported RP systems.<sup>68</sup>

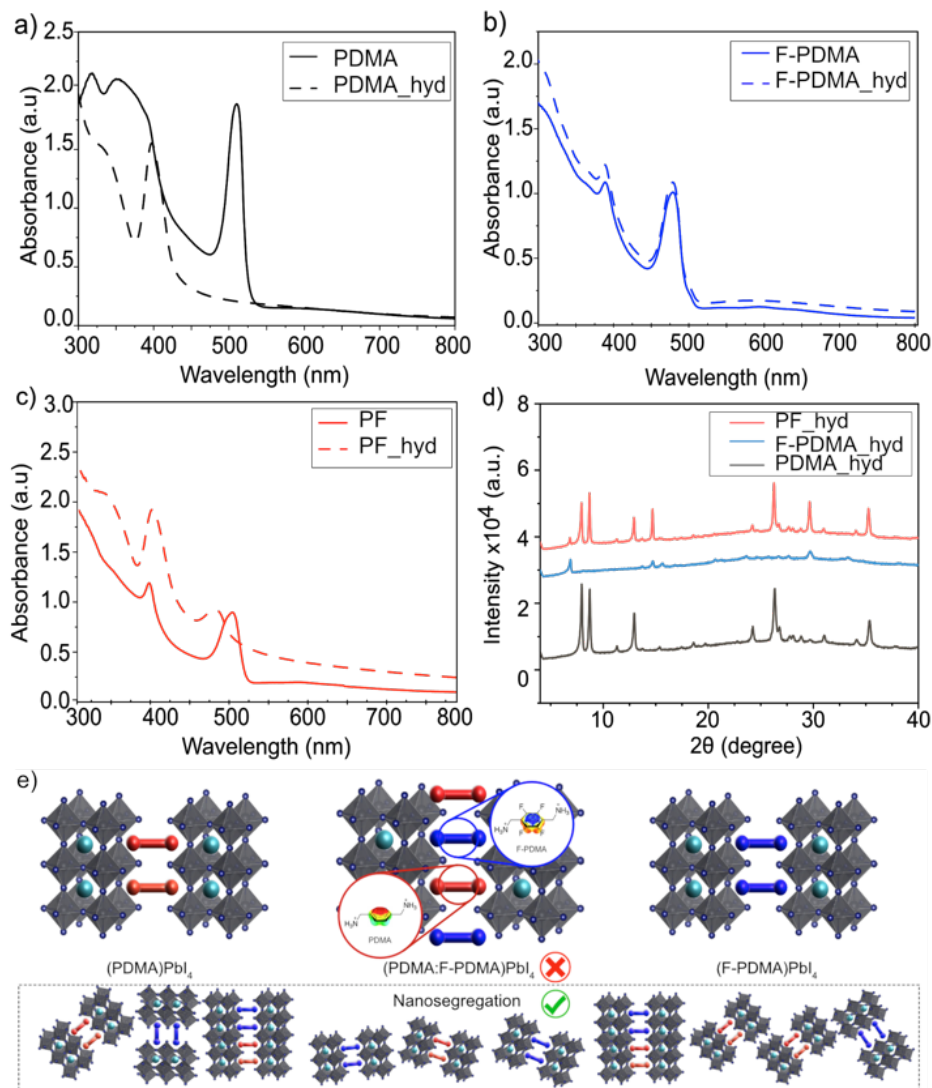


Figure 4.6. Environmental stability of layered hybrid perovskites. (a–c) UV-vis spectra of (PDMA)PbI<sub>4</sub> (black), (F-PDMA)PbI<sub>4</sub> (blue), and (PF)PbI<sub>4</sub> (red) on microscope glass before (plain lines) and after (dashed lines) exposure to a relative humidity of 70±5% for 15 min. (d) XRD patterns of (PDMA)PbI<sub>4</sub> (black), (F-PDMA)PbI<sub>4</sub> (blue), and (PF)PbI<sub>4</sub> (red) on microscope glass after exposure to humid conditions (referred to as hyd). (e) Schematic representation of layered and nanosegregated PDMA/F-PDMA perovskite structures.

### 4.3 Conclusions

In summary, we investigated arene and perfluoroarene spacers, namely 1,4-phenylenedimethylammonium (PDMA) and its analogue containing a perfluorinated phenyl moiety (F-PDMA), for their propensity to form hybrid Dion-Jacobson layered perovskite materials through self-assembly. The analysis showed that PDMAI, F-PDMA, and their 1:1 mixture form layered perovskite materials, which are not well oriented in the case of F-PDMA-based films. Moreover, while the F-PDMA-based system showed resilience to moisture, its addition to the PDMA-based composition did not prevent hydration, suggesting the possible formation of a segregated structure which was confirmed by solid-state

---

NMR spectroscopy. This provides insights into the design of Dion-Jacobson perovskites incorporating arene-perfluoroarene  $\pi$ -systems, stimulating further studies on their application in optoelectronics.

---

# Chapter 5 Pressure induced changes in RP and DJ perovskites

This chapter is based on the publication in *Advanced Materials* entitled:

## **Reversible Pressure-Dependent Mechanochromism of Dion–Jacobson and Ruddlesden–Popper Layered Hybrid Perovskites**

by:

Loreta A. Muscarella,\* Algirdas Dučinskas,\* Mathias Dankl, Michał Andrzejewski, Nicola Pietro Maria Casati, Ursula Rothlisberger, Joachim Maier, Michael Graetzel, Bruno Ehrler, Jovana V. Milić

\*(equally contributed)

My contribution:

Prepared samples, measured thin film XRD, analysed data, established collaboration, and wrote half of the manuscript.

DOI:

<https://doi.org/10.1002/adma.202108720>

## 5.1 Introduction

Layered two-dimensional (2D) hybrid perovskites have attracted considerable interest due to their unique optoelectronic properties and highly modular structure that can be tailored by altering both organic and inorganic components.<sup>94,95,135,191</sup> These materials are composed of organic spacer (*S*) layers connecting adjacent perovskite slabs consisting of *n* layers of 3D perovskite based on the  $S_xA_{n-1}M_nX_{3n+1}$  formula, where *x* is the number of spacer molecules connecting two neighbouring perovskite layers, involves a central (*A*) cation (*e.g.* Cs<sup>+</sup>, methylammonium (MA<sup>+</sup>), formamidinium (FA<sup>+</sup>), etc.) embedded in the {MX<sub>6</sub>} octahedral metal-halide framework based on divalent metal ions (Pb<sup>2+</sup> or Sn<sup>2+</sup>) and halide (*X*<sup>−</sup>) anions (I<sup>−</sup>, Br<sup>−</sup>, or Cl<sup>−</sup>). Their structural characteristics are the result of a subtle interplay between the organic spacer layer and the inorganic slabs and they are often broadly classified into Ruddlesden–Popper (RP)<sup>98</sup> and Dion–Jacobson (DJ) phases.<sup>99</sup> In the case of RP perovskites, the perovskite layers are displaced by half the length of the unit cell vectors along the in-plane direction, which mostly involves monofunctional spacers (*x* = 2),<sup>135</sup> whereas DJ perovskites attain the alignment in the structure without relative displacement and are commonly based on bifunctional spacer molecules (*x* = 1; Figure 5:1a).<sup>192</sup> The monofunctional spacers in RP phases form bilayers with van der Waals gap,<sup>164</sup> whereas bifunctional spacers in DJ layered perovskites directly connect the neighbouring perovskite slabs.<sup>99</sup> They are further classified based on the number of perovskite layers (*n*) which are separated by the organic spacer layer (*e.g.*, *n* = 1, 2, 3, etc.).<sup>95,99,135</sup> Since the spacers are mostly

electronically insulating, the charge carriers in these materials are predominantly confined to the inorganic slabs, resulting in natural quantum well (QW) behaviour (Figure 5:1b), where optical bandgap decreases with the width of the QW because of reduced quantum confinement.<sup>51,96</sup> This implies that their optical properties can be modulated by changing the number of perovskite layers ( $n$ ). Furthermore, quantum confinement can be tuned by the width of the potential barrier, which is controlled by the spacer size that further affects their optoelectronic properties.<sup>158,159</sup>

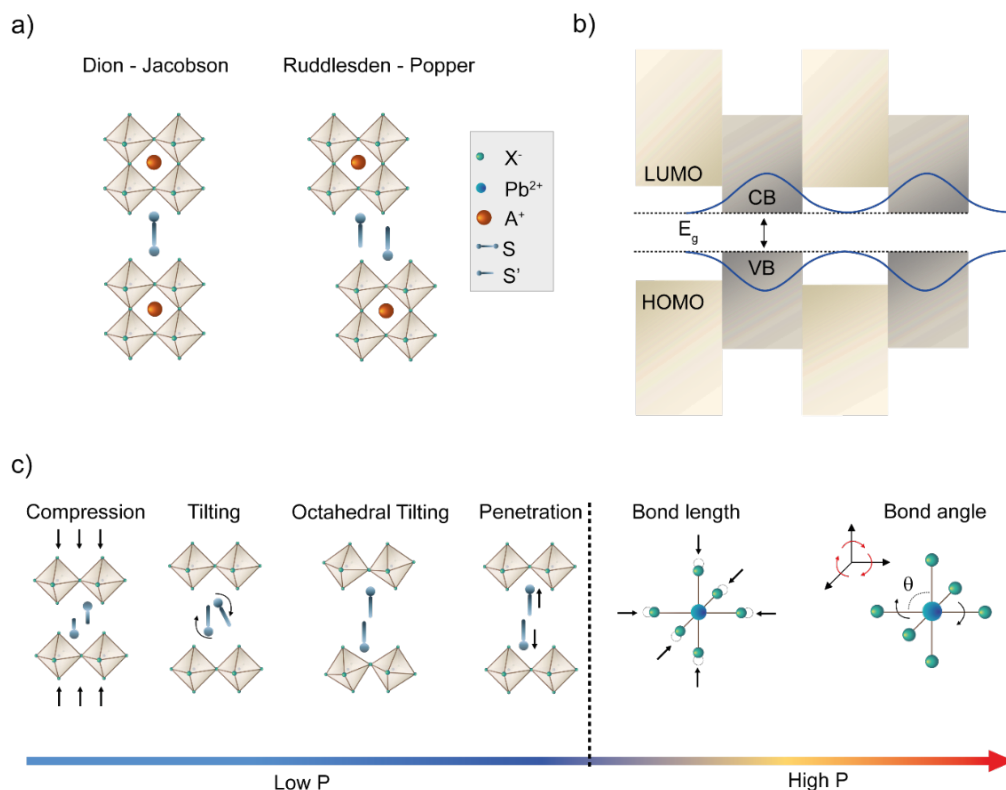


Figure 5:1. Schematic representation of a) Dion–Jacobson (DJ) and Ruddlesden–Popper (RP) phases and b) their quantum well behaviour, with the energy bandgap ( $E_g$ ) defined by conduction band (CB) and valence band (VB) edges of the inorganic slabs and the highest occupied (HOMO) and lowest unoccupied (LUMO) molecular orbitals of the organic spacer layer. In blue, the electronic wavefunction is shown, located mostly in the inorganic framework. c) Illustration of the different possible structural changes that control the optoelectronic properties of layered 2D perovskites by external pressure: at low pressure, the main effect is reflected in changes in the organic spacer and octahedral tilting, whereas at high pressure an additional effect on the bond length and angle is expected. A representative RP perovskite is used in the illustration.

It would be of interest to control these effects on the potential barrier width without changing the perovskite composition, which can be achieved by relying on their mechanical properties and responsiveness to external stimuli, such as pressure.<sup>77,193</sup> Thus, understanding the structure-property relationships in such layered perovskites can serve as a guide to design materials with specific properties, whereas understanding the behavior of  $n = 1$  layered 2D perovskites provides a limiting case for the analysis of  $n > 1$  systems in the future.



---

Moreover, knowing the pressure response of these materials might open opportunities for sensing applications, where high sensitivity to external mechanical stimuli and reversibility are highly desirable, and is relevant also in other contexts, such as for flexible solar cells, where strain might be induced during operation.

The relatively low bulk modulus ( $K$ ) of hybrid 3D perovskites (of the order of 10s of GPa) renders them soft materials that are more easily compressible across different pressure ranges, demonstrating mechanochromic behaviour.<sup>194–198</sup> For comparison, halide perovskites show at least a five times smaller bulk modulus than their oxide analogues ( $> 100$  GPa).<sup>199,200</sup>

For 2D hybrid halide perovskites, the bulk modulus might not be an appropriate descriptor of their mechanical properties since compression in these materials is mostly anisotropic.<sup>77,162</sup> Alternatively, their mechanical properties can be better described by in-plane or out-of-plane Young's modulus ( $E$ ),<sup>201</sup> which is more commonly used for layered perovskites as it defines the material's ability to deform along a given axis when force is applied. In-plane  $E$  is typically determined by the M–X bond strength, whereas out-of-plane  $E$  depends on the organic spacer.<sup>87,88,135</sup> An appropriate choice of organic spacers can lead to a much smaller  $E$  in the 2D layered hybrid perovskites than the 3D analogous,<sup>87,88</sup> suggesting a higher pressure sensitivity for tuning their optoelectronic and transport properties. The anisotropy of layered hybrid perovskites renders their compression predominant in out-of-plane ( $a$ -axis) direction under pressure.<sup>77,162,202</sup> This is expected to be mainly determined by the organic spacer layer and it could result in different structural changes, including the compression of the organic spacer, its tilting, and increased penetration depth, inducing also possible changes in the octahedral tilting of the inorganic layer (Figure 5:1c, *left*). These structural distortions are expected to change the QW structure or the M and X orbital overlap and, consequently, optical properties. More specifically, the compression of spacer molecules or M–X bonds lowers the optical bandgap due to increased overlap of wave functions between adjacent perovskite layers or increased antibonding atomic overlap between the metal and halide orbitals, respectively. The deviation of M–X–M angle from the  $180^\circ$  (*i.e.* octahedral tilting) leads to an opposite effect.<sup>141</sup> Under higher pressures, the compressed inorganic perovskite lattice relaxes through two competing processes, namely M–X bond tilting or M–X bond contraction (Figure 5:1c, *right*),<sup>192,203,204</sup> which directly affect the optoelectronic properties.<sup>193,205</sup>

While previous work primarily involved analysing the behaviour of hybrid perovskites under high pressure,<sup>193,205</sup> it is of great importance to study effects in mild pressure regimes ( $< 1$  GPa), since induced levels of strain are comparable with polaron effects,<sup>206,207</sup> chemical (*i.e.* conformational) strain<sup>85,208</sup> or strain due to lattice mismatch<sup>86,209</sup> especially in 2D/3D perovskite composites.<sup>210</sup> In that regard, the behaviour under mild pressures may serve as a powerful tool for controlling the properties of these materials in a manner comparable to other processes inducing internal strain. However, the investigations of layered 2D perovskites in such

---

mild-pressure ranges are underrepresented and the differences in the pressure-dependent behaviour of RP and DJ phases remain elusive.

Herein, we investigated representative DJ and RP 2D perovskites based on 1,4-phenylenedimethylammonium (PDMA) and benzylammonium (BzA) spacers under hydrostatic pressure up to 0.35 GPa. These aromatic spacer moieties are closely comparable, and they have already demonstrated the capacity to form well-defined 2D perovskite phases,<sup>115,119,141</sup> which makes them appropriate models to analyse the differences in compression between RP and DJ type perovskites. We further study the effect of the halide counter ion on their structure-property relationship by comparing systems based on (BzA)<sub>2</sub>PbX<sub>4</sub> and (PDMA)PbX<sub>4</sub> compositions for X = I, Br ions by means of pressure-dependent UV-vis absorption, photoluminescence (PL) emission spectroscopy and X-ray scattering measurements, as well as density functional theory (DFT) calculations. One might expect that the additional degrees of freedom due to van der Waals gap in RP spacer layers would render them more compressible as compared to their DJ analogues. Similarly, the differences in the lattice compression of I- and Br-based systems are expected to become apparent.<sup>161</sup>

We find that the bulk modulus of RP and DJ is comparable under mild pressure despite the different binding mode of the spacers. The compression is predominant along the stacking direction (*a*-axis). In addition, we establish no direct pressure-dependent difference between the I- and Br-based compositions as their differences under pressure are more subtle. For all compositions, we observe that the unit cell monotonically shrinks with the applied pressure, which is accompanied by a red shift of the optical absorption upon increasing the pressure to 0.35 GPa. Moreover, (BzA)<sub>2</sub>PbBr<sub>4</sub> shows the most significant red shift of the optical absorption (-54.9 meV) as compared to the other compositions where a comparable shift (~30 meV) is observed. Synchrotron diffraction measurements and DFT calculations suggest that this is due to the smaller lattice spacing of the Br-based perovskite planes that initially enables only a shallow penetration of the Bz cations into the inorganic layer, but leads to a stronger pressure response with larger structural rearrangements as compared to its I-based system and PDMA-based DJ analogues. The pressure responses are found to be reversible, stimulating future applications.

## 5.2 Results and discussion

### 5.2.1 Structural characterization by means of XRD

To gain insights into the pressure response of RP and DJ perovskites, we prepared I- and Br-based precursor solutions using the monofunctional BzA and the bifunctional PDMA as organic spacers.<sup>115,119,141,164,211</sup> These aromatic spacers were selected based on their comparable structural features that permit the formation of phase-pure 2D RP and DJ perovskites. We fabricated thin films based on (PDMA)PbX<sub>4</sub> and (BzA)<sub>2</sub>PbX<sub>4</sub> (X = I, Br) compositions, as described in the Appendix, Section 8.4.1. We

focused the analysis on these  $n = 1$  2D systems, since they represent the most well-defined layered structures which are typically oriented parallel with respect to the substrate.<sup>95,96,135</sup>

Layered perovskite structure in the given thin films is confirmed by well-defined periodic diffraction patterns measured by X-ray diffraction (XRD) at ambient pressure, which exhibit the (h00) reflections that confirm parallel orientation of the perovskite slabs with respect to the substrate (Figure 5:2). A shift towards higher angles is observed when the iodide in the PDMA-based system is replaced by the bromide counter ion (Figure 5:2a), in accordance with the smaller halide radius, which in turn led to a smaller unit cell. On the contrary, when the iodide is replaced by bromide in the BzA-based systems, we observe the opposite behavior and a shift toward lower angles, indicating a larger lattice parameter  $a$  (Figure 5:2b). This finding could suggest a difference in the packing of the spacer for different halide counter ions, implying a larger distance between the perovskites slabs in  $(\text{BzA})_2\text{PbBr}_4$  as compared to the iodide counterpart.

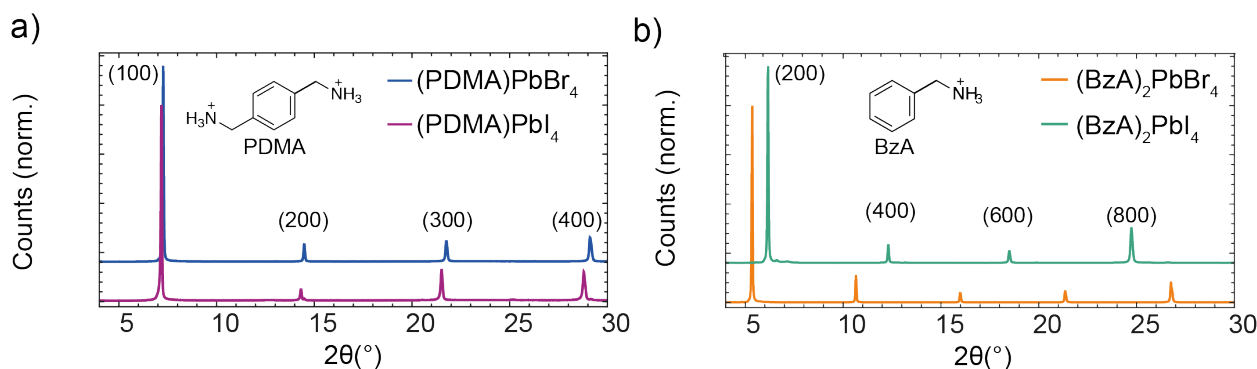


Figure 5:2. X-Ray diffraction pattern (Cu K $\alpha$  1.5406 Å) of thin films based on a)  $(\text{PDMA})\text{PbX}_4$  and b)  $(\text{BzA})_2\text{PbX}_4$  ( $X = \text{I}, \text{Br}$ ) composition on microscope glass slides at ambient pressure.

To understand this peculiar behavior as a function of halide counter ion and to elucidate the role of the physical pressure on the structural properties of these compositions, we investigated pressure-induced changes in the lattice parameters by pressure-dependent X-ray scattering. Diffraction data of perovskite powders for each composition were acquired using a synchrotron source at several pressure points in a membrane diamond-anvil cell (experimental details are provided in the Appendix, Section 8.4.1). I-based samples contained only the perovskite phase, while signals of precursors were detected in Br counterparts (Appendix, Figure 8:4:7). Yet the diffractions of the perovskite phase were easily identifiable allowing to perform reliable data analysis as the beam damage on the samples is negligible (Appendix, Figure 8:4:6).

At low pressures, the monoclinic  $P2_1/c$  space group is assigned to  $(\text{PDMA})\text{PbI}_4$  and  $(\text{PDMA})\text{PbBr}_4$ , the orthorhombic  $Pcab$  with non-standard settings of  $Pbca$  in order to keep consistently the organic spacers along [100] direction to  $(\text{BzA})_2\text{PbI}_4$ , and the orthorhombic  $Cmc2_1$  to  $(\text{BzA})_2\text{PbBr}_4$ . Despite compression along all the axes (Figure 5:3a,b), the largest compression is found to be along the  $a$ -axis (stacking direction) for all

systems, which is in accordance with previous reports.<sup>162,202</sup> This trend is significantly more pronounced for the  $(\text{BzA})_2\text{PbBr}_4$  (Figure 5:3b), which is the only one amongst the studied compositions that features a non-centrosymmetric structure. It shows a larger compression in the stacking direction ( $-6\%$  relative change) and an elongation of the in-plane lattice parameters ( $b$  and  $c$  axis) followed by a compression (Appendix, Figure 8:4:1d) – a rare structural feature known as negative area compressibility. Furthermore, the non-centrosymmetric  $(\text{BzA})_2\text{PbBr}_4$  crystal structure reveals two distinct values of Pb–X–Pb angles ( $\phi_1$  and  $\phi_2$  in the  $b$ - $c$  plane), whereas the octahedral tilting in the other three compositions is defined only by single Pb–X–Pb angle ( $\phi_1$ ; as shown in  $(\text{BzA})_2\text{PbI}_4$ , Figure 5:3c).

Perovskite layers are more distorted in  $(\text{BzA})_2\text{PbBr}_4$  composition since the deviation of  $\phi_1$  and  $\phi_2$  from  $180^\circ$  is larger as compared to its iodide analogue (Figure 5:3d). Therefore, the cavities between  $\text{PbBr}_6$  octahedra are smaller, which in turn hinders the penetration of organic spacer into the perovskite layers that could lead to the higher interlayer spacing in  $(\text{BzA})_2\text{PbBr}_4$  (Figure 5:2b). The angle between two adjacent octahedra hardly changes under pressure in the case of  $(\text{BzA})_2\text{PbI}_4$ , whereas both Pb–Br–Pb angles in  $(\text{BzA})_2\text{PbBr}_4$  change significantly between  $0.15$  –  $0.25$  GPa, the range where the compression along the  $a$ -axis is the strongest (Figure 5:3d). Although these changes are remarkable, the  $\text{Cmc}2_1$  space group is preserved, implying that  $(\text{BzA})_2\text{PbBr}_4$  undergoes an isostructural phase transition in this pressure range.<sup>212</sup>

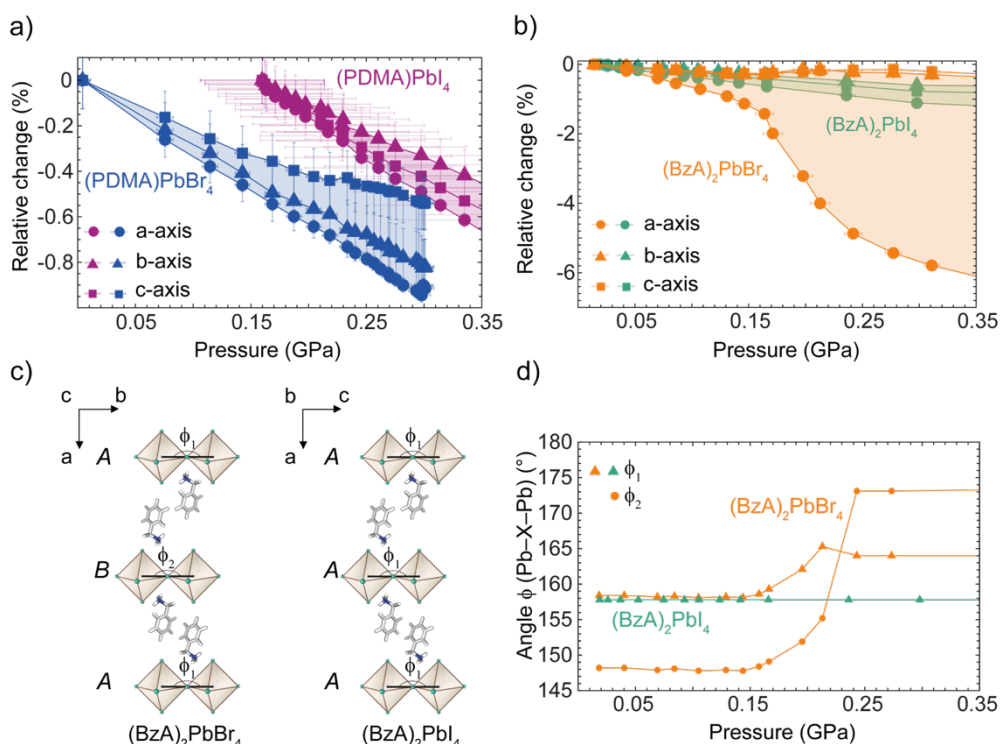


Figure 5:3. a) Relative change of the lattice parameters as a function of pressure for  $(\text{PDMA})\text{PbX}_4$  and b)  $(\text{BzA})_2\text{PbX}_4$  compositions. c) Schematic representation of  $(\text{BzA})_2\text{PbBr}_4$  alternating inorganic sheet (ABA) in comparison with its iodide counterpart (AAA) and the corresponding d) inter-octahedral tilting angles in  $(\text{BzA})_2\text{PbBr}_4$  and  $(\text{BzA})_2\text{PbI}_4$  systems, as extracted from the refinement of X-ray powder diffraction measurements.

To quantify at a first approximation the compressibility of the compositions in study, we calculate the isothermal bulk modulus, which is the inverse of compressibility, from the pressure-volume relationship (Figure 5:4) assuming mostly isotropic response to pressure by relying on the second order Birch-Murnaghan equation of state.<sup>213</sup>

$$P = \frac{3}{2}K_{T0} \left[ \left( \frac{V_0}{V} \right)^{\frac{7}{3}} - \left( \frac{V_0}{V} \right)^{\frac{5}{3}} \right]$$

Equation 5:1 – Steady-state condition formula

Here,  $K_{T0}$  is the isothermal bulk modulus at standard temperature,  $V_0$  is the initial volume,  $V$  is the volume at pressure  $P$ . To account for the isostructural phase transition in  $(\text{BzA})_2\text{PbBr}_4$ , the two-phase transition regimes are fitted separately and two  $K_{T0}$  are obtained for this composition (Figure 5:4b). As a result, there was no effect of the halide ion in PDMA-based systems since both  $(\text{PDMA})\text{PbI}_4$  and  $(\text{PDMA})\text{PbBr}_4$  show comparable bulk moduli (Figure 5:4a and Table 5:1). Furthermore, van der Waals gap renders both  $(\text{BzA})_2\text{PbI}_4$  and  $(\text{BzA})_2\text{PbBr}_4$  slightly more compressible (i.e. having lower bulk moduli) as compared to PDMA-based systems (Figure 5:4b and Table 5:1). In addition, two distinct bulk moduli for  $(\text{BzA})_2\text{PbBr}_4$  composition have been identified, which are attributed to isostructural phases at low and elevated pressure.<sup>214</sup> These results suggest the important role of the spacer cation in the resulting behavior. Since elucidating the local orientation and environment of the organic spacer molecules remains challenging based on the X-ray powder diffraction data, we further investigate the effect of pressure on the organic spacer layer by DFT calculations.

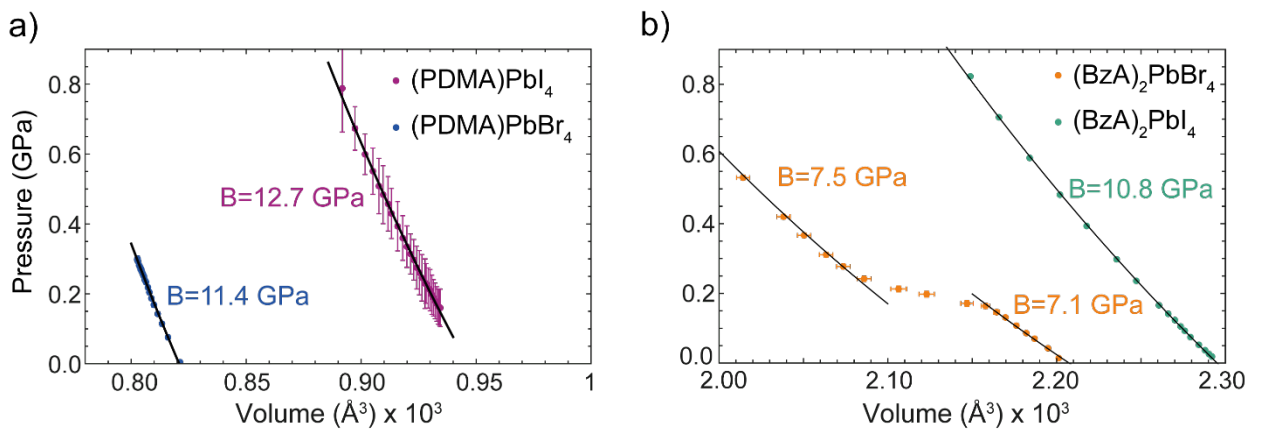


Figure 5:4. Pressure-Volume (P-V) relationship as a function of pressure fitted with second order Birch-Murnaghan equation of state fit (solid black line) for a)  $(\text{PDMA})\text{PbX}_4$  and b)  $(\text{BzA})_2\text{PbX}_4$ .

Table 5:1. Isothermal bulk moduli for the layered 2D perovskites studied.

Composition	$K_{T0}$ (GPa)
(PDMA)PbI <sub>4</sub>	11.40 ± 0.11
(PDMA)PbBr <sub>4</sub>	12.68 ± 0.14
(BzA) <sub>2</sub> PbI <sub>4</sub>	10.82 ± 0.04
(BzA) <sub>2</sub> PbBr <sub>4</sub> (< 0.14 GPa)	7.14 ± 0.22
(BzA) <sub>2</sub> PbBr <sub>4</sub> (> 0.14 GPa)	7.48 ± 0.27

### 5.2.2 Structural characterization by means of DFT

For DFT calculations, the data obtained from the synchrotron scattering measurements was used as initial starting point. For each pressure the coordinates of the atoms were relaxed without any constraints while fixing the lattice parameters at the experimentally measured values in order to better account for the thermal expansion of the lattice parameters at the measured temperature. The results suggest that the compression along the a-axis is due to reduced distance between the two neighboring spacers and their closer packing (Figure 5:5a). The initial vertical distance between the two BzA spacers,  $d(\text{BzA-BzA})$ , defined from the center of the benzyl ring, is significantly larger in the case of (BzA)<sub>2</sub>PbBr<sub>4</sub> (4.43 Å) as compared to (BzA)<sub>2</sub>PbI<sub>4</sub> (2.97 Å; Figure 5:5a). This distance decreases by 0.4 Å for (BzA)<sub>2</sub>PbBr<sub>4</sub>, whereas for the I-based analog the decrease accounts to only 0.08 Å within the same pressure range, resulting in a larger compression for (BzA)<sub>2</sub>PbBr<sub>4</sub>.

Calculations further suggest the presence of two distinct octahedra tilting angles (141.5° and 154.5°) in (BzA)<sub>2</sub>PbBr<sub>4</sub> (Appendix, Figure 8:4:2a). These angles are lower than the one in (BzA)<sub>2</sub>PbI<sub>4</sub> (by 4° and 16°, respectively), which represents a higher distortion of the octahedra, thereby leaving less room for the BzA spacers to penetrate than the already shorter Pb–Br distances would allow. The penetration depth of the spacer into the inorganic framework is the result of an interplay of interactions between the organic and inorganic components and it changes continuously upon increasing pressure for the PDMA-based compositions (Appendix, Figure 8:4:2a) and (BzA)<sub>2</sub>PbI<sub>4</sub> (Figure 5:5b), whereas in (BzA)<sub>2</sub>PbBr<sub>4</sub> there is an abrupt change leading to higher penetration depth (Figure 5:5b). This difference in the (BzA)<sub>2</sub>PbBr<sub>4</sub> system could primarily originate from the changes in the octahedral tilting angles, the spacer packing and orientation.<sup>161</sup>

In addition, the Pb–X bond length could potentially also change under pressure. The equatorial Pb–Br bond lengths in (BzA)<sub>2</sub>PbBr<sub>4</sub> at low pressure (2.98 Å and 3.02 Å; Appendix, Figure 8:4:2c) are smaller than the ones in (BzA)<sub>2</sub>PbI<sub>4</sub> (3.21 Å and 3.25 Å; Appendix, Figure 8:4:2c), leading to a denser octahedral packing, which could potentially limit the spacer penetration into the Pb–Br lattice at ambient pressure as evidenced in Figure 5:2b. However, the axial Pb–X bond lengths remain constant over the entire pressure range (Appendix, Figure 8:4:2c). DFT calculations suggest a very small compression of Pb–X bonds with pressure that can affect the Pb–X antibonding overlap and thereby the bandgap, which has however not been experimentally detected in the studied pressure range. This implies that the measured compressions are not caused by the changes in the Pb–X bond lengths. Instead, the response to mild pressure is the result of changes in the packing within the organic spacer layer. This packing within the organic spacer layer has been previously associated with the non-centrosymmetric structure of the (BzA)<sub>2</sub>PbBr<sub>4</sub> composition,<sup>141</sup> which is unique for this composition as compared to others. The calculations for (BzA)<sub>2</sub>PbI<sub>4</sub> and (PDMA)PbX<sub>4</sub> show comparable change under pressure (Figure 5:6a-c), whereas the two BzA spacers in (BzA)<sub>2</sub>PbBr<sub>4</sub> were found to move closer together as shown in the Figure 5:6d. In the pressure range between 0.164 GPa to 0.213 GPa, the BzA spacers were found to penetrate deeper into the inorganic lattice, hence affecting the resulting properties (Figure 5:5b). It is important to note that the zero is set at the halide planes and larger penetration corresponds to more negative values. This process is accompanied by a decrease in the BzA tilting angle,  $\phi(\text{BzA} \dots \text{nPbX})$ , defined as the angle between the a-axis and the benzyl plane (Appendix, Figure 8:4:2d). Such a change corresponds to a rearrangement of the BzA spacers into a more parallel orientation with respect to the a-axis (Appendix, Figure 8:4:2d). Moreover, this is reflected in the changes in the horizontal direction that are uniquely observed for the (BzA)<sub>2</sub>PbBr<sub>4</sub> composition (Appendix, Figure 8:4:2e). Consequently, the significant change in the distance between the neighboring BzA groups is qualitatively in accordance with the experimental observation of a larger compression for (BzA)<sub>2</sub>PbBr<sub>4</sub>. Such changes in the assembly of the spacer layer in response to pressure are further reflected in their optoelectronic properties and thus mechanochromism.

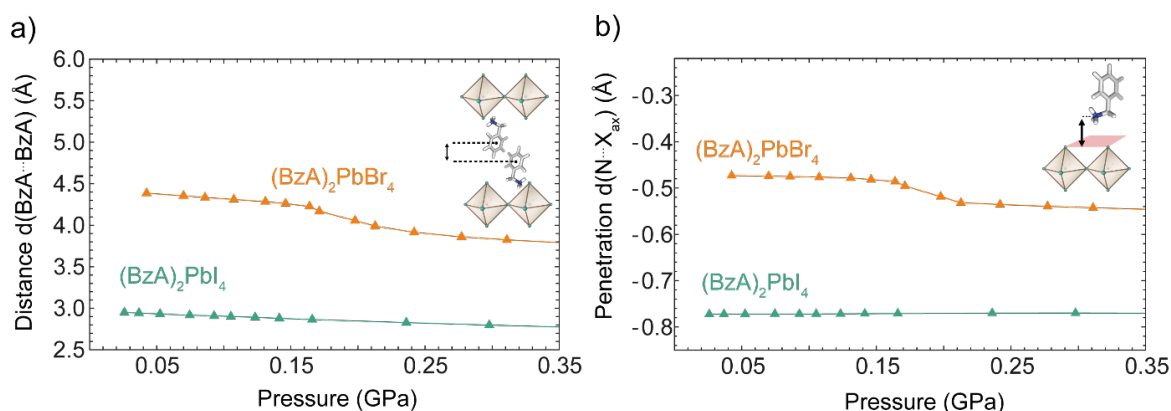


Figure 5:5. Calculated a) average distances of the (vertically) neighboring BzA rings  $d(\text{BzA} \dots \text{BzA})$  in the RP layer and b) nitrogen penetration depth in the halide plane  $d(\text{N} \dots \text{X}_{\text{ax}})$  as a measure of the penetration depth based on the DFT-optimized structures (PBEsol).

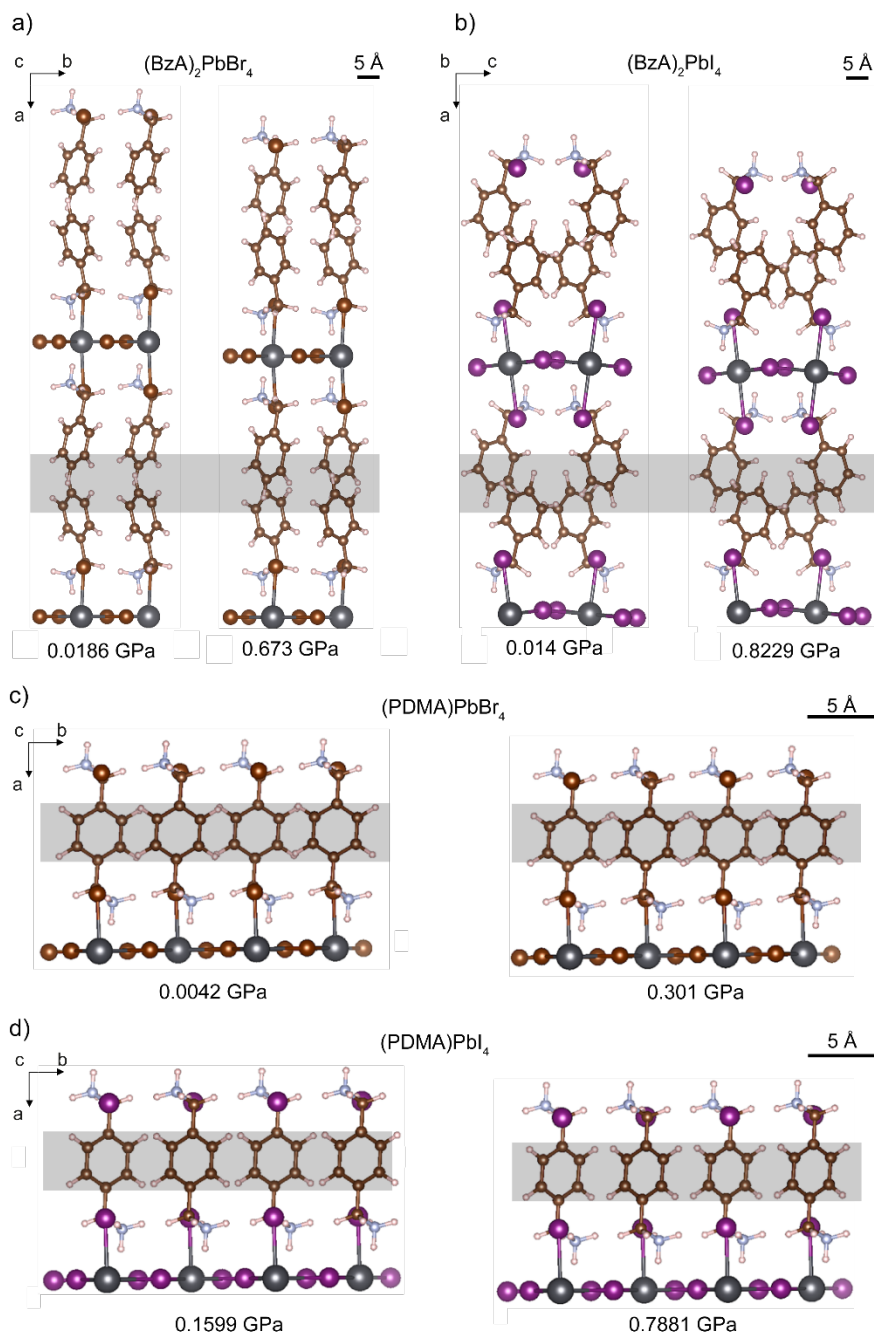


Figure 5:6. Relaxed structures of a)  $(\text{BzA})_2\text{PbBr}_4$  at 0.014 GPa and at 0.673 GPa, b)  $(\text{BzA})_2\text{PbI}_4$  at 0.0186 GPa and at 0.8229 GPa. c)  $(\text{PDMA})\text{PbBr}_4$  at 0.0042 GPa and at 0.3011 GPa, d)  $(\text{PDMA})\text{PbI}_4$  at 0.1598 GPa and 0.7881 GPa. The rectangle in grey highlights the change in the spacer distances for all the systems at a representative low and high pressure.

### 5.2.3 Mechanochromic properties

To assess the mechanochromic properties, we monitored the optical absorption properties as a function of applied external stress by measuring pressure-dependent absorption on  $(\text{PDMA})\text{PbX}_4$  and



(BzA)<sub>2</sub>PbX<sub>4</sub> (X = Br, I). The samples were placed inside a hydrostatic pressure cell filled with an inert liquid (tetradecafluorohexane, FC-72, as detailed in the Appendix, Section 8.4.1). A schematic representation of the measurement cell is shown in Figure 5:7a. We applied pressure from 0 to 0.35 GPa in steps of 0.05 GPa through a manual pump. Quantum and dielectric confinement effects give rise to an intense and narrow excitonic absorption feature (Appendix, Figure 8:4:3), typical of layered 2D perovskites.<sup>215,216</sup> We observe a continuous shift of the excitonic peak toward lower energies for all analyzed perovskite compositions (Figure 5:7b–e). In addition, the red-shift confirms that a mild external pressure can be sufficient to tune the optical properties in these materials. Similarly, pressure-dependent PL measurements show a red-shift toward smaller energy upon increasing pressure (Figure 5:8).

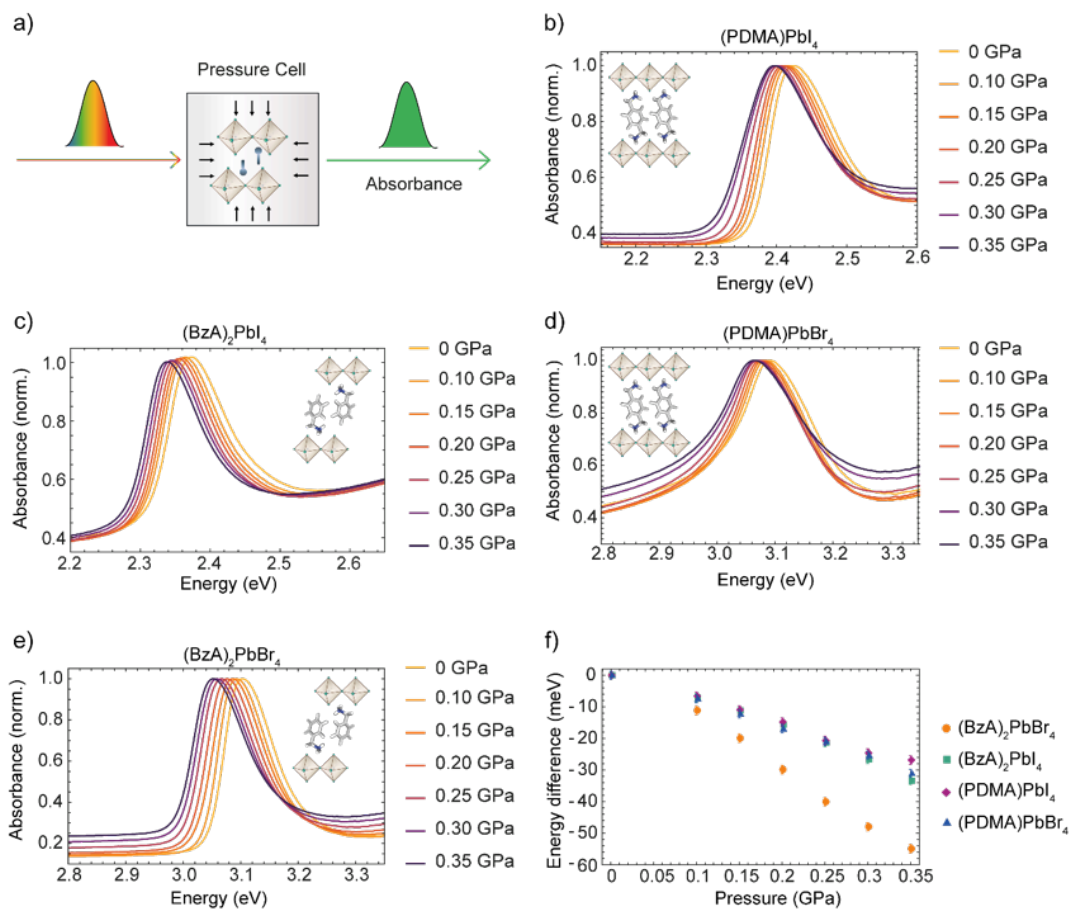


Figure 5:7. Schematic of the a) experimental setup for pressure-dependent absorbance measurements and b) pressure-dependent absorbance collected (PDMA)PbI<sub>4</sub>, c) (BzA)<sub>2</sub>PbI<sub>4</sub>, d) (PDMA)PbBr<sub>4</sub> and e) (BzA)<sub>2</sub>PbBr<sub>4</sub> in the pressure range from ambient to 0.35 GPa. The inset shows a schematic representation of the layered structures. f) Energy difference of the excitonic peak energy as a function of applied pressure.

We obtained the excitonic peak energy of the (PDMA)PbI<sub>4</sub> and (BzA)<sub>2</sub>PbI<sub>4</sub> as a function of pressure fitting a skewed Gaussian function to the absorption spectra. At ambient pressure, the excitonic peak energy of

(PDMA)PbI<sub>4</sub> and (BzA)<sub>2</sub>PbI<sub>4</sub> is 2.41 eV and 2.36 eV, respectively. Upon increasing the pressure, the excitonic-peak shift at 0.30 GPa as compared to ambient pressure is about  $(-25 \pm 0.6)$  meV for (PDMA)PbI<sub>4</sub> and  $(-27 \pm 1)$  meV for (BzA)<sub>2</sub>PbI<sub>4</sub> (Figure 5:7f). We observed a similar linear trend for both RP and DJ perovskites until the pressure of 0.30 GPa, where the response to external pressure causes a comparable energy shift. For pressures higher than 0.3 GPa, the (BzA)<sub>2</sub>PbI<sub>4</sub> appears to shift to a larger extent in comparison with the (PDMA)PbI<sub>4</sub>, showing an energy shift of  $(-33 \pm 1)$  meV and  $(-27 \pm 0.5)$  meV, respectively (Figure 5:7f). A more pronounced difference in the response for higher pressures (above 0.3 GPa) is likely to be associated with the structural differences of the corresponding RP and DJ phases, in accordance with the previous reports.<sup>162,202</sup> Further investigations at pressures above 0.35 GPa are not possible with the same experimental setup because of the limitations of the hydrostatic pressure cell. Nevertheless, monitoring the shift of the excitonic peak by its maximum intensity reveals the same slope as fitting the skewed Gaussian with a larger error given by the resolution of the absorbance measurement (Appendix, Figure 8:4:4). For Br-based analogues, the excitonic peak energy is 3.06 eV and 3.07 eV for (PDMA)PbBr<sub>4</sub> and (BzA)<sub>2</sub>PbBr<sub>4</sub>, respectively. Upon increasing the pressure to 0.35 GPa, the energy shifts for both (PDMA)PbBr<sub>4</sub> and (BzA)<sub>2</sub>PbBr<sub>4</sub> by  $(-31 \pm 1)$  meV and  $(-55 \pm 0.2)$  meV, respectively. The (BzA)<sub>2</sub>PbBr<sub>4</sub> has a notably larger energy shift than its I- and PDMA-based systems (Figure 5:7f).

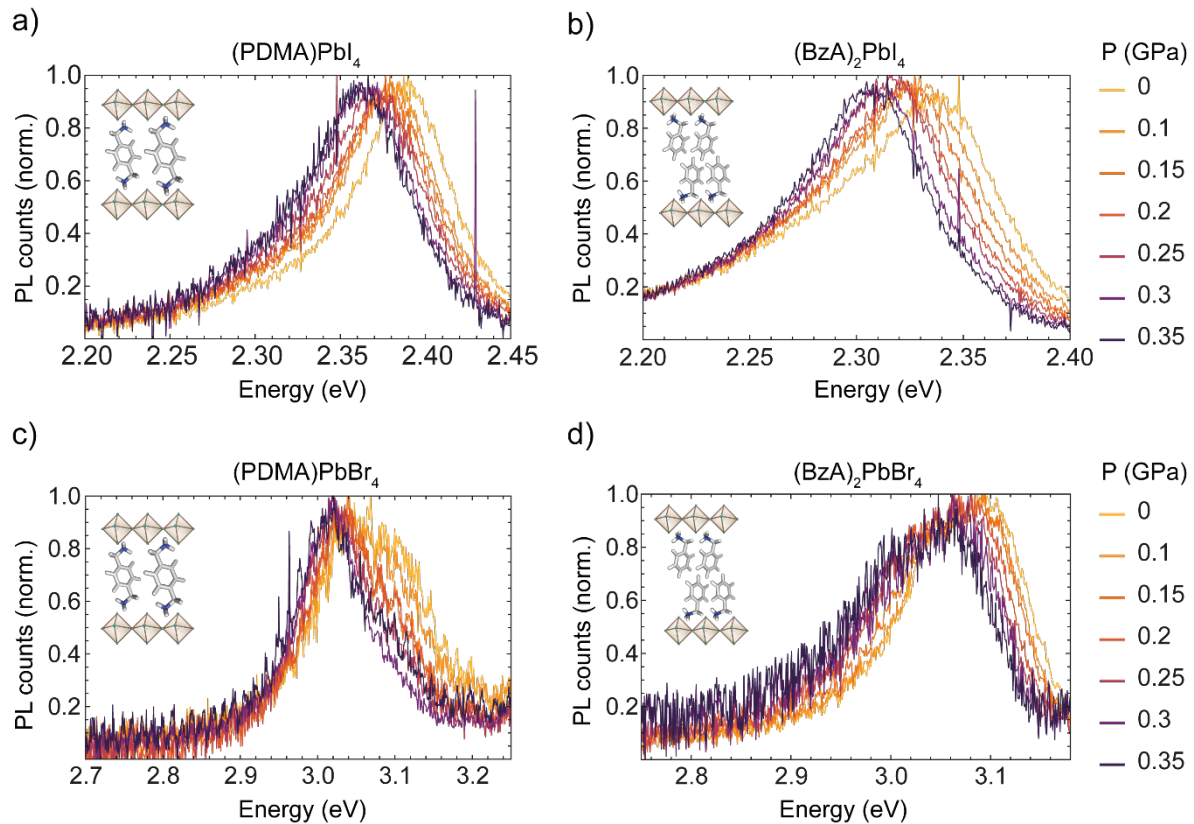


Figure 5:8. Pressure-dependent photoluminescence for a) (PDMA)PbI<sub>4</sub>, b) (BzA)<sub>2</sub>PbI<sub>4</sub>, c) (PDMA)PbBr<sub>4</sub>, d) (BzA)<sub>2</sub>PbBr<sub>4</sub>. The photoluminescence peak shifts towards smaller energy as a function of pressure for all the compositions studied.

To sum up, the energy shifts in I-based samples closely correspond to each other, which suggests that pressure-dependent properties are comparable for RP and DJ phases in this pressure range. However, Br-based systems show contrasting differences, with  $(\text{BzA})_2\text{PbBr}_4$  having substantially larger shifts as compared to  $(\text{PDMA})\text{PbBr}_4$  and I-based systems. Such larger shift in  $(\text{BzA})_2\text{PbBr}_4$  is in accordance with the more significant compressibility of  $(\text{BzA})_2\text{PbBr}_4$  as compared to its I-based analogs and PDMA-based systems (Table 5:1). Furthermore, the isostructural phase transition induced by the reduction of octahedral tilting (*i.e.* the Pb–Br–Pb angle is closer to  $180^\circ$ ) is associated with the change of penetration depth of the BzA spacers into the perovskite lattice and the distance between the neighboring spacers. This is related to the quantum confinement, which is reduced by the change in potential barrier width. The qualitative variations of the band gaps as a function of pressure are well reproduced theoretically (Appendix, Figure 8:4:5).

The shifts of the excitonic peaks are fully recovered for both I- and Br-based RP and DJ perovskites upon decompression from 0.35 GPa to ambient pressure, implying that the process is reversible in this pressure range. The corresponding absorption spectra of both materials almost perfectly overlap after decompression (Figure 5:9a–d). The reversibility of the optical features strongly suggests structural reversibility, which is in agreement with the DFT predictions and in contrast with the amorphization commonly reported at higher pressures.<sup>217–219</sup> This reversibility of the mechanochromic response of layered hybrid perovskites is of interest to their use as model systems for elucidating structure-property relationships in hybrid layered materials, which is relevant for the long-term stability of flexible perovskite devices, but also points towards the use of mechanophores in the development of smart materials and pressure sensors.<sup>220–222</sup>

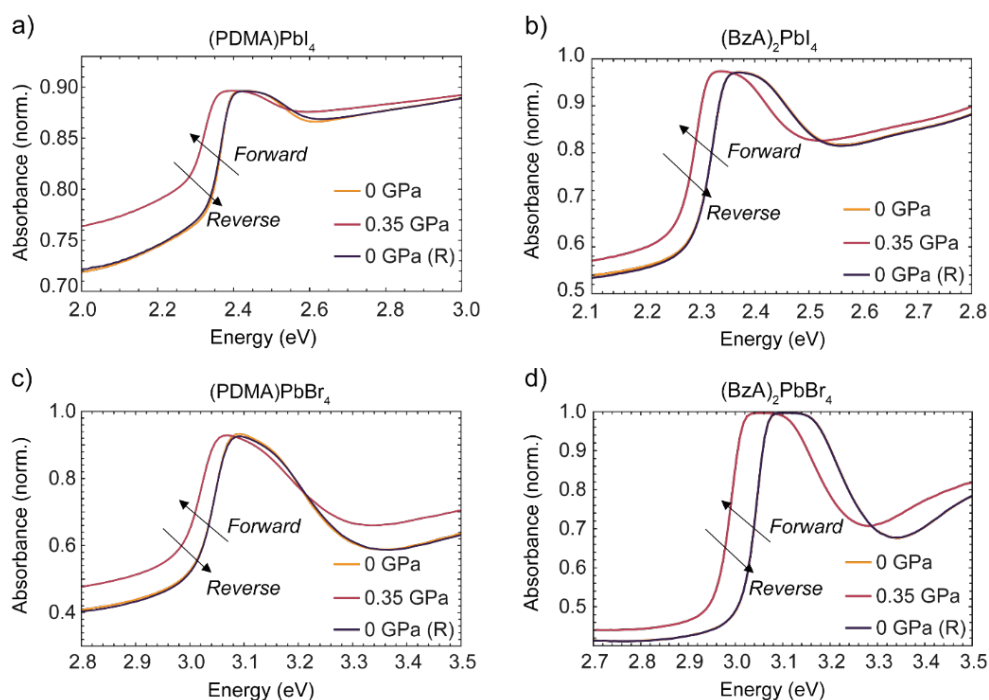


Figure 5:9. Pressure-dependent absorbance recorded using UV-VIS at three characteristic pressures in the forward and reverse direction for a)  $(\text{PDMA})\text{PbI}_4$  and b)  $(\text{BzA})_2\text{PbI}_4$ , c)  $(\text{PDMA})\text{PbBr}_4$  and d)  $(\text{BzA})_2\text{PbBr}_4$ .

### 5.2.4 Correlation between structural and optical properties

We can directly correlate the experimental structural parameters obtained by pressure-dependent XRD measurements with the changes in the optical absorption. The relationship between the shift in the exciton absorption peak and the length of the *a*-axis is linear for both PDMA-based and BzA-based samples (Figure 5:10a,b), with the exception in (BzA)<sub>2</sub>PbBr<sub>4</sub>, where we observe two different regimes which are attributed to the isostructural phase transition. A linear fit of the energy shift as a function of the *a*-axis length results in a comparable slope of  $0.223 \pm 0.009$  eV/Å and  $0.228 \pm 0.005$  eV/Å for (PDMA)PbBr<sub>4</sub> and (PDMA)PbI<sub>4</sub>, respectively. The slope of  $0.078 \pm 0.003$  eV/Å was obtained for (BzA)<sub>2</sub>PbI<sub>4</sub>, whereas  $0.052 \pm 0.01$  eV/Å and  $0.036 \pm 0.001$  eV/Å for (BzA)<sub>2</sub>PbBr<sub>4</sub> below and above the isostructural phase transition, respectively (Figure 5:10a,b). This suggests a stronger dependency of the optical properties of PDMA systems on the change of the *a*-axis compared to the BzA systems. No correlation was observed between Pb–X–Pb angle and the optical absorption (Figure 5:10c,d), except in the case of isostructural phase transition regime in (BzA)<sub>2</sub>PbBr<sub>4</sub> (Figure 5:10d). Thus, we find that the bandgap change is largely caused by the compression of the *a*-axis in the representative DJ and RP layered 2D perovskites, which is expected based on the reduced quantum confinement, whereas the changes do not correlate with the Pb–X–Pb angles within the same structural phase. This further implies that the differences in the mechanochromic response for different organic moieties are directly associated with the interactions within the spacer layer and their contacts with the perovskite slabs.

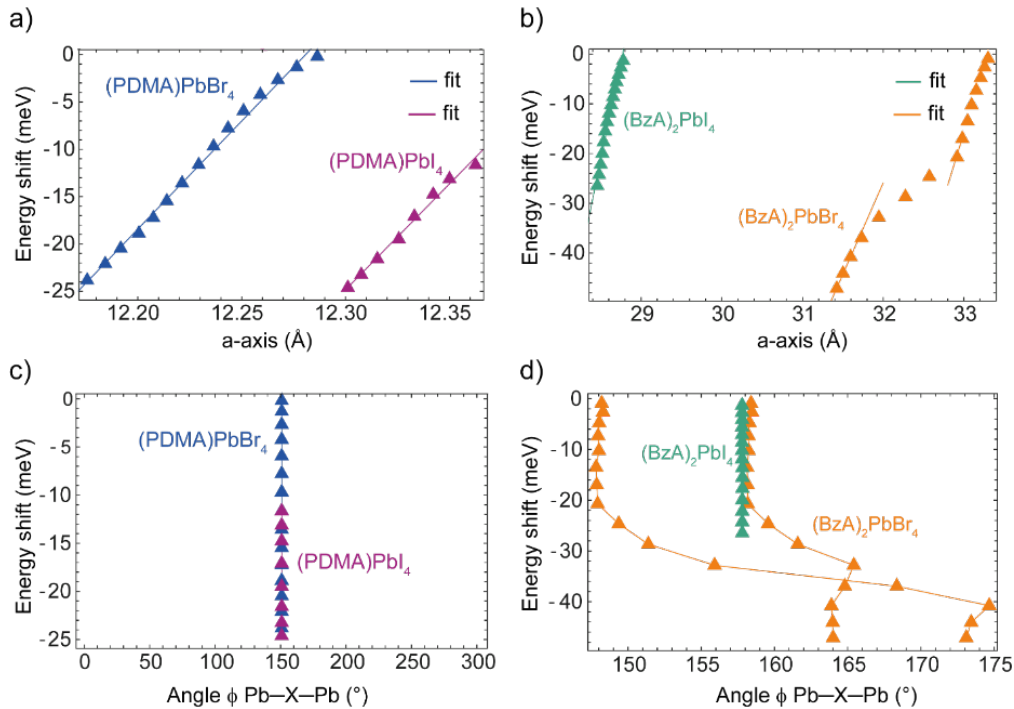


Figure 5:10. Optical absorption shift as a function of a) the *a*-axis length for PDMA- and b) BzA-systems, and as a function of the Pb–X–Pb angles for c) for PDMA- and d) BzA-systems based on the experimental data.

---

### 5.3 Conclusions

In summary, we report a direct comparison of the response of iodide and bromide-based RP and DJ 2D perovskites to pressure by using comparable aromatic spacer moieties, namely benzylammonium (BzA) and 1,4-phenylenedimethylammonium (PDMA), respectively. We applied a mild pressure up to 0.35 GPa to all the compositions and detected a red shift of the excitonic peak upon increasing the pressure. Despite different binding mode of the spacers, we find that the RP and DJ perovskites behave similarly in this pressure range, with an anisotropic response predominantly in the out-of-plane (*a*-axis) direction. Moreover, while PDMA-based perovskites were not found to be susceptible to changes associated with the halide ion, presumably due to higher geometric constraints in DJ phases, BzA-based perovskite results in a larger excitonic peak shift in bromide-based compositions that is in contrast with their higher expected level of rigidity as compared to iodide-based phases. Furthermore, X-ray scattering experiments in conjunction with DFT calculations under pressure suggest that this effect is related to the structural properties of the 2D perovskite phases. Specifically, X-ray scattering experiments reveal significant relaxation of Pb–X–Pb angle in (BzA)<sub>2</sub>PbBr<sub>4</sub>, which is evidenced by the isostructural phase transition, whereas no phase transition is detected for the other compositions. DFT computations further indicate that this isostructural space group transition is associated with a decrease in the distance between BzA spacers and with an increased penetration depth of the spacers into the Pb–Br lattice. Moreover, this phase is the only one among the studied compositions that features a non-centrosymmetric lattice, which is likely to further amplify its mechanochromic response. These differences explain the large compression of (BzA)<sub>2</sub>PbBr<sub>4</sub> under mild pressures. This study thereby provides important insights into the mechanochromic properties of layered hybrid perovskites while highlighting the importance of an interplay between the organic and the inorganic layers in the resulting structure. Moreover, the unique reversibility of their mechanochromic response in this mild pressure range opens new perspective towards the utility of layered hybrid perovskites as potential platforms for amphidynamic materials<sup>223,224</sup> and mechanophores,<sup>220–222</sup> which expands the perspectives for their future applications.

---

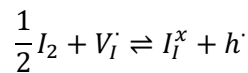
# Chapter 6 Mixed conductivity of layered hybrid perovskites

This chapter will discuss the mixed conductivity of layered hybrid perovskites by using (PDMA)PbI<sub>4</sub> and (BzA)<sub>2</sub>PbI<sub>4</sub> as representatives of DJ and RP perovskite phases, respectively. This is the subject of a manuscript that is currently in preparation.

## 6.1 Introduction

Unlike classical semiconductors such as Si, GaAs, and CdTe, hybrid halide perovskites are mixed ionic-electronic conductors.<sup>225–227</sup> This has been evidenced by the appearance of hysteresis in current-voltage characteristics of solar cells,<sup>228</sup> photo-induced halide mixing,<sup>229</sup> photodecomposition,<sup>230,231</sup> field-switchable photovoltaic effects,<sup>232</sup> and perceptible electromotive force voltage,<sup>227</sup> which point to the significant ion conduction in these materials. Previous extensive studies on the electrical properties of MAPbI<sub>3</sub> provide strong indications that iodide vacancies are the primary mobile species.<sup>233,234</sup> There is no strong consensus on the dominant defect disorder as both anti-Frenkel<sup>235</sup> and the Schottky-type intrinsic disorders<sup>227,236,237</sup> are feasible.

Under equilibrium dark conditions, the iodide defect concentration( $\delta$ ), which is defined by material stoichiometry (MAPbI<sub>3+ $\delta$</sub> ), is directly coupled with the electronic carrier concentration. The nature of the electronic conductivity relies on the concentration levels of iodide vacancies, which can be denoted ( $V_I$ ) according to Kröger-Vink notation  $M_L^C$ , where  $M$  is atom type,  $L$  represents the regular site in the perfect crystal, and  $C$  stands for the effective (relative) charge. Specifically, the reduction in iodide vacancies upon iodine ( $I_2$ ) incorporation would lead to an increased hole concentration ( $h^\cdot$ ), converting the material to a p-type system, in accordance with the equation 6:1.<sup>185</sup>



Equation 6:1 – Iodine incorporation reaction.

Moreover, variation in the concentration of ionic defects can be altered by subjecting the sample to the electrical potential difference, which induces ion redistribution if electrodes are used that block the ions. This process involves a coupled transport of electrons and ions via the chemical diffusion process. Quantitatively, this process is characterized by a chemical resistance ( $R^\delta$ ) and a chemical capacitance ( $C^\delta$ ).<sup>238</sup> When the sample is sandwiched between ion-blocking electrodes to which a voltage is applied, in such a stoichiometric polarization, the redistribution of ions leads to a compositional gradient in the sample. Under steady-state

condition (Figure 6:1a), the electrochemical potential of halide ions ( $\tilde{\mu}_{X^-}$ ) is constant, whereas the electron's electrochemical potential ( $\tilde{\mu}_e$ ) and, consequently, the halogen ( $\mu_X$ ) chemical potential follow the gradient established by the applied potential. Assuming a small perturbation and an approximately linear relationship between iodine defect concentration and the iodine chemical potential, the stoichiometry profile would follow the  $\mu_X$ . Under these steady-state conditions, the stoichiometric variations within the material can be evaluated by a relationship described by the equation 6:2, where  $U_{ss}$  is external steady-state bias and  $F$  stands for Faraday's constant. The process of ion redistribution might cause reversible degradation in perovskite solar cells under operational conditions.<sup>239,240</sup> However, voltages exceeding the stability limit of materials could drive them to decomposition, as the induced stoichiometric variations exceed the stability window (Figure 6:1b). For instance, voltages above 1.4 V could trigger MAPbX<sub>3</sub> (X = I, Br, Cl) decomposition into methylamine, lead halides (PbX<sub>2</sub>), and hydrogen halides (HX).<sup>185</sup>

$$\frac{-\Delta\mu_X}{F} = U_{ss}$$

Equation 6:2 – Steady-state condition formula

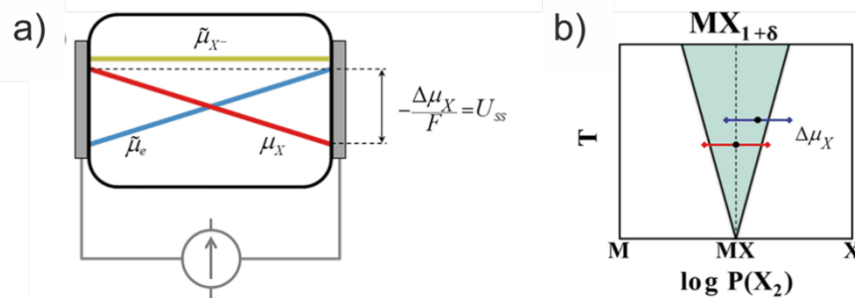


Figure 6.1. Schematic representation of (a) of the steady-state situation when the mixed conductor is sandwiched between ionic blocking electrodes; (b) stability window of the binary materials, here y-axis represents temperature, while x is the activity of the constituting elements. Adopted from the reference.<sup>185</sup>

Similarly, a chemical bias can also induce degradation, whereas light can be detrimental in the process. It has been demonstrated that a significant enhancement of ion conduction occurs upon exposure to light.<sup>230</sup> The current proposition of the underlying mechanism driving this process relies on the assumption that photo-generated holes localize on the iodide, which promotes the formation of neutral iodine interstitials. By increasing the concentration of neutral iodine interstitials under light, the composition of the material could exceed the limit of the stability window, leading to photodecomposition via iodine excorporation. This effect is more pronounced in iodide-based perovskites, supposedly due to more polarizable iodine.<sup>241</sup> Another phenomenon related to ion migration is photo de-mixing, whereby mixed halide compositions suffer from

---

halide segregation when the material is exposed to light.<sup>229</sup> This effect might hinder the material's performance, as the electronic carriers can get trapped in iodide-rich domains.<sup>242</sup>

Ion migration is a critical factor undermining stability and performance of the hybrid halide perovskites.<sup>185</sup> To tackle this problem, it is important to reduce ion migration, or in an ideal case, eliminate it. Compositional engineering can to an extent reduce the problem of ion migration. More specifically, mixed A cation compositions may benefit from an increased activation energy for ion migration, while ion conductivity in Br-based compositions is less susceptible to the photoinduced effects.<sup>241</sup> However, compositional engineering does not eliminate the issue. Alternatively, dimensionality engineering might be a more effective way to tune ionic transport properties. The structure of perovskite materials with reduced dimensionality is templated by the large organic spacer cations, which could effectively act as physical barriers preventing ion migration. For example, layered perovskites based on BA organic spacers are reported to have imperceptible ion migration,<sup>90,243</sup> while systems based on PEA still exhibit high activation energy for ion migration.<sup>91</sup> However, the effects of spacer cations on ion transport properties have to be carefully investigated, since it has been demonstrated that spacer molecules have a significant role in controlling photo-induced halide segregation, which is directly related to ion migration.<sup>137</sup> Until now, only the ionic properties of 2D perovskites based on monofunctional spacers, which form RP-type perovskites, have been studied. Given the earlier evidence on the substantial role of spacer cations in determining electrical properties, studies on DJ-type perovskites employing bifunctional spacers would provide new insights. This especially refers to the effects of the reduced interlayer spacing and the removal of the van der Waals gap on the ionic conductivity. To this end, this thesis focuses on the electrical properties of both RP and DJ type layered perovskites utilizing structurally closely comparable spacers, allowing to elucidate the aforementioned effects related to mixed conductivity.

## 6.2 Results and discussion

### 6.2.1 Thin films for in-plane conductivity

This study focuses on representative layered hybrid perovskites based on  $n = 1$  compositions comprising benzylammonium (BzA), which crystallize in RP type  $(\text{BzA})_2\text{PbI}_4$  structure, and phenylenedimethan ammonium (PDMA) spacers, forming DJ  $(\text{PDMA})\text{PbI}_4$  perovskites. The corresponding samples were prepared from perovskite solutions, which were obtained by dissolving stoichiometric quantities of  $(\text{BzA})\text{I}$  and  $\text{PbI}_2$  in dimethylformamide (DMF) or  $(\text{PDMA})\text{I}_2$  and  $\text{PbI}_2$  in 4:1 (v:v) DMF: dimethyl sulfoxide (DMSO) to yield 0.4 M  $(\text{BzA})_2\text{PbI}_4$  and  $(\text{PDMA})\text{PbI}_4$  solutions, respectively. The precursor solutions were thereafter spin-coated at 1000 rpm for 10 sec and 4000 rpm for 20 sec and subsequently annealed for 10 min at 100 °C  $(\text{BzA})_2\text{PbI}_4$  and 150 °C  $(\text{PDMA})\text{PbI}_4$ . Quartz substrates with gold interdigitated electrodes were used for the



electrical measurements with the total overlap area between electrode fingers of  $0.0016 \text{ cm}^2$  and the distance between each electrode of  $10 \text{ }\mu\text{m}$  (Figure 6:2a).

X-ray diffraction pattern of a  $(\text{BzA})_2\text{PbI}_4$  thin film shows (00l) reflection peaks (Figure 6:2b), which indicate the presence of crystallites with basal planes that are oriented parallel to the substrate. For the  $(\text{PDMA})\text{PbI}_4$  thin films, the most intense peaks have Miller indices (h00), corresponding to the parallel orientation of perovskite layers with respect to the substrate. In addition, there are (0kl) reflections (Figure 6:2b) coming from perpendicularly orientated perovskite layers.<sup>133</sup> Nonetheless, the intensity of these peaks is low, implying that the dominant crystallite orientation is parallel to the substrate. Considering the electrode architecture and the orientation of the crystallites in the analyzed films, one could presume that in such device architecture mainly in-plane conductivity was measured (Figure 6:2a, inset). Good electrical contact is established contact between electrodes and perovskite, as both  $(\text{PDMA})\text{PbI}_4$  (Figure 6:2d) and  $(\text{BzA})_2\text{PbI}_4$  (Figure 6:2e) thin films have compact and uniform morphology, with different domain sizes, whose effects will be discussed in the later sections.

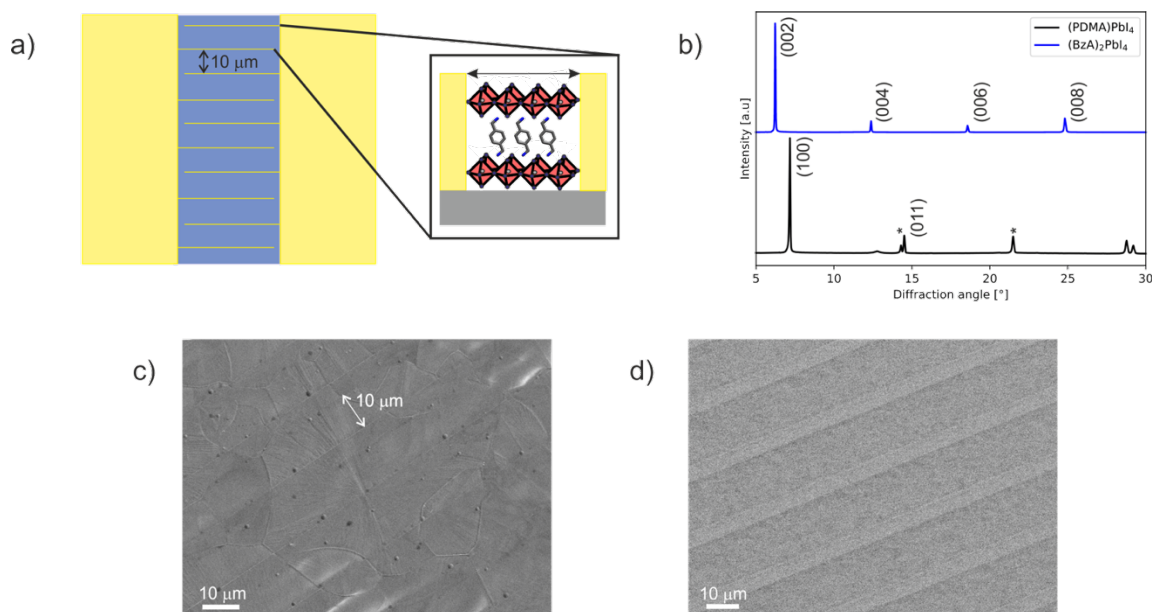


Figure 6:2. (a) Schematic representation of the electrode substrate used for electrical measurements. Inset: graphic illustration of a  $(\text{PDMA})\text{PbI}_4$  perovskite placed between two electrodes (b) X-ray diffraction patterns of  $(\text{BzA})_2\text{PbI}_4$  in blue and of  $(\text{PDMA})\text{PbI}_4$  in black. Here \* corresponds to higher-order (h00) reflections and # - to (0kl) ones. (c–d) SEM images of (c)  $(\text{PDMA})\text{PbI}_4$  and (d)  $(\text{BzA})_2\text{PbI}_4$  thin films deposited on the electrode substrates.

### 6.2.2 Galvanostatic measurements of RP and DJ samples

The electrical properties were measured by galvanostatic polarization experiments (more information about the technique and the data analysis is available in Appendix section 8.5.1). The shape of the polarization curves of  $(\text{PDMA})\text{PbI}_4$  and  $(\text{BzA})_2\text{PbI}_4$  thin-film recorded in Argon atmosphere at  $60 \text{ }^\circ\text{C}$  (Figure

6:3a,c) are indicative of a mixed conductor. Electronic and ionic conductivities of the DJ samples are closely comparable and in the range of  $4 \times 10^{-11} - 5 \times 10^{-11}$  S/cm, while RP exhibits lower electronic ( $2.5 \times 10^{-11}$  S/cm) and ionic ( $1.5 \times 10^{-11}$  S/cm) conductivities (Figure 6:3e, yellow region). The higher resistivity of RP samples could be associated with the larger interlayer spacing, though the difference between RP and DJ conductivity values is not sufficiently significant to draw an unambiguous conclusion.

Dimensionality reduction has a substantial effect on electrical properties. Both RP and DJ samples have several orders of magnitude lower conductivity in comparison to MAPbI<sub>3</sub> with the reported values on the order of  $10^{-6} - 10^{-9}$  S/cm.<sup>227,230,233,241,244</sup> Lower electronic conductivity of layered hybrid perovskites might be attributed to their larger bandgap, reducing the concentration of thermally excited electronic carriers. In addition, carrier confinement effects that could hamper charger transport, should be considered as well. These effects would be lower in quasi-2D perovskites ( $n > 1$ ), as their structural properties approach 3D perovskites. Similarly, multiple factors might be playing a role in the case of reduced ionic conductivity, such as defect formation energy, anisotropy effects, or ion migration energy barrier.<sup>13</sup> The activation energy associated with the material's conductivities is a function of all these factors and will be discussed later in this chapter.

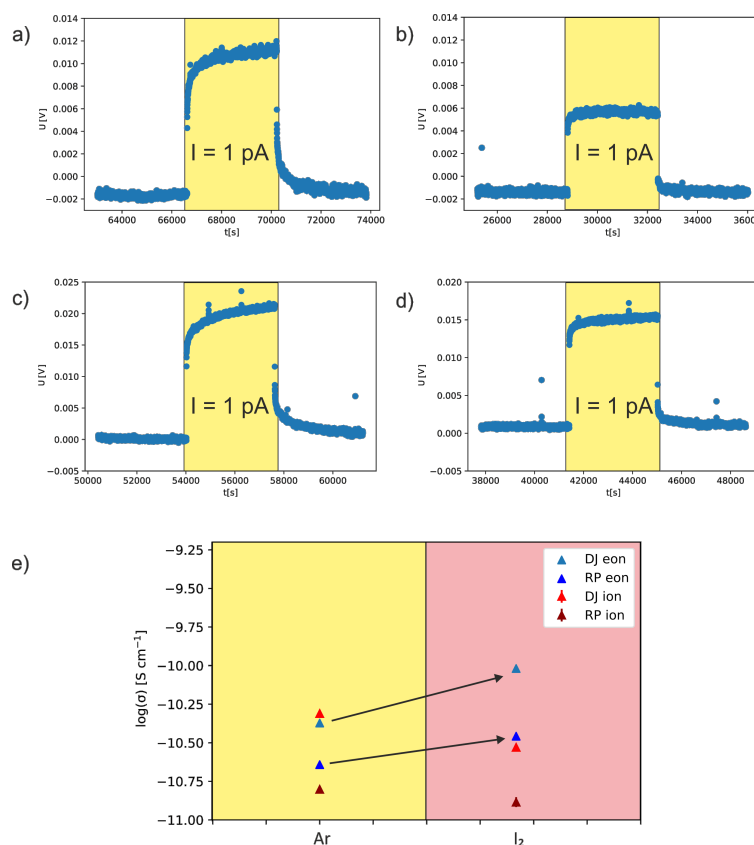


Figure 6:3. Galvanostatic polarization curves of (a) (PDMA)PbI<sub>4</sub> and (c) (BzA)<sub>2</sub>PbI<sub>4</sub> in argon atmosphere at 60 °C; (b) (PDMA)PbI<sub>4</sub> and (d) (BzA)<sub>2</sub>PbI<sub>4</sub> under iodine atmosphere P(I<sub>2</sub>) (0.685 × 10<sup>-6</sup> bar; argon carrier gas) at 60 °C. (e) Extracted electronic (eon) and ionic (ion) conductivity values of (PDMA)PbI<sub>4</sub> (labeled as DJ) and (BzA)<sub>2</sub>PbI<sub>4</sub> (denoted as RP).

The conductivity of mixed conductors can be modulated by changing their stoichiometry. For example, in iodine-deficient conditions, MAPbI<sub>3</sub> is an n-type semiconductor, while in the iodine-rich case it is a p-type semiconductor, as the concentration of holes and iodide vacancies are interrelated by the equation 6:1. This has been experimentally demonstrated by measuring electrical properties under constant iodine partial pressure ( $P(I_2)$ ).<sup>185,244</sup> Assuming that halide defects are the primary defects contributing to the ionic conductivity in layered hybrid perovskites, the iodine partial pressure might also be a gauge to tune electrical properties. To this end, both RP and DJ samples were exposed to iodine partial pressure ( $0.685 \times 10^{-6}$  bar; more information about the experimental setup for iodine pressure control is available in Appendix section 8.5.2). The shapes of equilibrated polarization curves of (PDMA)PbI<sub>4</sub> (Figure 6:3b) and (BzA)<sub>2</sub>PbI<sub>4</sub> (Figure 6:3d) have changed as compared to inert (argon) conditions. Firstly, the samples are less resistive as the voltage rise is smaller under similar current levels. Secondly, the transient voltage step is shorter, implying an increased contribution of electronic conductivity. This has been confirmed by qualitative analysis revealing an augmented electronic conductivity in both (PDMA)PbI<sub>4</sub> and (BZA)<sub>2</sub>PbI<sub>4</sub>, while their ionic conductivity is slightly reduced (Figure 6:3e). These results provide strong evidence for mixed conductivity in layered hybrid perovskites.

### 6.2.3 Iodine incorporation and excorporation kinetics

We have shown that the conductivities of (PDMA)PbI<sub>4</sub> and (BzA)<sub>2</sub>PbI<sub>4</sub> change when they are exposed to a fixed external iodine partial pressure compared rather than to pure argon. This observation implies iodine incorporation into the crystal lattice via gas-solid reaction. The detailed study on oxygen incorporation in SrTiO<sub>3</sub> revealed that this reaction could consist of several steps.<sup>245</sup> This involves surface reactions in which bonds between molecules are broken, redox reactions where atoms are ionized, bulk transport via chemical diffusion, and grain boundary transport processes, which are expected to occur in the incorporation/excorporation process. These reaction steps are not well understood in halide perovskites. The overall reaction rate is limited by the step with the slowest process. Therefore, the equilibration time constant of the conductivity upon a change in iodine partial pressure is an excellent parameter to evaluate the incorporation reaction kinetics. For instance, it has been reported that the iodine exchange rate can be significantly suppressed by doping MAPbI<sub>3</sub> with ethylenammonium (en) as the equilibration time of conductivity increases.<sup>246</sup> In this case, doping did not modify substantially the bulk transport properties since the conductivities of pristine and en-MAPbI<sub>3</sub> samples are comparable. Therefore, slower iodine incorporation is attributed to the reduced surface reaction rate.

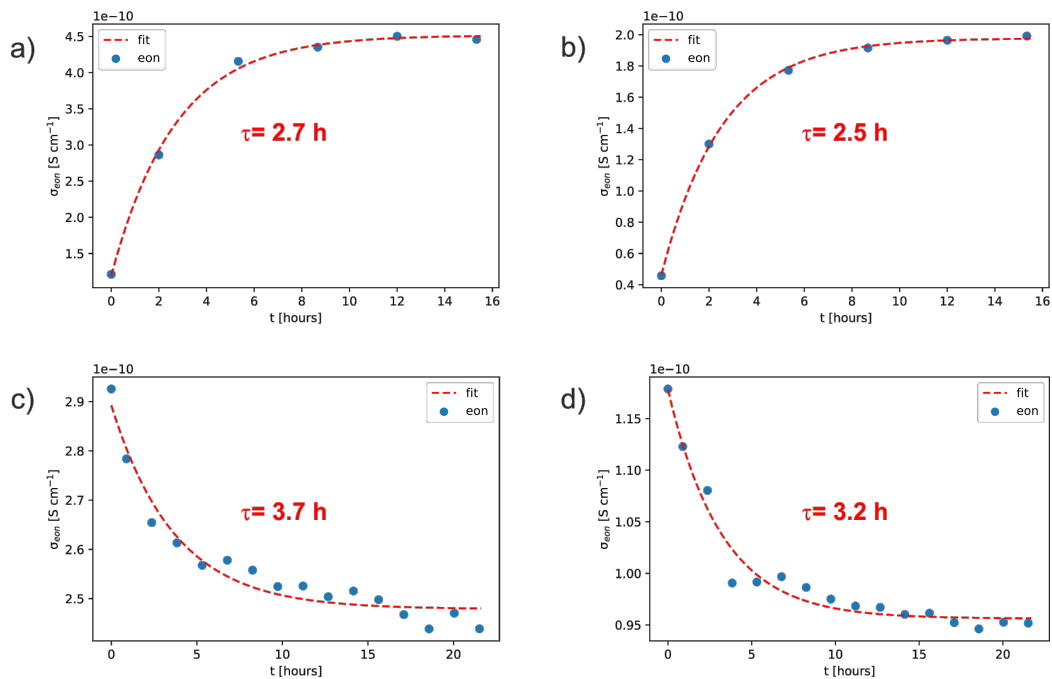


Figure 6:4. Electronic conductivity equilibration curves obtained from data of galvanostatic polarization measurements of (PDMA)PbI<sub>4</sub> when (a) P(I<sub>2</sub>) changed from  $3.45 \times 10^{-7}$  to  $1.45 \times 10^{-5}$  bar, (c) P(I<sub>2</sub>) varied from  $4.55 \times 10^{-6}$  to  $2.5 \times 10^{-6}$  bar, and of (BZA)<sub>2</sub>PbI<sub>4</sub> when (c) P(I<sub>2</sub>) is adjusted from  $3.45 \times 10^{-7}$  to  $1.45 \times 10^{-5}$  bar and (d) from  $4.55 \times 10^{-6}$  to  $2.5 \times 10^{-6}$  bar. The carrier gas is argon and the sample temperature 60 °C.

Despite the fact that layered perovskites are more resistive than MAPbI<sub>3</sub> and that iodine incorporation is expected to occur across the layers, given the sample architecture used (Figure 6:2c), the equilibration kinetics have a characteristic time constant of 2–4 h (Figure 6:4), which are comparable to MAPbI<sub>3</sub>.<sup>247</sup> These results suggest that the bulk diffusion does not limit the overall reaction. Moreover, this could also point to a relatively efficient surface reaction step. The rate of iodine exchange might be faster when iodine diffuses within the perovskite layers. Moreover, fast diffusion might occur through the pinholes present in the thin film. This suggests the importance of sample morphology as well as orientation of the layered perovskite phases. Despite the morphological differences between RP and DJ samples (Figure 6:2d,e), the incorporation and excoorporation kinetics are found to be comparable. The rate of iodine exchange renders these materials good gas permeation substrates but undermines their applications as passivation layers for perovskite solar cells.

#### 6.2.4 Defect chemistry model

Until now, there has been no defect chemistry model which can be applied to the layered hybrid perovskites. Previous extensive studies on MAPbI<sub>3</sub> suggest the dominance of iodide vacancies in ionic conductivity.<sup>185,248</sup> There is no strong consensus on the dominant disorder type in hybrid perovskites. However, the intrinsic-Schottky disorder is more commonly considered, as there is experimental evidence of a high concentration of MA defects, which would compensate for the halide defects in MAPbI<sub>3</sub>.<sup>236,249</sup> Assuming that the

intrinsic-Schottky disorder is dominant, the defect chemical equations for (PDMA)PbI<sub>4</sub> and (BzA)<sub>2</sub>PbI<sub>4</sub> can be expressed as follows (equation 6.3). For simplicity, we used structure-element formulation for the building units, where vacancies are denoted as V.

$$\emptyset \rightleftharpoons V_{PDMA}'' + 2V_I' \quad (1a)$$

$$\emptyset \rightleftharpoons V_{BZA}' + V_I' \quad (1b)$$

$$\emptyset \rightleftharpoons e' + h' \quad (2)$$

$$\frac{1}{2}I_2 + V_I' \rightleftharpoons I_I^x + h' \quad (3)$$

Equation 6:3 – Defect equation for Schottky disorder in (1a) (PDMA)PbI<sub>4</sub> and (1b) (BzA)<sub>2</sub>PbI<sub>4</sub>. Equation (2) for electronic disorder and (3) iodine incorporation reaction.

From the defect equations, one could obtain the defect concentration dependence on the iodine partial pressure, which is commonly represented using Kröger–Vink diagrams (Figure 6:5a,b) that are divided into three distinct regions. Specifically, N regime represents iodine-poor conditions when the majority carriers are electrons ( $e'$ ) and iodine vacancies ( $V_I'$ ), the I region corresponds to the situation when ionic defects are dominant charge carriers, whereas at high iodine partial pressures materials enter the P region, where the holes become predominant charge carriers. Assuming that the charge carrier mobility is independent of defect concentration, the conductivity should be directly proportional to the defect concentration. Thus, conductivity dependence on iodine partial pressure might be investigated with the help of in Kröger-Vink diagrams. For MAPbI<sub>3</sub>, the experimentally obtained slopes of ionic and electronic conductivities as function of iodine partial pressure are in good match with Kröger-Vink diagrams in I and P regions.<sup>227,244</sup> This is further corroborated by the experimental and theoretical studies on defect concentrations that point to I and P-type conductivity properties.<sup>250,251</sup>

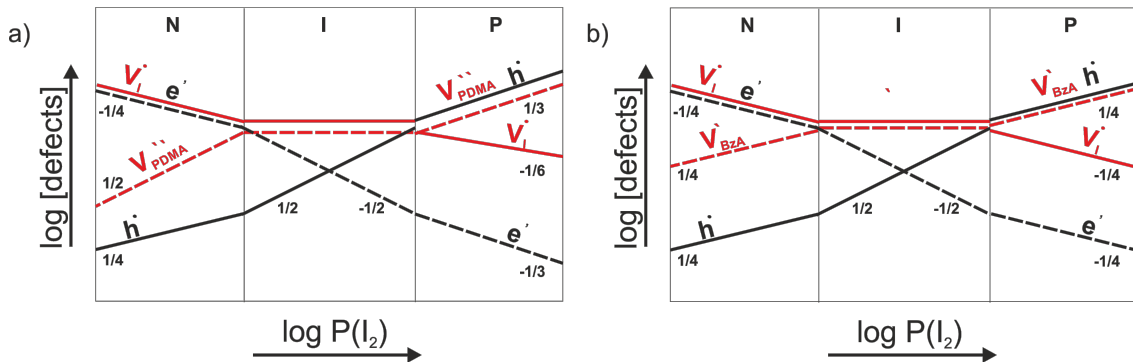


Figure 6:5. Kröger-Vink diagrams of (a) (PDMA)PbI<sub>4</sub> and (b) (BzA)<sub>2</sub>PbI<sub>4</sub>, considering the Schottky disorder and assuming that Pb defects are frozen-in.

---

### 6.2.5 Iodine partial pressure dependent conductivity measurements

(PDMA)PbI<sub>4</sub> and (BzA)<sub>2</sub>PbI<sub>4</sub> conductivities have been analyzed as a function of iodine partial pressure (shown in Figure 6:6). The scanned iodine partial pressure was varied in the range from  $3.45 \times 10^{-7}$  to  $1.41 \times 10^{-5}$  bar, whereas samples were measured in two different rounds for the purpose of reversibility assesment. During the first set of measurements iodine partial pressure was increased, whereas in the second round of measurements the samples were returned to the lower iodine partial pressure. Direct (DC) and alternative (AC) current electrical characterization methods were used to characterize the electrical properties. This involved DC galvanostatic polarization measurements according to the data analysis method described in Appendix section 8.1 to estimate both ionic and electronic conductivity. The results (Figure 6:6b,c) show reversible electronic conductivity in both samples since values from the first and second measurements are closely comparable. In addition, electronic conductivity increases with iodine partial pressure, indicating p-type conduction. The  $0.36 \pm 0.06$  slope of electronic conductivity suggests sample stoichiometries between I and P regimes, according to the Kröger-Vink diagram for (PDMA)PbI<sub>4</sub> (Figure 6:5a). However, the ionic conductivity is not reversible and its dependence on iodine partial pressure is not in line with the model (Figure 6:5a). In the case of (BzA)<sub>2</sub>PbI<sub>4</sub>, electronic conductivity exhibits a  $0.41 \pm 0.06$  slope pointing to the I regime (Figure 6:6b), which is corroborated by insignificantly changed ionic conductivity with the slope  $-0.04 \pm 0.05$  (Figure 6:6c).

While electronic conductivity from galvanostatic polarization measurements could be extracted without reservations, the assessment of the total conductivity might have constraints due to the limited time resolution of the instrument, which is typically around 1 sec. To overcome these shortcomings, electrical properties were characterized in a frequency domain using electrochemical impedance spectroscopy (EIS) allowing to measure conductivity changes in the subsecond time intervals. This technique utilizes frequency-dependent sine wave bias to perturb the sample. The response of these samples can be modeled in terms of equivalent circuits including resistors and capacitors and the impedance data are plotted in the complex plane (Nyquist plot).<sup>252</sup> Typically, the recorded spectrum of hybrid halide perovskite mixed conductors measured using ion-blocking contacts consists of several features. The high-frequency feature can be ascribed to a resistance associated with the total conductivity (ionic and electronic) and to the high frequency dielectric capacitance of the sample. The low frequency feature is ascribed to the polarization of the mixed conductor, whereby ionic carriers are blocked at the interface with the contacts, such that the resulting resistance at very low frequencies is purely electronic.<sup>253,254</sup> To extract information about resistance or capacitance involved in each process, an equivalent circuit model is fitted to the spectrum. Usually, each feature can be fitted with a single resistor-capacitor (RC) element. In a complex plane, the fit has a semicircle shape, where the diameter corresponds to the resistance of the given process.

EIS spectra of the layered perovskites thin films measured in a horizontal device configuration do not contain well resolved features (as shown in the representative spectrum, Figure 6:6d), complicating the analysis. In this case, the total conductivity is obtained by fitting a single RC element at a high and medium frequency range, taking a high degree of uncertainty into account. Under these conditions, the ionic conductivity is found from the equation 8.5 in Appendix section 8.5.1, where electronic conductivity values are taken from galvanostatic measurements. The acquired ionic conductivities for both (PDMA)PbI<sub>4</sub> and (BzA)<sub>2</sub>PbI<sub>4</sub> (Figure 6:6e,f) display systematically higher values than the ones obtained from the galvanostatic polarization method, suggesting that the total conductivity is underestimated using the DC method. The  $-0.18 \pm 0.13$  slope of (PDMA)PbI<sub>4</sub> is in line with the Kröger-Vink diagram in the I, P regime (slopes between 0 and 0.16), whereas the results of (BzA)<sub>2</sub>PbI<sub>4</sub> are puzzling as the extracted ionic conductivity increases slightly with iodine partial pressure.

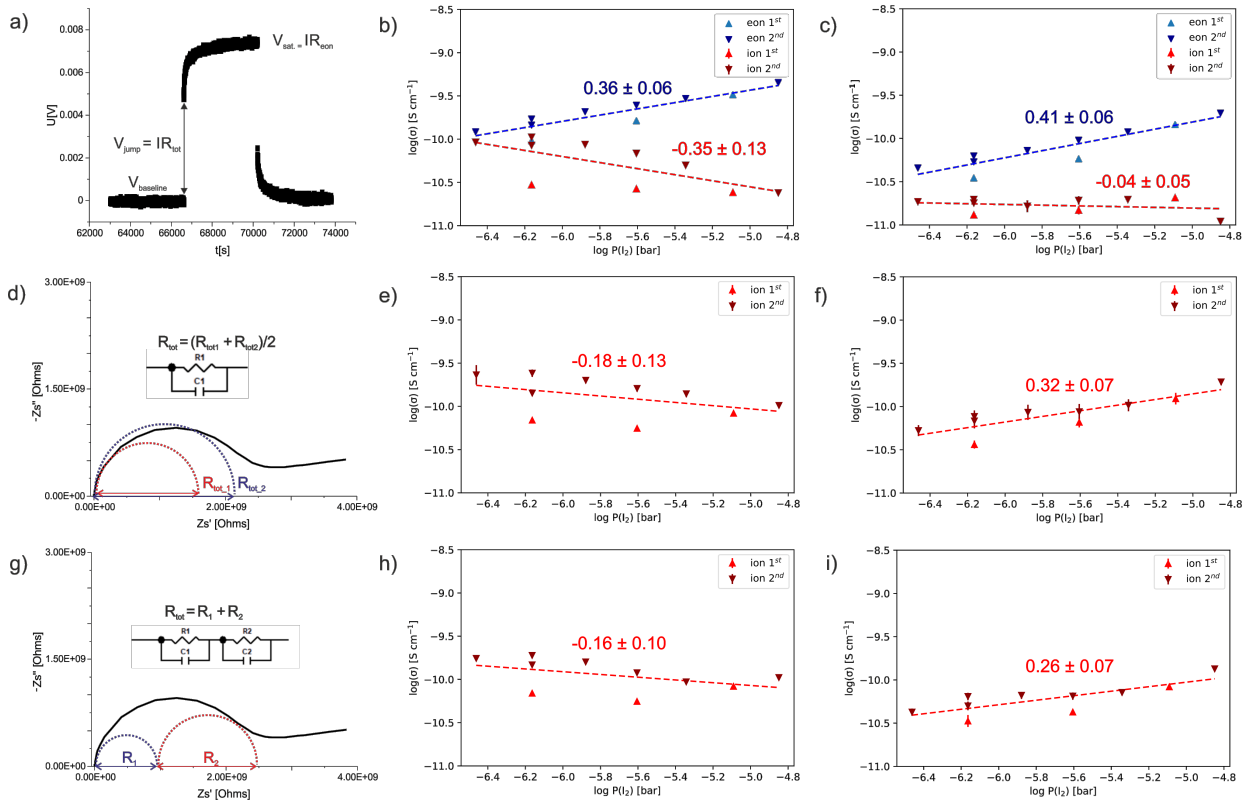


Figure 6:6. Representation of DC polarization curve (a) and electronic and ionic conductivities of (b) (PDMA)PbI<sub>4</sub> and (c) (BzA)<sub>2</sub>PbI<sub>4</sub>. An example of EIS spectra and fits with (d) single RC element and the corresponding ionic conductivities of (e) (PDMA)PbI<sub>4</sub> and (f) (BzA)<sub>2</sub>PbI<sub>4</sub>. (g) Representation of a fit with two RC elements and ionic conductivities for (h) (PDMA)PbI<sub>4</sub> and (i) (BzA)<sub>2</sub>PbI<sub>4</sub>.

Considering all the techniques discussed below, it is challenging to draw an unambiguous picture of the defect chemistry in (PDMA)PbI<sub>4</sub> and (BzA)<sub>2</sub>PbI<sub>4</sub> perovskite thin films. While electronic conductivities show reversibility and slopes suggest I and P region according to the Kröger-Vink diagrams, the ionic conductivities are not following the expected trends. The defect chemistry model might be more complex as the

compositions of the investigated materials involve bulky organic molecules. The picture of defect chemistry of quasi layered hybrid perovskites ( $n > 1$ ) might thus have more resemblance to the one of MAPbI<sub>3</sub>, as their compositions involve typical A cations (MA, FA or Cs), where their respective defects could compensate for halide vacancies. In this regard, further studies on the electrical properties of 2D materials with  $n = 1$  compositions are needed to deepen the understanding and provide a more general model.

## 6.2.6 Thermal stability

The conductivity measurements were performed at the constant temperature of 60 °C. However, additional information about the electrical properties can be extracted by changing the temperature to provide more information about the activation energy. Before performing these measurements, it is essential to evaluate the thermal stability of materials.

In this study, thin films were analyzed using the in-situ temperature-dependent XRD technique. By tracking the intensities of diffraction peaks over time (Figure 6:7a-c) we reveal that (BzA)<sub>2</sub>PbI<sub>4</sub> (002) and (004) peaks diminish at 90 °C, indicating layered structure disruption (Figure 6:7a). Moreover, the peak at 6.9°, which is attributed to the intermediate phase, becomes more intense, implying layered structure conversion to the intermediate phase for Bz-based RP phases. At higher temperatures, this phase is further transformed into PbI<sub>2</sub> (Figure 6:7b). To verify whether (BzA)<sub>2</sub>PbI<sub>4</sub> is meta-stable and kinetically trapped at lower temperatures, samples were kept at 60 °C for 42 days. The film showed no decomposition (Figure 6:7d), indicating comparable thermal stability with MAPbI<sub>3</sub>.<sup>255</sup> On the other hand, (PDMA)PbI<sub>4</sub>, the samples show remarkably improved thermal stability as no degradation was observed in the temperature range up to 150 °C (Figure 6:7c).

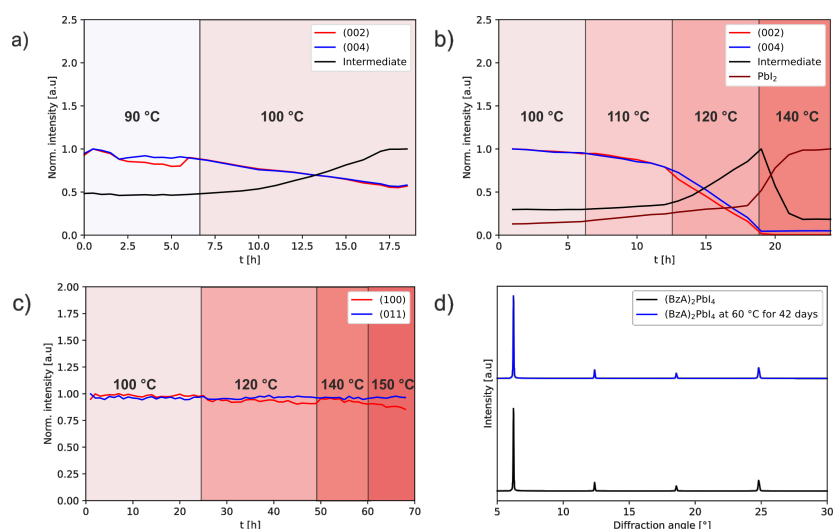


Figure 6:7. XRD peak intensity change over time of (BzA)<sub>2</sub>PbI<sub>4</sub> sample in the temperature range of (a) 90–100 °C, (b) 100–140 °C, and of (PDMA)PbI<sub>4</sub> sample in the temperature range of (c) 100–150 °C. The peak intensities were normalized by taking the initial values at starting temperatures. (d) XRD diffraction of graphs of (BzA)<sub>2</sub>PbI<sub>4</sub> before (black) and after exposure to 60 °C for 42 days (blue).



This can be related to the van der Waals gap between organic layers in RP hybrid halides perovskites. Weakly bound spacer molecules might be more susceptible to thermal stress, which could eventually induce material degradation. On the other hand, bifunctional spacers in DJ analogs do not form a van der Waals gap between adjacent perovskite layers. Therefore, a more rigid structure renders materials more robust against heat,<sup>83,106</sup> which was corroborated by the results of our study. This makes DJ perovskites more promising materials for designing protection and passivation layers in the perovskite solar cells.

### 6.2.7 Activation energy

We have analyzed ionic and electronic conductivity dependence on temperature to further investigate electrical properties. From these measurements, the activation energy of ionic and electronic conductivity can be obtained using the Nernst-Einstein relation:

$$\sigma(T) = \frac{\sigma_0}{T} \exp\left(\frac{-E_A}{kT}\right)$$

Equation 6:4 – Nernst-Einstein equation.

Here,  $\sigma_0$  is constant,  $k$  Boltzmann constant,  $E_A$  activation energy, and  $T$  temperature in Kelvin. Considering the thermal stability, which has been addressed in the previous section, (PDMA)PbI<sub>4</sub> was measured in the range between 333 and 393 K, while (BzA)<sub>2</sub> from 323 K to 353 K. The extracted activation energies of electronic carriers are  $0.5 \pm 0.11$  eV and  $0.66 \pm 0.13$  eV for (PDMA)PbI<sub>4</sub> and (BzA)<sub>2</sub>PbI<sub>4</sub>, respectively (Figure 6:8a,c). Generally, the activation energy involves a migration and a formation term. The latter can be calculated from the mass action law for the respective defect reactions. In the case of electronic carriers with a negligible migration energy, the activation energy of electronic carriers corresponds to the thermal excitation (formation) energy.

The activation energy  $E_A$  of ionic defects for optoelectronic applications should be so high, that ionic defects can be considered frozen-in. However, ionic conductivity in hybrid halide perovskites is significant, and the activation energy is not high enough to prevent ion transport from being activated. The currently available studies report activation energies of iodide defects in MAPbI<sub>3</sub> in the range 0.2 – 0.6 eV.<sup>227,249,256–259</sup> These values are very dispersed because activation energy depends on several parameters. First, variations in the local structure might significantly affect the activation energy barrier. For instance, it has been demonstrated that partial A cation substitution could result in increased,<sup>260,261</sup> or decreased activation energy.<sup>262</sup> Second, sample morphology is also an essential factor affecting activation energy as grain boundaries might facilitate ion transport.<sup>263</sup> Lastly, dimensionality reduction has been proven to be an effective strategy to increase

activation energy. More specifically, suppressed ion migration along the in-plane direction has been reported in  $(\text{BA})_2(\text{MA})_2\text{Pb}_3\text{I}_{10}$ ,<sup>90</sup> while others have shown 0.74 eV activation energy in  $(\text{PEA})_2\text{Pb}(\text{Br},\text{I})_4$  thin films.<sup>91</sup>

Results of this study revealed an activation energy of  $0.87 \pm 0.14$  eV and  $0.55 \pm 0.13$  eV for  $(\text{PDMA})\text{PbI}_4$  and  $(\text{BzA})_2\text{PbI}_4$ , respectively (Figure 6:8b,d). It is worth noting that RP samples underwent clear changes during the measurement, though no noticeable degradation was detected. The slightly larger activation energy for  $(\text{PDMA})\text{PbI}_4$  might be attributed to a higher degree of octahedral distortion<sup>264</sup> or smaller role of grain boundaries<sup>263</sup> due to larger domains (Figure 6:2d). In addition, anisotropy effects due to layered crystal structure have to be taken into account. In this regard, activation energy across perovskite layers is expected to be larger than for the in-plane direction since the jump distance of iodide ions might increase, and transition states might have higher energy. Thus, the activation energy of  $(\text{PDMA})\text{PbI}_4$  might be influenced by crystallites with basal planes perpendicular to the substrate (Figure 6:2b), while  $(\text{BzA})_2\text{PbI}_4$  sample consists of crystallites allowing to measure in-plane activation energy. Attempts to record the out-of-plane activation energy were unsuccessful since there is no strategy to effectively control the crystal orientation at this point. Direct electrode deposition on top of perovskites also did not yield measurable devices. For this purpose, measurements on single crystals might be a good alternative. Nevertheless, in this study, we have demonstrated that layered hybrid perovskites have higher activation energies as compared to ones of their three-dimensional counterparts, confirming that dimensionality reduction is an effective strategy to mitigate ion migration.

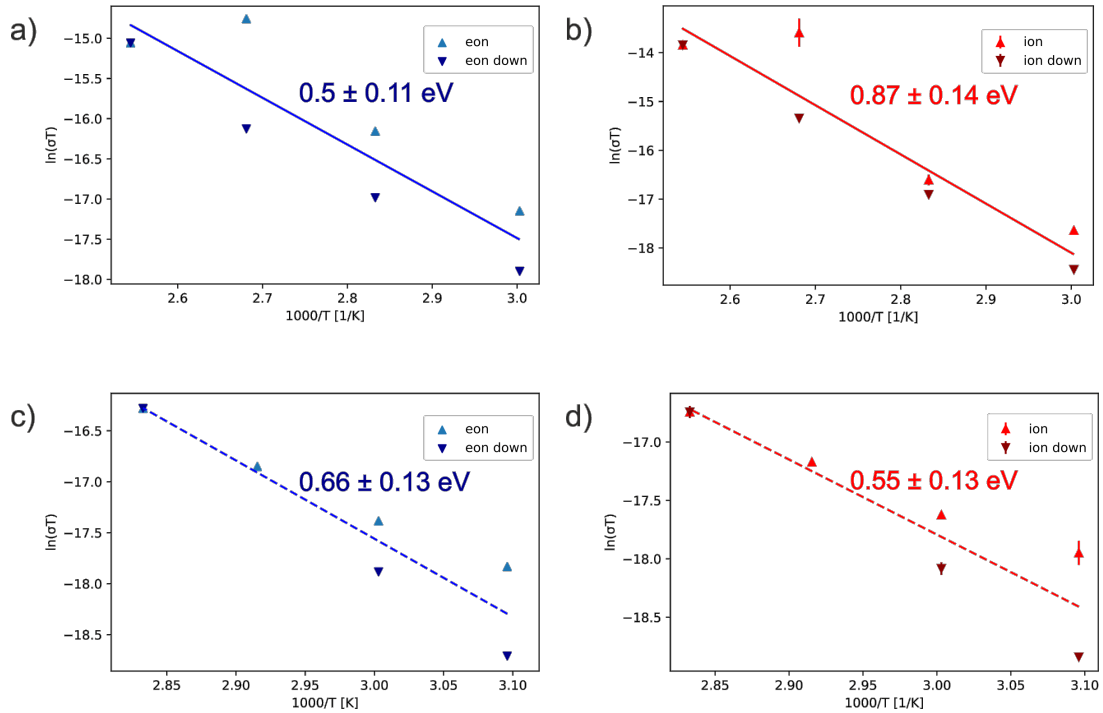


Figure 6:8. Arrhenius plots of  $(\text{PDMA})\text{PbI}_4$  for (a) electronic and (b) ionic carriers, of  $(\text{BzA})_2\text{PbI}_4$  for (c) electronic and (d) ionic carriers. Here, in the legend label, ‘down’ is assigned to the values obtained from high to low temperature.

---

## 6.3 Conclusions

Based on the results presented in this work, we conclude that (PDMA)PbI<sub>4</sub> and (BzA)<sub>2</sub>PbI<sub>4</sub> materials are mixed conductors. In the dark close to equilibrium at 60 °C the samples exhibit ionic conductivities on the order of 10<sup>-10</sup> S/cm, which is comparable to their electronic conductivity values. Results suggest no significant role of van der Waals gap, since measured conductivities of DJ and RP samples are in good correspondence. On the other hand, these materials are 2-4 orders of magnitude more resistive as compared to 3D hybrid perovskites, underscoring the effect of dimensional reduction. Exposure of samples to iodine partial pressure revealed fast incorporation and excorporation processes, whose timescales are comparable to-MAPbI<sub>3</sub>. Upon iodine incorporation materials were p-doped, which was evidenced by the increased electronic conductivity. From the results of temperature dependent conductivity measurements, we obtained higher activation energies of ion migration than for 3D hybrid perovskites, which is inline with the suppressed ionic conductivity. In addition to these results, we found that (BzA)<sub>2</sub>PbI<sub>4</sub> suffers from lower thermal stability, which might be the result of weak van der Waals interactions between spacer molecules.

On a broader perspective, the results of this study reveal that layered perovskites compositions based on phenyl-derived spacers might not be the ideal candidates to solve the ion migration problem, given the fast iodine excorporation/incorporation kinetics. Despite significantly reduced ion migration, effective iodine would still undermine material stability. Furthermore, quasi-hybrid layered perovskites ( $n > 1$ ) might have even more compromised stability due to inherited features from three-dimensional perovskites. This finding challenges the current perspective on the role of these materials in stabilizing hybrid perovskite devices and stimulates further investigations to realize the potential of these materials.

# Chapter 7      Summary

## 7.1      Achieved results

In Chapter 2, I have presented the case study of Dion-Jacobson hybrid perovskite hydration. Specifically, we demonstrated that perovskites employing 1,4-phenylenedimethylammonium (PDMA) spacers hydrate within minutes when exposed to 60 – 70 % relative humidity. Upon hydration layered structure is converted to 1D dimensional dihydrate with the formula  $(\text{PDMA})\text{Pb}_2\text{I}_6 \cdot 2\text{H}_2\text{O}$ . A similar process was observed for both  $n = 1$  and  $n = 2$  compositions (with FA cation). Due to reduced dimensionality, dihydrate exhibits a larger optical bandgap, which on one hand might be beneficial for the protective layers due to reduced absorption. On the other hand, these materials are very resistive making them less attractive for optoelectronic applications. Nonetheless, hydration is reversible and initial material properties can be restored upon sample annealing at 150 °C. We found that the environment for the dehydration process is very important. Samples annealed in air showed dramatically increased robustness to humidity. This has been attributed to  $\text{PbI}_2$ , which is generated during the annealing process. Our study suggests that  $\text{PbI}_2$  resides mainly at the surface, pointing to the importance of surface chemistry and its implications on material stability.

In Chapter 3, I have investigated spacer size effects on the perovskite properties. For this study, the size of phenyl-based spacers was changed by changing the length of the alkyl chain tethering group to obtain 1,4-phenylenediammonium (PDA), PDMA, and 1,4-phenylenediethylammonium (PDEA). Our results revealed, that only PDMA and PDEA spacers template the layered perovskite growth. Systems employing PDA spacer, which is the most rigid, form 1D perovskite. Thus, a certain degree of flexibility in the spacer molecule is necessary to form a layered structure. Furthermore, we found the link between material stability and spacer length. PDEA based perovskites showed no hydration, while both PDMA and PDA based perovskites have a propensity to hydrate. Large spacer molecules could induce stronger confinement effects, which could impede charge transfer across perovskite layers, leading to compromised charge transport properties. Hence, there is a trade-off between stability and conductivity, and the size of the spacer plays a crucial role in this balance.

---

In Chapter 4, I have further extended the investigation on the effects of spacer functionalization. For this purpose, the core of PDMA was fluorinated to obtain perfluorinated PDMA (F-PDMA). This turned out to be an effective strategy to improve the material stability as no hydration was observed in F-PDMA samples, which could be attributed to increased hydrophobicity. Furthermore, given the opposite quadrupole moments in PDMA and F-PDMA we investigated the opportunity of enhanced  $\pi$ - $\pi$  interactions which would facilitate the compact spacer packing. Our results revealed that systems based on PDMA/F-PDMA consist of segregates without long range ordered packing of alternating spacers. This was further evidenced by the stability test in a humid atmosphere. Post-treatment analysis revealed the co-existence of hydrated PDMA and pristine F-PDMA, corroborating the segregation of the spacers.

In Chapter 5, I have looked into the difference in mechanical properties of RP and DJ perovskites. To this end, four compositions (eg.  $(\text{BzA})_2\text{PbI}_4$ ,  $(\text{BzA})_2\text{PbBr}_4$ ,  $(\text{PDMA})\text{PbI}_4$ ,  $(\text{PDMA})\text{PbBr}_4$ ) were chosen for this study. Mechanical properties were tested by applying 0 – 0.35 GPa external pressure on the samples. Structural analysis revealed anisotropic lattice compression, with the largest degree of contraction along the out-of-plane direction, which is dictated by the organic spacers. The analysis of bulk modulus revealed that DJ layered hybrid perovskites are more rigid than their RP counterparts, pointing to the role of the van der Waals gap. In fact, the packing density of the organic spacers has a substantial effect on the compressibility of the material. More specifically, our study revealed that  $(\text{BzA})_2\text{PbBr}_4$  is the softest material, exhibiting almost 5 times larger compression along the out-plane direction. This has been attributed to loosely packed spacer layers, rendering them more susceptible to compression. We found a link between the compression of interlayer distance and the optical bandgap reduction. We suggest that a shorter interlayer distance weakens the confinement effects, which cause a red shift in optical absorption. Alternatively, local structural rearrangements such as octahedral tilting (Pb-X-Pb angle) might also influence the optical absorption, which is reversible together with structural properties in the pressure range of 0 – 0.35 GPa.

In Chapter 6, I have presented a study on the electrical properties of layered hybrid perovskites. Namely,  $(\text{BzA})_2\text{PbI}_4$  and  $(\text{PDMA})\text{PbI}_4$  were investigated. These materials are semiconductors since we could measure ionic conductivity, which is comparable to electronic conductivity. In dark conditions close to equilibrium at 60 °C, the measured conductivity values are in the order of  $10^{-10}$  S/cm, which could be attributed to the higher activation energy for ion migration. We did not find a link between structural properties (van der Waals gap) and conductivity, as the conductivity of both samples is very comparable. Nonetheless, dimensionality reduction from 3D to 2D has a substantial effect, since  $\text{MAPbI}_3$  is 2 – 4 orders of magnitude more

---

conductive. Moreover, data of iodine partial pressure conductivity measurements suggest that iodine defects are the primary ionic carriers, however clear defect model could be drawn. Interestingly, the iodine exorption and incorporation kinetics in investigated materials is comparable to MAPbI<sub>3</sub>. Thus, these materials, especially (BzA)<sub>2</sub>PbI<sub>4</sub>, which in addition to that suffers from poor thermal stability, might not be good candidates for passivation layers in perovskite solar cells.

## 7.2 Future development

Over the course of my doctoral studies, I have investigated mainly  $n = 1$  layered hybrid perovskites based on phenyl-derived spacers in DJ structure. Given their propensity to hydrate, the design rules for organic spacers have to be revised. From this work, I suggest two potential strategies: functionalize the spacer or increase its size. While the former might only increase hydrophobicity, the latter might lead to the more suppressed ion migration due to insulating spacers. However, this might dramatically reduce the electronic conductivity, which cannot be compromised in optoelectronic applications. In this regard, electroactive spacers might come into play. Good alignment of their HOMO, LUMO with perovskite VB and CB might facilitate the electronic carrier transport, while their usually bulky and large core might be beneficial for stability and ion migration issues. Furthermore, investigations on quasi-layered hybrid perovskites ( $n > 1$ ) might provide more insights.

In addition, layered perovskites might be designed not only for the PV or LED applications but also for other applications such as sensing, second harmonic generation, and piezoelectricity. This can be available thanks to the vast chemical space for spacers molecules. The field of layered perovskites is in its infancy, and more systematic studies on spacer's role in structure-property relationships are needed to realize some of the prospects of layered hybrid perovskites.

---

## References

1. Wikipedia. Climate change scenario. [https://en.wikipedia.org/wiki/Climate\\_change\\_scenario](https://en.wikipedia.org/wiki/Climate_change_scenario).
2. Intergovernmental Panel On Climate Change (IPCC). *Climate Change 2022: Mitigation of Climate Change*. (2022).
3. Rebecca Lindsey. Climate Change: Atmospheric Carbon Dioxide. <https://www.climate.gov/news-features/understanding-climate/climate-change-atmospheric-carbon-dioxide>.
4. Nick Lioudis. OPEC's Influence on Global Oil Prices. <https://www.investopedia.com/ask/answers/060415/how-much-influence-does-opek-have-global-price-oil.asp>.
5. Wikipedia. 1979 oil crisis.
6. Wikipedia. 2020 Russia–Saudi Arabia oil price war.
7. Richard Perez and Marc Perez. A Fundamental Look At Energy Reserves For The Planet. *The International Energy Agency SHC Programme Solar Update* 2–3 (2009).
8. NREL. Best Research-Cell Efficiency Chart. <https://www.nrel.gov/pv/cell-efficiency.html>.
9. Jena, A. K., Kulkarni, A. & Miyasaka, T. Halide Perovskite Photovoltaics: Background, Status, and Future Prospects. *Chemical Reviews* **119**, 3036–3103 (2019).
10. van Le, Q., Jang, H. W. & Kim, S. Y. Recent Advances toward High-Efficiency Halide Perovskite Light-Emitting Diodes: Review and Perspective. *Small Methods* **2**, 1700419 (2018).
11. Travis, W., Glover, E. N. K., Bronstein, H., Scanlon, D. O. & Palgrave, R. G. On the application of the tolerance factor to inorganic and hybrid halide perovskites: A revised system. *Chemical Science* **7**, 4548–4556 (2016).
12. Correa-Baena, J.-P. *et al.* Promises and challenges of perovskite solar cells. *Science (1979)* **358**, 739–744 (2017).
13. Lee, J. W., Tan, S., Seok, S. il, Yang, Y. & Park, N. G. Rethinking the A cation in halide perovskites. *Science (1979)* **375**, eabj1186 (2022).
14. Saliba, M. Polyelemental, Multicomponent Perovskite Semiconductor Libraries through Combinatorial Screening. *Advanced Energy Materials* **9**, 1803754 (2019).
15. Jesper Jacobsson, T. *et al.* Exploration of the compositional space for mixed lead halogen perovskites for high efficiency solar cells. *Energy and Environmental Science* **9**, 1706–1724 (2016).
16. Noh, J. H., Im, S. H., Heo, J. H., Mandal, T. N. & Seok, S. il. Chemical management for colorful, efficient, and stable inorganic-organic hybrid nanostructured solar cells. *Nano Letters* **13**, 1764–1769 (2013).

- 
17. Protesescu, L. *et al.* Nanocrystals of Cesium Lead Halide Perovskites (CsPbX<sub>3</sub>, X = Cl, Br, and I): Novel Optoelectronic Materials Showing Bright Emission with Wide Color Gamut. *Nano Letters* **15**, 3692–3696 (2015).
  18. Hao, F., Stoumpos, C. C., Chang, R. P. H. & Kanatzidis, M. G. Anomalous band gap behavior in mixed Sn and Pb perovskites enables broadening of absorption spectrum in solar cells. *J Am Chem Soc* **136**, 8094–8099 (2014).
  19. Tao, S. *et al.* Absolute energy level positions in tin- and lead-based halide perovskites. *Nature Communications* **10**, 2560 (2019).
  20. Pitaro, M., Tekelenburg, E. K., Shao, S. & Loi, M. A. Tin Halide Perovskites: From Fundamental Properties to Solar Cells. *Advanced Materials* **34**, 2105844 (2022).
  21. Eperon, G. E. *et al.* Formamidinium lead trihalide: A broadly tunable perovskite for efficient planar heterojunction solar cells. *Energy and Environmental Science* **7**, 982–988 (2014).
  22. Pellet, N. *et al.* Mixed-organic-cation perovskite photovoltaics for enhanced solar-light harvesting. *Angewandte Chemie - International Edition* **53**, 3151–3157 (2014).
  23. Prasanna, R. *et al.* Band Gap Tuning via Lattice Contraction and Octahedral Tilting in Perovskite Materials for Photovoltaics. *J. Am. Chem. Soc.* **139**, 11117–11124 (2017).
  24. Kim, H. S. *et al.* Lead iodide perovskite sensitized all-solid-state submicron thin film mesoscopic solar cell with efficiency exceeding 9%. *Scientific Reports* **2**, 591 (2012).
  25. Min, H. *et al.* Perovskite solar cells with atomically coherent interlayers on SnO<sub>2</sub> electrodes. *Nature* **598**, 444–450 (2021).
  26. Kim, J. Y., Lee, J. W., Jung, H. S., Shin, H. & Park, N. G. High-Efficiency Perovskite Solar Cells. *Chemical Reviews* **120**, 7867–7918 (2020).
  27. Ehrler, B. *et al.* Photovoltaics reaching for the shockley-queisser limit. *ACS Energy Letters* **5**, 3029–3033 (2020).
  28. Stoumpos, C. C., Malliakas, C. D. & Kanatzidis, M. G. Semiconducting tin and lead iodide perovskites with organic cations: Phase transitions, high mobilities, and near-infrared photoluminescent properties. *Inorganic Chemistry* **52**, 9019–9038 (2013).
  29. Senocrate, A., Kim, G. Y., Grätzel, M. & Maier, J. Thermochemical Stability of Hybrid Halide Perovskites. *ACS Energy Letters* **4**, 2859–2870 (2019).
  30. Tress, W. *et al.* Understanding the rate-dependent J-V hysteresis, slow time component, and aging in CH<sub>3</sub>NH<sub>3</sub>PbI<sub>3</sub> perovskite solar cells: The role of a compensated electric field. *Energy and Environmental Science* **8**, 995–1004 (2015).
  31. Moia, D. & Maier, J. Ion Transport, Defect Chemistry, and the Device Physics of Hybrid Perovskite Solar Cells. *ACS Energy Letters* **6**, 1566–1576 (2021).



- 
32. Kim, G. Y. *et al.* Large tunable photoeffect on ion conduction in halide perovskites and implications for photodecomposition. *Nature Materials* **17**, 445–449 (2018).
  33. Motti, S. G. *et al.* Controlling competing photochemical reactions stabilizes perovskite solar cells. *Nature Photonics* **13**, 532–539 (2019).
  34. Cheng, Y. & Ding, L. Pushing commercialization of perovskite solar cells by improving their intrinsic stability. *Energy and Environmental Science* **14**, 3233–3255 (2021).
  35. Siegler, T. D. *et al.* The Path to Perovskite Commercialization: A Perspective from the United States Solar Energy Technologies Office. *ACS Energy Letters* **7**, 1728–1734 (2022).
  36. Grancini, G. *et al.* One-Year stable perovskite solar cells by 2D/3D interface engineering. *Nature Communications* **8**, 15684 (2017).
  37. Alharbi, E. A. *et al.* Atomic-level passivation mechanism of ammonium salts enabling highly efficient perovskite solar cells. *Nature Communications* **10**, 3008 (2019).
  38. Jiang, Q. *et al.* Surface passivation of perovskite film for efficient solar cells. *Nature Photonics* **13**, 460–466 (2019).
  39. Chen, J. & Park, N. G. Materials and Methods for Interface Engineering toward Stable and Efficient Perovskite Solar Cells. *ACS Energy Letters* **5**, 2742–2786 (2020).
  40. Smith, I. C., Hoke, E. T., Solis-Ibarra, D., McGehee, M. D. & Karunadasa, H. I. A Layered Hybrid Perovskite Solar-Cell Absorber with Enhanced Moisture Stability. *Angewandte Chemie - International Edition* **53**, 11232–11235 (2014).
  41. Quan, L. N. *et al.* Ligand-Stabilized Reduced-Dimensionality Perovskites. *J Am Chem Soc* **138**, 2649–2655 (2016).
  42. Gao, P., bin Mohd Yusoff, A. R. & Nazeeruddin, M. K. Dimensionality engineering of hybrid halide perovskite light absorbers. *Nature Communications* **9**, 5028 (2018).
  43. Myae Soe, C. M. *et al.* Structural and thermodynamic limits of layer thickness in 2D halide perovskites. *Proc Natl Acad Sci U S A* **116**, 58–66 (2019).
  44. González-Carrero, S., Galian, R. E. & Pérez-Prieto, J. Organometal Halide Perovskites: Bulk Low-Dimension Materials and Nanoparticles. *Particle and Particle Systems Characterization* **32**, 709–720 (2015).
  45. Saparov, B. & Mitzi, D. B. Organic-Inorganic Perovskites: Structural Versatility for Functional Materials Design. *Chemical Reviews* **116**, 4558–4596 (2016).
  46. Vargas, B., Rodríguez-López, G. & Solis-Ibarra, D. The Emergence of Halide Layered Double Perovskites. *ACS Energy Letters* **5**, 3591–3608 (2020).
  47. Stoumpos, C. C. *et al.* Ruddlesden-Popper Hybrid Lead Iodide Perovskite 2D Homologous Semiconductors. *Chemistry of Materials* **28**, 2852–2867 (2016).

- 
48. Mao, L. *et al.* Hybrid Dion-Jacobson 2D Lead Iodide Perovskites. *J Am Chem Soc* **140**, 3775–3783 (2018).
  49. Soe, C. M. M. *et al.* New Type of 2D Perovskites with Alternating Cations in the Interlayer Space,  $(\text{C}(\text{NH}_2)_3)(\text{CH}_3\text{NH}_3)_n\text{PbI}_{3n+1}$ : Structure, Properties, and Photovoltaic Performance. *J Am Chem Soc* **139**, 16297–16309 (2017).
  50. Blancon, J. C., Even, J., Stoumpos, C. C., Kanatzidis, M. G. & Mohite, A. D. Semiconductor physics of organic–inorganic 2D halide perovskites. *Nature Nanotechnology* **15**, 969–985 (2020).
  51. Blancon, J. *et al.* Scaling law for excitons in 2D perovskite quantum wells. *Nature Communications* **9**, 2254 (2018).
  52. Milić, J. v. Multifunctional layered hybrid perovskites. *Journal of Materials Chemistry C* **9**, 11428–11443 (2021).
  53. Xue, J. *et al.* Reconfiguring the band-edge states of photovoltaic perovskites by conjugated organic cations. *Science (1979)* **371**, 636–640 (2021).
  54. Passarelli, J. v *et al.* Enhanced Out-of-Plane Conductivity and Photovoltaic Performance in  $n = 1$  Layered Perovskites through Organic Cation Design. *J Am Chem Soc* **140**, 7313–7323 (2018).
  55. Proppe, A. H. *et al.* Photochemically Cross-Linked Quantum Well Ligands for 2D/3D Perovskite Photovoltaics with Improved Photovoltage and Stability. *J Am Chem Soc* **141**, 14180–14189 (2019).
  56. Li, X., Hoffman, J. M. & Kanatzidis, M. G. The 2D halide perovskite rulebook: How the spacer influences everything from the structure to optoelectronic device efficiency. *Chemical Reviews* **121**, 2230–2291 (2021).
  57. Seitz, M. *et al.* Exciton diffusion in two-dimensional metal-halide perovskites. *Nature Communications* **11**, 2035 (2020).
  58. Sichert, J. A., Hemmerling, A., Cardenas-Daw, C., Urban, A. S. & Feldmann, J. Tuning the optical bandgap in layered hybrid perovskites through variation of alkyl chain length. *APL Materials* **7**, (2019).
  59. Wu, G. *et al.* Molecular Engineering for Two-Dimensional Perovskites with Photovoltaic Efficiency Exceeding 18%. *Matter* **4**, 582–599 (2021).
  60. Spanopoulos, I. *et al.* Uniaxial Expansion of the 2D Ruddlesden-Popper Perovskite Family for Improved Environmental Stability. *J Am Chem Soc* **141**, 5518–5534 (2019).
  61. Li, F. *et al.* Effects of Alkyl Chain Length on Crystal Growth and Oxidation Process of Two-Dimensional Tin Halide Perovskites. *ACS Energy Letters* **5**, 1422–1429 (2020).
  62. Yao, Z. *et al.* Role of alkyl chain length in diaminoalkane linked 2D Ruddlesden-Popper halide perovskites. *CrystEngComm* **20**, 6704–6712 (2018).

- 
63. Xu, Z. *et al.* Phase Distribution and Carrier Dynamics in Multiple-Ring Aromatic Spacer-Based Two-Dimensional Ruddlesden-Popper Perovskite Solar Cells. *ACS Nano* **14**, 4871–4881 (2020).
64. Liu, C. *et al.* Tuning structural isomers of phenylenediammonium to afford efficient and stable perovskite solar cells and modules. *Nature Communications* **12**, 6394 (2021).
65. Rodríguez-Romero, J. *et al.* Widening the 2D/3D Perovskite Family for Efficient and Thermal-Resistant Solar Cells by the Use of Secondary Ammonium Cations. *ACS Energy Letters* **5**, 1013–1021 (2020).
66. Li, Z. *et al.* A New Organic Interlayer Spacer for Stable and Efficient 2D Ruddlesden-Popper Perovskite Solar Cells. *Nano Letters* **19**, 5237–5245 (2019).
67. Nagasaka, H., Yoshizawa-Fujita, M., Takeoka, Y. & Rikukawa, M. Tuning the Structures and Optical Properties of Perovskites by Varying the Alkylamine Type and Chain Length. *ACS Omega* **3**, 18925–18929 (2018).
68. Hope, M. A. *et al.* Nanoscale Phase Segregation in Supramolecular  $\pi$ -Templating for Hybrid Perovskite Photovoltaics from NMR Crystallography. *J Am Chem Soc* **143**, 1529–1538 (2021).
69. García-Benito, I. *et al.* Fluorination of Organic Spacer Impacts on the Structural and Optical Response of 2D Perovskites. *Frontiers in Chemistry* **7**, 946 (2020).
70. Hu, J. *et al.* Synthetic control over orientational degeneracy of spacer cations enhances solar cell efficiency in two-dimensional perovskites. *Nature Communications* **10**, 1276 (2019).
71. Schmitt, T. *et al.* Control of Crystal Symmetry Breaking with Halogen-Substituted Benzylammonium in Layered Hybrid Metal-Halide Perovskites. *J Am Chem Soc* **142**, 5060–5067 (2020).
72. Wang, D., Chen, S. C. & Zheng, Q. Enhancing the efficiency and stability of two-dimensional Dion-Jacobson perovskite solar cells using a fluorinated diammonium spacer. *Journal of Materials Chemistry A* **9**, 11778–11786 (2021).
73. Liu, Y. *et al.* Ultrahydrophobic 3D/2D fluoroarene bilayer-based water-resistant perovskite solar cells with efficiencies exceeding 22%. *Science Advances* **5**, eaaw2543 (2019).
74. Du, K. Z. *et al.* Two-Dimensional Lead(II) Halide-Based Hybrid Perovskites Templated by Acene Alkylamines: Crystal Structures, Optical Properties, and Piezoelectricity. *Inorganic Chemistry* **56**, 9291–9302 (2017).
75. Liu, G. *et al.* Isothermal pressure-derived metastable states in 2D hybrid perovskites showing enduring bandgap narrowing. *Proc Natl Acad Sci U S A* **115**, 8076–8081 (2018).
76. Mahal, E., Mandal, S. C. & Pathak, B. Understanding the role of spacer cation in 2D layered halide perovskites to achieve stable perovskite solar cells. *Materials Advances* **3**, 2464–2474 (2022).
77. Liu, S. *et al.* Manipulating efficient light emission in two-dimensional perovskite crystals by pressure-induced anisotropic deformation. *Science Advances* **5**, eaav9445 (2019).

- 
78. Yu, S. *et al.* Nonconfinement Structure Revealed in Dion–Jacobson Type Quasi-2D Perovskite Expedites Interlayer Charge Transport. *Small* **15**, 1905081 (2019).
  79. Yu, S., Abdellah, M., Pullerits, T., Zheng, K. & Liang, Z. Asymmetric Spacer in Dion–Jacobson Halide Perovskites Induces Staggered Alignment to Direct Out-of-Plane Carrier Transport and Enhances Ambient Stability Simultaneously. *Advanced Functional Materials* **31**, 2104342 (2021).
  80. Li, W. *et al.* Light-activated interlayer contraction in two-dimensional perovskites for high-efficiency solar cells. *Nature Nanotechnology* **17**, 45–52 (2022).
  81. Tsai, H. *et al.* High-efficiency two-dimensional Ruddlesden–Popper perovskite solar cells. *Nature* **536**, 312–316 (2016).
  82. Ahmad, S. *et al.* Dion–Jacobson Phase 2D Layered Perovskites for Solar Cells with Ultrahigh Stability. *Joule* **3**, 794–806 (2019).
  83. Zhao, R. *et al.* Rigid Conjugated Diamine Templates for Stable Dion–Jacobson-Type Two-Dimensional Perovskites. *J Am Chem Soc* **143**, 19901–19908 (2021).
  84. Gong, J., Hao, M., Zhang, Y., Liu, M. & Zhou, Y. Layered 2D Halide Perovskites beyond the Ruddlesden–Popper Phase: Tailored Interlayer Chemistries for High-Performance Solar Cells. *Angewandte Chemie - International Edition* **61**, e202112022 (2022).
  85. Zhu, C. *et al.* Strain engineering in perovskite solar cells and its impacts on carrier dynamics. *Nature Communications* **10**, 815 (2019).
  86. Liu, D. *et al.* Strain analysis and engineering in halide perovskite photovoltaics. *Nature Materials* **20**, 1337–1346 (2021).
  87. Tu, Q. *et al.* Out-of-Plane Mechanical Properties of 2D Hybrid Organic–Inorganic Perovskites by Nanoindentation. *ACS Applied Materials and Interfaces* **10**, 22167–22173 (2018).
  88. Tu, Q. *et al.* Exploring the Factors Affecting the Mechanical Properties of 2D Hybrid Organic–Inorganic Perovskites. *ACS Appl Mater Interfaces* **12**, 20440–20447 (2020).
  89. Yin, T. *et al.* Pressure-Engineered Structural and Optical Properties of Two-Dimensional (C<sub>4</sub>H<sub>9</sub>NH)<sub>3</sub> <sub>2</sub> PbI<sub>4</sub> Perovskite Exfoliated nm-Thin Flakes. *J Am Chem Soc* **141**, 1235–1241 (2019).
  90. Xiao, X. *et al.* Suppressed Ion Migration along the In-Plane Direction in Layered Perovskites. *ACS Energy Letters* **3**, 684–688 (2018).
  91. Cho, J., DuBose, J. T., Le, A. N. T. & Kamat, P. v. Suppressed Halide Ion Migration in 2D Lead Halide Perovskites. *ACS Materials Letters* **2**, 565–570 (2020).
  92. Senocrate, A., Kotomin, E. & Maier, J. On the Way to Optoionics. *Helvetica Chimica Acta* **103**, e2000073 (2020).
  93. Kieslich, G., Sun, S. & Cheetham, A. K. Solid-state principles applied to organic–inorganic perovskites: New tricks for an old dog. *Chemical Science* **5**, 4712–4715 (2014).

- 
94. Saparov, B. & Mitzi, D. B. Organic – Inorganic Perovskites : Structural Versatility for Functional Materials Design. *Chemical Reviews* **116**, 4558–4596 (2016).
  95. Grancini, G. & Nazeeruddin, M. K. Dimensional tailoring of hybrid perovskites for photovoltaics. *Nature Reviews Materials* **4**, 4–22 (2019).
  96. Mao, L., Stoumpos, C. C. & Kanatzidis, M. G. Two-Dimensional Hybrid Halide Perovskites: Principles and Promises. *J Am Chem Soc* **141**, 1171–1190 (2018).
  97. Chen, Y. *et al.* 2D Ruddlesden – Popper Perovskites for Optoelectronics. *Advanced Materials* **1703487** (2017).
  98. Stoumpos, C. C. *et al.* Ruddlesden – Popper Hybrid Lead Iodide Perovskite 2D Homologous Semiconductors. *Chemistry of Materials* **28**, 2852–2867 (2016).
  99. Mao, L. *et al.* Hybrid Dion–Jacobson 2D Lead Iodide Perovskites. *J Am Chem Soc* **140**, 3775–3783 (2018).
  100. Li, Y. *et al.* Bifunctional Organic Spacers for Formamidinium-Based Hybrid Dion – Jacobson Two-Dimensional Perovskite Solar Cells. *Nano Letters* **19**, 150–157 (2019).
  101. Yan, J. *et al.* Highly Oriented Two-Dimensional Formamidinium Lead Iodide Perovskite with a Small Bandgap of 1.51 eV. *Materials Chemistry Frontiers* **2**, 121–128 (2018).
  102. Schlipf, J. *et al.* Shedding Light on the Moisture Stability of 3D/2D Hybrid Perovskite Heterojunction Thin Films. *Applied Energy Materials* **2**, 1011–1018 (2019).
  103. Wygant, B. R. *et al.* Probing the Degradation Chemistry and Enhanced Stability of 2D Organolead Halide Perovskites. *J Am Chem Soc* **141**, 18170–18181 (2019).
  104. Wygant, B. R. *et al.* Moisture-Driven Formation and Growth of Quasi-2-D Organolead Halide Perovskite Crystallites. *ACS Applied Energy Materials* **3**, 6280–6290 (2020).
  105. Soe Myae, C. M. *et al.* Structural and thermodynamic limits of layer thickness in 2D halide perovskites. *PNAS* **116**, 58–66 (2019).
  106. Ahmad, S. *et al.* Dion-Jacobson Phase 2D Layered Perovskites for Solar Cells with Ultrahigh Stability. *Joule* **3**, 1–13 (2019).
  107. Li, X. *et al.* Two-Dimensional Dion-Jacobson Hybrid Lead Iodide Perovskites with Aromatic Diammonium Cations. *J Am Chem Soc* **141**, 12880–12890 (2019).
  108. Xu, Z., Chen, M. & Liu, S. F. First-Principles Study of Enhanced Out-of-Plane Transport Properties and Stability in Dion-Jacobson Two-Dimensional Perovskite Semiconductors for High-Performance Solar Cell Applications. *Journal of Physical Chemistry Letters* **10**, 3670–3675 (2019).
  109. Huang, P., Kazim, S., Wang, M. & Ahmad, S. Toward Phase Stability: Dion-Jacobson Layered Perovskite for Solar Cells. *ACS Energy Letters* **4**, 2960–2974 (2019).

- 
110. Lerner, C. *et al.* Completing the Picture of 2-(Aminomethylpyridinium) Lead Hybrid Perovskites: Insights into Structure, Conductivity Behavior, and Optical Properties. *Chemistry of Materials* **30**, 6289–6297 (2018).
  111. Lemmerer, A. & Billing, D. G. Two packing motifs based upon chains of edge-sharing PbI<sub>6</sub> octahedra. *Acta Crystallographica Section C: Crystal Structure Communications* **62**, 597–601 (2006).
  112. Cohen, B., Li, Y., Meng, Q. & Etgar, L. Dion–Jacobson Two-Dimensional Perovskite Solar Cells Based on Benzene Dimethan ammonium Cation. *Nano Letters* **19**, 2588–2597 (2019).
  113. Hou, M. *et al.* Aryl Diammonium Iodide Passivation for Efficient and Stable Hybrid Organ-Inorganic Perovskite Solar Cells. *Advanced Functional Materials* **30**, 2002366 (2020).
  114. Frisch, M. J.; Trucks, G. W.; Schlegel, H. B.; Scuseria, G. E.; Robb, M. A.; Cheeseman, J. R.; Scalmani, G.; Barone, V.; Mennucci, B.; Petersson, G. A.; Nakatsuji, H.; Caricato, M.; Li, X.; Hratchian, H. P.; Izmaylov, A. F.; Bloino, J.; Zheng, G.; Sonnenb, D. J. Gaussian 09, Revision A.1. (2009).
  115. Gélvez-Rueda, M. C. *et al.* Formamidinium-Based Dion-Jacobson Layered Hybrid Perovskites: Structural Complexity and Optoelectronic Properties. *Advanced Functional Materials* **30**, 2003428 (2020).
  116. Mao, L. *et al.* Role of Organic Counterion in Lead- and Tin-Based Two-Dimensional Semiconducting Iodide Perovskites and Application in Planar Solar Cells. *Chemistry of Materials* **28**, 7781–7792 (2016).
  117. Kagan, C. R., Mitzi, D. B. & Dimitrakopoulos, C. D. Organic-Inorganic Hybrid Materials as Semiconducting Channels in Thin-Film Field-Effect Transistors. *Science (1979)* **286**, 945–948 (1999).
  118. Chen, A. Z. *et al.* Origin of vertical orientation in two-dimensional metal halide perovskites and its effect on photovoltaic performance. *Nature Communications* **9**, 1336 (2018).
  119. Yu, S. *et al.* Nonconfinement Structure Revealed in Dion – Jacobson Type Quasi-2D Perovskite Expedites Interlayer Charge Transport. *Small* **15**, 1905081 (2019).
  120. Bondi, A. Van der waals volumes and radii. *Journal of Physical Chemistry* **68**, 441–451 (1964).
  121. Ishihara, T. Optical properties of PbI<sub>2</sub>-based perovskite structures. *Journal of Luminescence* **60–61**, 269–274 (1994).
  122. Cao, X. B. *et al.* Fabrication of high quality perovskite films by modulating the Pb-O bonds in Lewis acid-base adducts. *Journal of Materials Chemistry A* **5**, 8416–8422 (2017).
  123. Leguy, M. A. *et al.* Reversible Hydration of CH<sub>3</sub> NH<sub>3</sub>PbI<sub>3</sub> in Films, Single Crystals, and Solar Cells. *Chemistry of Materials* **27**, 3397–3407 (2015).

- 
124. Kamminga, M. E., De Wijs, G. A., Havenith, R. W. A., Blake, G. R. & Palstra, T. T. M. The Role of Connectivity on Electronic Properties of Lead Iodide Perovskite-Derived Compounds. *Inorganic Chemistry* **56**, 8408–8414 (2017).
  125. Wang, F. *et al.* Phenylalkylamine Passivation of Organolead Halide Perovskites Enabling High-Efficiency and Air-Stable Photovoltaic Cells. *Advanced Materials* **28**, 9986–9992 (2016).
  126. Ma, C. *et al.* High performance low-dimensional perovskite solar cells based on a one dimensional lead iodide perovskite. *Journal of Materials Chemistry A* **7**, 8811–8817 (2019).
  127. Lin, J. *et al.* Thermochromic halide perovskite solar cells. *Nature Materials* **17**, 261–267 (2018).
  128. Yang, J., Siempelkamp, B. D., Liu, D. & Kelly, T. L. Investigation of CH<sub>3</sub>NH<sub>3</sub>PbI<sub>3</sub> Degradation Rates and Mechanisms in Controlled Humidity Environments Using in Situ Techniques. *ACS Nano* **9**, 1955–1963 (2015).
  129. Ouyang, Y. *et al.* Photo-oxidative degradation of methylammonium lead iodide perovskite: mechanism and protection. *Journal of Materials Chemistry A* **7**, 2275–2282 (2019).
  130. Lin, Y. *et al.* Unveiling the operation mechanism of layered perovskite solar cells. *Nature Communications* **10**, 1008 (2019).
  131. Yinghong, H. *et al.* Identifying and controlling phase purity in 2D hybrid perovskite thin films †. *Journal of Materials Chemistry C* **6**, 22215–22225 (2018).
  132. Liang, C. *et al.* Two-dimensional Ruddlesden–Popper layered perovskite solar cells based on phase-pure thin films. *Nature Energy* **6**, 38–45 (2021).
  133. Dučinskas, A. *et al.* Unravelling the Behavior of Dion–Jacobson Layered Hybrid Perovskites in Humid Environments. *ACS Energy Letters* **6**, 337–344 (2021).
  134. Milić, J. v. Multifunctional layered hybrid perovskites. *Journal of Materials Chemistry C* **9**, 11428–11443 (2021).
  135. Blancon, J. C., Even, J., Stoumpos, C. C., Kanatzidis, M. G. & Mohite, A. D. Semiconductor physics of organic–inorganic 2D halide perovskites. *Nature Nanotechnology* **15**, 969–985 (2020).
  136. Wang, Y. *et al.* Photo de-mixing in Dion–Jacobson two-dimensional mixed halide perovskites. *Advanced Energy Materials* **12**, 2200768 (2022).
  137. Mathew, P. S., Dubose, J. T., Cho, J. & Kamat, P. v. Spacer Cations Dictate Photoinduced Phase Segregation in 2D Mixed Halide Perovskites. *ACS Energy Letters* **6**, 2499–2501 (2021).
  138. Yao, Z. *et al.* Role of alkyl chain length in diaminoalkane linked 2D Ruddlesden–Popper halide perovskites. *CrystEngComm* **20**, 6704–6712 (2018).
  139. Safdari, M. *et al.* Layered 2D alkylammonium lead iodide perovskites: Synthesis, characterization, and use in solar cells. *Journal of Materials Chemistry A* **4**, 15638–15646 (2016).

- 
140. Hu, J. *et al.* Synthetic control over orientational degeneracy of spacer cations enhances solar cell efficiency in two-dimensional perovskites. *Nature Communications* **10**, 1276 (2019).
141. Du, K. Z. *et al.* Two-Dimensional Lead(II) Halide-Based Hybrid Perovskites Templated by Acene Alkylamines: Crystal Structures, Optical Properties, and Piezoelectricity. *Inorganic Chemistry* **56**, 9291–9302 (2017).
142. Gélvez-Rueda, M. C. *et al.* Inducing Charge Separation in Solid-State Two-Dimensional Hybrid Perovskites through the Incorporation of Organic Charge-Transfer Complexes. *Journal of Physical Chemistry Letters* **11**, 824–830 (2020).
143. Quan, L. N. *et al.* Ligand-Stabilized Reduced-Dimensionality Perovskites. *J Am Chem Soc* **138**, 2649–2655 (2016).
144. Zhang, X. *et al.* Orientation Regulation of Phenylethylammonium Cation Based 2D Perovskite Solar Cell with Efficiency Higher Than 11%. *Advanced Energy Materials* **8**, 1702498 (2018).
145. Gélvez-Rueda, M. C. *et al.* Formamidinium-Based Dion-Jacobson Layered Hybrid Perovskites: Structural Complexity and Optoelectronic Properties. *Advanced Functional Materials* **30**, 2003428 (2020).
146. Hou, M. *et al.* Aryl Diammonium Iodide Passivation for Efficient and Stable Hybrid Organ-Inorganic Perovskite Solar Cells. *Advanced Functional Materials* **30**, 2002366 (2020).
147. Yao, Z. *et al.* Role of alkyl chain length in diaminoalkane linked 2D Ruddlesden-Popper halide perovskites. *CrystEngComm* **20**, 6704–6712 (2018).
148. Jahanbakhshi, F. *et al.* Organic Spacers in 2D Perovskites: General Trends and Structure-Property Relationships from Computational Studies. *Helvetica Chimica Acta* **104**, e2000232 (2021).
149. Jaroslav, S. I. S. The mechanism of the oxidative polymerization of aniline and the formation of supramolecular polyaniline structures. *Polym Int* **57**, 1295–1325 (2008).
150. Zheng, Y. *et al.* Oriented and Uniform Distribution of Dion–Jacobson Phase Perovskites Controlled by Quantum Well Barrier Thickness. *Solar RRL* **3**, 1900090 (2019).
151. Gómez, V. *et al.* Pressure-Modulated Broadband Emission in 2D Layered Hybrid Perovskite-Like Bromoplumbate. *Inorganic Chemistry* **59**, 12431–12436 (2020).
152. Merten, L. *et al.* Quantifying Stabilized Phase Purity in Formamidinium-Based Multiple-Cation Hybrid Perovskites. *Chemistry of Materials* **33**, 2769–2776 (2021).
153. Kubicki, D. J., Stranks, S. D., Grey, C. P. & Emsley, L. NMR spectroscopy probes microstructure, dynamics and doping of metal halide perovskites. *Nature Reviews Chemistry* **5**, 624–645 (2021).
154. Piveteau, L., Morad, V. & Kovalenko, M. V. Solid-State NMR and NQR Spectroscopy of Lead-Halide Perovskite Materials. *J Am Chem Soc* **142**, 19413–19437 (2020).



- 
155. Lee, J., Lee, W., Kang, K., Lee, T. & Lee, S. K. Layer-by-Layer Structural Identification of 2D Ruddlesden-Popper Hybrid Lead Iodide Perovskites by Solid-State NMR Spectroscopy. *Chemistry of Materials* **33**, 370–377 (2021).
156. Su, T. Sen *et al.* Crown Ether Modulation Enables over 23% Efficient Formamidinium-Based Perovskite Solar Cells. *J Am Chem Soc* **142**, 19980–19991 (2020).
157. Aebli, M. *et al.* Lead-Halide Scalar Couplings in  $^{207}\text{Pb}$  NMR of  $\text{APbX}_3$  Perovskites ( $\text{A} = \text{Cs}$ , Methylammonium, Formamidinium;  $\text{X} = \text{Cl}$ ,  $\text{Br}$ ,  $\text{I}$ ). *Scientific Reports* **10**, 8229 (2020).
158. Zhang, K. *et al.* Effects of organic ligands on efficiency and stability of perovskite light-emitting diodes. *Journal of Materials Science* **56**, 11436–11447 (2021).
159. Sichert, J. A., Hemmerling, A., Cardenas-Daw, C., Urban, A. S. & Feldmann, J. Tuning the optical bandgap in layered hybrid perovskites through variation of alkyl chain length. *APL Materials* **7**, 041116 (2019).
160. Ishihara, T., Takahashi, J. & Goto, T. Optical properties due to electronic transitions in two-dimensional semiconductors  $(\text{CnH}_{2n+1}\text{NH}_3)_2\text{PbI}_4$ . *Physical Review B* **42**, 11099–11107 (1990).
161. Du, K. Z. *et al.* Two-Dimensional Lead(II) Halide-Based Hybrid Perovskites Templated by Acene Alkylamines: Crystal Structures, Optical Properties, and Piezoelectricity. *Inorganic Chemistry* **56**, 9291–9302 (2017).
162. Liu, G. *et al.* Isothermal pressure-derived metastable states in 2D hybrid perovskites showing enduring bandgap narrowing. *Proc Natl Acad Sci U S A* **115**, 8076–8081 (2018).
163. Wang, G. E. *et al.* Crystal structures and optical properties of 1-D iodoplumbates templated by in situ synthesized p-phenylenediamine derivatives. *Inorganic Chemistry Communications* **14**, 1957–1961 (2011).
164. Kamminga, M. E. *et al.* Confinement Effects in Low-Dimensional Lead Iodide Perovskite Hybrids. *Chem. Mater* **28**, 2 (2016).
165. Roiati, V. *et al.* Stark effect in perovskite/ $\text{TiO}_2$  solar cells: Evidence of local interfacial order. *Nano Letters* **14**, 2168–2174 (2014).
166. Queloz, V. I. E. *et al.* Spatial Charge Separation as the Origin of Anomalous Stark Effect in Fluorous 2D Hybrid Perovskites. *Advanced Functional Materials* **30**, 2000228 (2020).
167. Walters, G. *et al.* The quantum-confined Stark effect in layered hybrid perovskites mediated by orientational polarizability of confined dipoles. *Nature Communications* **9**, 4214 (2018).
168. Sharma, D. K., Hirata, S., Biju, V. & Vacha, M. Stark Effect and Environment-Induced Modulation of Emission in Single Halide Perovskite Nanocrystals. *ACS Nano* **13**, 624–632 (2019).

- 
169. Cappel, U. B., Feldt, S. M., Schöneboom, J., Hagfeldt, A. & Boschloo, G. The influence of local electric fields on photoinduced absorption in dye-sensitized solar cells. *J Am Chem Soc* **132**, 9096–9101 (2010).
170. Giovanni, D. *et al.* Tunable room-temperature spin-selective optical Stark effect in solution-processed layered halide perovskites. *Science Advances* **2**, e1600477 (2016).
171. Jong, U. G. *et al.* Influence of water intercalation and hydration on chemical decomposition and ion transport in methylammonium lead halide perovskites. *Journal of Materials Chemistry A* **6**, 1067–1074 (2018).
172. Svane, K. L. *et al.* How Strong Is the Hydrogen Bond in Hybrid Perovskites? *Journal of Physical Chemistry Letters* **8**, 6154–6159 (2017).
173. Lu, D. *et al.* Thiophene-Based Two-Dimensional Dion-Jacobson Perovskite Solar Cells with over 15% Efficiency. *J Am Chem Soc* **142**, 11114–11122 (2020).
174. Xu, Z. *et al.* Highly Efficient and Stable Dion–Jacobson Perovskite Solar Cells Enabled by Extended  $\pi$ -Conjugation of Organic Spacer. *Advanced Materials* **33**, 2105083 (2021).
175. Sutton, C., Risko, C. & Brédas, J. L. Noncovalent Intermolecular Interactions in Organic Electronic Materials: Implications for the Molecular Packing vs Electronic Properties of Acenes. *Chemistry of Materials* **28**, 3–16 (2016).
176. Kim, K. S., Tarakeshwar, P. & Lee, J. Y. Molecular clusters of  $\pi$ -systems: theoretical studies of structures, spectra, and origin of interaction energies. *Chemical Reviews* **100**, 4145–4185 (2000).
177. Giese, M., Albrecht, M. & Rissanen, K. Anion- $\pi$  interactions with fluoroarenes. *Chemical Reviews* **115**, 8867–8895 (2015).
178. Wang, D. X. & Wang, M. X. Exploring Anion- $\pi$  Interactions and Their Applications in Supramolecular Chemistry. *Accounts of Chemical Research* **53**, 1364–1380 (2020).
179. Fu, H. Dion-Jacobson halide perovskites for photovoltaic and photodetection applications. *Journal of Materials Chemistry C* **9**, 6378–6394 (2021).
180. Milić, J. v., Zakeeruddin, S. M. & Grätzel, M. Layered Hybrid Formamidinium Lead Iodide Perovskites: Challenges and Opportunities. *Accounts of Chemical Research* **54**, 2729–2740 (2021).
181. Zhuang, Y. *et al.* Stability Improvement of 2D Perovskite by Fluorinated-Insulator. *Advanced Materials Interfaces* **8**, 2101343 (2021).
182. Ruiz-Preciado, M. A. *et al.* Supramolecular Modulation of Hybrid Perovskite Solar Cells via Bifunctional Halogen Bonding Revealed by Two-Dimensional  $^{19}\text{F}$  Solid-State NMR Spectroscopy. *J Am Chem Soc* **142**, 1645–1654 (2020).
183. Franssen, W. M. J. & Kentgens, A. P. M. Solid-state NMR of hybrid halide perovskites. *Solid State Nuclear Magnetic Resonance* **100**, 36–44 (2019).

- 
184. Bernard, G. M. *et al.* Methylammonium Cation Dynamics in Methylammonium Lead Halide Perovskites: A Solid-State NMR Perspective. *Journal of Physical Chemistry A* **122**, 1560–1573 (2018).
185. Senocrate, A. & Maier, J. Solid-State Ionics of Hybrid Halide Perovskites. *J Am Chem Soc* **141**, 8382–8396 (2019).
186. Kubicki, D. J., Stranks, S. D., Grey, C. P. & Emsley, L. NMR spectroscopy probes microstructure, dynamics and doping of metal halide perovskites. *Nature Reviews Chemistry* **5**, 624–645 (2021).
187. Dahlman, C. J., Kubicki, D. J. & Reddy, G. N. M. Interfaces in metal halide perovskites probed by solid-state NMR spectroscopy. *Journal of Materials Chemistry A* **9**, 19206–19244 (2021).
188. Smock, S. R., Chen, Y., Rossini, A. J. & Brutchey, R. L. The Surface Chemistry and Structure of Colloidal Lead Halide Perovskite Nanocrystals. *Accounts of Chemical Research* **54**, 707–718 (2021).
189. Mitzi, D. B., Medeiros, D. R. & Malenfant, P. R. L. Intercalated organic-inorganic perovskites stabilized by fluoroaryl-aryl interactions. *Inorganic Chemistry* **41**, 2134–2145 (2002).
190. Xu, Z. & Mitzi, D. B. SnI<sub>4</sub>--based hybrid perovskites templated by multiple organic cations: Combining organic functionalities through noncovalent interactions. *Chemistry of Materials* **15**, 3632–3637 (2003).
191. Li, X., Hoffman, J. M. & Kanatzidis, M. G. The 2D halide perovskite rulebook: How the spacer influences everything from the structure to optoelectronic device efficiency. *Chemical Reviews* **121**, 2230–2291 (2021).
192. Kong, L. *et al.* Highly tunable properties in pressure-treated two-dimensional Dion–Jacobson perovskites. *Proc Natl Acad Sci U S A* **117**, 16121–16126 (2020).
193. Jaffe, A., Lin, Y. & Karunadasa, H. I. Halide Perovskites under Pressure: Accessing New Properties through Lattice Compression. *ACS Energy Letters* **2**, 1549–1555 (2017).
194. Jaffe, A. *et al.* High-pressure single-crystal structures of 3D lead-halide hybrid perovskites and pressure effects on their electronic and optical properties. *ACS Central Science* **2**, 201–209 (2016).
195. Szafranski, M. & Katrusiak, A. Photovoltaic Hybrid Perovskites under Pressure. *Journal of Physical Chemistry Letters* **8**, 2496–2506 (2017).
196. Jaffe, A., Lin, Y., L. Mao, W. & I. Karunadasa, H. Pressure-Induced Conductivity and Yellow-to-Black Piezochromism in a Layered Cu–Cl Hybrid Perovskite. *J Am Chem Soc* **137**, 1673–1678 (2015).
197. Umeyama, D., Lin, Y. & I. Karunadasa, H. Red-to-Black Piezochromism in a Compressible Pb–I–SCN Layered Perovskite. *Chemistry of Materials* **28**, 3241–3244 (2016).
198. Li, Q. *et al.* High Pressure Structural and Optical Properties of Two-Dimensional Hybrid Halide Perovskite (CH<sub>3</sub>NH<sub>3</sub>)<sub>3</sub>Bi<sub>2</sub>Br<sub>9</sub>. *Inorganic Chemistry* **58**, 1621–1626 (2019).

- 
199. Mao, H. K. *et al.* Effect of Pressure , Temperature , and Composition on Lattice Parameters and Density of ( Fe , Mg ) SiO<sub>3</sub>-Perovskites to 30 GPa Earth ' s lower mantle Ito and the elasticity of the perovskite were made at ambient Knittle and Information on the physical con. *Journal of Geophysical Research* **96**, 8069–8079 (1991).
  200. Kung, J. & Rigden, S. Oxide perovskites: pressure derivatives of the bulk and shear moduli. *Physics and Chemistry of Minerals* **26**, 234–241 (1999).
  201. Tu, Q. *et al.* Stretching and Breaking of Ultrathin 2D Hybrid Organic-Inorganic Perovskites. *ACS Nano* **12**, 10347–10354 (2018).
  202. Liu, G. *et al.* Two Regimes of Bandgap Red Shift and Partial Ambient Retention in Pressure-Treated Two-Dimensional Perovskites. *ACS Energy Letters* **2**, 2518–2524 (2017).
  203. Kong, L. *et al.* Simultaneous band-gap narrowing and carrier-lifetime prolongation of organic-inorganic trihalide perovskites. *Proc Natl Acad Sci U S A* **113**, 8910–8915 (2016).
  204. Ashari-Astani, N. *et al.* Ruddlesden-Popper Phases of Methylammonium-Based Two-Dimensional Perovskites with 5-Ammonium Valeric Acid AVA<sub>2</sub>MAN-1PbnI<sub>3</sub> n+1 with n = 1, 2, and 3. *Journal of Physical Chemistry Letters* **10**, 3543–3549 (2019).
  205. Kong, L. *et al.* Simultaneous band-gap narrowing and carrier-lifetime prolongation of organic-inorganic trihalide perovskites. *Proc Natl Acad Sci U S A* **113**, 8910–8915 (2016).
  206. Guzelturk, B. *et al.* Visualization of dynamic polaronic strain fields in hybrid lead halide perovskites. *Nature Materials* **20**, 618–623 (2021).
  207. Limmer, D. T. & Ginsberg, N. S. Photoinduced phase separation in the lead halides is a polaronic effect. *Journal of Chemical Physics* **152**, 230901 (2020).
  208. Liu, D. *et al.* Strain analysis and engineering in halide perovskite photovoltaics. *Nature Materials* vol. 20 1337–1346 Preprint at <https://doi.org/10.1038/s41563-021-01097-x> (2021).
  209. Chen, Y. *et al.* Strain engineering and epitaxial stabilization of halide perovskites. *Nature* **577**, 209–215 (2020).
  210. Zhang, C. *et al.* Fabrication Strategy for Efficient 2D/3D Perovskite Solar Cells Enabled by Diffusion Passivation and Strain Compensation. *Advanced Energy Materials* **10**, 2002004 (2020).
  211. Li, Y. *et al.* Bifunctional Organic Spacers for Formamidinium-Based Hybrid Dion-Jacobson Two-Dimensional Perovskite Solar Cells. *Nano Letters* **19**, 150–157 (2019).
  212. Wang, L., Wang, K., Xiao, G., Zeng, Q. & Zou, B. Pressure-Induced Structural Evolution and Band Gap Shifts of Organometal Halide Perovskite-Based Methylammonium Lead Chloride. *Journal of Physical Chemistry Letters* **7**, 5273–5279 (2016).
  213. Katsura, T. & Tange, Y. A simple derivation of the Birch–Murnaghan equations of state (EOSs) and comparison with EOSs derived from other definitions of finite strain. *Minerals* **9**, 745 (2019).

- 
214. Liang, A. *et al.* First-Order Isostructural Phase Transition Induced by High Pressure in Fe(IO<sub>3</sub>)<sub>3</sub>. *Journal of Physical Chemistry C* **124**, 8669–8679 (2020).
  215. Kitazawa, N. Excitons in two-dimensional layered perovskite compounds: (C<sub>6</sub>H<sub>5</sub>C<sub>2</sub>H<sub>4</sub>NH<sub>3</sub>)<sub>2</sub>Pb(Br,I)<sub>4</sub> and (C<sub>6</sub>H<sub>5</sub>C<sub>2</sub>H<sub>4</sub>NH<sub>3</sub>)<sub>2</sub>Pb(Cl,Br)<sub>4</sub>. *Materials Science and Engineering B* **49**, 233–238 (1997).
  216. Hong, X., Ishihara, T. & Nurmikko, A. U. Dielectric confinement effect on excitons in PbI<sub>4</sub>-based layered semiconductors. *PHYSICAL REVIEW B* **45**, 6961–6964 (1992).
  217. Chen, Y. *et al.* Emission enhancement and bandgap retention of a two-dimensional mixed cation lead halide perovskite under high pressure. *Journal of Materials Chemistry A* **7**, 6357–6362 (2019).
  218. Qin, Y. *et al.* Tuning Pressure-Induced Phase Transitions, Amorphization, and Excitonic Emissions of 2D Hybrid Perovskites via Varying Organic Amine Cations. *J. Phys. Chem. C* **123**, 45 (2019).
  219. Zhang, L., Wu, L., Wang, K. & Zou, B. Pressure-Induced Broadband Emission of 2D Organic–Inorganic Hybrid Perovskite (C<sub>6</sub>H<sub>5</sub>C<sub>2</sub>H<sub>4</sub>NH<sub>3</sub>)<sub>2</sub>PbBr<sub>4</sub>. *Advanced Science* **6**, 1801628 (2019).
  220. Al-Qatatsheh, A. *et al.* Blood Pressure Sensors: Materials, Fabrication Methods, Performance Evaluations and Future Perspectives. *Sensors* **20**, 4484 (2020).
  221. Park, J. *et al.* A Hierarchical Nanoparticle-in-Micropore Architecture for Enhanced Mechanosensitivity and Stretchability in Mechanochromic Electronic Skins. *Advanced Materials* **31**, 1808148 (2019).
  222. Cho, S. *et al.* Large-Area Cross-Aligned Silver Nanowire Electrodes for Flexible, Transparent, and Force-Sensitive Mechanochromic Touch Screens. *ACS Nano* **11**, 7 (2017).
  223. Zhang, W. *et al.* Tunable and Switchable Dielectric Constant in an Amphidynamic Crystal. *J. Am. Chem. Soc* **135**, 7 (2013).
  224. Sun, Y. L., Shi, C. & Zhang, W. Distinct room-temperature dielectric transition in a perchlorate-based organic-inorganic hybrid perovskite. *Dalton Transactions* **46**, 16774–16778 (2017).
  225. Yang, T. Y., Gregori, G., Pellet, N., Grätzel, M. & Maier, J. The Significance of Ion Conduction in a Hybrid Organic-Inorganic Lead-Iodide-Based Perovskite Photosensitizer. *Angewandte Chemie - International Edition* **54**, 7905–7910 (2015).
  226. Walsh, A. & Stranks, S. D. Taking Control of Ion Transport in Halide Perovskite Solar Cells. *ACS Energy Letters* **3**, 1983–1990 (2018).
  227. Senocrate, A. *et al.* The Nature of Ion Conduction in Methylammonium Lead Iodide: A Multimethod Approach. *Angewandte Chemie - International Edition* **56**, 7755–7759 (2017).
  228. Tress, W. *et al.* Understanding the rate-dependent J-V hysteresis, slow time component, and aging in CH<sub>3</sub>NH<sub>3</sub>PbI<sub>3</sub> perovskite solar cells: The role of a compensated electric field. *Energy and Environmental Science* **8**, 995–1004 (2015).

- 
229. Hoke, E. T. *et al.* Reversible photo-induced trap formation in mixed-halide hybrid perovskites for photovoltaics. *Chemical Science* **6**, 613–617 (2015).
230. Kim, G. Y. *et al.* Large tunable photoeffect on ion conduction in halide perovskites and implications for photodecomposition. *Nature Materials* **17**, 445–449 (2018).
231. Motti, S. G. *et al.* Controlling competing photochemical reactions stabilizes perovskite solar cells. *Nature Photonics* **13**, 532–539 (2019).
232. Xiao, Z. *et al.* Giant switchable photovoltaic effect in organometal trihalide perovskite devices. *Nature Materials* **14**, 193–197 (2015).
233. Senocrate, A. *et al.* Charge carrier chemistry in methylammonium lead iodide. *Solid State Ionics* **321**, 69–74 (2018).
234. Haruyama, J., Sodeyama, K., Han, L. & Tateyama, Y. First-principles study of ion diffusion in perovskite solar cell sensitizers. *J Am Chem Soc* **137**, 10048–10051 (2015).
235. Minns, J. L., Zajdel, P., Chernyshov, D., van Beek, W. & Green, M. A. Structure and interstitial iodide migration in hybrid perovskite methylammonium lead iodide. *Nature Communications* **8**, 15152 (2017).
236. Senocrate, A. *et al.* Slow CH<sub>3</sub>NH<sub>3</sub><sup>+</sup> Diffusion in CH<sub>3</sub>NH<sub>3</sub>PbI<sub>3</sub> under Light Measured by Solid-State NMR and Tracer Diffusion. *Journal of Physical Chemistry C* **122**, 21803–21806 (2018).
237. Walsh, A., Scanlon, D. O., Chen, S., Gong, X. G. & Wei, S. H. Self-regulation mechanism for charged point defects in hybrid halide perovskites. *Angewandte Chemie - International Edition* **54**, 1791–1794 (2015).
238. Maier, J. Chemical resistance and chemical capacitance. *Zeitschrift für Naturforschung - Section B Journal of Chemical Sciences* **75**, 15–22 (2020).
239. Domanski, K. *et al.* Migration of cations induces reversible performance losses over day/night cycling in perovskite solar cells. *Energy and Environmental Science* **10**, 604–613 (2017).
240. Domanski, K., Alharbi, E. A., Hagfeldt, A., Grätzel, M. & Tress, W. Systematic investigation of the impact of operation conditions on the degradation behaviour of perovskite solar cells. *Nature Energy* **3**, 61–67 (2018).
241. Kim, G. Y., Senocrate, A., Wang, Y. R., Moia, D. & Maier, J. Photo-Effect on Ion Transport in Mixed Cation and Halide Perovskites and Implications for Photo-Demixing\*\*. *Angewandte Chemie - International Edition* **60**, 820–826 (2021).
242. Seitz, M. *et al.* Halide Mixing Inhibits Exciton Transport in Two-dimensional Perovskites Despite Phase Purity. *ACS Energy Letters* **7**, 358–365 (2022).
243. Lin, Y. *et al.* Suppressed Ion Migration in Low-Dimensional Perovskites. *ACS Energy Letters* **2**, 1571–1572 (2017).

- 
244. Leupold, N., Seibel, A. L., Moos, R. & Panzer, F. Electrical Conductivity of Halide Perovskites Follows Expectations from Classical Defect Chemistry. *European Journal of Inorganic Chemistry* **2021**, 2882–2889 (2021).
245. Merkle, R. & Maier, J. How is oxygen incorporated into oxides? A comprehensive kinetic study of a simple solid-state reaction with SrTiO<sub>3</sub> as a model material. *Angewandte Chemie - International Edition* **47**, 3874–3894 (2008).
246. Senocrate, A. *et al.* Tuning Ionic and Electronic Conductivities in the “hollow” Perovskite {en}MAPbI<sub>3</sub>. *Chemistry of Materials* **33**, 719–726 (2021).
247. Senocrate, A. *et al.* Interaction of oxygen with halide perovskites. *Journal of Materials Chemistry A* **6**, 10847–10855 (2018).
248. Moia, D. & Maier, J. Ion Transport, Defect Chemistry, and the Device Physics of Hybrid Perovskite Solar Cells. *ACS Energy Letters* **6**, 1566–1576 (2021).
249. Futscher, M. H. *et al.* Quantification of ion migration in CH<sub>3</sub>NH<sub>3</sub>PbI<sub>3</sub> perovskite solar cells by transient capacitance measurements. *Materials Horizons* **6**, 1497–1503 (2019).
250. Bertoluzzi, L. *et al.* Mobile Ion Concentration Measurement and Open-Access Band Diagram Simulation Platform for Halide Perovskite Solar Cells. *Joule* **4**, 109–127 (2020).
251. Park, J. & Walsh, A. Embrace your defects. *Nature Energy* **4**, 95–96 (2019).
252. Maier, Joachim. *Physical chemistry of ionic materials : ions and electrons in solids*. (John Wiley, 2004).
253. Lopez-Varo, P. *et al.* Device Physics of Hybrid Perovskite Solar cells: Theory and Experiment. *Advanced Energy Materials* **8**, 1702772 (2018).
254. Bou, A. *et al.* Beyond Impedance Spectroscopy of Perovskite Solar Cells: Insights from the Spectral Correlation of the Electrooptical Frequency Techniques. *Journal of Physical Chemistry Letters* **11**, 8654–8659 (2020).
255. Conings, B. *et al.* Intrinsic Thermal Instability of Methylammonium Lead Trihalide Perovskite. *Advanced Energy Materials* **5**, 1500477 (2015).
256. Eames, C. *et al.* Ionic transport in hybrid lead iodide perovskite solar cells. *Nature Communications* **6**, 7497 (2015).
257. Haruyama, J., Sodeyama, K., Han, L. & Tateyama, Y. First-principles study of ion diffusion in perovskite solar cell sensitizers. *J Am Chem Soc* **137**, 10048–10051 (2015).
258. García-Rodríguez, R., Ferdani, D., Pering, S., Baker, P. J. & Cameron, P. J. Influence of bromide content on iodide migration in inverted MAPb(I<sub>1-x</sub>Br<sub>x</sub>)<sub>3</sub> perovskite solar cells. *Journal of Materials Chemistry A* **7**, 22604–22614 (2019).

- 
259. Meloni, S. *et al.* Ionic polarization-induced current-voltage hysteresis in CH<sub>3</sub>NH<sub>3</sub>PbX<sub>3</sub> perovskite solar cells. *Nature Communications* **7**, 10334 (2016).
260. Ferdani, D. W. *et al.* Partial cation substitution reduces iodide ion transport in lead iodide perovskite solar cells. *Energy and Environmental Science* **12**, 2264–2272 (2019).
261. Tan, S. *et al.* Steric Impediment of Ion Migration Contributes to Improved Operational Stability of Perovskite Solar Cells. *Advanced Materials* **32**, 1906995 (2020).
262. Mahapatra, A. *et al.* Elucidation of the role of guanidinium incorporation in single-crystalline MAPbI<sub>3</sub> perovskite on ion migration and activation energy. *Physical Chemistry Chemical Physics* **22**, 11467–11473 (2020).
263. McGovern, L., Koschany, I., Grimaldi, G., Muscarella, L. A. & Ehrler, B. Grain Size Influences Activation Energy and Migration Pathways in MAPbBr<sub>3</sub> Perovskite Solar Cells. *Journal of Physical Chemistry Letters* **12**, 2423–2428 (2021).
264. Muscarella, L. A. *et al.* Reversible Pressure-Dependent Mechanochromism of Dion–Jacobson and Ruddlesden–Popper Layered Hybrid Perovskites. *Advanced Materials* **34**, 2108720 (2022).
265. Pines, A., Gibby, M. G. & Waugh, J. S. Proton-enhanced NMR of dilute spins in solids. *The Journal of Chemical Physics* **59**, 569–590 (1973).
266. Olve B. Peersen, X. W. I. K. and S. O. S. Variable-Amplitued Cross-Polarization MAS NMR. *Journal of Magnetic Resonance Series A* **104**, 334–339 (1993).
267. Fung, B. M., Khitrin, A. K. & Ermolaev, K. An Improved Broadband Decoupling Sequence for Liquid Crystals and Solids. *Journal of Magnetic Resonance* **142**, 97–101 (2000).
268. Kirchartz, T., Márquez, J. A., Stolterfoht, M. & Unold, T. Photoluminescence-Based Characterization of Halide Perovskites for Photovoltaics. *Advanced Energy Materials* **10**, 1904134 (2020).
269. Giannozzi, P. *et al.* Advanced capabilities for materials modelling with Quantum ESPRESSO. *Journal of Physics Condensed Matter* **29**, 465901 (2017).
270. Giannozzi, P. *et al.* Quantum ESPRESSO toward the exascale. *Journal of Chemical Physics* **152**, 154105 (2020).
271. Giannozzi, P. *et al.* QUANTUM ESPRESSO: A modular and open-source software project for quantum simulations of materials. *Journal of Physics Condensed Matter* **21**, (2009).
272. Willmott, P. R. *et al.* The Materials Science beamline upgrade at the Swiss Light Source. *Journal of Synchrotron Radiation* **20**, 667–682 (2013).
273. Angel, R. J., Allan, D. R., Miletich, R. & Finger, L. W. The Use of Quartz as an Internal Pressure Standard in High-Pressure Crystallography. *Journal of Applied Crystallography* **30**, 461–466 (1997).



- 
274. Prescher, C. & Prakapenka, V. B. DIOPTAS: a program for reduction of two-dimensional X-ray diffraction data and data exploration. <http://dx.doi.org/10.1080/08957959.2015.1059835> **35**, 223–230 (2015).
275. Coelho, A. A., Evans, J., Evans, I., Kern, A. & Parsons, S. The TOPAS symbolic computation system. *Powder Diffraction* **26**, S22–S25 (2011).
276. Rietveld, H. M. A profile refinement method for nuclear and magnetic structures. *Journal of Applied Crystallography* **2**, 65–71 (1969).
277. Jamnik, J. & Maier, J. Generalised equivalent circuits for mass and charge transport: Chemical capacitance and its implications. *Physical Chemistry Chemical Physics* **3**, 1668–1678 (2001).

---

# Chapter 8      Appendix

## 8.1      Supplementary information of Chapter 2

### 8.1.1    Materials and Methods

**Perovskite thin film preparation** involved a 0.4 M (PDMA)PbI<sub>4</sub> solution which was obtained by mixing PbI<sub>2</sub> and (PDMA)I<sub>2</sub> powders in 1:1 equivalent molar ratio with DMF:DMSO (9:1) (v:v). (PDMA)PbI<sub>4</sub> films were solution-processed by a spin-coating procedure. The perovskite solution was dropped on the glass substrate (Assistent 50), which afterwards was spun at 1000 rpm and 4000 rpm for 10 s and 20 s, respectively. Spin-coated films were annealed on a hot plate at 150 °C for 10 min. Both solution preparation and spin-coating/annealing procedures were carried out in an argon atmosphere glovebox (0.5 ppm < O<sub>2</sub> and 0.5 ppm < H<sub>2</sub>O). Prior to perovskite deposition the substrates were ultrasonically cleaned with acetone and ethanol sequentially for 5 minutes. Afterwards samples were cleaned by UV-Ozone for 15 min.

**Perovskite powder preparation** used mechanosynthesis. In this case the reactants were ground in a ball mill (Retsch Ball Mill MM-200) using a grinding jar (10 ml) and a ball (Ø10 mm) for 30 min at 25 Hz. The molar ratio of PbI<sub>2</sub> and (PDMA)I<sub>2</sub> powders was 1:1 which corresponds to the stoichiometry of (PDMA)PbI<sub>4</sub> perovskites. The resulting powders were annealed at 150 °C for 30 min.

**Powder X-Ray diffraction measurements** were carried out using PANalytical Empyrean Series 2 instrument in Bragg-Brentano configuration with Cu K $\alpha$  radiation at 40 kV voltage and 40 mA current. For the grazing incidence measurements, the X-ray incidence angle was set at 2°. In both conditions diffracted X-rays were detected using a PIXcel3d detector.

**Single crystal X-Ray diffraction.** Diffraction data for PDMA-PbI<sub>4</sub>·2H<sub>2</sub>O (Figure S1–S5) were collected on a Rigaku Oxford Diffraction XtaLAB Synergy-R DW diffractometer equipped with a HyPix ARC 150° Hybrid Photon Counting (HPC) detector and for (PDMA)I<sub>2</sub> on a Kuma KM4 diffractometer equipped with Sapphire CCD detector at 100 K using Mo K $\alpha$  ( $\lambda$  = 0.71073 Å). Data were processed using the *CrystAlisPro* software. The structures were solved by direct methods using SHELXS and refined by full-matrix least-squares methods based on  $F^2$  using SHELXL.

**UV-Vis measurements** were performed using a Shimadzu UV-2600 spectrophotometer. Films were placed in an air tight quartz cuvette. During in-situ measurements, the cuvette temperature was set at 29 ± 1 °C. In order to monitor humidity induced changes, the cuvette was flushed with argon gas bubbled through a

---

deionized water vial, which was kept in a bath at 22 °C. The bath temperature was controlled by a thermostat (Julabo). The flow rate of the humidified Ar gas was 200 standard cubic centimetres per minute (sccm). After the humidity equilibrium was reached (60–70%; fluctuations due to variations in cuvette temperature), the UV-Vis absorption spectrum was recorded every 90 seconds.

**AFM measurements:** surface morphology was examined by atomic force microscopy (AFM), using a Cypher instrument (Asylum Researcher) and silicon probes.

**PL measurements:** steady-state photoluminescence (PL) spectra of (PDMA)PbI<sub>4</sub> on glass substrates were recorded with a Fluorolog 322 spectrometer (Horiba Jobin Yvon iHr320 and a CCD) with a bandpass of 5 nm upon excitation at 350 nm (Xenon lamp) with a band pass of 2 nm.

**Thermogravimetric analysis (TGA):** (PDMA)PbI<sub>4</sub> powders were exposed to 70% RH atmosphere for approximately 72 hours. The hydrated powders were then transferred to a quartz crucible and loaded on the TGA balance. Hydrated powders were heated up to 150 °C with a ramp rate of 5 °C/min and then kept at 150 °C for 30 minutes. The mass of the powder was recorded every 15 seconds. The Experiment was performed in a nitrogen atmosphere.

**NMR:** <sup>1</sup>H solid-state NMR experiments were performed at 900 MHz (21.1 T) using 1.3 mm rotors at 50 kHz magic angle spinning (MAS) with a Hahn echo pulse sequence ( $\pi/2$ – $\tau$ – $\pi$ – $\tau$ –acquire), an echo delay,  $\tau$ , of a single rotor period (20  $\mu$ s), and a quantitative recycle delay of 10 s. The spectra were background subtracted with the spectrum of an empty rotor acquired under the same conditions and referenced to adamantane at 1.91 ppm. Spectra were deconvoluted using the dmfit software. 15 hydrated (PDMA)PbI<sub>4</sub> thin films deposited on microscope glass were scraped for the NMR sample.

**XPS:** The X-ray source was Al K $\alpha$  (1486.6 eV) and the binding energy scale was calibrated by setting the C—C (adventitious carbon) peak to 284.8 eV.

**DFT calculations** were performed with the Gaussian 09 Rev. D suite of programs on the Fidis computer cluster of EPFL. The spacer geometry optimizations were performed at the B3LYP/6-31G(d) level of theory.

### 8.1.2 X-ray Crystal Structure Analysis

The single crystals of (PDMA)Pb<sub>2</sub>I<sub>6</sub>×2H<sub>2</sub>O were obtained by aging of the precipitate from the post-reaction mixture obtained by mixing PDMA, MAI, PbO and concentrated aqueous solutions of HI and H<sub>3</sub>PO<sub>2</sub>. The

structure is available on the Cambridge Structural Database under CCDC number 2041350, whereas the structure of (PDMA)I<sub>2</sub> can be found under CCDC number 2041787.

### 8.1.3 Thermogravimetric analysis of (PDMA)PbI<sub>4</sub> and (PDMA)I<sub>2</sub> powders

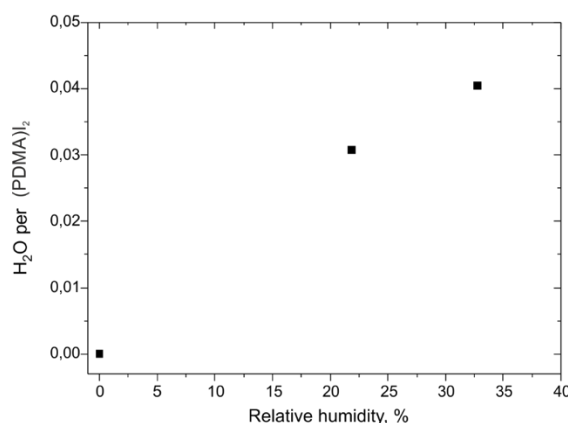


Figure 8:1:1. Hydration degree dependence of (PDMA)PbI<sub>4</sub> powders on the relative humidity (RH) in the range 0–37 %. Results are obtained from an in-situ hydration TGA experiment.

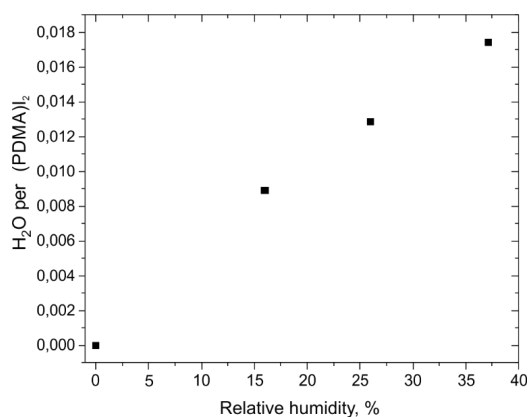


Figure 8:1:2. Hydration degree dependence of (PDMA)I<sub>2</sub> powders on the relative humidity (RH) in the range 0–37 %. Results are obtained from an in-situ hydration TGA experiment.

To determine the hydration degree at 70% RH, powders were hydrated ex-situ and then dehydrated during TGA measurements. The initial, anhydrous (PDMA)PbI<sub>4</sub> mass was 128.6 mg. After hydration and dehydration cycle the powder mass was 128.8 mg. This suggest that during the hydration and dehydration cycle only water molecules were incorporated and expelled from the powders. The in-situ recorded mass change profile with buoyancy effects included is shown in Figure S8. Considering that  $2.65 \pm 0.05$  mg of water was taken by the powders, the ratio between water and Pb atoms is  $98 \pm 2$  %.

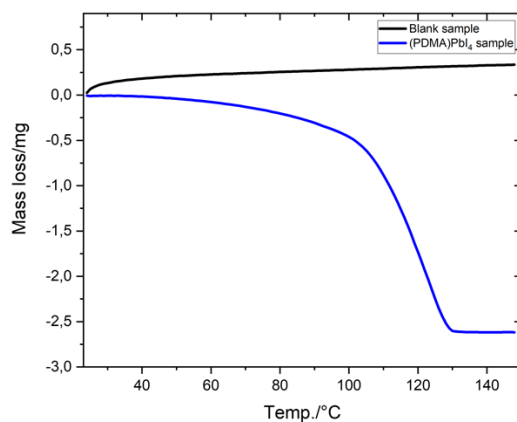


Figure 8:1:3. Mass change profile of (PDMA)PbI<sub>4</sub> powders that were hydrated ex-situ at 65±5 % RH for 53 hours. In order to perform the dehydration of the samples, they were heated up to 150 °C.

#### 8.1.4 Solid-state NMR Spectroscopy

Quantification: Integrating the relative intensities of the NH<sub>3</sub> + aromatic (a + c) and CH<sub>2</sub> (b) resonances in (PDMA)I<sub>2</sub> yields a ratio of 2.67, which is in reasonable agreement with the expected ratio of 2.5 from the stoichiometry of PDMA<sup>2+</sup>. For the hydrated sample, it is not possible to fully resolve and assign the H<sub>2</sub>O resonance which overlaps with the CH<sub>2</sub> signals from both phases. However, by taking the integration of the NH<sub>3</sub> + aromatic (a + c) signal, the expected integration of the CH<sub>2</sub> resonances can be calculated (Table S1). This integration can then be subtracted from the total integration of the CH<sub>2</sub> + H<sub>2</sub>O resonances, leaving the integrated intensity for the H<sub>2</sub>O. Comparing this intensity to the PDMA<sup>2+</sup> NH<sub>3</sub> + aromatic resonance allows the stoichiometry of hydration to be calculated, noting that a factor of 5 is needed to account for the 10 PDMA<sup>2+</sup> NH<sub>3</sub> + aromatic protons compared to two H<sub>2</sub>O protons. If the (NH<sub>3</sub> + aromatic):CH<sub>2</sub> ratio is taken as 2.5, this yields 0.86 H<sub>2</sub>O per PDMA<sup>2+</sup>. If the ratio of 2.67 measured for (PDMA)I<sub>2</sub> is used, then the calculated stoichiometry is 0.99 H<sub>2</sub>O per PDMA<sup>2+</sup>.

Table 8:1:1. Quantification of the H<sub>2</sub>O stoichiometry in hydrated (PDMA)PbI<sub>4</sub>.

<b>NH<sub>3</sub> +aromatic intensity</b>	61.45	
<b>CH<sub>2</sub> + H<sub>2</sub>O intensity</b>	35.17	
<b>(NH<sub>3</sub> + aromatic):CH<sub>2</sub> ratio</b>	2.50	2.67
<b>CH<sub>2</sub> intensity</b>	61.45 × 2.50 = 24.58	61.45 × 2.67 = 23.01
<b>H<sub>2</sub>O intensity</b>	35.17 – 24.58 = 10.59	35.17 – 23.01 = 12.16
<b>Stoichiometry</b>	5 × 10.59 / 61.45 = 0.86	5 × 12.16 / 61.45 = 0.99

### 8.1.5 Supplementary Spectral Data

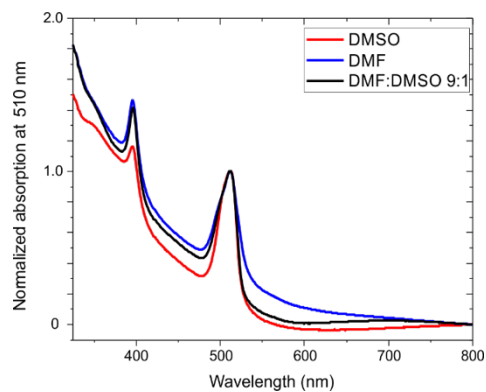


Figure 8:1:4. UV-Vis spectra of (PDMA)PbI<sub>4</sub> thin films that were synthesized using DMF, DMSO and DMF:DMSO 9:1 (v:v) solvents. All spectra show a resonant absorption peak located at 395 nm.

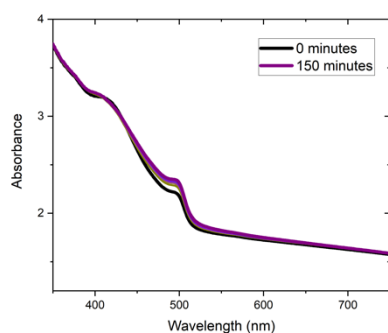


Figure 8:1:5. In-situ UV-Vis absorption spectra of a PbI<sub>2</sub> film during exposure to 60–70% RH. The absorption has been recorded every 90 seconds for 150 minutes.

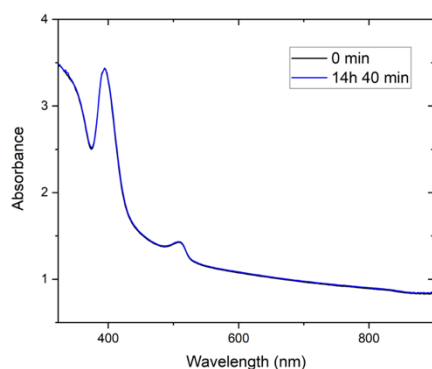


Figure 8:1:6. In-situ UV-Vis absorption of a (PDMA)PbI<sub>4</sub> film just after hydration (black line) and after exposure to 15% RH atmosphere for 14 h 40 min (blue line).

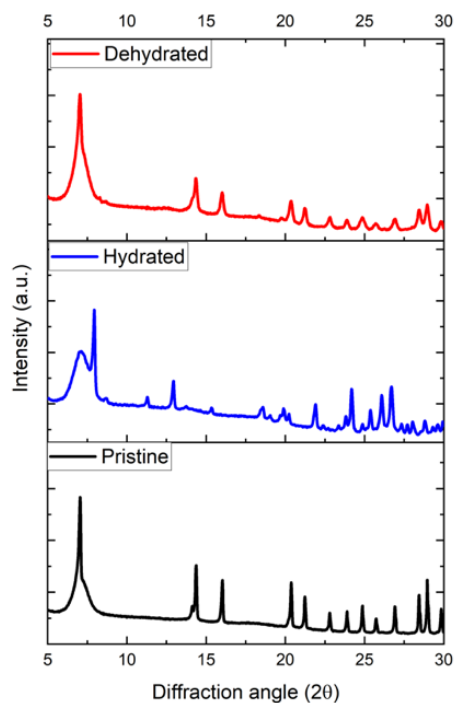


Figure 8:1:7 XRD patterns of (PDMA)PbI<sub>4</sub> powders in pristine (black), hydrated (blue) and dehydrated (red) condition. The dehydration was done under nitrogen atmosphere at 150 °C. The broad signal/background in the region of 7° may be due to the dome used for the in-situ measurements.

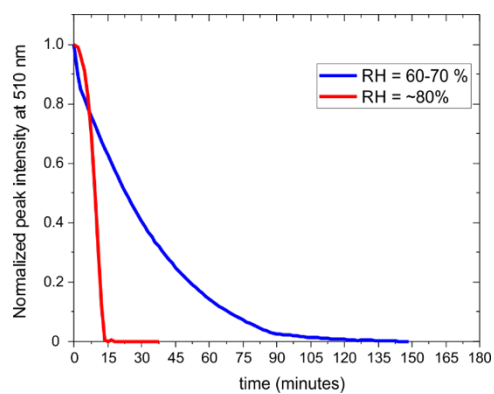


Figure 8:1:8. Time dependence of the 510 nm UV–Vis signal arising from (PDMA)PbI<sub>4</sub> for (PDMA)PbI<sub>4</sub> films at 60–70% RH (blue curve) and at ~80 % RH (red curve), showing faster hydration at 80% RH.

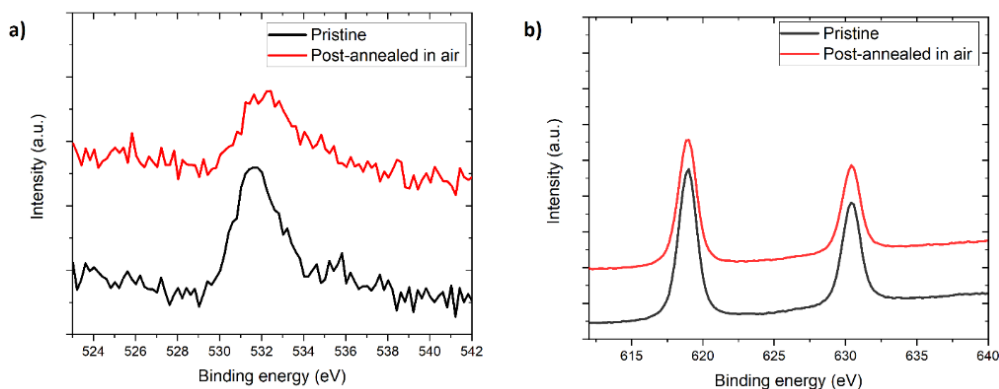


Figure 8:1:9. (a) O 1s XPS spectra of pristine (black) and post-annealed in air (red) samples. (b) I 3d XPS spectra of pristine (black) and post-annealed in air (red) samples.

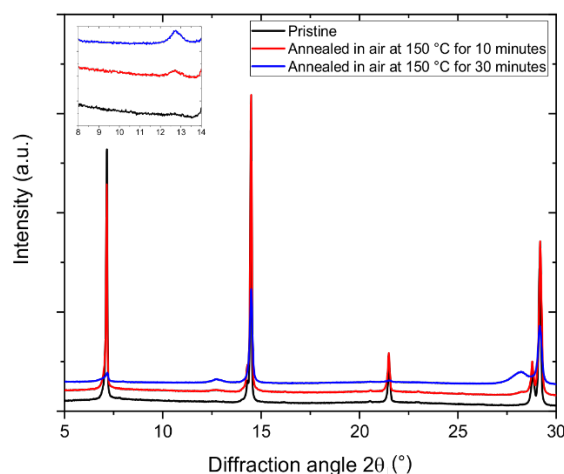


Figure 8:1:10. XRD patterns of (PDMA)PbI<sub>4</sub>, for the pristine film (black) and for films post-annealed in air at 150 °C for 10 minutes (blue) and for 30 min (red). The inset shows the region from 8 to 14°. Here the 12.8° peak becomes more pronounced after longer annealing time, suggesting that during the air annealing process PbI<sub>2</sub> is gradually generated.

## 8.2 Supplementary information of Chapter 3

### 8.2.1 Materials and Methods

**Chemicals used for the perovskite solution.** 1,4-Benzene diammonium iodide (PDA)I<sub>2</sub> (CAS Number: 116469-02-4) and 1,4- Benzene diammonium bromide (PDA)Br<sub>2</sub> (CAS Number: 116469-01-3) were acquired from GreatCell. 1,4-phenylenedimethyleneammonium (PDMA) and 1,4-phenylenediethylammonium



---

(PDEA) spacers were synthesized in house.  $\text{PbI}_2$  inorganic salt with 99.999% purity was bought from Alfa Aesar and  $\text{PbBr}_2$  with >98% purity (CAS Number: 10031-22-8) from TCI. Organic solvents dimethyl sulfoxide (DMSO) with 99.7% purity and dimethylformamide (DMF) with 99.8% purity were acquired from Acros Organics.

**1,4-phenylenediethylammonium iodide (PDEAI<sub>2</sub>).** The solution of 2,2'-(1,4-phenylene)diacetonitrile (500 mg, 3.11 mmol) was suspended in tetrahydrofuran (THF, 5 mL) in an ice-water bath and treated with borane tetrahydrofuran complex solution (9.3 mL, 1.0 M in THF, 3 equiv) under an argon atmosphere. The reaction mixture was stirred for 24 h at ambient temperature. The resulting solution of the amine intermediate was quenched with EtOH (10 mL), treated with HI (1.2 mL, 57% aqueous solution, 3 equiv) in an ice-water bath and stirred for 6 h. The resulting solution was concentrated under vacuum, re-dispersed into EtOH (5 mL) and re-evaporated three times. Then it was poured dropwise into diethyl ether (50 mL). The obtained precipitate was filtered, extensively washed with diethyl ether and dried under vacuum to afford PDEAI<sub>2</sub> (1.08 g, 83%) as a crystalline white solid.

<sup>1</sup>H NMR (400 MHz, (CD<sub>3</sub>)<sub>2</sub>SO):  $\delta$  = 7.59 (bs, 6H), 7.23 (s, 4H), 3.01 (dd,  $J$  = 9.7, 6.2 Hz, 4H), 2.85 (dd,  $J$  = 9.7, 6.2 Hz, 4H) ppm; <sup>13</sup>C NMR (101 MHz, (CD<sub>3</sub>)<sub>2</sub>SO):  $\delta$  = 136.12, 129.48, 40.36, 33.11 ppm.

**1,4-phenylenediethylammonium bromide (PDEABr<sub>2</sub>).** The solution of 2,2'-(1,4-phenylene)diacetonitrile (500 mg, 3.11 mmol) was suspended in tetrahydrofuran (THF, 5 mL) in an ice-water bath and treated with borane tetrahydrofuran complex solution (9.3 mL, 1.0 M in THF, 3 equiv) under an argon atmosphere. The reaction mixture was stirred for 24 h at ambient temperature. The resulting solution of the amine intermediate was quenched with EtOH (10 mL), treated with HBr (1.5 mL, 48% aqueous solution, 4.27 equiv) in an ice-water bath and stirred for 6 h. The resulting solution was concentrated under vacuum, re-dispersed into EtOH (5 mL) and re-evaporated, three times. Then it was poured dropwise into diethyl ether (50 mL). The obtained precipitate was filtered, extensively washed with diethyl ether and dried under vacuum to afford PDEABr<sub>2</sub> (0.78 g, 77%) as a crystalline white solid.

<sup>1</sup>H NMR (400 MHz, (CD<sub>3</sub>)<sub>2</sub>SO):  $\delta$  = 7.85 (bs, 6H), 7.23 (s, 4H), 3.02 (dd,  $J$  = 9.7, 6.2 Hz, 4H), 2.87 (dd,  $J$  = 9.7, 6.2 Hz, 4H) ppm; <sup>13</sup>C NMR (101 MHz, (CD<sub>3</sub>)<sub>2</sub>SO):  $\delta$  = 136.19, 129.38, 40.41, 33.0 ppm.

**Perovskite thin film preparation** included a 0.4 M perovskite (SPbX<sub>4</sub>) solution that was prepared by mixing PbX<sub>2</sub> and SX<sub>2</sub> powders in a 1:1 equivalent molar ratio. Mixtures of iodide containing compounds were dissolved in DMF:DMSO (4:1) (v:v), whereas bromide ones in DMF:DMSO (1:1) (v:v). Spin-coating method was used to prepare the samples. The perovskite solution was dropped on the glass substrate (As-sitent 50), which afterwards was spun at 1000 rpm and 4000 rpm for 10 s and 20 s, respectively. Spin-coated

---

films were annealed on a hot plate at 150 °C for 10 min. Solution preparation procedure was done in an argon atmosphere glovebox ( $0.5 \text{ ppm} < \text{O}_2$ ,  $0.5 \text{ ppm} < \text{H}_2\text{O}$ ), whereas spin-coating was performed in a dry air glovebox ( $\text{RH} < 5\%$ ). Before perovskite deposition the substrates were ultrasonically cleaned with acetone and ethanol sequentially for 5 min. Afterwards samples were cleaned by UV-Ozone for 15 min.

**Sample hydration** was performed in ambient atmosphere. The humidity was controlled with a humidifier, which was filled with deionized water. During hydration samples were kept at 28 °C.

**Perovskite powder preparation** used mechanosynthesis. In this case the reactants were ground in a ball mill (Retsch Ball Mill MM-200) using a grinding jar (10 ml) and a ball ( $\varnothing 10 \text{ mm}$ ) for 30 min at 25 Hz. The molar ratio of  $\text{PbX}_2$  and  $(\text{S}'')\text{X}_2$  ( $\text{X} = \text{I}$ ;  $\text{A}'' = \text{PDEA}$ ) powders was 1:1 which corresponds to the stoichiometry of  $(\text{PDEA})\text{PbI}_4$  perovskites. The resulting powders were annealed at 150 °C for 30 min.

**X-Ray diffraction measurements** were carried out using a PANalytical Empyrean Series 2 instrument in Bragg-Brentano configuration with Cu  $\text{K}\alpha$  radiation at 40 kV voltage and 40 mA current. A nickel filter was used to reduce the  $\text{K}\beta$  contribution.

**GIWAXS** was measured at beamline ID10 of the ESRF and beamline P08 at DESY. Beam energies were 22 keV and 18 keV respectively, with incidence angles from  $0\text{--}0.3^\circ$ . All measurements were done in a nitrogen atmosphere. A Pilatus 300K detector (ESRF) and a Perkin Elmer 2D detector (DESY) were used.

**Solid-state NMR experiments** were performed at 11.7 T with a Bruker Avance III spectrometer. Direct  $^{207}\text{Pb}$  experiments were performed at 15 kHz magic angle spinning (MAS) with a low temperature 3.2 mm probe, using a non-rotor-synchronised spin echo experiment with a 10  $\mu\text{s}$  echo delay, a 0.1 s recycle delay, and 8000 scans. Echo-detected  $^{207}\text{Pb} \rightarrow ^1\text{H}$  HETCOR experiments were performed with a low temperature 1.3 mm probe at 30 kHz MAS, using a contact time of 6 ms with rf powers of  $\sim 120$  and  $\sim 150$  kHz for  $^{207}\text{Pb}$  and  $^1\text{H}$ , respectively, and an effective recycle delay of 80 ms. 32 steps were recorded in the indirect dimension with a 4  $\mu\text{s}$  increment and 24000 scans.  $^1\text{H}$  and  $^{13}\text{C}$  experiments were referenced to adamantane at 1.91 ppm and 38.5 ppm, respectively, and  $^{207}\text{Pb}$  experiments were referenced to  $\text{Pb}(\text{NO}_3)_2$  at  $-3492$  ppm at room temperature.

**UV-Vis measurements** were performed using a Shimadzu UV-2600 spectrophotometer.

---

**PL measurements:** steady-state photoluminescence (PL) spectra of perovskite films on glass substrates were recorded with a Fluorolog 322 spectrometer (Horiba Jobin Yvon iHr320 and a CCD) with a bandpass of 5 nm upon excitation at 370 nm (Xenon lamp) with a band pass of 5 nm and integration time of 0.2s.

**Transient absorption measurements:** Transient absorption (TA) measurements were performed for the samples deposited on the glass substrate. The humidity of the lab was around 30%. For the samples which were susceptible to hydration (PDMA-I), the measurements were done inside of an argon filled cell to ensure that sample hydration was stopped. TA spectra were measured using a femtosecond pump-probe spectrometer based on a Ti:sapphire laser (Clark-MXR, CPA-2001) delivering 778 nm pulses with a width of 150 fs at a 1 kHz repetition rate. Part of the fundamental was passed through a BBO crystal, undergoing second harmonic generation in order to generate the 389 nm pump beam. The probe beam consisted of a broadband white light continuum (400–1050 nm) generated by passing the remainder of the fundamental through a 5 mm-thick oscillating CaF<sub>2</sub> plate. The pump and probe beams were set at magic angle polarization and were spatially and temporally overlapped with respect to each other using a delay stage. The probe beam was split into a signal beam, which passed through the sample, and a reference beam passing next to it in order to account for shot-to-shot fluctuations. The signal and reference beams were dispersed in two separate grating spectrographs (SpectraPro 2500i, Princeton Instruments) and detected shot-to-shot at 1 kHz by 512x58 pixel back-thinned charge-coupled device cameras (Hamamatsu S07030-0906). The frequency of the pump beam was modulated using a chopper set at 500 Hz, which allowed for the absorption with and without the pump to be acquired simultaneously.

### 8.2.2 PDA Solution Instability and its Effects on Thin Film Properties

After complete dissolution, both PDA-I and PDA-Br precursor solutions were transparent. However, over several hours of storage the color changed and eventually they became dark and opaque (Figure S1.) This process can be accelerated if solutions are heated and it is likely associated with the oxidation followed by a polymerization of the corresponding spacer moieties, which is known for anilinium systems.

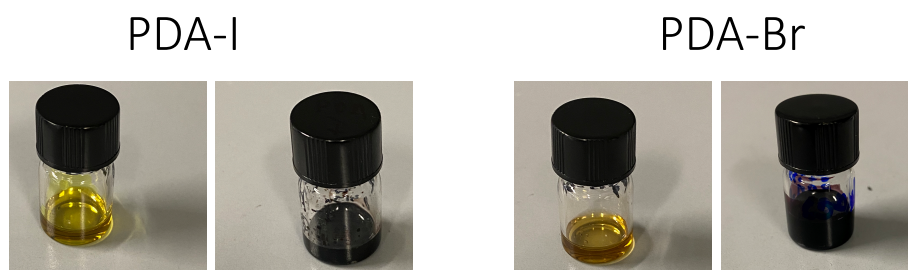


Figure 8:2:1. Photographs of vials with fresh (yellow) and aged (black) solutions of PDA-I and PDA-Br solutions.

Films synthesized using the aged solutions exhibited different optical and structural properties as compared to the ones obtained from fresh solutions. Absorption spectra of samples from aged solution showed a bump in the 500–600 nm interval, which might be attributed to the oxidized spacer since phenylenediammonium salts are known to be very hygroscopic and sensitive to oxygen. X-ray diffraction patterns disclose that the structure of the films obtained from the aged solutions is completely different. In case of PDA-I, samples prepared from a fresh form well defined 1D structure, whereas an aged solution yields a completely different structure with no overlapping diffraction peaks. Similarly, PDA-Br gives a completely different structure.

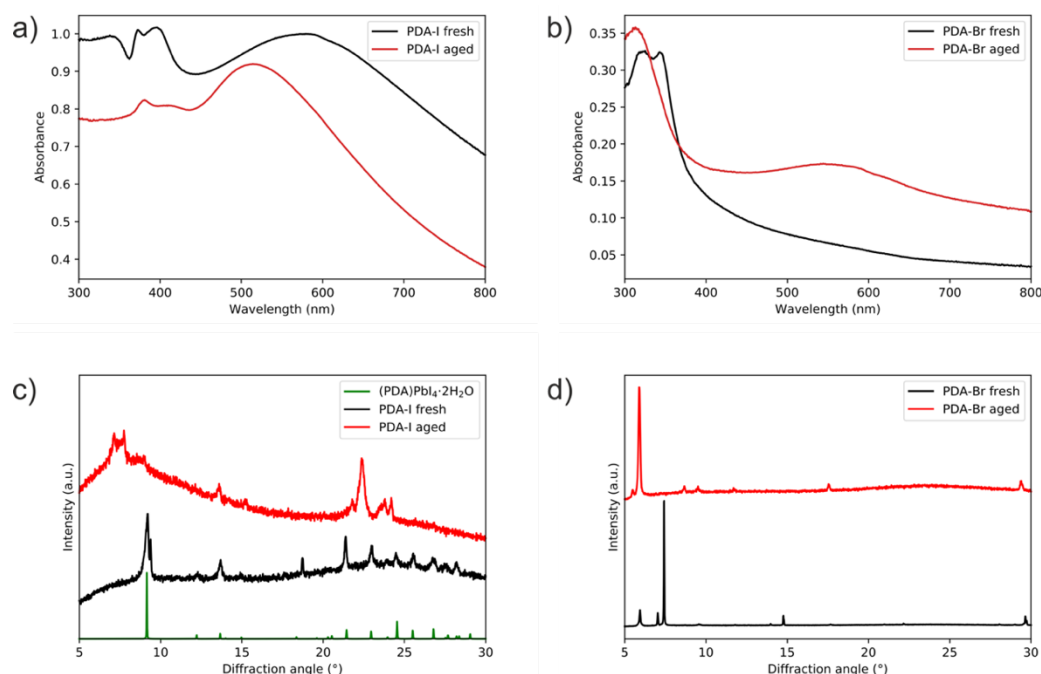


Figure 8:2:2. UV-vis spectra of (a) PDA-I films from fresh (black) and aged (red) precursor solutions, (b) PDA-Br from fresh (black) and aged (red) solutions. X-ray diffractograms of (c) PDA-I from fresh (black), and aged (red) precursor solutions as well as (PDA)PbI<sub>4</sub>·2H<sub>2</sub>O (green), (d) PDA-Br from fresh (black) and aged (red) precursor solutions.

### 8.2.3 Grazing Incidence Wide Angle X-ray Scattering (GIWAXS)

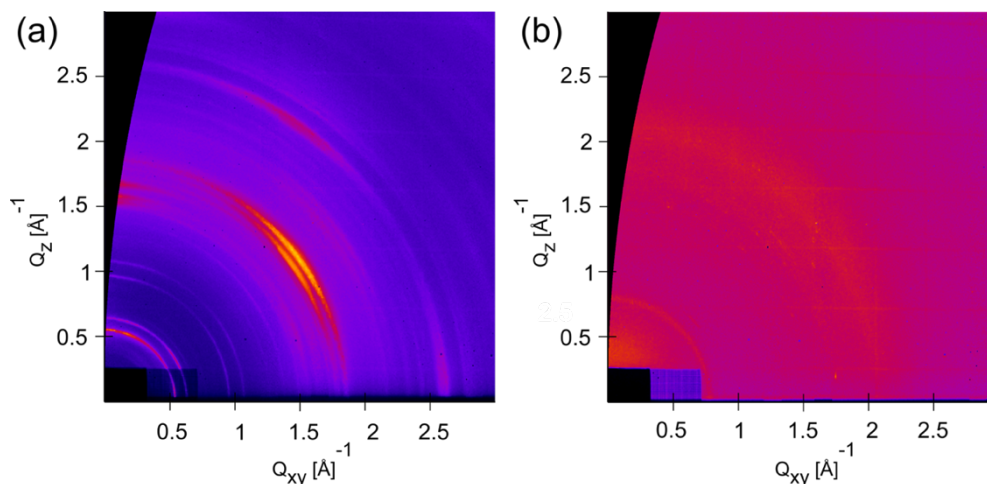


Figure 8:2:3. GIWAXS data of (a) (PDA)PbI<sub>4</sub>, (b) (PDA)PbBr<sub>4</sub>. Please note that thin films used for the measurements were obtained from aged solutions.

### 8.2.4 Transient Absorption Spectroscopy

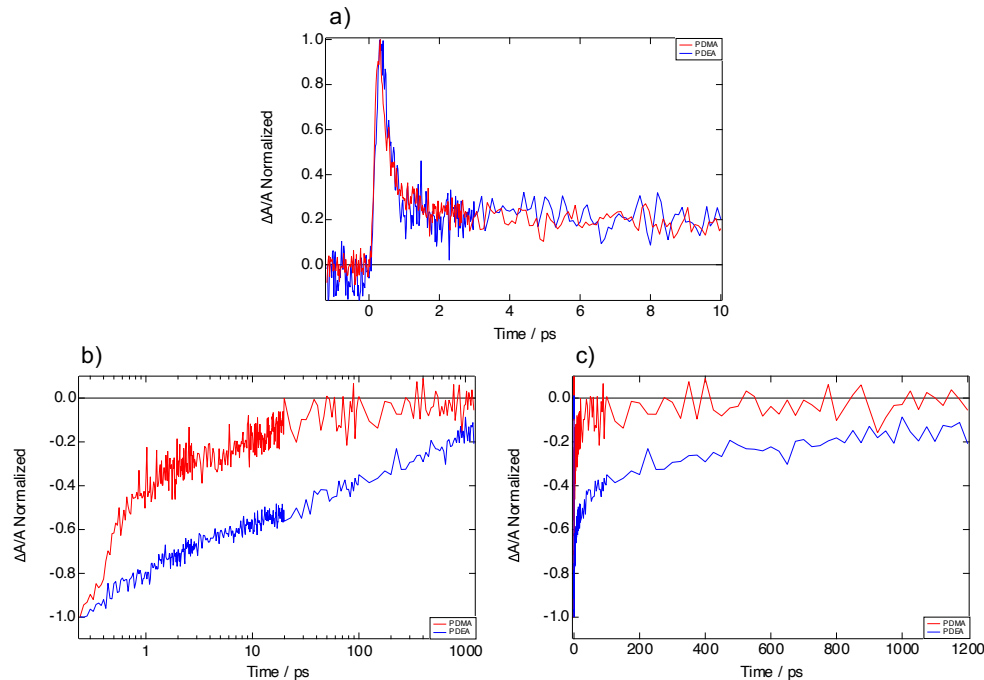
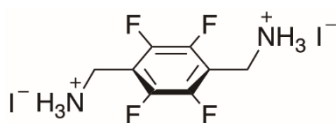


Figure 8:2:4. (a-d) Normalized kinetic traces of the Stark effect feature (a) and the ground state bleaching in logarithmic time scale (b) and in linear time scale (c) taken from TA measurements of PDMA-I (red) and PDEA-I (blue). It is evident from (a) that the dynamics of the Stark effect feature does not change when the spacer size increases from PDMA to PDEA. Therefore, we can say that the difference in size between the two spacers is insufficient to cause a difference in the lifetime of the charge transfer excitons. However, there is a slower decay of the ground state bleaching in the PDEA sample.

## 8.3 Supplementary information of Chapter 4

### 8.3.1 Materials and methods

**The spacers were synthesized** by protonation (PDMAI<sub>2</sub>) and reduction followed by protonation (F-PDMAI<sub>2</sub>), as detailed below. The starting materials were commercially available, and conditions were based on previous reports.<sup>100,133</sup>



**(Perfluoro-1,4-phenylene)dimethanamonium iodide (F-PDMAI<sub>2</sub>):** A solution of 2,3,5,6-tetrafluoroterephthalonitrile (506.1 mg, 2.53 mmol) under nitrogen was suspended in anhydrous tetrahydrofuran (THF) (15 mL) in an ice-water bath and treated with borane tetrahydrofuran complex solution (12 mL, 1.0 M in THF, 12 mmol). The reaction mixture was stirred for 24 h at ambient temperature. The solution of the resulting amine intermediate was quenched with EtOH (25 mL), treated with HI (1.5 mL, 57% aqueous solution, 11.4 mmol) in an ice-water bath and stirred for 6 h. The resulting suspension was then concentrated *in vacuo*, re-dispersed into EtOH (5 mL) and poured dropwise into diethyl ether (200 mL). The obtained precipitate was filtered, extensively washed with diethyl ether and isopropanol, and dried to afford **F-PDMAI<sub>2</sub>** (278 mg, 24%) as a crystalline white solid.

<sup>1</sup>H NMR (400 MHz, (CD<sub>3</sub>)<sub>2</sub>SO):  $\delta$  = 8.33 (bs, 6H), 4.22 (s, 4H) ppm; <sup>13</sup>C NMR (101 MHz, (CD<sub>3</sub>)<sub>2</sub>SO):  $\delta$  = 144.9 (d,  $J$  = 247.4 Hz), 114.3, 30.9 ppm; <sup>19</sup>F NMR (377 MHz, (CD<sub>3</sub>)<sub>2</sub>SO):  $\delta$  = -140.6 ppm.

**Perovskite thin films were prepared** based on  $n = 1$  S<sub>2</sub>PbI<sub>4</sub> compositions (S = PDMA; F-PDMA and 1:1 PDMA:F-PDMA, denoted as PF) through solution processing. Specifically, stoichiometric amounts of PbI<sub>2</sub> and the spacers (or their 1:1 mixture) were dissolved in a solvent mixture of *N,N*-dimethylformamide (DMF)/dimethyl sulfoxide (DMSO) (4:1 v/v). The solution was heated at 60 °C for a few minutes to facilitate this process and the resulting solution was obtained with a concentration of 0.4 M. Both solution preparation and spin-coating/annealing procedures were carried out in an argon atmosphere glovebox (0.5 ppm < O<sub>2</sub> and 0.5 ppm < H<sub>2</sub>O). Prior to perovskite deposition the substrates were ultrasonically cleaned sequentially with acetone and ethanol for 5 min. Thereafter, the samples were cleaned by UV-Ozone for 15 min. The films were deposited on microscope slides (Assistent 50) by spin-coating 30  $\mu$ L of the solution by using a two-step program with an acceleration of 100 rpm/s for 10 s and 2000 rpm/s up to 4000 rpm/s for 20 s followed by annealing at 150 °C for 10 min.

---

**Perovskite thin films for grazing incidence wide angle X-ray scattering** measurements were prepared based on  $n = 1$   $\text{S}_2\text{PbI}_4$  compositions ( $\text{S} = \text{PDMA}$ ;  $\text{F-PDMA}$  and  $1:1 \text{ PDMA:F-PDMA}$ , denoted as PF) through solution processing. Stock solutions of  $\text{PbI}_2$ ,  $\text{PDMA}$ , and  $\text{F-PDMA}$  with a concentration of  $0.4 \text{ M}$  were prepared followed by mixing these stock solutions to obtain the resulting perovskite precursor solutions. The subsequent spin-coating/annealing procedures were in accordance with the previous procedure. In this case, we observed excess  $\text{PbI}_2$  in the measurements.

**Perovskite powders were prepared** based on  $n = 1$   $\text{S}_2\text{PbI}_4$  compositions ( $\text{S} = \text{PDMA}$ ;  $\text{F-PDMA}$  and  $1:1 \text{ PDMA:F-PDMA}$ , denoted as PF) through mechanosynthesis. Stoichiometric amounts of  $\text{PbI}_2$  and the corresponding spacers were ground with beads in a ball mill (Retsch Ball Mill MM-200) using a grinding jar ( $10 \text{ mL}$ ) and a ball ( $\varnothing 10 \text{ mm}$ ) for  $1 \text{ h}$  at  $25 \text{ Hz}$  followed by subsequent annealing in an oven at  $150^\circ \text{C}$  for  $30 \text{ min}$  to get the final powder.

**Powder X-Ray diffraction measurements** were carried out using a PANalytical Empyrean Series 2 instrument in Bragg-Brentano configuration with  $\text{Cu K}\alpha$  radiation at  $40 \text{ kV}$  voltage and  $40 \text{ mA}$  current. For the grazing incidence measurements, the X-ray incidence angle was set at  $2^\circ$ . Under both conditions diffracted X-rays were detected using a PIXcel3d detector.

**Grazing incidence wide angle X-ray scattering (GIWAXS)** of the thin films on microscope glass was measured at  $1.5^\circ$  incidence angle with a D8 Discover Plus TXS (Bruker) equipped with a rotating anode ( $\text{Cu}$ ), a Dectris Eiger2 2D detector, and using a point-collimated beam of approx.  $300 \mu\text{m}$ , at a power of  $5.4 \text{ kW}$ .

**UV-vis measurements** were performed using a Shimadzu UV-2600 spectrophotometer.

**Steady-state photoluminescence (PL) spectra** were recorded with a Fluorolog 322 spectrometer (Horiba Jobin Yvon iHr320 and a CCD) with a bandpass of  $5 \text{ nm}$  upon excitation at  $350 \text{ nm}$  (Xenon lamp) with a band pass of  $2 \text{ nm}$ .

**Solid-state NMR spectra** of mechanochemically prepared powders were recorded on a  $500 \text{ MHz}$  Bruker spectrometer ( $11.7 \text{ T}$ ) equipped with an Avance III console and a  $3.2 \text{ mm}$  three-channel low temperature MAS probe. Samples were packed into  $3.2 \text{ mm}$  zirconia rotors under ambient conditions and spun at a frequency up to  $20 \text{ kHz}$  using nitrogen gas.

<sup>19</sup>F NMR spectra were acquired using a Hahn echo pulse sequence with  $\pi/2$  pulses of 4.5  $\mu$ s, echo delays of four rotor periods and 128 accumulated transients. Recycle delays were set to 1.3 times  $T_1$ . <sup>19</sup>F chemical shifts were referenced to the secondary reference polytetrafluoroethylene (PTFE, -121 ppm). <sup>13</sup>C CP MAS spectra were obtained by transferring polarization either from <sup>1</sup>H or from <sup>19</sup>F to <sup>13</sup>C nuclei by cross polarization (CP)<sup>265</sup> with variable amplitude during a contact time of 1.5 and 2.0 ms respectively.<sup>266</sup> Heteronuclear decoupling of either <sup>1</sup>H or <sup>19</sup>F nuclei was achieved using the spinal64 pulse sequence<sup>267</sup> (<sup>1</sup>H) or continuous wave irradiation (<sup>19</sup>F) at 64 or 80 kHz, respectively. Recycle delays were set to 1.3 times  $T_1$  of the <sup>1</sup>H, respectively <sup>19</sup>F signal and 1024 scans were accumulated for every spectrum. <sup>13</sup>C chemical shifts were referenced to the secondary reference adamantane (left peak at 38.48 ppm).

<sup>13</sup>C CP spectra were obtained by transferring polarisation from either <sup>1</sup>H (dark blue spectra in Figure 4:5c) or from <sup>19</sup>F nuclei (black spectra in Figure 4:5c). The <sup>1</sup>H $\rightarrow$ <sup>13</sup>C CP NMR spectrum of neat PDMA exhibits two signals, one from -CH<sub>2</sub>- (44 ppm) and another from aromatic carbons (134 ppm). In the equivalent spectrum of fluorinated spacers, there are two signals from aromatic carbons (145, 113 ppm) and the -CH<sub>2</sub>- signal is shifted (34 ppm) due to the presence of the fluorine atoms. The <sup>1</sup>H $\rightarrow$ <sup>13</sup>C CP NMR spectrum of the mixture of the two spacers is a linear combination of the spectra of the individual spacers. The spectra of the two perovskite samples are almost identical to the spectra of the pristine spacers used for the synthesis.

The <sup>19</sup>F $\rightarrow$ <sup>13</sup>C CP NMR spectra are composed of significantly broader signals, with more than an order of magnitude larger line width. This is explained by residual dipolar interactions of the protons, which remains significant at the applied magnetic field strength (11.7 T) and the used spinning speed (20 kHz magic angle spinning). For technical reasons, decoupling of <sup>1</sup>H is not possible in the experimental configuration in which <sup>19</sup>F $\rightarrow$ <sup>13</sup>C CP transfer is conducted. An increase of the applied magnetic field and the spinning speed should lead to sufficient reduction of the residual dipolar interaction of the <sup>1</sup>H spins which is necessary to record better resolved <sup>13</sup>C spectra after polarization transfer from <sup>19</sup>F nuclei.

**Contact angle measurements** were recorded with a drop shape analyzer (KRÜSS, DSA100) at ambient temperature to assess hydrophilicity of surfaces.

**Photoluminescence quantum yield (PLQY)** was measured using an integrating sphere (Fluorolog, Horiba Jobin Yvon), an Andor Kymera 193i spectrograph, and a 660 nm continuous-wave laser (OBIS, Coherent) set at 1-Sun equivalent photon flux (1.1  $\mu$ m beam full-width half-maximum, 632  $\mu$ W); photoluminescence was collected at normal incidence using a 0.1 NA, 110  $\mu$ m-diameter optical fiber. For the absolute spectral calibration of the PLQY measurement system, we used a radiometrically calibrated halogen lamp (HL-3 plus CAL from Ocean Optics). PLQY is defined as the emitted photon flux divided by the absorbed photon flux



measured under open circuit; the emitted photon flux is limited by non-radiative recombination processes under this condition.<sup>268</sup>

### 8.3.2 NMR spectroscopy

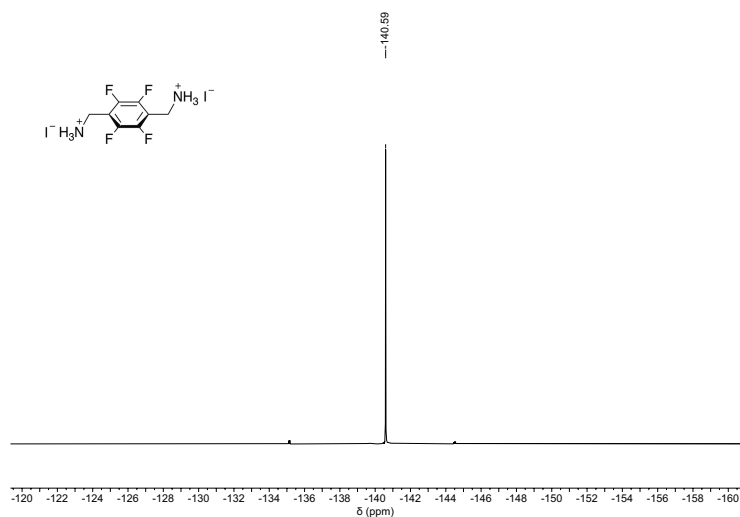


Figure 8:3:1.  $^{19}\text{F}$  NMR spectrum of F-PDMAI<sub>2</sub> in  $(\text{CD}_3)_2\text{SO}$  (400 MHz, 298 K).

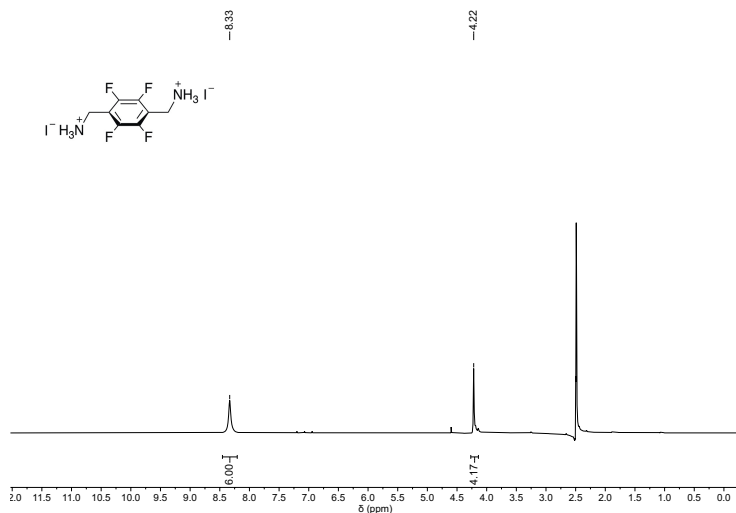


Figure 8:3:2.  $^1\text{H}$  NMR spectrum of F-PDMAI<sub>2</sub> in  $(\text{CD}_3)_2\text{SO}$  (400 MHz, 298 K).

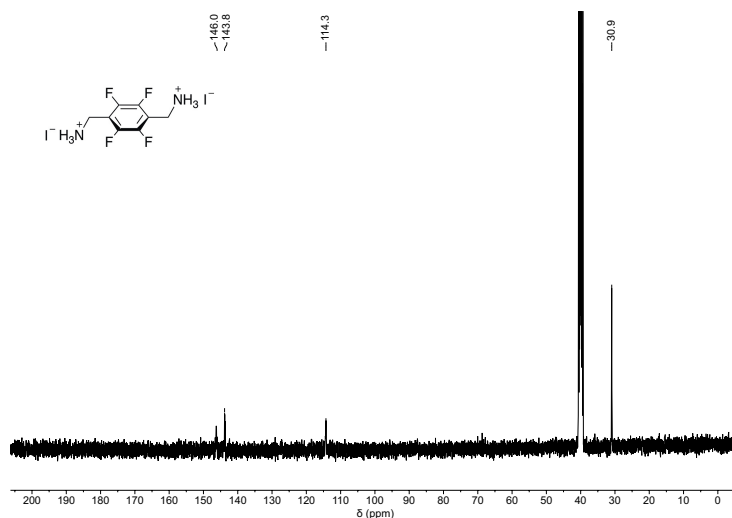


Figure 8:3:3. <sup>13</sup>C NMR spectrum of F-PDMAI<sub>2</sub> in (CD<sub>3</sub>)<sub>2</sub>SO (101 MHz, 298 K).

### 8.3.3 Supplementary data

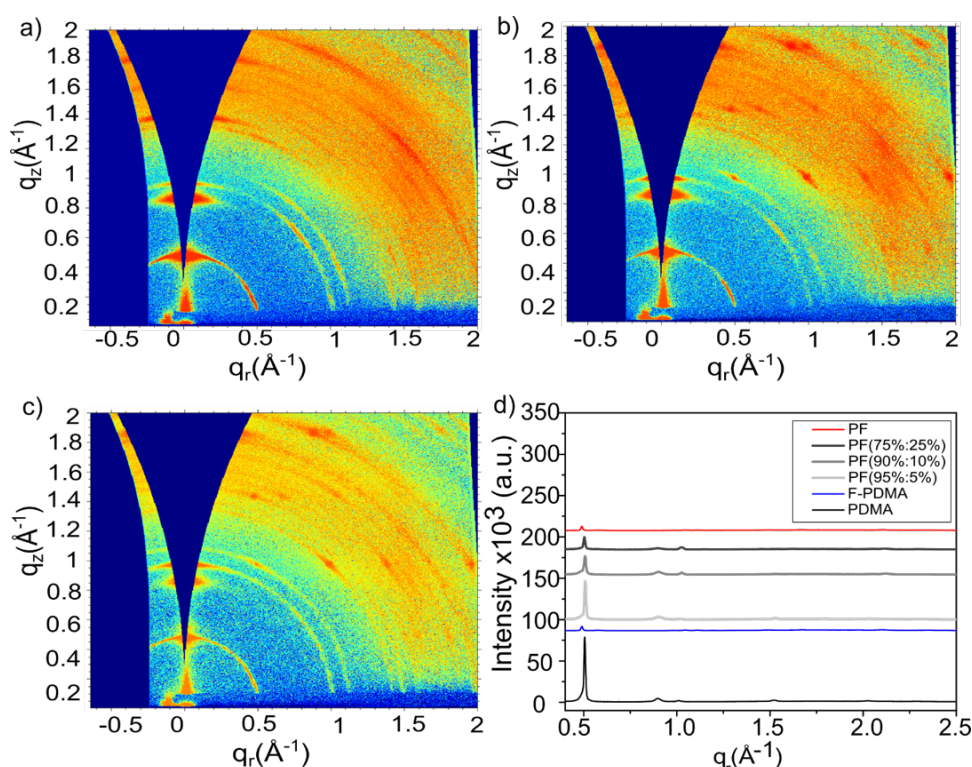


Figure 8:3:4. Grazing incidence wide angle X-ray scattering (GIWAXS) data at incidence angles of ca. 1.5° map of the films with F-PDMA content of a) 5%, b) 10%, and c) 25%. d) Integrated diffraction patterns (from GIWAXS images) for thin films containing PDMA (black), F-PDMA (blue), and their mixtures (PF) based on F-PDMA content of 5% (light grey), 10% (medium grey), 25% (dark grey), and 50% (red) compositions. The data for 2D perovskites based on PF mixtures with 1:1 PDMA and F-PDMA are presented in Figure 2 of the main manuscript.

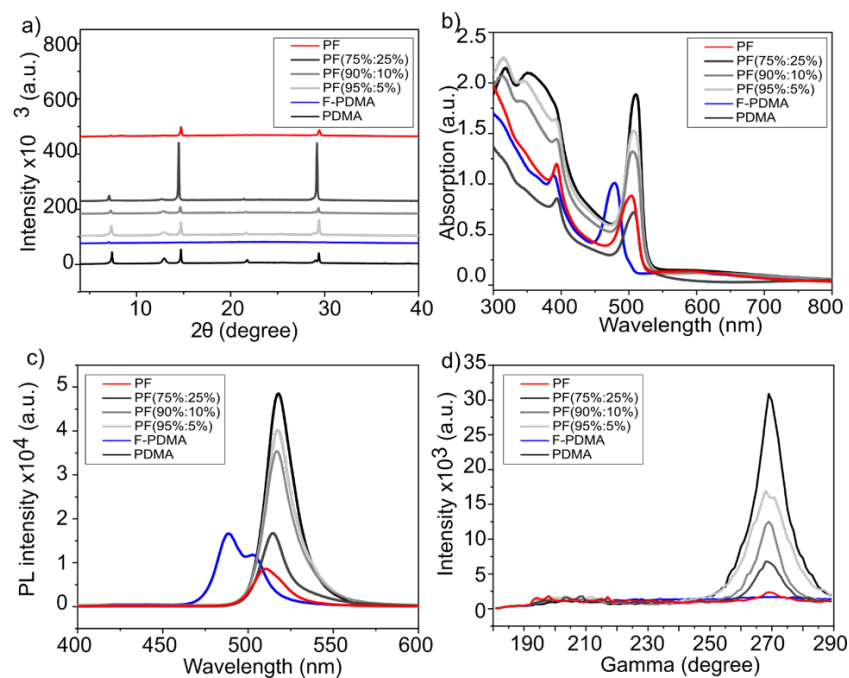


Figure 8:3:5. (a) XRD patterns, b) UV-vis absorption spectra, c) PL spectra d) Gamma scans integration for the peak at  $7.3^\circ$  with  $\gamma = 270^\circ$  corresponds to out-of-plane vector for thin films containing PDMA (black), F-PDMA (blue), and their mixture (PF) with F-PDMA content of 5% (light grey), 10% (medium grey), 25% (dark grey), and 50% (red).

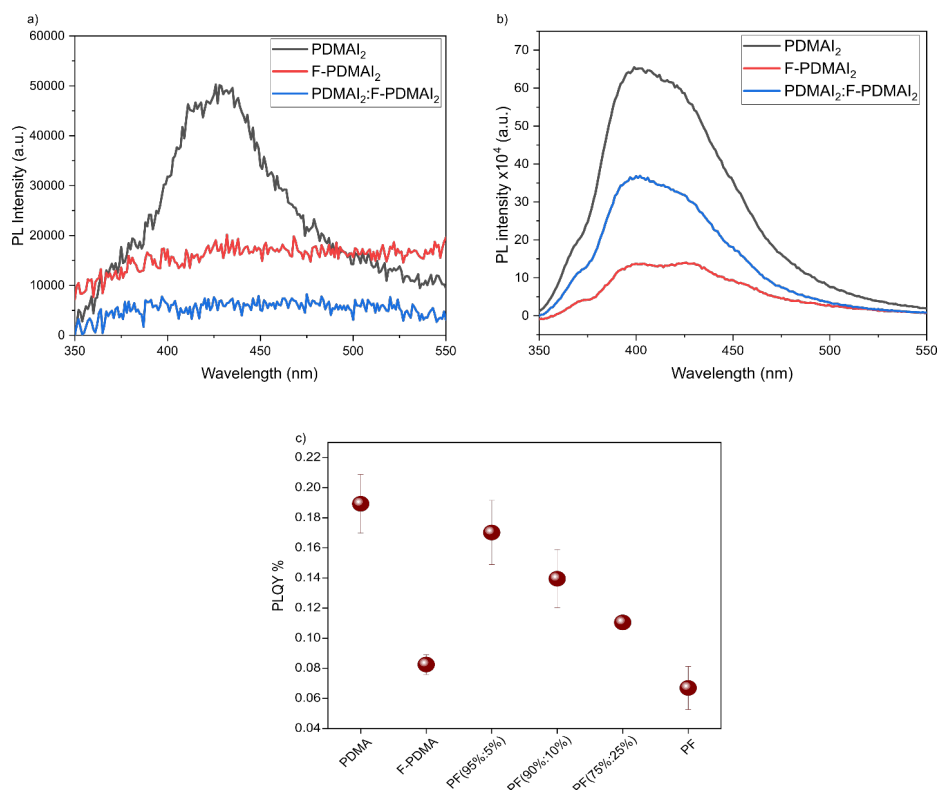


Figure 8:3:6. PL spectra for neat PDMAI<sub>2</sub>, F-PDMAI<sub>2</sub> and their mixture in a) thin films and b) solution of DMSO. c) Photoluminescence quantum yield (PLQY) for thin films based on different compositions.

## 8.4 Supplementary information of Chapter 5

### 8.4.1 Materials and Methods

**Sample preparation.** Iodide-based solutions were obtained mixing PbI<sub>2</sub> and (PDMA)I<sub>2</sub> powders in 1:1 stoichiometric ratio for (PDMA)PbI<sub>4</sub>, whereas 1:2 ratio of PbI<sub>2</sub>:(BzA)I for (BzA)<sub>2</sub>PbI<sub>4</sub>. Subsequently, solid mixtures were dissolved in the *N,N*-dimethylformamide (DMF) and dimethyl sulfoxide (DMSO) solvent mixture (4:1, v/v) to obtain 0.2 M solutions. Bromide-based solutions were made mixing PbBr<sub>2</sub>:(PDMA)Br<sub>2</sub> in 1:1 ratio for (PDMA)PbBr<sub>4</sub> and in 1:2 PbBr<sub>2</sub>:(BzA)Br for (BzA)<sub>2</sub>PbBr<sub>4</sub>. The mixtures were then dissolved in (DMF:DMSO) (1:1, v/v) solvent to obtain 0.2 M solutions. All the films were solution-processed by spin-coating. Before deposition, the glass substrates were ultrasonically cleaned with acetone and ethanol sequentially for 5 min, followed by UV-Ozone cleaning/treatment for 15 min. Precursor solution was dropped on the glass substrate (Assitent 50), which was afterwards spun at 1000 rpm and 4000 rpm for 10 s and 20 s, respectively. Spin-coated films were annealed on a hot plate at 150 °C for 10 min. Solution preparation was

---

carried out in an argon atmosphere glovebox ( $0.5 \text{ ppm} < \text{O}_2$  and  $0.5 \text{ ppm} < \text{H}_2\text{O}$ ), whereas sample deposition in the dry air glovebox ( $RH \approx 5\%$ ).

**Perovskite powder preparation.** Perovskite powders were prepared using mechanosynthesis by grinding the precursor salts in a ball mill (Retsch Ball Mill MM-200) using a grinding jar (10 ml) and a ball ( $\varnothing 10 \text{ mm}$ ) for 30 min at 25 Hz. The molar ratios of all the precursors were stoichiometric and the resulting powders were annealed at  $150^\circ\text{C}$  for 30 min.

**Pressure-dependent absorption.** We measured pressure-dependent absorption using LAMBDA 750 UV/Vis/NIR Spectrophotometer (Perkin Elmer). The samples were placed inside a pressure cell (ISS Inc.) filled with inert liquid (perfluorohexane, FC-72, 3M). The increase in the volume of the liquid inside the pressure cell upon pumping generates high pressure. Measurements are performed from ambient to 0.35 GPa pressure in steps of 0.05 GPa, waiting 7 min before each step to ensure equilibration of the sample under pressure. Prior to use, the liquid is degassed in a Schlenk line to remove oxygen, responsible for scattering of light above 0.300 GPa and consequent reduction of the transmitted signal. We estimate an error of the reading of 0.020 GPa.

**X-Ray diffraction.** Measurements were carried out using PANalytical Empyrean Series 2 instrument in Bragg-Brentano configuration with  $\text{Cu K}\alpha$  radiation at 40 kV voltage and 40 mA current. A nickel filter was used to reduce  $\text{K}\beta$  contribution. A PIXcel3d X-rays detector was used.

**Steady-state photoluminescence.** We measured photoluminescence (PL) with a home-built setup equipped with a 405 nm CW laser source (S1FC405, Thorlabs) for the iodide-based perovskite composition,  $(\text{BzA})_2\text{PbI}_4$  and  $(\text{PDMA})\text{PbI}_4$ . To measure the PL of bromide-based perovskite composition,  $(\text{BzA})_2\text{PbBr}_4$  and  $(\text{PDMA})\text{PbBr}_4$ , a 375 nm laser was used. The PL was coupled into a fiber connected to an OceanOptics USB4000 spectrometer. To remove the excitation laser from the acquired signal, a long-pass filter LP500 was mounted before the spectrometer for the iodide-based compositions. An integration time of 1 s was used for each measurement.

**Density Functional Theory.** All computations were done at the DFT level of theory with the software package Quantum ESPRESSO v6.6 using ultrasoft pseudopotentials from the pslibrary 1.0.0, a wavefunction cut-off of 60 Ry, a charge density cutoff of 480 Ry, a  $\Gamma$ -point centered k-point Monkhorst-Pack grid (according to **Table S1**), Gaussian spreading of 0.005 Ry and the semiempirical Grimme's DFT-D3 vdW correction.<sup>269–</sup>

<sup>271</sup> Relaxations were performed using the PBEsol functional in which the energies and forces are converged up to  $10^{-7}$  Ry and  $10^{-6}$  Ry/Bohr, respectively. For each pressure, the experimentally obtained structure files

were taken as initial starting point. The coordinates of the atoms are fully relaxed (without any constraints) while fixing the lattice parameters at the experimentally measured values. For the PDMA based systems, a  $2 \times 2 \times 1$  supercell was created prior to relaxation. For the computations of the bandgap, single point energy computations were done on the relaxed structures using the Perdew-Burke-Ernzerhof (PBE) functional with a wavefunction convergence up to  $10^{-8}$  Ry and (apart from  $(\text{BzA})_2\text{PbBr}_4$ ) at a denser k-point Monkhorst-Pack grid (Table 8:4-1).

Table 8:4:1. k-point Monkhorst-Pack grid used for the relaxation and SPE of the systems.

System	Relaxation	SPE
$(\text{BzA})_2\text{PbBr}_4$	$8 \times 8 \times 2$	$8 \times 8 \times 2$
$(\text{BzA})_2\text{PbI}_4$	$6 \times 6 \times 2$	$9 \times 10 \times 3$
$(\text{PDMA})\text{PbX}_4$ (X=Br,I)	$4 \times 4 \times 6$	$6 \times 6 \times 9$

**High-pressure powder X-ray diffraction.** High-pressure powder XRD measurements were performed with synchrotron radiation in the Swiss Light Source ( $\lambda = 0.49217 \text{ \AA}$  and Pilatus 6M detector).<sup>272</sup> The samples were compressed in a membrane diamond-anvil cell using DAPHNE oil as a pressure-transmitting medium. Prior to the measurement, the cell is pre-pressurized applying a pressure of 3-4 bars on the membrane to avoid leaks and ensure a good sealing. This results in a slightly higher value for the first datapoint with respect to ambient pressure. We note that the response of the membrane used to measure the  $(\text{PDMA})\text{PbBr}_4$  is higher than for the other compositions, resulting in higher starting pressure. We used  $\alpha$ -quartz as a pressure calibrant, blended together with a sample, and diffraction patterns of the mixture were collected. The equation of state of quartz was used to determine pressure with accuracy of approximately 0.005 GPa.<sup>273</sup> Raw data was processed in Dioptas<sup>274</sup> extracting patterns of the mixtures after masking diffraction spots from the diamonds. PXRD patterns were treated with TOPAS software and unit-cell parameters were determined using Rietveld refinement.<sup>275,276</sup> Positions of the atoms in all the four compounds were refined isotropically, the exception is  $(\text{BzA})_2\text{PbBr}_4$  where the inorganic fragment was treated as a rigid body and refined anisotropically.

## 8.4.2 Supplementary figures and tables

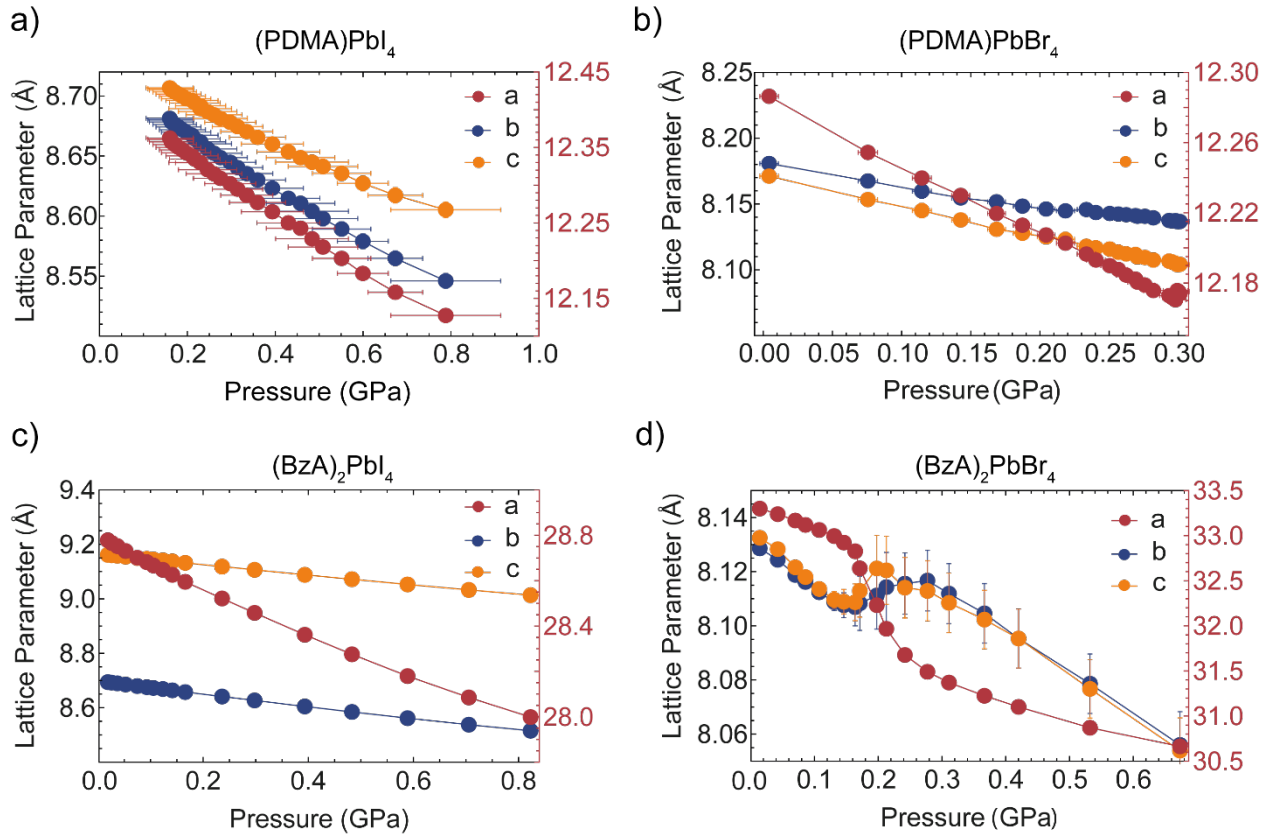


Figure 8:4:1. Lattice parameters as a function of pressure obtained from Rietveld refinements of diffraction patterns for a) (PDMA)PbI<sub>4</sub>, b) (BzA)<sub>2</sub>PbI<sub>4</sub>, c) (PDMA)PbBr<sub>4</sub>, d) (BzA)<sub>2</sub>PbBr<sub>4</sub>. The red axis refers to the *a*-axis (in red). When not present, the error bars are smaller than the symbol size.

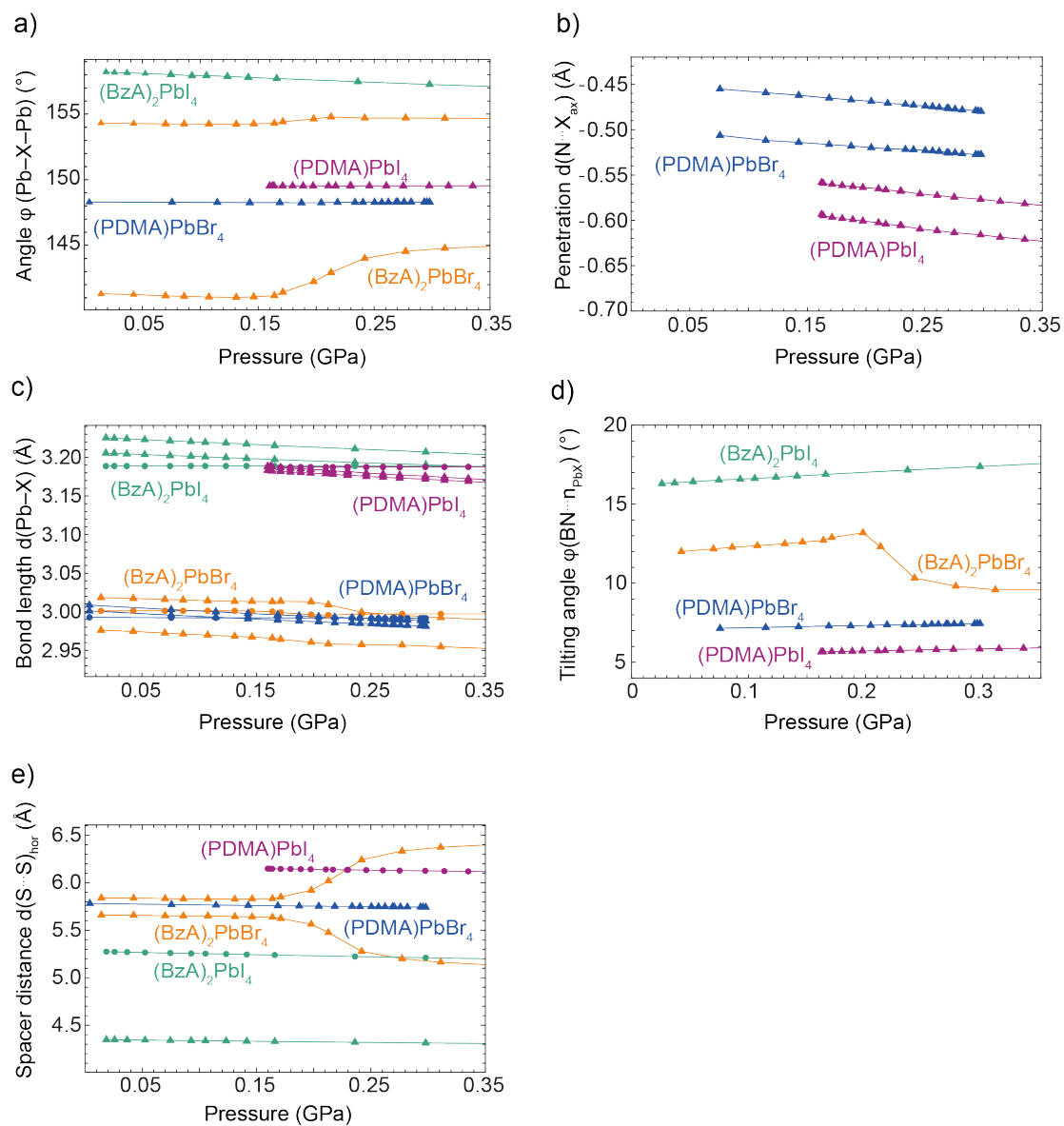


Figure 8:4.2. Computed a)  $\phi(Pb-X-Pb)$  tilting angle and b) nitrogen penetration depth in the plane formed by the halide atoms  $d(N \cdots X_{ax})$ . The penetration depths of the two nitrogens in the PDMA spacer are not equivalent. Computed c) average equatorial (triangle) and axial (disk) Pb-X bond lengths  $d(Pb-X)$ . The octahedra has two inequivalent equatorial bonds and one axial bond and d) average tilting angles of the benzyl ring relative to the *a*-axis  $\phi(BzA \cdots n_{PBX})$ . e) Computed horizontal distance between the spacers  $d(S \cdots S)_{hor}$ .



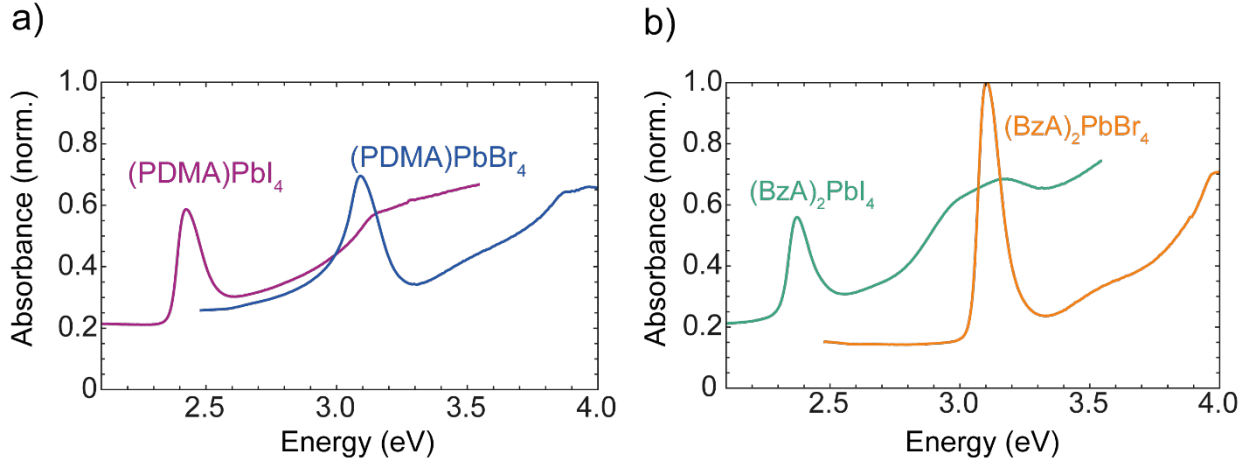


Figure 8:4:3. Absorbance collected at ambient pressure for a) (PDMA)PbI<sub>4</sub> and (PDMA)PbBr<sub>4</sub>, b) (BzA)<sub>2</sub>PbI<sub>4</sub> and (BzA)<sub>2</sub>PbBr<sub>4</sub> highlighting the presence of the typical excitonic feature observed in layered 2D perovskites.

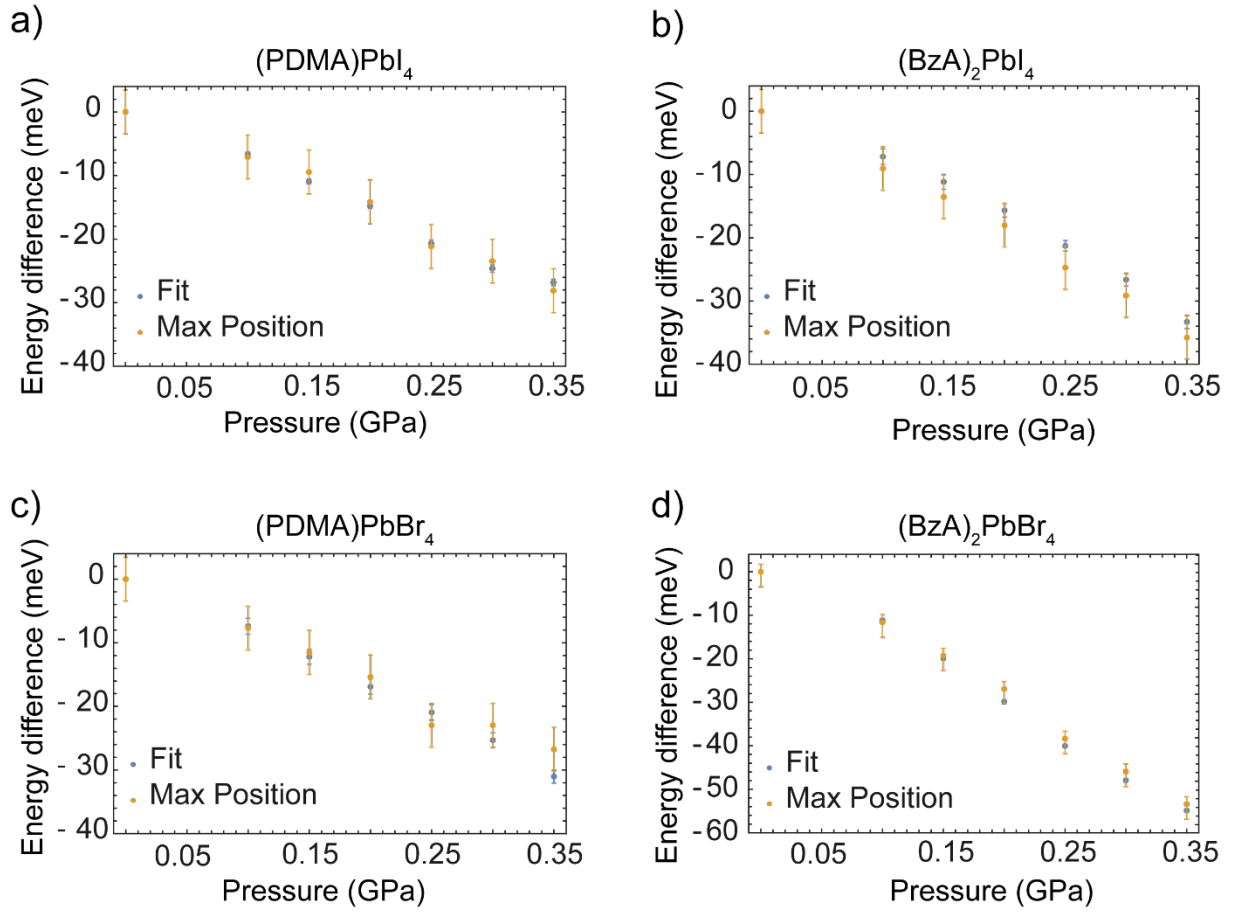


Figure 8:4:4. Excitonic peak estimated using a skewed Gaussian fit (blue) and the maximum intensity position of the excitonic feature (in orange) for a) (PDMA)PbI<sub>4</sub>, b) (BzA)<sub>2</sub>PbI<sub>4</sub>, c) (PDMA)PbBr<sub>4</sub>, d) (BzA)<sub>2</sub>PbBr<sub>4</sub>. The two methods result in comparable results. The larger error in the second method is given by the resolution of the absorbance measurement.

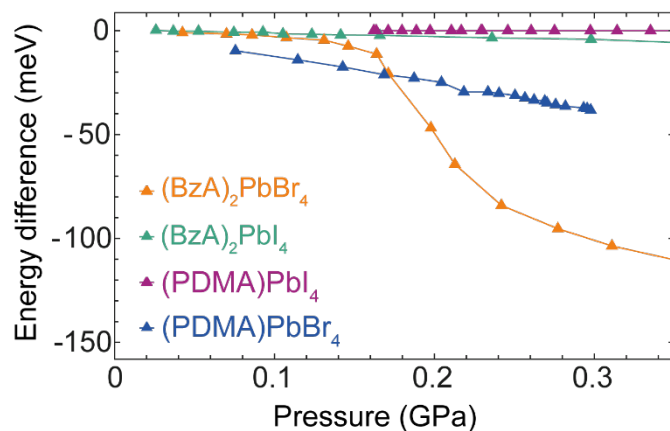


Figure 8:4:5. DFT calculation of the change of bandgap  $E_{\text{gap}}$  relative to the corresponding structure at low pressure for all the compositions in study.

#### 8.4.3 Synchrotron data analysis and beam damage

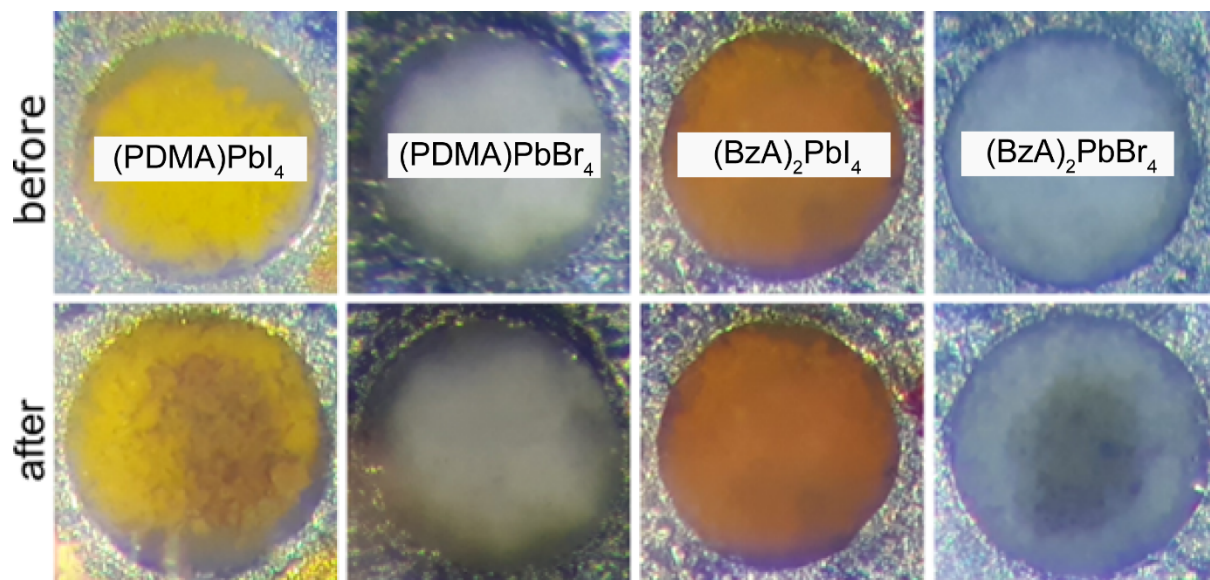


Figure 8:4:6. The samples inside a diamond anvil cell with a visible radiation damage after the experiments. The presence of this damage does not affect the reliability of our experiments because the main reflection of the phases we analyze correspond to their reference crystal structures.

A detailed description of the XRD patterns for all the four samples (Figure 8:4-7) is reported below.

---

**The mechanosynthesis of (BzA)<sub>2</sub>PbI<sub>4</sub>** resulted in almost a full conversion of the precursors into the desired product. The fitting of SiO<sub>2</sub> (red) and (BzA)<sub>2</sub>PbI<sub>4</sub> (green) patterns left just a few unidentified Bragg peaks (black plot), which were assigned neither to PbI<sub>2</sub> nor BzA-I.

**The reaction leading to (BzA)<sub>2</sub>PbBr<sub>4</sub>** is slower and apart from the product identified (35.9%) the sample contains unreacted precursor BzA-Br and PbBr<sub>2</sub> (18.4 and 11.5%, respectively) and the remaining 34.2% is quartz. All significant reflections were fitted during the refinement (black).

**The scattering of (PDMA)PbI<sub>4</sub> sample** was weaker, thus no strong high-angle reflections appeared for  $2\theta > 26^\circ$ . Only the product and quartz were identified, but some remaining Bragg peaks (black) could come from the phases. Although the fitting of the full substrate's patterns was unsuccessful, some of the reflections matched, which indicates partial amorphisation and/or preferential orientation of the substrate crystals after mechanosynthesis.

**The reaction yield of (PDMA)PbBr<sub>4</sub>** within the given conversion time is not full as PbBr<sub>2</sub> (28.8%) and PDMA-Br (18.6%) were identified in the mixture together with the product (21.7%) and the pressure sensor (30.9%). As indicated before, lack of some reflection (*e.g.* 001  $2\theta \sim 3.7^\circ$ ) may suggest preferential orientation of PDMA-Br crystals. On the other hand, no distinguishable Bragg peaks for  $2\theta > 12^\circ$  and broad reflections below may indicate partial amorphisation of the organic precursor. The crystal structure of (PDMA)PbBr<sub>4</sub> is unknown and for the research purposes, it was assumed it is isostructural to the I-analogue, which gave a good agreement with the collected data. Attempts to obtain a single crystal confirming the crystal structure were unsuccessful.

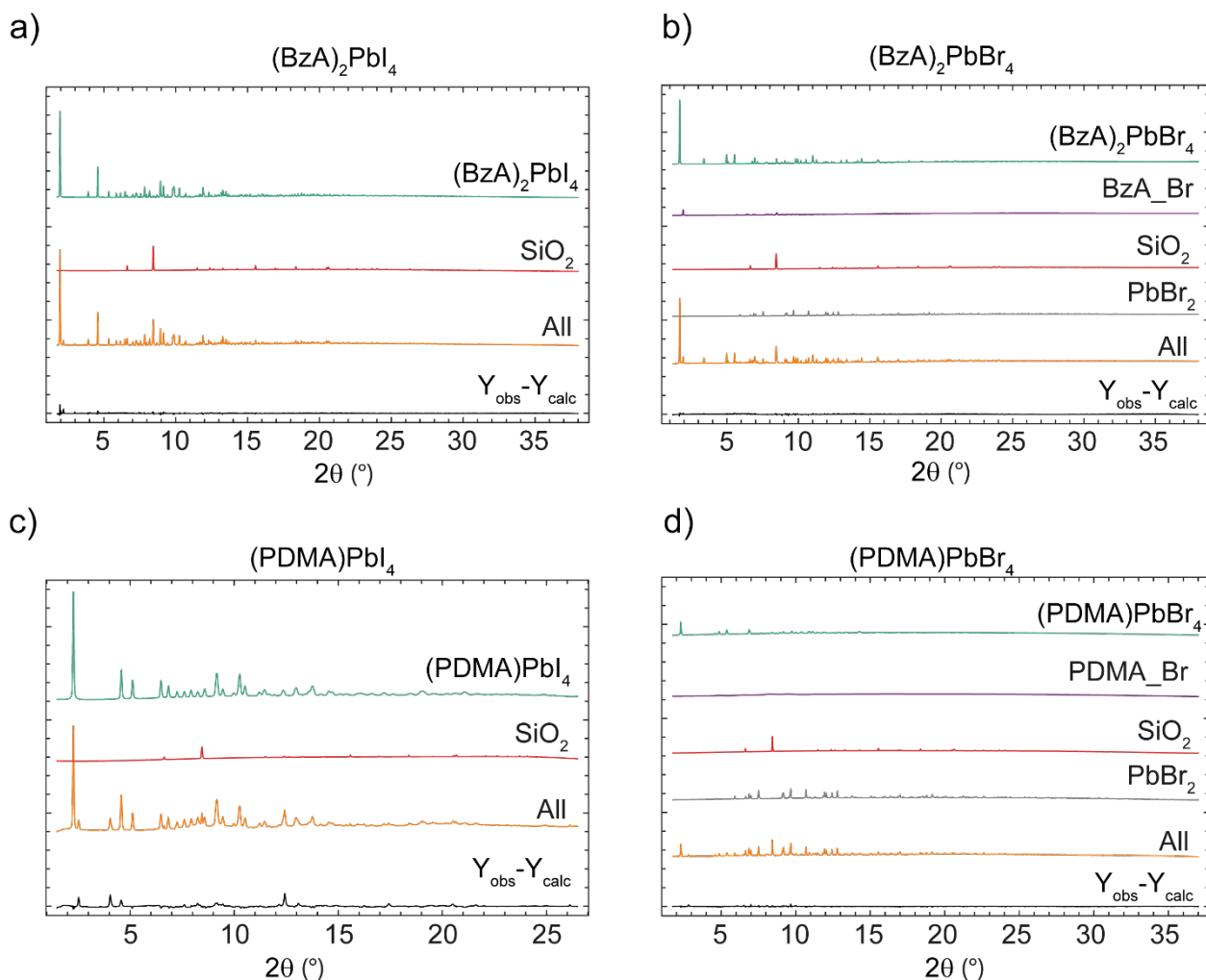


Figure 8:4:7. XRD patterns of a)  $(\text{BzA})_2\text{PbI}_4$ , b)  $(\text{BzA})_2\text{PbBr}_4$ , c)  $(\text{PDMA})\text{PbBr}_4$  and d)  $(\text{PDMA})\text{PbBr}_4$  showing the mixtures (orange) and separated patterns of the components, quartz (red), products (green) and unreacted substrates (if present, gray and magenta).

## 8.5 Supplementary information of Chapter 6

### 8.5.1 Galvanostatic measurements of mixed conductors

The electrical properties of the materials can be investigated using galvanostatic polarization. As the name implies, constant current in the square-wave form is applied during these measurements while the voltage is recorded over time. If the specimen under investigation is solely an electronic conductor, the recorded voltage profile will have the shape of square-wave (Figure 8:5:1a), where Ohm's law defines the maximum voltage. Then using the relationship (equation 8:5:1), conductivity can be calculated. Here,  $A$  – is

the electrode overlap area,  $l$  – the gap between electrode fingers. In order not to violate the linearity assumption from Ohm's law, the polarization measurements should be performed under small voltages. This especially applies to semiconductors.

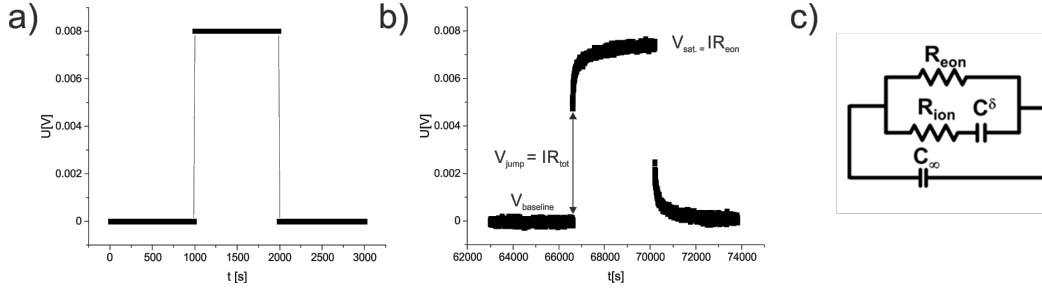


Figure 8:5:1. Representation of galvanostatic polarization profile of (a) electronic conductor and (b) mixed conductor. (c) Simplified equivalent circuit model for the transport in a mixed conductor, adopted from the reference.<sup>277</sup>

$$\sigma = \frac{I}{U} \frac{l}{A}$$

Equation 8:5:1 – Conductivity formula.

In the case of mixed conductors, the voltage profile has a different shape (Figure 8:5:1b). Here, the voltage transient is ascribed to the chemical diffusion, which can be interpreted using the simplified equivalent circuit (Figure 8:5:1c). The polarization process can be divided into three steps based on this model. In the first instance, when current is applied, the current flows through both  $R_{eon}$  (electronic resistance) and  $R_{ion}$  (ionic resistance) rails. Thus, the initial voltage jump ( $V_{jump}$ ) arises from the total conductivity  $R_{tot}$  (equation 8:5:2). Afterward, there is exponential voltage transient with a characteristic time constant ( $\tau^\delta$ ), which is defined by equation 8:5:3, where  $R^\delta$  (equation 8:5:4) – chemical resistance and  $C^\delta$  – chemical capacitance. Lastly, when  $C^\delta$  is fully charged, the voltage reaches saturation ( $V_{sat}$ ) point since the current passes only through the  $R_{eon}$ . Having all this data, the ionic conductivity can be calculated using equation 8:5:5.

$$R_{tot} = \frac{R_{eon}R_{ion}}{R_{eon} + R_{ion}}$$

Equation 8:5:2 – Total resistance formula

$$\tau^\delta = R^\delta C^\delta$$

Equation 8:5:3 – Characteristic time constant formula

$$R^\delta = R_{ion} + R_{eon}$$

Equation 8:5:4 – Chemical resistance formula

$$\sigma_{ion} = \sigma_{tot} - \sigma_{eon}$$

Equation 8:5:5 – Ion conductivity formula

## 8.5.2 Iodine partial pressure control

Given iodine's propensity to directly transform from solid to the gas state, which is called sublimation, we used iodine powder as the source material. In order to control the saturation vapor, the iodine container was kept at a constant temperature inside the thermostat. Table 8:5:1 indicates the temperature ranges for the studied iodine partial pressures, which can be calculated using the 8:5:6 equation. The measurement cell and the iodine container were connected by leakage-proof plastic gas lines. Argon was used as a carrier gas. The exhaust line from the measurement cell was inside the fume hood for the safety since iodine vapor is highly toxic.

$$\log P = -\frac{3512.8}{T} - 2.013 \log T + 13.374$$

Equation 8:5:6 – Relationship between iodine temperature and its partial pressure

Table 8:5:1. Temperatures and their corresponding iodine partial pressure levels on a logarithmic scale.

T (K)	Log P (bar)
233.1	-6.46179
238.1	-6.16388
240.1	-6.0483
243.1	-5.87861
245.1	-5.76786
248.1	-5.60519
252.1	-5.39452
253.1	-5.34293
254.1	-5.29175
258.1	-5.09116
261.1	-4.94488
263.1	-4.84928

---

## Curriculum Vitae

### **Algirdas Dučinskas**

Born on 1 April 1993

Mobile: +41762121051

E-Mail: a.ducinskas@gmail.com / LinkedIn: [www.linkedin.com/in/ducinskas](http://www.linkedin.com/in/ducinskas)

### **Education**

10/2018 – 08/2022

#### **PhD candidate at EPFL University (Switzerland)**

Laboratory of Photonics and Interfaces

Topic: Structure-property relationships and mixed conductivity of layered hybrid perovskites  
(Supervisor: Prof. Michael Graetzel)

- Teaching assistant of Physical Chemistry of Interfaces and Electromagnetism courses

#### **PhD student researcher at Max Planck Institute for Solid State Research (Germany)**

Department of Physical Chemistry of Solids

Topic: Mixed conductivity of layered hybrid perovskites  
(Supervisor: Prof. Joachim Maier)

09/2016 – 09/2018

#### **InnoEnergy master's school, double degree programme**

##### **TU/e Eindhoven University of Technology (The Netherlands)**

**GPA: 8.0/10 (with great appreciation)**

Master of Science in Sustainable Energy Technology / Applied Physics  
09/2017 – 09/2018

Thesis: "Atomic layer deposited nickel oxide for perovskite solar cells"  
(Supervisor: dr. Mariadriana Creatore)

##### **KTH Royal Institute of Technology (Sweden)**

Master of Science in Sustainable Energy Technology  
09/2016 – 09/2017

##### **ESADE Business & Law School (Spain)**

Introductory Crash Course in Entrepreneurship  
01/2017 – 02/2017

09/2012 – 06/2016

#### **Bachelor's degree in Physics, Vilnius University (Lithuania)**

**GPA: 9.4/10, cum laude (with honors)**

Thesis: "Influence of non-local pseudopotential on inter-band optical conductivity spectra in metals."

(Supervisor: Prof. Vytautas Karpus)

### **Professional Experience**

10/2015 – 06/2016

#### **Center for Physical Sciences and Technology, Research Intern, Vilnius**

- Theoretical analysis of inter-band optical transitions in metals (C++ programming)

---

## Awards

- 06/2017 - 07/2017 **Full scholarship holder (Top 30 students), European Campus of Excellence**
- 09/2016 - 09/2018 **Full scholarship holder, InnoEnergy master's school**
- 10/2012 - 06/2016 **Scholarship for outstanding academic results, Vilnius University**

## Participations

- 06/2017 - 07/2017 **Participant in European Campus of Excellence summer school at EPFL and ETH**
- Topic: Energy Systems in Transition and Sustainable Mobility
- 06/2013 - 07/2016 **President and active member of Vilnius University Energy Society**
- Organizing and participating in lectures and conferences related to the energy sector

## Publications

- 2019 **Plasma-assisted atomic layer deposition of nickel oxide as a hole transport layer for hybrid perovskite solar cells**, Koushik, Jošt, Dučinskas, et al., *J. Mater. Chem. C*, 2019, 7, 12532
- 2020 **Unravelling the structural complexity and photophysical properties of adamantyl-based layered hybrid perovskites**, Jahanbakhshi, Mladenović, Kneschaurek, et al., *J. Mater. Chem. A*, 2020, 8, 17732
- 2020 **Formamidinium-Based Dion-Jacobson Layered Hybrid Perovskites: Structural Complexity and Optoelectronic Properties**, Gélvez-Rueda, Ahlawat, Merten, et al., *Adv. Funct. Mater.*, 2020, 30, 2003428
- 2021 **Unravelling the Behavior of Dion–Jacobson Layered Hybrid Perovskites in Humid Environments**, Dučinskas, Kim, Moia, et al., *ACS Energy Lett.*, 2021, 6, 337-344
- 2021 **The Role of Alkyl Chain Length and Halide Counter Ion in Layered Dion–Jacobson Perovskites with Aromatic Spacers**, Dučinskas, Fish, Hope, et al., *J. Phys. Chem. Lett.*, 2021, 12, 10325-10332
- 2022 **Arene-Perfluoroarene  $\pi$ -Systems for Hybrid Layered Dion–Jacobson Perovskites**, Almalki, Dučinskas, Carbone, et al., *Nanoscale*, 2022, Advance Article
- 2022 **Reversible Pressure-Dependent Mechanochromism of Dion-Jacobson and Ruddlesden-Popper Layered Hybrid Perovskites**, Muscarella, Dučinskas, Dankl, et al., *Adv. Mater.*, 2022, 34, 2108720
- 2022 **Photo de-mixing in Dion-Jacobson two-dimensional mixed halide perovskites**, Wang, Senocrate, Mladenović et al., *Adv. Energy Mater.*, 2022, accepted

## Conferences and workshops

- 2019 **International Conference on Perovskite Solar Cells and Optoelectronics (PSCO)**, Lausanne (CH), participant
- 2019 **Max Planck - EPFL Center for Molecular Nanoscience & Technology Science Day**, Lausanne (CH), oral presentation



---

2020 **Max Planck - EPFL Center for Molecular Nanoscience & Technology Science Day**, online, oral presentation

2021 **Max Planck - EPFL Center for Molecular Nanoscience & Technology Science Day**, online, oral presentation

2022 **MRS Spring Meeting & Exhibit**, Honolulu (US), oral presentation

### **Languages and IT skills**

**Lithuanian** (native); **English** (full professional proficiency, IELTS 7.5/9); **German** (limited); **French** (limited)

**Python** (Pandas, PyTorch, Scikit-learn, Seaborn), **Latex**, **Origin Pro**, **Microsoft Office**, **C++**